Control, Readout, and Entanglement of Molecular Qubits

a dissertation presented
by
Lewis Russell Bartos Picard
to
The Department of Physics

in partial fulfillment of the requirements
for the degree of
Doctor of Philosophy
in the subject of
Physics

Harvard University
Cambridge, Massachusetts
August 2024

Thesis advisor: Professor Kang-Kuen Ni Lewis Russell Bartos Picard

Control, Readout, and Entanglement of Molecular Qubits

Abstract

Ultracold polar molecules possess a manifold of long-lived molecular rotational states, which can be coherently controlled using microwave fields and entangled by the long-range dipole-dipole interactions between molecules. The ability to control these features at the individual molecule level provides a rich toolbox with which to engineer quantum simulations of exotic materials or build a molecular quantum computer. Until recently, this level of single molecule control has eluded researchers due to the challenges inherent in taming the complex internal structure of molecules.

In this thesis, we demonstrate full control over the internal quantum states and coherent interactions of individual NaCs molecules in optical tweezers. This platform is based on coherent assembly of ultracold Na and Cs atoms trapped and cooled in separate arrays, before being magnetoassociated at a Feshbach resonance to form weakly-bound molecules. Using high-resolution spectroscopy of electronically excited molecular states, we identify an efficient two-photon pathway to the rovibrational ground state of NaCs that we use to prepare an array of ground state molecules in tweezers. We demonstrate a “magic ellipticity” technique to eliminate differential light shifts be-

tween two molecular rotational states and achieve coherence times of up to 250(40) ms for a superposition of those states. We then show that we can rearrange molecules in an array to eliminate defects and perform single-shot readout of multiple rotational states using controlled molecule dissociation and imaging of constituent atoms at high magnetic field. Finally, we coherently control the dipole-dipole interactions between two molecules, producing a Bell state with a fidelity of 94(3)% and demonstrating a universal entangling iSWAP gate for qubits encoded in molecular hyperfine states.

Contents

Citations to previously published work

This thesis contains material originally distributed in the following publications:

1. Picard, L. R. B., Zhang, J. T., Cairncross, W. B., Wang, K., Patenotte, G. E., Park, A. J., Yu, Y., Liu, L. R., Hood, J. D., González-Férez, R., & Ni, K.-K. (2023). High resolution photoassociation spectroscopy of the excited $c^3\Sigma_1^+$ potential of $^{23}Na^{133}Cs$. *Phys. Rev. Research*, 5(2), 023149.

2. Park, A. J.,* Picard, L. R. B.,* Patenotte, G. E., Zhang, J. T., Rosenband, T., & Ni, K.-K. (2023). Extended Rotational Coherence of Polar Molecules in an Elliptically Polarized Trap. *Phys. Rev. Lett.*, 131(18), 183401.

3. Picard, L. R. B.,* Patenotte, G. E.,* Park, A. J.,* Gebretsadkan, S. F., & Ni, K.-K. (2024). Site-Selective Preparation and Multistate Readout of Molecules in Optical Tweezers. *PRX Quantum*, 5(2), 020344.

4. Picard, L. R. B.,* Park, A. J.,* Patenotte, G. E., Gebretsadkan, S., Wellnitz, D., Rey, A. M., & Ni, K.-K. (2024). Sub-millisecond Entanglement and iSWAP Gate between Molecular Qubits. arXiv.2406.15345.

* denotes authors who contributed equally to each work.

Listing of figures

Acknowledgments

Science is fundamentally a collective enterprise. As such, the work presented in this thesis would not have been possible without the involvement of the many people I have relied on throughout my PhD. This includes everyone from my direct scientific collaborators in the Ni Lab to the friends and family that have provided me with support and community for the past six years. I want to take the time here to acknowledge the particular contributions that a number of these people have made.

Firstly, I want to thank my advisor, Kang-Kuen Ni, for giving me the opportunity to join the lab and for her continued support during my PhD. Throughout my time on the molecule experiment, Kang-Kuen's steady guidance kept us on track, while always leaving room for students and postdocs to come up with new ideas and collaborate in determining our scientific direction. I will always be grateful to her for teaching me how to think clearly about scientific problems, and to never forget the big picture. Kang-Kuen has also done a fantastic job of selecting the researchers who make up the Ni Lab, which has become a joyful, intellectually stimulating, and supportive scientific community. I want to highlight a few specific members of the lab with whom I have worked closely on the molecule experiment, and who have contributed in particularly signifi-

cant ways to the work in this thesis. When I first joined the molecule experiment, I was welcomed by Jessie Zhang, the senior graduate student at the time, and Will Cairncross, a postdoc. I gained so much from Jessie and Will, who were not only patient with me as I learned the ropes, but also consistently kind, supportive, and funny, even through the difficult days of COVID occupancy restrictions and lonely experiment shifts. Jessie also built the experiment, and so absolutely none of this work would have been possible without the years of effort she put in beforehand. In the second half of my PhD, I had the good fortune to work with postdoc Annie Park and PhD student Gabriel Patenotte, who were co-producers of all of the experimental results presented herein. Annie is both incredibly hard working and always willing to lend her time to help her labmates, and it was a joy working alongside her through all the ups and downs of the last few years of molecule-making. Gabriel's creativity and enthusiasm have been a true asset to the experiment and, from almost the moment he joined, his attention to detail and meticulous analysis began contributing in fundamental ways to our understanding of molecules and their interactions. In 2023 we were joined by a new graduate student, Sam Gebretsadkan, who has already made himself an invaluable member of the team, bringing new ideas, enthusiasm, and an open and collaborative spirit. We were also recently joined by a visiting resident theorist, David Wellnitz, whose insights and generosity with his time were vital for the work presented in Chapter 6. I feel so grateful to

have worked alongside these great scientists, and I am excited to see where they take the experiment next!

Many other members of the lab provided me with support and training when I was just starting out. In particular I want to thank former grad student Lee Liu and post-doc Jonathan Hood, who dedicated themselves to teaching me both experimental and theoretical fundamentals in my first year, and my fellow grad student Kenneth Wang, who was the first person to welcome me into the lab and has been a consistent friend, collaborator, and advisor during the entire course of my PhD. I also want to thank other Ni lab members and associates with whom I have worked directly, including Yichao Yu, Yen-Wei Lin and Till Rosenband, along with every other member of the lab that has contributed to making it such a welcoming and supportive community. The day-to-day operations of the group would not be possible without the dedicated aministrative staff who have worked with us over the time that I have been in the group: Felixander Negron, Patricia McGarry, Keneisha Murphy, and Gina Yildirim.

I also want to acknowledge the other members of my committee, John Doyle and Susanne Yelin, who have provided me with additional support and advice over the course of my PhD. Both of them have also contributed in significant ways to maintaining the community of the Harvard-MIT Center for Ultracold Atoms, a true powerhouse of scientific collaboration and outreach which it has been my great pleasure to participate

in during my time at Harvard. Additionally, I want to thank the administrative and student support staff of the Harvard Physics Department and CUA, particularly Lisa Cacciabaudo, Hannah Belcher, Samantha Dakoulas, and Silke Exner, who work tirelessly to keep everything running smoothly and make sure grad students are sane and healthy. I further want to acknowledge the Harvard custodial staff, whose labor keeps our lab and community spaces clean and livable, and the CCB facilities staff, who keep our lab's systems running behind the scenes and have stepped in many times to help us troubleshoot.

Before coming to Harvard, my scientific trajectory was shaped by several excellent mentors. In particular I want to thank Francesca Ferlaino at the University of Innsbruck, who took a chance on me and invited me to spend a summer in her lab as an undergraduate intern, and Rick van Bijnen, a postdoc at Innsbruck who worked closely with me during that summer and on a subsequent paper. This early research experience undoubtedly set me on the path towards pursuing a PhD. At Durham University, I was supervised by Eckart Wrede, whose support was invaluable as I continued to learn and complete my M.Sci. Finally, before starting grad school I had the opportunity to work in the group of Síle Nic Chormaic at the Okinawa Institute of Science and Technology, which was a fantastic experience that allowed me to significantly broaden my research horizons.

I am grateful to all the members of my Harvard Physics and Applied Physics PhD cohort, which formed a bedrock of community throughout my time here. I am still so proud of us for pulling off a whole virtual puppet show (and I hold out hope it won't be the last one; future G1s take note). I have lived with several wonderful fellow physicists during grad school, and them and their partners have become lifelong friends; thank you Nick, Jon, Eve, Nathaniel, Hanna, Jonathan, Cindy, DaLi, and Mar for all of your kindness, laughter and support. Thank you also to the other friends I have made in and beyond the department that have immesurably enriched my life these last few years, including Kara, Caroline, Madelyn, Alex, Taylor, Jon, Soumya, Rodrigo, Eliot, and many more. A core part of my grad school experience outside of the lab has been my involvement in the Harvard Graduate Students Union (HGSU-UAW Local 5118), through which I have met countless kind and brilliant people who have dedicated themselves to supporting their fellow grad workers. My first piece of advice to any new graduate student worker is to join your union, and remember that scientific work is work, and you're not in it alone.

There is no way I can adequately acknowledge how much I owe to my parents, Mary and Michael. They have always been there for me, always trusted and encouraged me to make my own choices, always supported me in every way they can. They have been an example for me to emulate in a million different ways, from their intellectual and

academic pursuits to their deep wells of kindness and care. I feel immensely lucky to have had the upbringing I did, and to have been continuously sustained by my parents' love and support throughout my PhD.

Finally, I want to thank my partner, Alba, who has been with me through every step of this journey. All my greatest moments of joy have been with her, and she has helped pull me up from every low point. I genuinely could not have done this without her, and I will be eternally grateful to her for choosing to share her life with me.

1

Introduction

1.1 Why molecules?

Experimental atomic, molecular, and optical physics in the last half century has transitioned from characterizing quantum systems to now also controlling them. This shift has been enabled by the development of increasingly effective methods for cooling and trapping quantum particles. The development of laser cooling was initially used as a means to realize higher precision spectroscopy, first of ions [133] then soon after of ensembles of neutral atoms [214]. At the same time, however, this technique opened the door to precise control of the internal states of small numbers of atoms. This led to a

boom in experimental quantum information science using individual electrostatically trapped ions, which could now be treated as almost ideal two-level quantum systems, also known as qubits (quantum bits) [64, 290]. In neutral atoms, laser cooling and optical trapping enabled the creation of a new phase of matter: the Bose-Einstein condensate (BEC) [11, 72], that has been extensively studied and controlled over the past three decades. More recently, neutral atoms have also been trapped and controlled at the single particle level in optical tweezers and lattices, emerging as another promising candidate for scalable quantum computing [38, 132, 136, 184]. As cooling and trapping techniques have increased in sophistication and efficiency, the range of atomic species that can be controlled has also expanded, from the simple hydrogen-like alkali atoms to alkaline-earth atoms, transition metals, and lanthanides [2, 70, 103, 179, 207, 232].

In comparison to atoms, molecules have been relatively resistant to full quantum control. If one spends any time talking to ultracold molecular physicists, it is not long before one will encounter the oft-repeated mantra that we are interested in molecules because of their "rich internal structure." By this, we mean that the interaction of the two or more atoms that form a molecule creates new quantum degrees of freedom that we can seek to harness. Specifically, molecules intrinsically possess both vibrational and rotational degrees of freedom, in addition to the electronic orbital angular momentum and electronic and nuclear spin degrees of freedom common to both atoms and molecules. This dissertation deals with heteronuclear diatomic molecules, specifically NaCs, in which there is only one allowed mode each for vibration and rotation. However, for more complex polyatomic molecules there can be many independent ways for the molecule to vibrate or rotate. This means that molecules can exhibit a dense

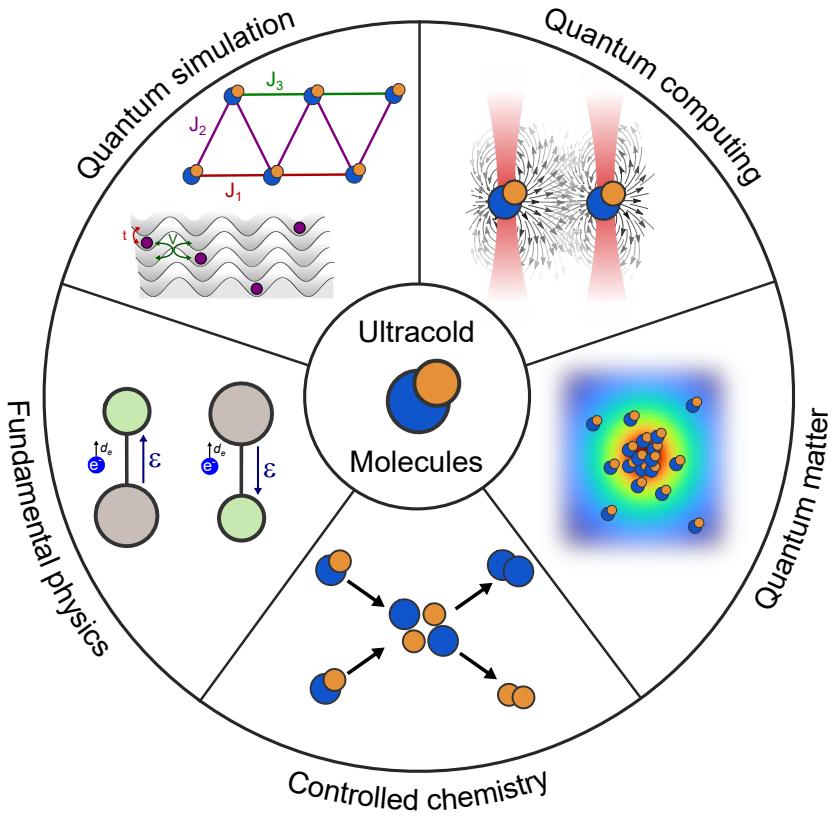

Figure 1.1: Representations of several research areas in which ultracold polar molecules have proposed or recently experimentally demonstrated applications. These areas are: quantum computing using individually trapped molecules [17, 117, 215]; creation of dipolar quantum matter using ultracold molecules cooled to quantum degeneracy [33, 75, 236]; coherent control of quantum states in chemical reactions between molecules [16, 123]; probes of fundamental physics using high-precision molecular spectroscopy [12, 194, 228]; and quantum simulation of spin models [20, 54, 63, 191, 296].

energy level spectrum, with layered structure spanning all the way from Hz to 100s of THz and very few truly empty spectral regions in between. This lies in stark contrast to atoms, which generally possess a relatively sparse array of electronic transitions in the optical range of the electromagnetic spectrum, overlaid with hyperfine structure on the GHz scale. The dense energy landscape of molecules means that there are many different tools that can be used to manipulate them, from radio-frequency and mi-

crowave antennas through to far-IR, visible, and ultraviolet lasers. Molecules can also possess permanent electric-dipole moments, allowing them to interact at long range via dipole-dipole coupling and to be oriented using DC or AC electric fields. These properties have given rise to a wide range of proposed applications of ultracold molecules, including quantum simulation of exotic spin models [20, 191, 281], quantum computing [202, 219, 300], quantum control of chemical reactions [27, 157], and searches for physics beyond the standard model [129, 194, 268]. Some of these applications are illustrated in Fig. 1.1.

The complexity of molecules is a double-edged sword—it is both the reason why they hold so much potential as engineered quantum systems as well as the reason why they are so difficult to control. An ensemble of hot molecules will occupy a wide distribution of rotational, and potentially vibrational, levels [49]. Performing any kind of coherent quantum manipulation of molecules requires, at a minimum, being able to initialize them in a single internal quantum state. For precision control—as with atoms—one also needs to reduce the external kinetic energy of the molecules, opening the door to trapping and addressing individual molecules. Unlike atoms, however, these aims cannot be achieved straightforwardly using laser cooling and optical pumping. Since transitions between many vibrational and rotational levels of molecules are allowed, spontaneous emission of photons from an excited molecular electronic state can lead to scrambling of the internal states of the molecule, making laser cooling very challenging.

1.2 Methods for producing and trapping ultracold molecules

Methods for overcoming this complexity in order to produce and trap ultracold neutral molecules can be divided into two streams, that have recently converged to very similar results. The first stream tackles the challenge of laser cooling directly, using a combination of judicious selection of molecular species and a large number of repump lasers to cool molecules to ultracold temperatures. This approach draws from the field of molecular beam physics, where techniques have been developed over many decades to produce translationally cold beams of molecules for spectroscopic and collisional studies. The second stream has its source in ultracold atomic physics, and relies on coherently producing molecules at initially ultracold temperatures from mixtures of ultracold atoms. I will briefly review both of these methods here, with a particular focus on the coherent assembly approach, which is the one we use in the Ni Lab to produce ultracold NaCs molecules in optical tweezers. Note that the rich field of trapping and manipulating molecular ions is outside the scope of this review, although it has undoubtedly cross-pollinated with the techniques described here [76].

Molecular beams have been widely used to study the properties and interactions of atoms and molecules for most of the last century [220]. These beams consist of a sample of molecules (or atoms) travelling in the same direction, which can have a relatively small spread of transverse velocities resulting from velocity filtering of a molecular gas expanding from a hot vapor source [86]. Following the development of this technique, a primary focus of research being conducted at the time was finding ways to reduce the internal temperature of molecules in the beam to allow for high-resolution spectroscopy. A major breakthrough in this area came in the form of the supersonic expan-

sion technique, where a mixture of target molecules and an inert atomic gas expand through a small orifice into a vacuum, leading to cooling of the transverse motion of the atoms, which, in turn, cools the internal rotational states of the molecules through collisions [138, 256]. A more recently developed related technique known as cryogenic buffer gas cooling has become particularly important in ultracold molecule experiments. This method relies on cooling the inert atomic gas to a few Kelvin in a cryogenic cell and allowing the molecules to be cooled directly in the cell through collisions with the atoms. Afterwards, they can escape through an orifice to produce a beam with both a low internal temperature and smaller forward velocity than a supersonic jet [131, 189].

Since the turn of the century, several methods have been developed to further reduce the forward velocity of molecular beams to the point that molecules can be confined in electrostatic, magnetic, or optical traps. The initial leader among these methods was Stark deceleration, which used electrodes along the path of the beam to engineer a series of rising potential hills that the molecules would have to traverse, gradually dissipating their forward velocity [29]. The related method of Zeeman deceleration applied the same principle, creating potential gradients using the magnetic Zeeman shift [289]. In the 2010s, it was experimentally demonstrated that certain classes of diatomic molecules possessed optical transitions that were sufficiently closed that, with the addition of a few repump lasers, they could cycle enough photons to allow effective laser cooling of the transverse motion and laser slowing of the forward motion of molecular beams [23, 114, 252, 312]. This method proved to be so effective that it enabled the demonstration of the first magneto-optical traps of diatomic molecules, with molecules loaded from molecular beams and laser-cooled to the Doppler limit or be-

low [8, 22, 125, 274]. This approach has since been successfully extended to polyatomic molecules [279]. Among various applications, these techniques have notably been used to load individual molecules into optical tweezers [10], which recently led to the first demonstrations of entanglement between individual ultracold molecules via the dipole-dipole interaction [17, 117]. Buffer gas cooling, combined with optical pumping and quantum state control, has also been central to setting new bounds on the electron electric dipole moment measured using transition shifts of cold ThO molecules [12].

The bottom-up assembly approach to creating ultracold molecules dates back to the 1980s, relatively early in the history of laser cooling, when photoassociation of laser-cooled atoms was proposed as a means of spectroscopically investigating bound molecular states of Na atoms [272]. This type of incoherent photoassociation was observed for all the homonuclear dimers of the stable alkalis in the 1990s [1, 89, 166, 193, 283]. Among the first heteronuclear dimers to be investigated in this way was, in fact, NaCs, the subject of this thesis, which was simultaneously photoassociated and ionized by the Bigelow group at Rochester [249]. This method of molecule production was incoherent, however, transferring molecules to short-lived electronically excited states that could spontaneously decay to a large number of other vibrational and rotational levels. In order to produce molecules suitable for further experimentation, a different approach was needed.

The first evidence of coherent molecule creation through magnetoassociation was the loss of atoms from a Na BEC when an applied magnetic field was swept from above to below a Na-Na Feshbach resonance [261]. This loss was theoretically explained shortly thereafter as arising due to the coherent transfer of atom pairs to the weakly-

bound vibrational state of the Na_2 molecule that gives rise to the Feshbach resonance [192]. This method was soon used to reversibly prepare pure bulk samples of weakly-bound ultracold molecules, which could be detected directly through absorption imaging [81, 115, 221, 295]. It was subsequently shown that, by performing the magnetoassociation in a deep 3D optical lattice, collisional losses of molecules could be avoided, thus extending their lifetimes [209]. An alternative method of creating weakly-bound molecules—first demonstrated in [293]—is to use a detuned optical Raman transition with the frequency difference of the Raman lasers tuned to the energy separation of an atomic scattering state and a weakly-bound molecular state. This method was applied to coherently produce Sr_2 molecules in an optical lattice [222, 260], as well as Rb_2 [113] and, in our group, NaCs in optical tweezers [303]. I refer readers to the thesis of Yichao Yu for a detailed treatment of this technique [301].

From weakly-bound molecules, the next challenge was to transfer them to the fully stable rovibronic (*ro*tational-*vib*rational-electr*onic*) ground state of the molecules. This was demonstrated in 2008 for bulk samples of both homonuclear [164] and polar heteronuclear molecules [202] using two-photon transfer via an electronically excited intermediate state. This method has become the standard in the ultracold molecule community and has more recently been extended to systems with single-molecule resolution, such as NaCs molecules in optical tweezers in our group [48, 310], RbCs in tweezers at Durham University [229], and NaRb molecules in a quantum gas microscope at Princeton [226].

A wide range of applications of coherently assembled molecules have already been demonstrated experimentally. Dipolar interactions between lattice-confined molecules

were first observed in [296], and were used in combination with quantum gas microscopy to engineer a tuneable lattice spin model with single-site resolution in [63]. In Chapter 6 of this thesis, we use the dipole-dipole interaction to entangle individual molecules in tweezers. Chemical reactions between molecules have been probed with unprecedented precision by combining ultracold molecules with detection methods pioneered in physical chemistry [122, 176]. Feshbach resonances between molecules have also recently been observed and used to controllably form weakly-bound polyatomic molecules [56, 211]. A variety of techniques have been developed to eliminate light shifts between internal states of optically-trapped molecules, leading to observations of long hyperfine and rotational coherence times [101, 212] and the development of an optical clock based on vibrational transitions [150]. One such technique, so-called "magic ellipticity" trapping, is demonstrated in Chapter 4. Finally, both a degenerate Fermi gas [75, 236] and a Bose-Einstein condensate [33] of polar molecules have now been created, opening up a new frontier in the study of strongly dipolar quantum matter. This list, which is necessarily incomplete, represents only a small subset of what can be achieved with ultracold polar molecules.

The remainder of this thesis is organized as follows: In Chapter 2, I provide a description of the current state of the Ni Lab ultracold molecular assembly experiment; in Chapter 3, I discuss our high-resolution spectroscopic investigation of electronically excited states of NaCs to identify a narrow intermediate state for two-photon transfer to the rovibronic ground state; in Chapter 4, I describe our demonstration of "magic ellipticity" trapping to extend the rotational coherence time of molecules in optical tweezers; in Chapter 5, I present a set of techniques that we have implemented for im-

proved state-preparation and measurement of molecules in tweezers; in Chapter 6, I discuss our demonstration of dipolar entanglement between the rotational states of molecules; in Chapter 7, I detail our characterization of the first universal two-qubit gate between individually trapped ultracold molecules; and, finally, in Chapter 8, I outline some possible future scientific applications of ultracold molecules in tweezers and discuss remaining challenges.

Invention, it must be humbly admitted, does not consist in creating out of void, but out of chaos.

Mary Shelley

2

Molecules: A step-by-step assembly guide

2.1 Overview of the experimental apparatus

A detailed description of the Ni Group's ultracold molecular assembler experiment, including information on the initial construction of the apparatus, can be found in the thesis of Jessie Zhang [308]. In this chapter, I will provide a broad overview of the current state of the experiment, with a more detailed focus on methods and aspects of the apparatus that have changed in the intervening years.

Fig. 2.1 shows the overall layout of the experiment optical table, with different regions labelled corresponding to optical beam paths with different functions. The exper-

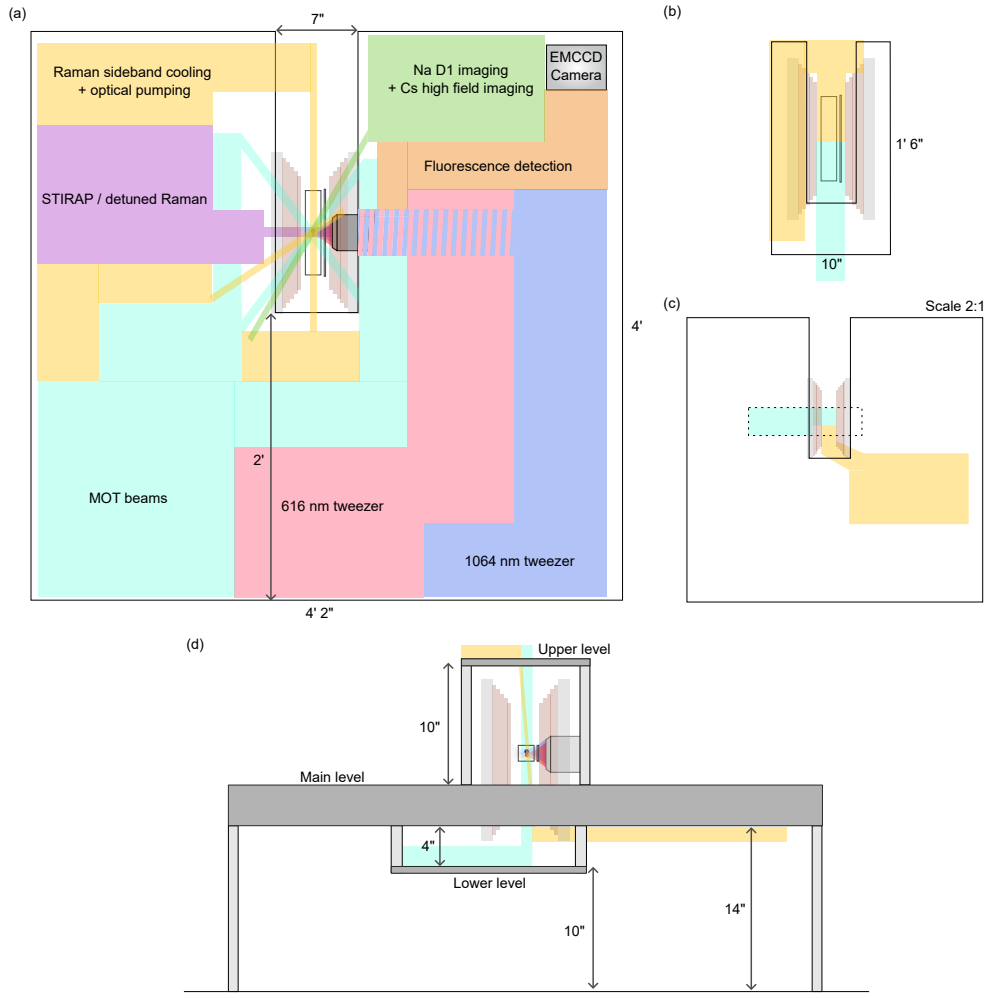

Figure 2.1: Illustration of the overall layout of the experiment optical table, centered on the glass cell. Optics are distributed across three levels: above, level with, and below the glass cell. The height of the Feshbach coils spans the three levels. (a) Depicts the main level of the optical table. The table has a large rectangular slit in its center in which the Feshbach coil and glass cell assembly is mounted. The optical setup is divided into different colored regions which are labelled by the primary purpose of the optics within them. Full beam paths within the tweezer, Na D_1 + Cs high field imaging, and STIRAP regions are provided in figures 2.3, 2.8, and 2.12, respectively. (b) Depicts the upper level, which is a small breadboard held above the glass cell by optical posts, with a rectangular slit through the center allowing MOT and Raman sideband cooling beams to be directed downward to the glass cell. (c) Depicts the lower level, which actually has two components: the underside of the main breadboard, and an additional breadboard suspended directly below the glass cell. The latter is denoted by the dashed line in the figure. MOT and Raman sideband cooling beams are directed upwards towards the glass cell, through the slit in the main optical table. (d) Side view of the three levels of the optical table.

iment is built around a glass cell under ultra high vacuum, fitted with Na and Cs atomic dispensers that we use to fill the cell with a low density vapor of both alkali species. Within the glass cell, we form a dual species magneto-optical trap (MOT) from which we directly load Cs into an array of 1064 nm optical tweezers. For Na, we first apply a gray molasses cooling step before loading atoms into 616 nm tweezers [309]. Subsequently, we rearrange the stochastically loaded atoms into smaller near-unity-filled arrays, and perform Raman sideband cooling to prepare both species close to the 3D motional ground state of the optical tweezers [302, 309]. We then apply a large magnetic field of 864 G using a pair of high-current coils (henceforth referred to as Feshbach coils). Following this, we merge the tweezer arrays, and ramp the magnetic field over an interspecies Feshbach resonance to magnetoassociate the atom pair into a molecule [310]. We then transfer the molecule to its rovibrational ground state via a two-photon process [48, 309]. The rotational states of the ground state molecules can at this point be manipulated with resonant microwaves, and the molecules can be entangled via the long-range dipole-dipole interaction. To read out the state of the molecules, we reverse the molecule formation steps and image the resultant atoms (both Na and Cs in Chapter 4 and just Cs in Chapters 5 to 7). A representative timing diagram of this sequence is shown in Fig. 2.2.

The experiment is controlled primarily using three hardware devices:

1. An FPGA (Xilinx ZC702), which controls transistor-transistor logic (TTL) outputs for digital triggers and switches, and direct digital synthesis (DDS) outputs to produce radio-frequency control signals.

2. An analog output device (NI PCI-6733), providing voltages between -10 and 10 V.

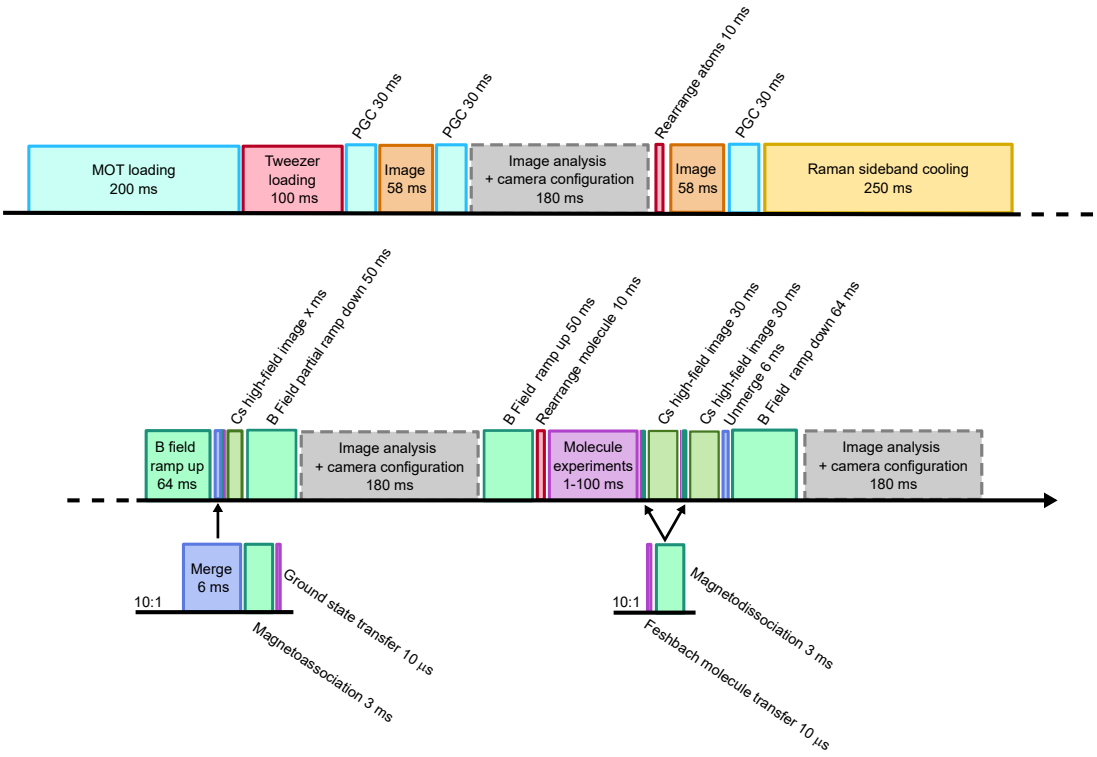

Figure 2.2: Timing diagram for a typical experimental sequence involving assembly of rovibrational ground state NaCs molecules. The molecule detection protocol represented here is described in detail in Chapter 5, and consists of sequentially selectively dissociating molecules in two different rotational states and imaging the resultant Cs atoms at high magnetic field to read out the population in each state.

3. An arbitrary waveform generator (AWG, Spectrum Instrumentation M4i.6622-x8), that is used to output radio-frequency (RF) tones to generate tweezer arrays.

These hardware devices are controlled via a unified MATLAB frontend, which is used to specify the timing of all pulses in a given experimental sequence. Any given sequence written in the frontend is first "generated", producing corresponding sets of hardware commands that are transmitted to the backend of each hardware device to actually run a sequence. For further information on the computer control system, see the thesis of Yichao Yu [301]. The optical tweezer arrays themselves are generated using Acousto-

Optic Deflectors (AOD, IntraAction), which can be driven by multiple RF tones to deflect an incoming beam into multiple output beams. The deflection angle of the beams is determined by the frequency of the RF tones, and, in turn, determines the spacing between the tweezers. The tweezer beam paths are illustrated in Fig 2.3. Readout is performed through fluorescence imaging of individual atoms. Depending on the particular experimental sequence being performed, the probability of detecting an atom in a given image can be mapped onto the population of molecules in a particular internal state (see Chapter 5). For imaging, atoms are excited using light resonant with the D_2 (for Cs) or D_1 (for Na) lines, and fluorescence is collected on an electron multiplying CCD camera (EMCCD, Andor iXon Ultra). Images are analyzed using the frontend control computer to determine the presence of an atom in each tweezer.

2.2 Building blocks: Ultracold atoms in optical tweezers

The first step of every molecule experiment that we perform is to load Na and Cs atoms into parallel arrays of optical tweezers. By individually trapping neutral atoms in tweezers, we can control their quantum state with high precision. This is one of the reasons this platform has gained a great deal of prominence in recent years for quantum computing [37, 181, 184], simulation [242, 248], and metrology [88, 237]. In our experiment, we are particularly concerned with controlling the motional state of the atoms, which will be inherited by the molecules created through magnetoassociation [310]. Using Raman sideband cooling, we can prepare both atoms close to their 3D motional ground state, following a procedure detailed in [308]. In recent years, we have focused on increasing both the number and density of atoms in the arrays, with the goal of trans-

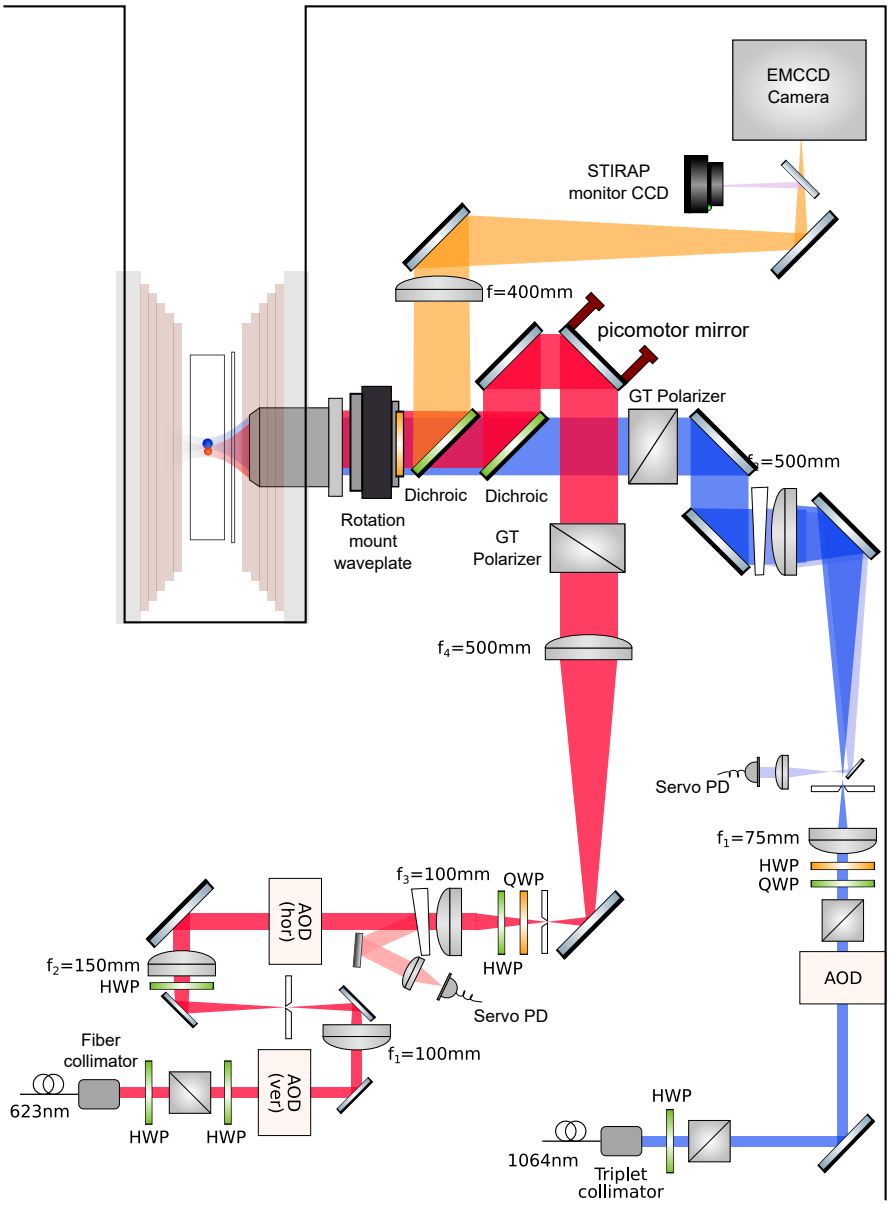

Figure 2.3: Beam paths used for generating optical tweezers at 1064 and 616 nm, as well as for collecting atomic fluorescence onto EMCCD. In comparison to earlier iterations of the apparatus [308], the position and orientation of the dichroic used to combine the two tweezer beams has been changed to make room for a rotation-mounted waveplate that we use to go to a magic ellipticity condition for trapping molecules in the 1064 nm beam (see Chapter 4). We also added a second CCD camera to monitor the positions of the STIRAP / detuned Raman beams, which are transmitted through the objective and partially reflected into the imaging beam path. This and other beam path diagrams use art from ComponentLibrary developed by Alexander Franzen [91].

forming them into a dense molecular array for molecule-molecule interaction experiments. Towards this goal, we have implemented two significant upgrades to the experiment, which I will describe in detail in the following subsections: gray molasses cooling and enhanced loading of Na atoms using the D_1 line, and in-situ rearrangement of atoms to form near unity-filled arrays.

2.2.1 Gray molasses cooling and enhanced loading of Na

2.2.1.1 Λ-enhanced gray molasses

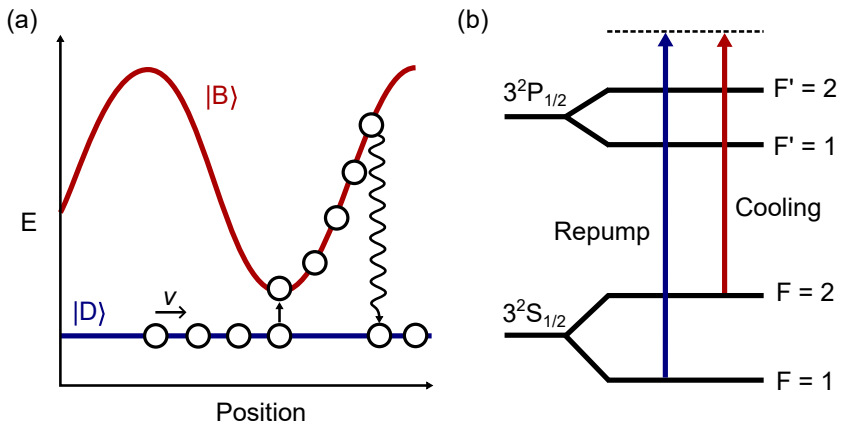

Figure 2.4: (a) Typical cycle of non-adiabatic transition from dark to bright state followed by optical pumping from bright to dark state, ultimately producing the Sisyphus-cooling mechanism of gray molasses. (b) Relevant energy levels and cooling laser frequencies for implementing gray molasses on the D_1 line of Na. Note that while the transition from $F = 1$ is labelled as "repump," this is largely a matter of historical convention, and the beam is not only acting as a repump but is also key to forming the dark dressed state in the Λ-enhanced scheme.

As a starting point for tweezer loading, we implemented a Λ-enhanced gray molasses cooling step for Na atoms, directly following the MOT stage. Gray molasses cooling, first proposed in Refs. [106, 287], is a method of sub-doppler cooling that relies on the formation of bright and dark dressed states of atoms in a standing wave of near-

resonant cooling light. It can be implemented on transitions with $F' = F$ or $F' = F - 1$, and uses light blue-detuned from the transition. Even with just a single cooling beam, this leads to the formation of one or more dark states, the energy of which is unaffected by the intensity of the light. It also produces bright states, the energy of which are determined by the intensity, and which can be light-shifted above the dark state. In the presence of a standing wave of the intensity [287] and/or polarization [224] of the light, this leads to atoms in the bright state traversing a hilly potential landscape, while the energy of the atoms in the dark state is position-independent. The sub-doppler cooling is provided by a Sisyphus-like mechanism composed of two processes that can lead to transitions between bright and dark states: first, when atoms in the bright state absorb cooling photons, they can scatter into the dark state; and second, atoms in the dark state can non-adiabatically transfer to the bright state, at a rate determined by the energy separation between states and the velocity of the atoms [287]. For blue-detuned cooling light, the non-adiabatic transfer occurs with the highest probability at the energy minima, when the separation between the bright and dark states is smallest. This leads to cooling since, on average, atoms that transfer to the bright state climb some fraction of the potential hill before scattering back into the dark state. This cooling mechanism is illustrated in Fig. 2.4. Atoms travelling with higher velocities have a higher probability of non-adiabatic transfer from dark to bright states since the velocity of the atom determines the rate of change of the bright state energy, and hence the adiabaticity parameter, as the atom traverses the standing wave. This velocity-dependence leads to an effect akin to velocity-selective coherent population trapping, wherein atoms that have been cooled to low velocities are more likely to remain in the

dark state. The method is called "gray" molasses because, unlike a conventional optical molasses, there is minimal fluorescence from the atoms once they are cooled, as they mostly remain in the dark state.

For Na atoms, a gray molasses can be realised most efficiently on the D_1 line's $F = 2$ to $F' = 2$ transition. In some alkali species it is possible to implement a gray molasses using the $F = F'$ component of the D_2 line, but its efficiency will generally be reduced by the effect of being red detuned from the $F' = F+1$ transition [121, 227]. In a standard alkali gray molasses configuration, an additional repumping beam is added to prevent population from accumulating in the lower F component of the ground state ($F = 1$ for Na), as illustrated in Fig. 2.4. In the early 2010s, it was noted that the final achievable atom temperature exhibited a significant dependence on the relative detuning between the cooling and repump lasers, with the minimum temperature occurring for the exact Raman condition, when the frequency difference between the lasers matched the ground hyperfine splitting [224]. Subsequent theoretical investigation revealed that this occurs due to the formation of dark states that are a superposition of the two ground hyperfine levels, which are generally even more uncoupled from the light field than the dark states of a single-frequency gray molasses, leading to more efficient cooling and population trapping [253]. This configuration came to be known as Λ-enhanced gray molasses.

To implement Λ-enhanced gray molasses cooling for Na, we generate up to 2 W of 589 nm light using a Raman fiber amplifier (MPB Photonics) seeded with a laser locked to the $F = 2 \rightarrow F' = 1/2$ crossover peak of the D_1 line. The single-photon detuning from the $F = 2 \rightarrow F' = 2$ transition is controlled via a double-pass AOM (Gooch

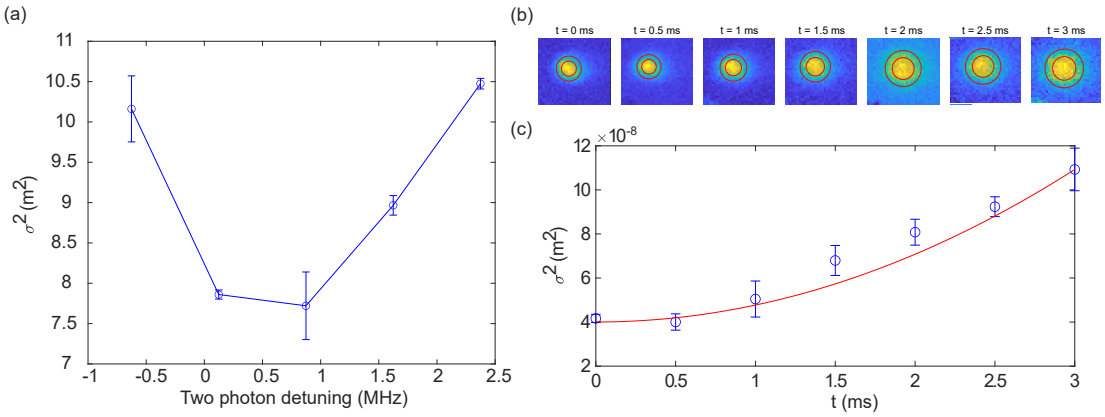

Figure 2.5: (a) Na atom cloud size after 1.5 ms time-of-flight expansion following gray molasses cooling, as a function of repump beam detuning from Raman resonance. (b) Series of time-of-flight images of cloud with optimized gray molasses cooling parameters. (c) Gaussian fits to images of expanding cloud during time-of-flight, from which we extract a temperature of 21.2 μK

and Housego), and the repump light is provided by a resonant EOM (Qubig PM-Na_1.7) that creates a sideband at the Na ground hyperfine splitting of 1.772 GHz. This D_1 light is combined with the D_2 MOT light before being delivered to the experiment table, so the polarization configuration for the gray molasses beams is the same set of opposite circular polarizations used for the MOT [308]. Before loading from the gray molasses into tweezers, we optimized the parameters of a single 1 ms gray molasses pulse using time-of-flight expansion of the atom cloud. Scanning the EOM frequency, we observed a minimum cloud size following 1.5 ms time-of-flight for a two-photon detuning of close to zero (Fig. 2.5(a)). Once the gray molasses parameters had been optimized, we measured the expansion of the cloud and extracted a temperature of 21.2 μK (Fig. 2.5(b-c)). The temperature of the MOT cloud before gray molasses is 138 μK.

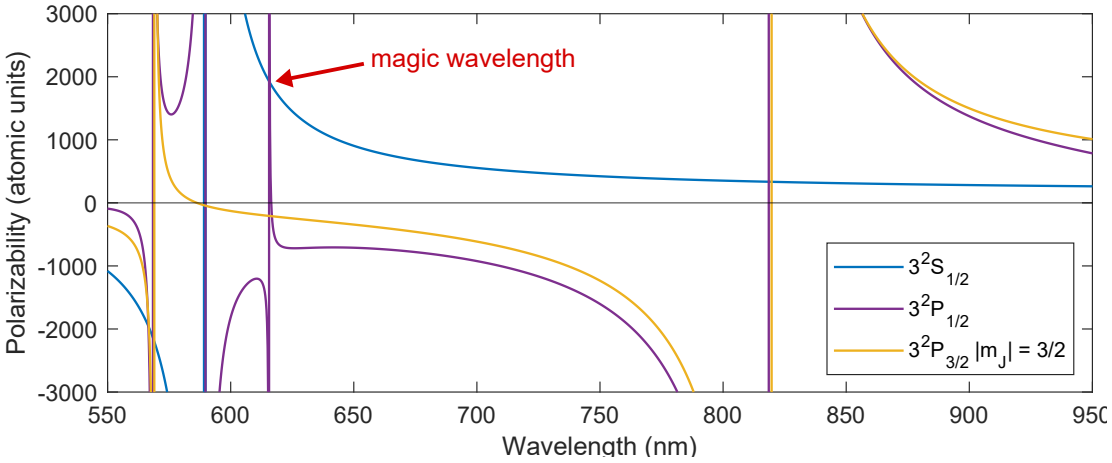

Figure 2.6: Polarizabilities of the $3^2S_{1/2}$, $3^2P_{1/2}$ states and the $|m_J| = 3/2$ component of the $3^2P_{3/2}$ state of Na, between 550 and 950 nm. Data are taken from Ref. [19].

2.2.1.2 Magic wavelength trapping and enhanced loading

Loading Na atoms into tweezers directly from the D_1 gray molasses provides both a lower initial temperature and the possibility of loading a larger and higher density array. In previous work in which we directly loaded Na atoms from the D_2 MOT, we needed to strobe the MOT and trapping light out of phase with one another [130]. This is because, for trapping wavelengths between the D_2 line itself at 589 nm and 820 nm, the $3^2P_{3/2}$ state is anti-trapped. Thus, if the atom is excited on the D_2 line while the trapping light is on, it will be pushed away from the center of the tweezer, leading to heating. Rapidly strobing the cooling and trapping light out of phase eliminates this issue [130]. However, it leads to a significant increase in the power requirements for both beams to make up for the off-time. If cooling is performed on the D_1 line, this problem can be sidestepped entirely, as there is a wavelength region close to 616 nm for which the $3^2P_{1/2}$ state is trapped. This can be seen in Fig. 2.6, which compares the polarizabil-

ity of the 3S and the two 3P states for Na. Not only is $3^2P_{1/2}$ trapped, but, if the trapping wavelength is chosen correctly, it is possible to achieve a "magic" trapping condition, where the polarizability of the excited state matches exactly that of the ground state [6, 13, 19]. Trapping at this magic wavelength can lead to particularly efficient cooling and imaging since any excess heating caused by displacement of the trapping potential for the excited state is eliminated [187]. This occurs for Na at 615.88 nm, which is where the polarizabilities of the $3^2S_{1/2}$ and $3^2P_{1/2}$ states intersect in Fig. 2.6. We generate trapping light at the magic wavelength using a sum-frequency-generation system (Precilaser), combining separately amplified 1550 nm and 1020 nm beams to produce 616 nm in a nonlinear crystal.

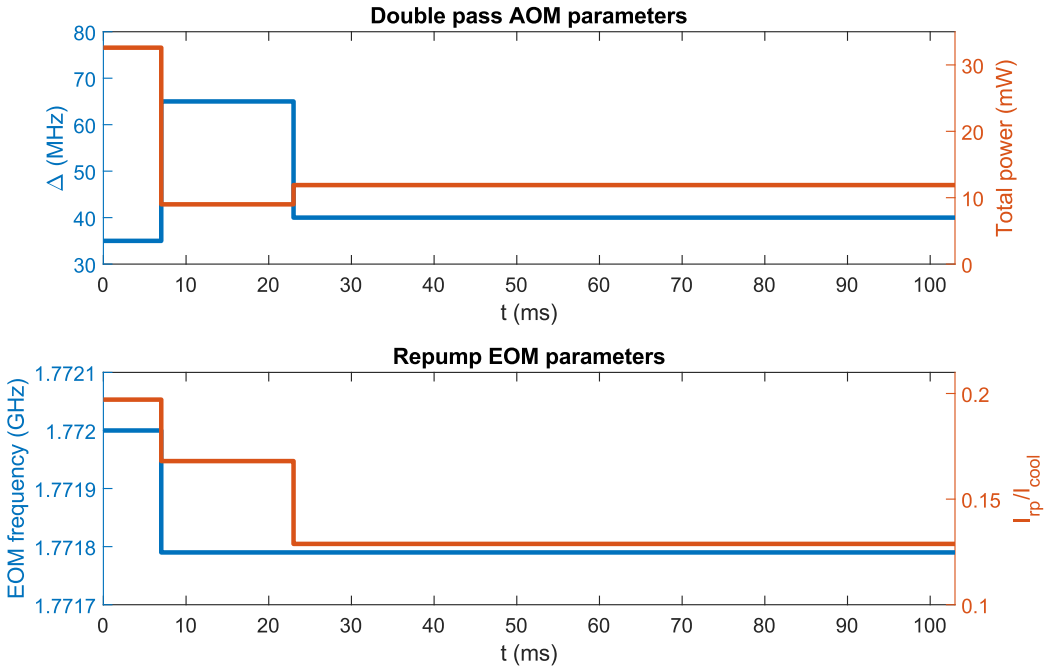

Figure 2.7: Three-stage gray molasses sequence used for enhanced loading of Na atoms in tweezers.

Along with avoiding the need for strobing, the other major advantage of loading

a magic wavelength tweezer from a gray molasses cloud is that it allows atoms to be loaded with a probability of > 50% per tweezer. In typical tweezer loading in the presence of red-detuned cooling light, the light couples pairs of atoms to the attractive molecular potential curve, leading to short-range collisions and loss of both atoms from the trap. This gives so-called "parity-projected" loading where any tweezers containing an even number of atoms will end up containing none after collisions, and any with an odd number will contain one remaining atom. The initial filling of an array loaded in this way is thus close to 60 %, slightly higher than a pure parity-projected limit due to the possibility of only one atom of a pair being ejected [238, 257]. Using light blue-detuned from all atomic transitions, however, will instead couple to the repulsive potential of the two atoms, leading to inelastic collisions with a smaller amount of excess kinetic energy determined by the laser detuning. By choosing the detuning to give the atom pair just enough energy for one atom, but not both, to escape the trap, it is possible to preferentially eject only one atom if the initial distribution of kinetic energies of the pair is at all imbalanced. This conversion of pairs of loaded atoms into single atoms allows enhanced loading of between 80 and 90% per tweezer, significantly higher than the limit imposed by parity-projection [46, 107]. Enhanced loading of Na atoms in magic wavelength optical tweezers was first demonstrated by the group of Huanqian Loh in Ref. [6]. The gray molasses sequence that we use for loading is depicted in Fig. 2.7. Following Refs. [6, 69], we perform three stages of gray molasses cooling, beginning with a high intensity and low detuning stage to maximize the atom capture velocity, before reducing the intensity and increasing the detuning to reduce the atom temperature. This is followed by the tweezer-loading stage, with a duration of

80 ms, in which the detuning is again reduced to control the amount of excess energy imparted to the atoms during collisions. Using this sequence, we achieved an average Na loading probability of 80%.

2.2.1.3 D_1 imaging

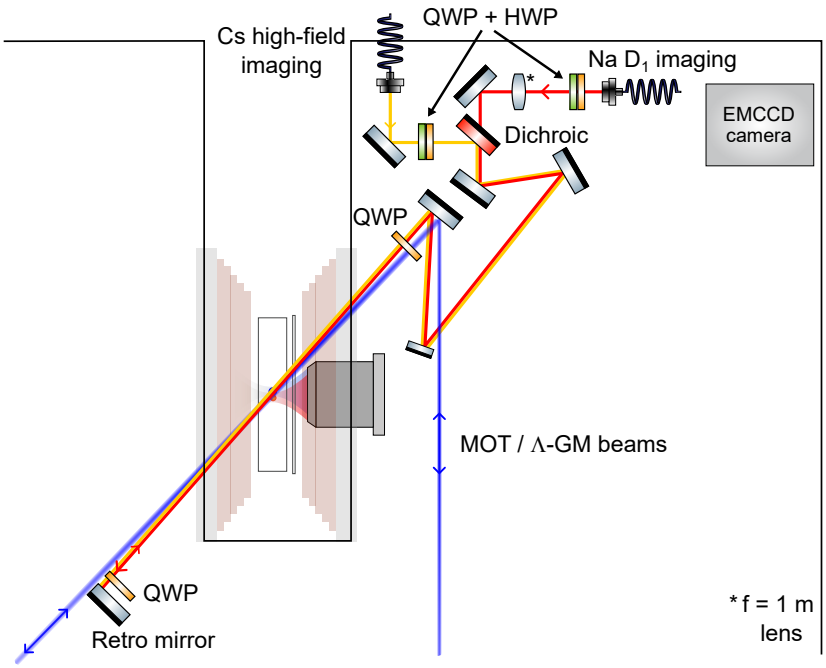

Figure 2.8: Na D_1 and Cs high-field imaging beam paths. The two beams are combined on a dichroic mirror and directed to the atoms by a mirror that they share with one of the pairs of MOT / Λ-enhanced gray molasses cooling beams. The beams are retroreflected on the other side of the glass cell using a mirror positioned so as to avoid clipping the MOT beams. The polarization of the Na D_1 light is circular, chosen to match the polarization of the MOT beams. It is rotated by an additional quarter waveplate in front of the retroreflection mirror, such that the retroreflected beam has opposite circular polarization. The Cs high-field imaging light is aligned to produce vertical polarization after the first quarter waveplate, and the fast axis of the retroreflection waveplate is aligned to the vertical such that the polarization of the high-field imaging beam is unaffected by it. We add a 1 meter focal length lens in the D_1 path to counteract the divergence of the beams, resulting in retroreflected beams that are slightly focusing and thus similar in diameter to the incoming beams.

The blue-detuned gray molasses light can also be used for imaging of single Na

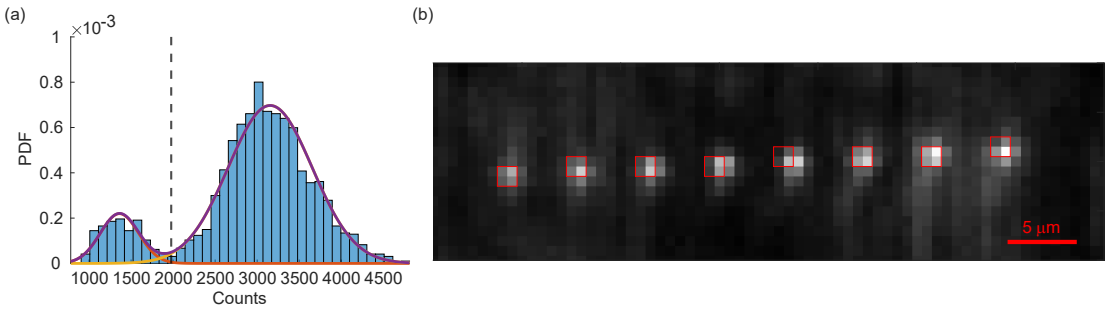

Figure 2.9: (a) Average histogram of photoelectron counts for D_1 imaging of Na, where the left peak corresponds to empty sites and the right peak to sites containing one atom. False positive and negative rates are determined by fitting a sum of Gaussians to the peaks. (b) Average image of an 8-site array corresponding to the histograms on the left.

atoms [6]. However, since the atomic fluorescence is significantly reduced in a gray molasses compared to a red-detuned MOT or polarization gradient cooling configuration, the signal-to-noise ratio will be less favorable for imaging. In prior work we imaged Na atoms using the MOT beams themselves. However, we found that when trying to image the atoms with gray molasses, there was so much excess scattering of the imaging light from the glass cell onto the camera that the imaging signal was not resolvable. To overcome this issue, we added a dedicated imaging beam with a diameter of $\sim$1 mm, significantly smaller than the MOT beams. This beam is combined with the Cs high-magnetic-field imaging light (discussed in Chapter 5) and retroreflected close to the glass cell. This beam path is illustrated in Fig. 2.8. The use of this small beam allowed us to achieve high intensities of incident imaging light with comparatively little scattering. This comes at the expense of reduced cooling efficiency during imaging, due to only having a single cooling axis. Nevertheless, using a small blue detuning of 18 MHz, we were able to achieve good imaging histogram separation—as shown in Fig. 2.9—corresponding to false positive and false negative rates of 0.9% and 0.4%, respectively,

and an overall imaging survival of 95.5%.

2.2.2 In-situ rearrangement of atoms

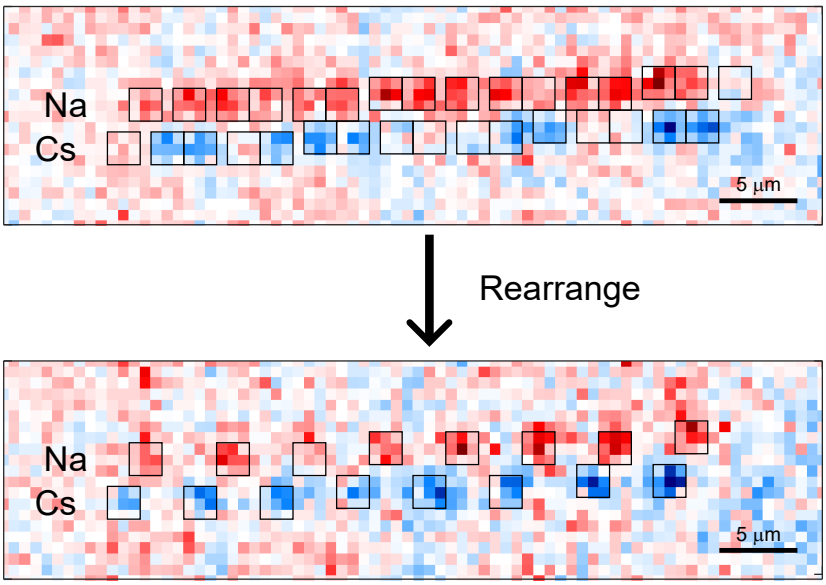

Figure 2.10: Single-shot images of Na and Cs atoms before and after rearrangement from 16-site to 8-site arrays. The images of the two species are independently normalized, and are superimposed with different colors. Black boxes are centered on the individual sites in the array, rounded to the nearest pixel.

An important step towards preparing a dense array of NaCs molecules is being able to begin with densely-filled arrays of Na and Cs atoms. By implementing enhanced loading for Na, we were able to increase the initial filling fraction to 80%, but for Cs we remain limited to the ∼60% parity-projected filling. To produce atomic arrays with close to unity filling, we implemented deterministic in-situ rearrangement of atoms. To perform said rearrangement, we first load 16-site arrays of both atoms and perform fluorescence imaging to determine which sites contain atoms. All of the empty sites are then dropped, and the tweezers containing atoms are shuttled to one side to cre-

ate smaller 8-site arrays with close to unity filling. This method was introduced by the group of Mikhail Lukin in Ref. [85], and has become a workhorse technique in neutral atom tweezer experiments. The rearrangement process is demonstrated in Fig. 2.10, which shows consecutive single-shot images of the Na and Cs arrays before and after rearrangement.

The RF tones defining the AOD deflection angles of the different tweezers are generated on-the-fly, allowing the tweezer positions to be reconfigured arbitrarily during the sequence. To minimize dead-time between cycles of the experiment, the entire experimental sequence is generated once at the start of a given run of data collection, but the precise sequence of moves for the rearrangement is left unspecified at generation time. Immediately following the pre-rearrangement image, the image is loaded from the EMCCD camera onto the control computer, where it is analyzed and the necessary sequence of moves is determined. These instructions are then transferred to the computer running the AWG, where they are read from memory at runtime. The total time between taking the first image and executing the rearrangement is between 150 and 200 ms. This includes overhead time for loading from and readying the camera, analyzing the images, and configuring all the output devices for the next portion of the sequence.

2.3 Coherent creation of ground state molecules, or *There and Back Again*

2.3.1 Magnetoassociation of atom pairs

The first step in molecule formation is to create weakly-bound molecules through magnetoassociation. This was first demonstrated for single molecules in optical tweez-

ers by our group in Ref. [310]. We begin by ramping the magnetic field in the glass cell to 866 G using two large Feshbach coils in a Helmholtz configuration. The magnetic field is controlled through active stabilization of the current in the coils, which is monitored using a Hall probe. For details of the coil assembly and calibration, see Ref. [308]. At some magnetic fields between 0 and 100 G, the Zeeman shift of the atoms can cause the energy difference between pairs of atomic states to become resonant with the frequency separation of neighboring optical tweezers, which can result in tweezer-induced Raman transitions [309]. To avoid these regions, we jump the magnetic field to 100 G as fast as possible and then ramp the rest of the way in 39 ms. Once the magnetic field is at its maximum value, we merge the two tweezers by sweeping the frequency of the 616 nm vertical AOBD, and then ramp down the amplitude of the 616 nm tweezer to adiabatically lower the Na atoms into the 1064 nm tweezer. We then use a smaller pair of coils around the glass cell—referred to as shim coils—to ramp the magnetic field back down by 2.5 G, crossing the interspecies Feshbach resonance at 864.1 G. This results in atom pairs that are in the relative motional ground state being transferred to a weakly bound molecular state which we refer to as a "Feshbach molecule."

While the magnetoassociation process itself is close to 100% efficient, we typically achieve an overall two-way conversion efficiency from atoms to molecules of between 30 and 40%. This is primarily limited by the Raman sideband cooling of Na, which has a 3D ground state fraction of close to 60% after cooling. This ground state fraction is itself limited primarily by scattering of the 616 nm tweezer light. Cs cooling is generally more straightforward due to its heavier mass, with typical final 3D ground state fractions in the 80-90% range. Some additional heating can then be introduced at the

merge stage. Although the merge parameters, including the move rate, trap depths, and minimum-jerk trajectory, are optimized to minimize heating, there may still be some residual heating due to misalignment of the trap centers along the axial direction. There is some additional imperfection in the state preparation of both atoms in the $|F = 1, m_F = 1\rangle_{\mathrm{Na}} |F = 3, m_F = 3\rangle_{\mathrm{Cs}}$ hyperfine state combination in which the Feshbach resonance occurs. All of these factors contribute to the final Feshbach molecule creation efficiency.

2.3.2 Two-photon transfer to the rovibrational ground state

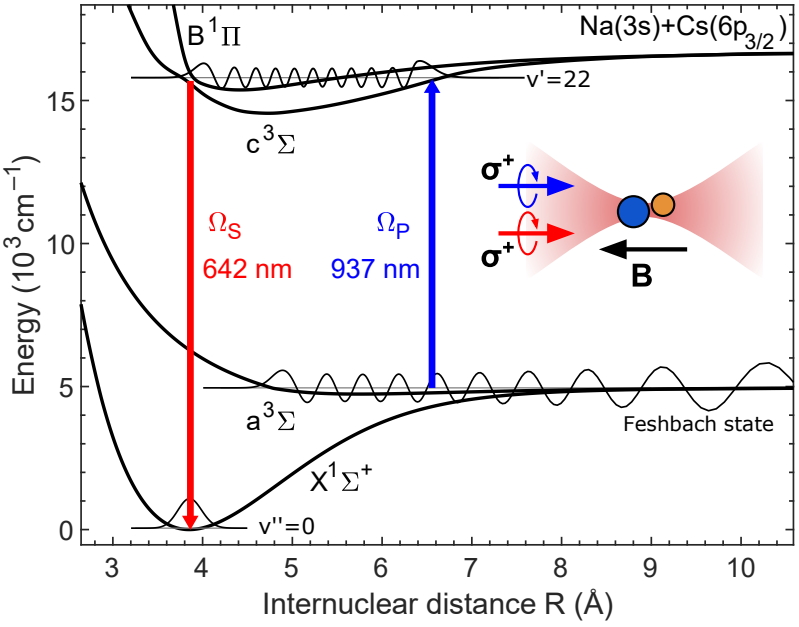

Figure 2.11: Two-photon pathway from the Feshbach molecule to the $X^1\Sigma^+$ ground state of NaCs, via the $v' = 22$ vibrational level of the electronically excited $c^3\Sigma_1^+$ state. Figure adapted from [48].

Following Feshbach molecule creation, we transfer molecules to the $X^1\Sigma^+$ rovibrational ground state using a two-photon scheme—illustrated in Fig. 2.11. In previous

work, we used the $v' = 26$ vibrational level of the $c^3\Sigma_1^+$ electronic state as an intermediate for two-photon transfer [48, 309]. However, this state had an anomalously broad linewidth of 120 MHz, making it difficult to apply the standard method of resonant two-photon transfer via Stimulated Raman Adiabatic Passage (STIRAP). We found that it was possible to overcome this limitation using detuned Raman transfer with a detuning of several GHz [48]. We subsequently performed a spectroscopic investigation of other potential intermediate states to identify a narrower line that would overcome this limitation, settling on the $v' = 22$ level of $c^3\Sigma_1^+$. This spectroscopic investigation is described in detail in Chapter 3. Using $v' = 22$, we succesfully transferred molecules to the rovibrational ground state using STIRAP, which is the method we use for molecule preparation in Chapter 4. In Chapters 5, 6, and 7 we, in fact, return to using detuned Raman, albeit for different reasons. In this case, we tune the lasers to be blue-detuned by 500 MHz from the intermediate state, a detuning that is specifically chosen to avoid transitions from the next rotationally excited state to $c^3\Sigma_1^+$. This allows us to dissociate molecules in the rotational ground state without disturbing population in the rotationally excited state, as described in Chapter 5.

2.4 Molecular manipulations: Rotational structure and microwave control

Once we have produced molecules in their rovibrational ground state, the next challenge is to actually coherently control some of the rich internal structure that we have been seeking to exploit. We are particularly interested in controlling the rotational states of the molecule. For this task, our tool of choice is resonant microwave fields. Microwaves have been used to probe and control the states of molecules for close to 100

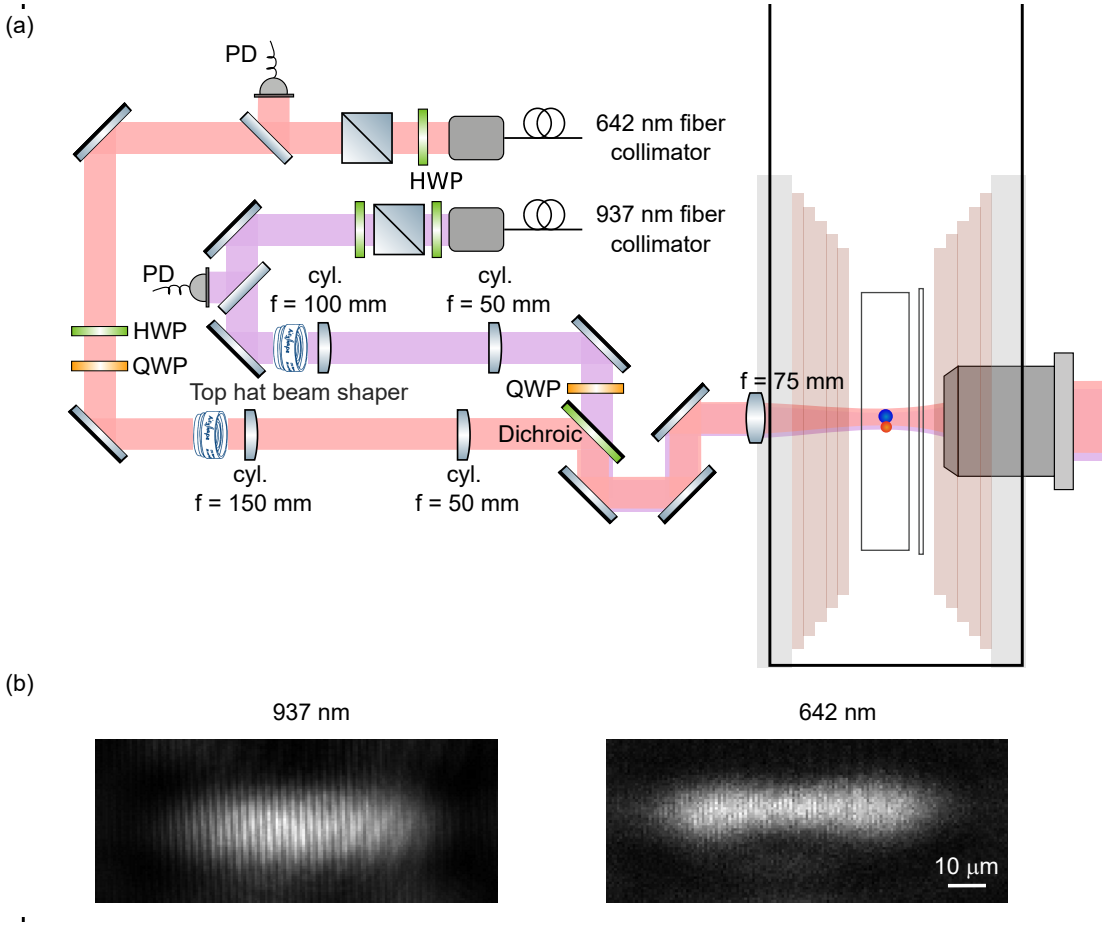

Figure 2.12: (a) Beam path for two-photon transfer of molecules from the Feshbach to the ground state, via STIRAP or detuned Raman. (b) An Airy disk phase pattern is imprinted on the beams using passive beam shaping optics (Asphericon AiryShape), resulting in top hat beam profiles at the focus, that we use for uniform addressing of all the sites in the array.

years. The first use of microwaves to control the state of a molecule occurred in 1934, when they were used to drive the inversion of the pyramidal ammonia molecule [65]. The technique was not further developed, however, until the boom in microwave technology following the Second World War, at which point it quickly became a standard method of performing rotational spectroscopy of molecules [97]. Famously, the same ammonia transition which was first investigated in 1934 was later used to construct the

maser (microwave amplification by spontaneous emission of radiation) [96], that went on to inspire the invention of its optical equivalent: the laser.

The rotation of polar molecules can be controlled via microwaves due to the molecule's electric dipole moment. The dipole interacts directly with the applied electric field of the microwaves. The change in average orientation of the dipole depending on the rotational state of the molecule produces transition dipole moments that allow rotational transitions to be driven by resonant microwaves. The energy spacing between rotational levels is determined by the moment of inertia of the molecule about the axis of rotation. Small, light molecules such as H_2, will rotate faster, yielding rotational transitions that can reach energies as high as the near-infrared optical regime [45]. Most molecules, however, have rotational energies broadly within the microwave and mm-wave region of the electromagnetic spectrum. The first rotational transition of NaCs, the only one we currently address, occurs at 3.47 GHz, corresponding to a wavelength of 8.64 cm.

2.4.1 Microwave generation

The hardware used for generating and delivering resonant microwaves at 3.47 GHz is depicted schematically in Fig. 2.13. We generate the microwave signal by mixing a stable crystal oscillator at exactly 3.42 GHz (Luff Research) with one of the DDS outputs of our FPGA system at close to 50 MHz. Both the oscillator and the clock of the DDS chip are referenced to the same 10 MHz Rb clock (Stanford Research Systems). The amplitude and precise frequency of microwave pulses are controlled dynamically in-sequence using the DDS. Pulse durations can be specified with a precision of 10 ns, and

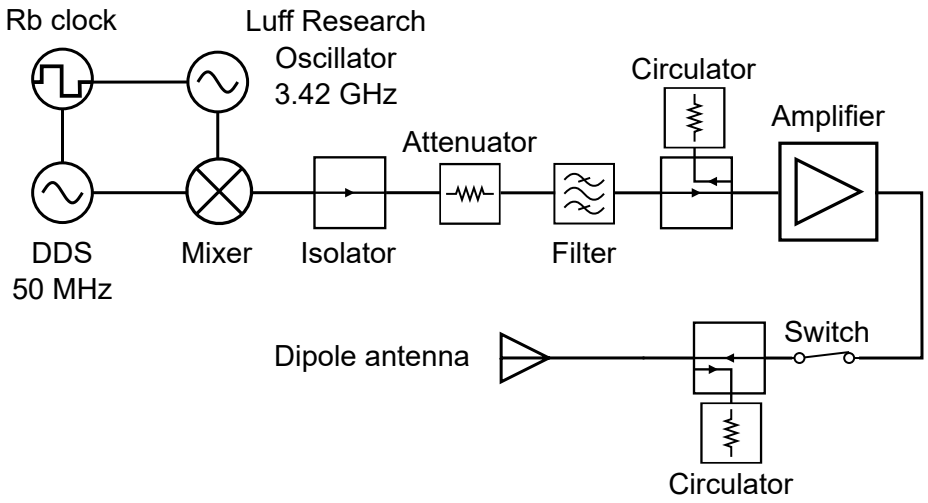

Figure 2.13: Electronics path for generating 3.47 GHz microwaves to address the $N = 0$ to $N = 1$ rotational transition in NaCs. Schematic created using symbol library Ref. [93].

a minimum on-time of 500 ns. The signal after the mixer is sent through an isolator to minimize reflections, followed by a 10 dB attenuator and a narrow band-pass filter that significantly attenuates all but the positive sideband of the mixed signal at 3.47 GHz. The filtered microwaves then pass through a microwave circulator that provides additional isolation. The return port of the circulator is directed towards an attenuator to absorb any reflected signals, but it can also be used for monitoring of the microwave pulses. The signal is then amplified by a 45 dB high-power amplifier (Minicircuits ZHL-16W-43-S+), passing through a final circulator and a switch, which is opened whenever microwaves are not on, to prevent any electrical noise being directed to the molecules.

The microwaves are finally transmitted to the molecules using a dipole antenna, that is suspended above the glass cell. A picture of the dipole antenna is shown in Fig. 2.14.

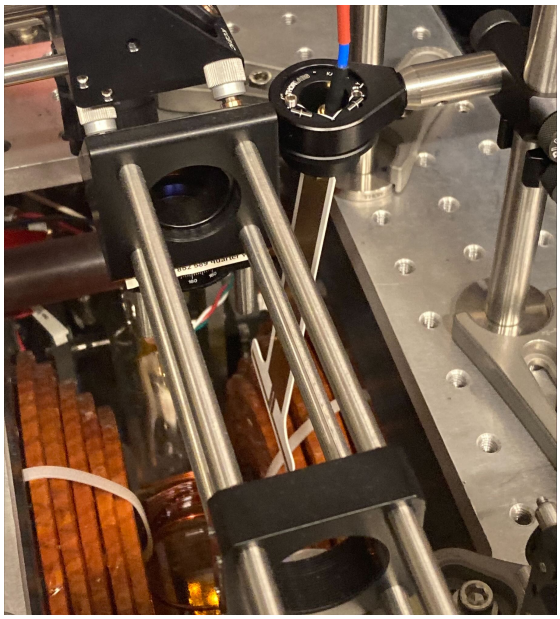

Figure 2.14: Resonant dipole antenna used to direct 3.47 GHz microwaves to the molecules.

There is nothing like looking, if you want to find something. You certainly usually find something, if you look, but it is not always quite the something you were after.

J.R.R. Tolkien

3

High-resolution spectroscopy of the $c^3\Sigma_1^+$ state of NaCs

Material in this chapter, including portions of the text and figures, originally appeared in print in [217], and include some data from a different experiment within the Ni group built to study all-optical association of NaCs molecules [171, 301]. The coupled-channel model codebase used here was originally developed by William Cairncross for use in [48].

3.1 Electronic and rotational structure of bialkali molecules

In this section, I provide a brief introduction to the electronic and rotational structure of bialkali molecules, with a particular focus on NaCs. This introduction is designed to help orient a reader with little to no prior molecular physics knowledge, but it is by no means a complete picture of the complexities of molecular structure, which is rich and replete with interesting edge cases. For a more complete picture, I recommend readers turn to Brown and Carrington, *Rotational Spectroscopy of Diatomic Molecules* ([45]), a true reference tome for both the structure of particular classes of diatomic molecules and for the details of spherical tensor algebra and coupling of angular momenta required for a full quantum mechanical treatment of molecular structure. For a modern treatment including recent developments in studies of ultracold molecules, I recommend Krems, *Molecules in Electromagnetic Fields* ([158]). Both of these books are significant sources throughout this section.

3.1.1 Molecular electronic potentials

The fundamental problem of quantum chemistry is to determine the energy of a molecule, given a specific set of positions and momenta for all its constituent particles. This task is, it turns out, Herculean in scale, and performing it both efficiently and accurately has been the life's work of countless researchers over the last century. In the comparatively simple case of atoms, where we need only consider a single fixed nucleus and some number of mobile electrons, we are used to thinking of the states as forming a ladder in energy. The rungs of this ladder consist of the eigenstates of the atomic Hamiltonian, defined by, in order of decreasing energy scale: the radial quantum number, n, of the

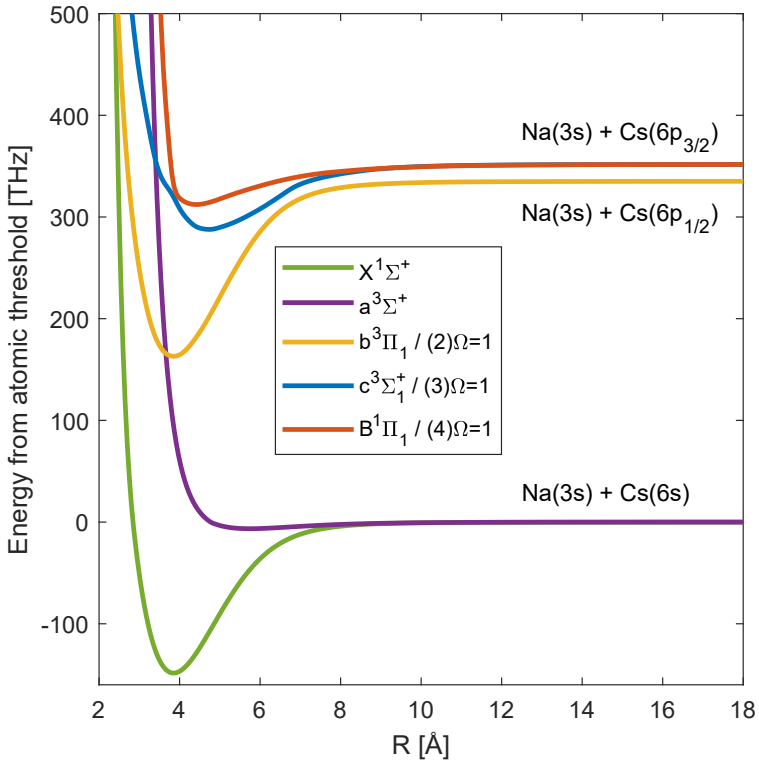

Figure 3.1: Relevant potential energy curves of NaCs. Singlet $X^1\Sigma^+$ (green) and triplet $a^3\Sigma^+$ (purple) curves at the Na(3s) + Cs(6s) threshold are from Ref. [44]. At the two Na(3s) + Cs(6p) thresholds, we show empirical potentials for the $\Omega = 1$ components of the $b^3\Pi$ (yellow), $c^3\Sigma^+$ (blue) and $B^1\Pi$ (orange) curves from Refs. [104, 105, 305]. These states can also be labelled in the Hund's case (c) basis as $(2)\Omega = 1$, $(3)\Omega = 1$ and $(4)\Omega = 1$, respectively.

outermost electron(s), their total orbital angular momentum, **L**, total spin, **S**, and coupling to total nuclear spin, **I**. These properties define a relatively sparse progression of energy eigenstates, with n defining electronic states separated by 100s to 1000s of THz (for low-lying states), superimposed with substructure given by coupling between **L** and **S**, defining the fine structure on the GHz to THz scale, and coupling between **L**, **S** and **I**, resulting in hyperfine structure on the few GHz scale.

In the case of molecules, the introduction of multiple nuclei complicates the prob-

lem by orders of magnitude. Since the energy of the molecule is primarily determined by the interaction of the electrons with the combined electric field of all the nuclei, the relative positions of those nuclei will be of critical importance. However, the nuclei are themselves bound together by their interaction with all the electrons, so finding the energy eigenstates requires solving the Schrödinger equation simultaneously for the coupled system of nuclei and electrons. This rapidly becomes intractable even for small molecules. As a result, much of quantum chemistry is concerned with choosing an appropriate set of approximations that allow this problem to be solved relatively accurately. The first and most important of these is the *Born-Oppenheimer Approximation*, which states that since the mass of the electron is so much smaller than the mass of the nuclei, one can assume that the electrons instantly respond to any changes in the positions of the nuclei. As a result, to calculate the electronic energy of a molecule, one can, to first order, neglect the quantum mechanical motion of the nuclei, and just treat them as fixed charges with some set of positions $\{\mathbf{r}_i\}$. For every possible combination of $\mathbf{r}_i$, one can compute the resulting electric field and find the lowest energy eigenstates of the electrons moving in that field. This process defines the molecular potential; that is the energy of the electrons in the coordinate space defined by the nuclear positions $\mathbf{r}_i$. The molecular potential is the primary conceptual tool used to explain the structure of molecules [275].

For diatomic molecules, the simplest class of molecules that exist, the molecular potential is defined by a single variable: the distance R between the nuclei. We can thus visually represent the energetic structure of the molecule by plotting the electron energy against R. If we plot only the lowest energy eigenstates of the electrons for each value of

R, then this defines the ground electronic potential. We can also consider higher energy configurations of the electrons, that may have a very different dependence on R to the ground state. Figure 3.1 shows the potential energy curves for a five electronic states of NaCs that are relevant to this chapter (reproduced from [217] and using potentials computed in [44, 104, 105, 305]). Each of these curves is labelled by a set of quantum numbers, which will be discussed in detail below. At large values of R, the potential curves are labelled by a pair of single-atom states, e.g. Na(3s) + Cs($6p_{1/2}$). This is the dissociation limit of the molecule, where it can again be treated as two non-interacting atoms in independently defined electronic states. Notice, however, that any given combination of electronic states for Na and Cs can produce multiple different molecular potentials, with very different energies. These differing energies are caused by the strong interactions between the electrons at small internuclear separations. We will turn shortly towards a quantum mechanical description of these interactions, but first we should briefly return to the question of the motion of the nuclei.

Within the Born-Oppenheimer Approximation, although we can calculate an energy for the electronic states at every internuclear separation R, the real internuclear separation will not be fixed. In fact, one can think of the nuclei as acting like a quantum (an)harmonic oscillator with a confining potential $V(R)$ defined by the electronic states. The minimum of the electronic potential as a function of R defines the equilibrium internuclear separation R_e, and, like any quantum oscillator, the lowest energy eigenstate of the system corresponds to some zero-point vibration about this equilibrium. The energy separation between the ground and first vibrationally excited eigenstates is typically on the order of a few THz, such that every electronic potential can support around

one hundred distinct vibrational eigenstates. These eigenstates are labelled in order of increasing energy by the vibrational quantum number v, starting from $v = 0$. Near the minimum of an electronic potential, its shape is approximately harmonic, but at high energies it becomes very anharmonic as it approaches the energy of the free atom pair, which is known as the dissociation threshold. Near the dissociation threshold, the vibrational level spacing becomes much smaller as the vibrational wavefunction approaches the unbound scattering wavefunction of a pair of atoms.

As well as vibrating along the bond axis, the whole system of nuclei and electrons can rotate with quantized angular momenta determined by the masses and separation of the two nuclei. The typical spacing of rotational levels for diatomics is several GHz. Rotational levels are labelled by the rotational angular momentum quantum number $\mathbf{R}$. Finally, magnetic interactions within the molecule can induce additional splittings that can range typically from Hz to hundreds of MHz. Already, the dense and complex energy level structure of molecules is apparent. Unlike atoms, each electronic state corresponds to a potential curve covering an enormous range of energies, which can support hundreds of vibrational levels. Each of these vibrational levels in turn has hundreds of rotational sublevels, which are then further split by hyperfine structure. This hierarchy of energy scales is illustrated in Fig. 3.2.

3.1.2 Molecular quantum numbers

In developing the molecular potential picture within the Born-Oppenheimer approximation, we have only discussed the relative positions and momenta of the nuclei. In other words, we have been operating in the molecule frame, where the coordinate sys-

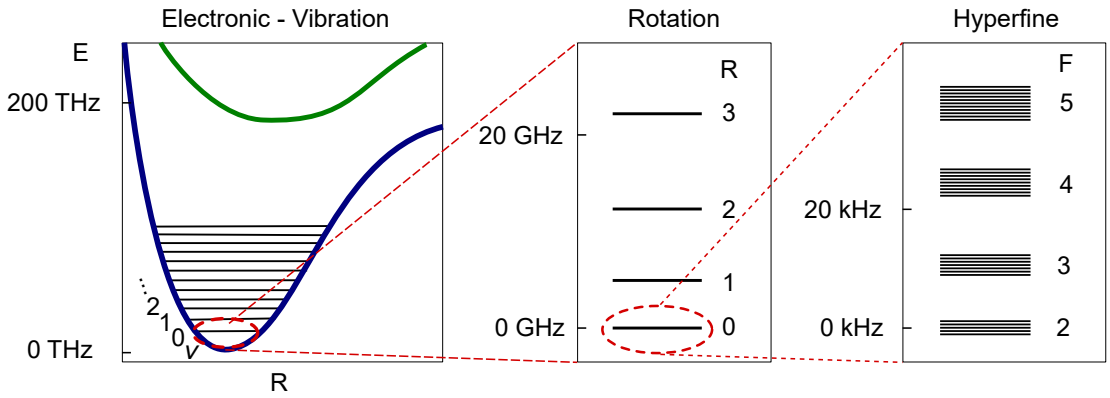

Figure 3.2: Illustration of energy scales of a diatomic bialkali molecule, ranging from the electronic and vibrational levels on the THz scale (left), to rotational levels on the GHz scale (center), to hyperfine structure on the kHz scale (right). Energies and structure are approximately based on the rovibrational ground state of NaCs in the absence of applied electric and magnetic fields.

tem is defined by the molecular bond axis, along which the nuclei vibrate and about which the electrons orbit. But what happens when the bond axis is rotating? It turns out that this rotation is of fundamental importance, because it determines the relationship between the molecule frame and the lab frame, which is the stationary coordinate system defined with respect to our experimental apparatus. In order for a quantum mechanical property of the molecule to be measurable, it must have some well-defined projection in the lab frame, enabling it to interact with whatever lab frame field we apply to probe it. However, many molecular quantum numbers are only well-defined in the molecule frame. To actually predict how the molecule will interact with our measurement apparatus, we thus need to understand how these quantum numbers couple to molecular rotation. We can then convert between the molecule frame and the lab frame using rotation operators: the Wigner D-matrices, which depend on the rotational state. In general, we will specify the full state of the molecule using some combination of lab frame and molecule frame quantum numbers.

The quantum state of an atom is primarily determined by the total orbital and spin angular momenta of its electrons. This is thus a sensible place to start devising a set of molecular quantum numbers. We can define the total electron orbital angular momentum, **L**, and spin, **S**, as the vector sum of the angular momenta of all the individual angular momenta:

$$\mathbf{L} = \sum_i \mathbf{l}_i \tag{3.1}$$

$$\mathbf{S} = \sum_i \mathbf{s}_i \tag{3.2}$$

where i indexes the valence electrons (of which there are two for bialkalis). In the case of atoms, the total orbital angular momentum **L** of the electrons is conserved due to the spherical symmetry of the atomic potential. We do not have any such spherical symmetry in molecules, and thus **L** alone is not a good quantum number. We do, however, have cylindrical symmetry along the molecular bond direction. As a result, the projection of **L** along the internuclear axis, which we label Λ, *is* a good quantum number [158], at least some of the time, as we will see shortly. By analogy with the standard labelling of atomic states with the letters s, p, d for $L = 0, 1, 2$, we label molecular states with the capital Greek letters Σ, Π, Δ for $|\Lambda| = 0, 1, 2$. The electron spin does not interact with the nuclear electric potential, so **S** is a good quantum number, along with its projection onto the internuclear axis, which we label Σ. The electron orbital angular momentum, electron spin, and molecular rotation can couple together to give multiple other quantum numbers, that may be more or less useful depending on the particular molecular state we are describing. A list of all relevant molecular quantum numbers is given in

Table 3.1.

There is one other fundamental quantum number that is not described by any combination of properties we have discussed so far, which I will briefly mention: parity. Parity describes how the total state of the system transforms under the application of the spatial inversion operator, $\hat{P}$, which corresponds to making the lab frame transformation $(x, y, z) \rightarrow (-x, -y, -z)$. In the absence of an external field applied in the lab frame to break inversion symmetry, this inversion cannot change the state of the molecule, meaning that the molecule's eigenstates must also be eigenstates of parity. Applying the parity operator twice is equivalent to performing the transformation $(x, y, z) \rightarrow (-x, -y, -z) \rightarrow (x, y, z)$, i.e. $\hat{P}^2$ is the identity. This means that the eigenvalue of a parity eigenstate can only take two possible values: 1 and -1. The sign of the parity eigenvalue of a molecular state is its parity quantum number. For most molecular states, the parity is determined by the projection of the orbital angular momentum as $(-1)^{\Lambda}$. However, this is not the case for $\Lambda = 0$ states, which can have either positive or negative parity depending on the specific combination of electronic orbital angular momenta summed to produce the state. We thus label all $\Lambda = 0$ states with a $+$ or $-$ to denote their parity eigenvalues. For a more thorough discussion and derivation of the parity quantum number, see [45].

3.1.3 Hund's coupling cases

We now have an inventory of potential molecular quantum numbers, but which ones do we actually need to uniquely identify quantum states? As can be seen in Table 3.1, the majority of the possible quantum numbers are listed as "sometimes" conserved. In

Quantum number	**Symbol**	**Derived**	**Frame**	**Conserved?**
Energy	E		Lab, Molecule	Yes
Parity	ϵ		Lab, molecule	Yes
Electron orbital A.M.	$\mathbf{L}$	$\mathbf{L} = \sum_i \mathbf{l}_i$	Lab	No
Electron orbital A.M. projection on internuclear axis	Λ		Molecule	Sometimes
Total electron spin	$\mathbf{S}$	$\mathbf{S} = \sum_i \mathbf{s}_i$	Lab	Sometimes
Electron spin projection on internuclear axis	Σ		Molecule	Sometimes
Rotation	$\mathbf{R}$		Lab	Sometimes
Total orbital A.M.	$\mathbf{N}$	$\mathbf{N} = \mathbf{L} + \mathbf{R}$	Lab	Sometimes
Total spin and orbital A.M.	$\mathbf{J}$	$\mathbf{J} = \mathbf{L} + \mathbf{R} + \mathbf{S}$	Lab	Yes
Total A.M. projection in lab	m_J		Lab	Yes
Total A.M. projection on internuclear axis	Ω	$\Omega = \Lambda + \Sigma$	Molecule	Yes (usually)
Total electronic A.M.	$\mathbf{J_a}$	$\mathbf{J_a} = \mathbf{L} + \mathbf{S}$	Lab	Sometimes

Table 3.1: Relevant molecular quantum numbers.

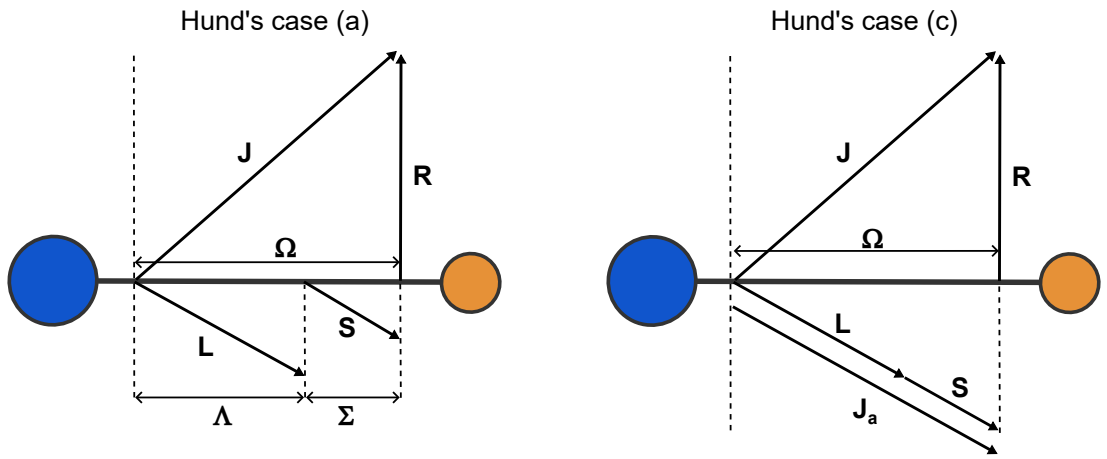

Figure 3.3: Illustration of the couplings of angular momenta for (left) Hund's case (a) and (right) Hund's case (c) molecules.

fact, ignoring nuclear spins which we have not yet introduced, there are only four quantum numbers which are always strictly conserved: energy, E, parity ϵ, total angular momentum, $\mathbf{J}$, and its projection in the lab frame, m_J. All of the other potential quantum numbers will, to some extent, be mixed by interactions within the molecule such that they do not have a single well-defined value. However, if a state can be described as being, for example, 99% in $S = 1$, then S may still be a useful way to label the state.

Hund's coupling cases, named for German physicist Friedrich Hund, are a widely used categorization of diatomic molecules by their dominant couplings. Determining which coupling case a molecule falls into allows us to choose an appropriate set of quantum numbers with which to label it. Hund's cases are labelled alphabetically from (a) to (e). Two of these cases are particularly relevant to this chapter: (a) and (c).

Hund's case (a) is the most commonly used. The strongest coupling in this case is of $\mathbf{L}$ to the internuclear axis to give the projection Λ. The electron spin $\mathbf{S}$ is in turn coupled to the internuclear axis via spin-orbit coupling, giving well-defined projection Σ. Since

Λ and Σ are both good quantum numbers, their sum Ω is also good. Rotation is relatively independent, and can be added to the sum of orbital and spin angular momenta to give the total angular momentum $\mathbf{J}$. Because the rotational angular momentum is by definition orthogonal to the internuclear axis for a diatomic molecule, the projection of $\mathbf{J}$ onto the internuclear axis is still equal to $\Omega = \Lambda + \Sigma$. Hund's case (a) gives us the standard spectroscopic labelling of molecular states,

$$\eta^{2S+1}\Lambda_{(\Omega)}^{(\epsilon)} \tag{3.3}$$

Some of these only need to be specified for certain states; ϵ is only needed for Σ states, and Ω is only specified if at least one of $\mathbf{L}$ or $\mathbf{S}$ is nonzero. The η quantum number is an index used to label the different electronic in ascending order of energy, which has a slightly odd convention. The ground electronic state is always labelled X, e.g. the ground state of NaCs is denoted $X^1\Sigma^+$. The electronic states that are nominally accessible by single-photon optical transitions from the ground state are then labelled alphabetically with capital letters, e.g. $A^1\Sigma^+$, $B^1\Pi_0$, etc. By "nominally accessible," we mean that the transition does not change the total spin state S. The transitions that are not accessible by single photon transitions are labelled with lower case letters, e.g. $a^3\Sigma_1^+$, $b^3\Pi$, $c^3\Sigma_1^+$, etc. Hund's case (a) provides the most comprehensive set of molecular quantum numbers, making it particularly useful. Even when a state cannot be described purely in case (a), we will sometimes express it as a linear combination of some set of case (a) states.

Hund's case (c) is slightly messier. In this case, the spin-orbit coupling is so strong that $\mathbf{L}$ and $\mathbf{S}$ first couple to form $\mathbf{J_a}$ before they couple to the internuclear axis. The indi-

Hund's Case	**Description**	**Good quantum numbers**
(a)	Strong coupling to internuclear axis, some spin-orbit coupling	$\Lambda, S, \Sigma, J, \Omega$
(b)	No spin-orbit coupling and/or $\Lambda = 0$	Λ, N, S, J
(c)	Very strong spin-orbit coupling	J, Ω
(d)	Strong orbit-rotation coupling but weak spin-orbit coupling to internuclear axis	L, R, N, S, J
(e)	Strong spin-orbit but weak coupling to interncular axis and rotation	J_a, R, J

Table 3.2: Hund's coupling cases.

vidual projections onto the internuclear axis Λ and Σ are no longer well defined. However, their sum Ω, the projection of $\mathbf{J_a}$ onto the internuclear axis, is still a good quantum number. Rotation is then added to Ω to give the total angular momentum J. Because Λ and Σ are no longer good quantum numbers, we cannot generally label states using the spectroscopic notation introduced for case (a). Instead, the standard case (c) labelling is of the form $(\eta)\Omega^{(\epsilon)}$, where ϵ is only specified for $\Omega = 0$ and η now just numbers the electronic states in order of increasing energy starting from 1, e.g. $(1)\Omega = 2$ is the lowest energy state with $\Omega = 2$. The other coupling cases are briefly described in Table 3.2, but are not used to describe NaCs.*

*Technically, the electronic ground state of NaCs could be considered case (b), but for $\Lambda = 0$ states case (a) and case (b) are identical, so we do not draw a distinction.

3.1.4 Molecular hyperfine structure in magnetic fields

The hyperfine structure of a molecule is defined by the mutual interactions of the electron spin and nuclear spins. Because its effect on the molecular energy levels is very small, we can generally treat the hyperfine structure as a perturbation that splits the rovibronic energy levels. As a result of this weak interaction, the spins of two nuclei in a diatomic molecule generally do not significantly couple either to the internuclear axis or to one another, so we can describe the hyperfine structure in terms of interactions between $\mathbf{S}$ and each of the nuclear spins $\mathbf{I_i}$ individually.

For states with $S \neq 0$, the hyperfine structure is dominated by direct interactions between the electron and nuclear spins. This has two components, a short-range Fermi contact interaction and long-range magnetic dipole-dipole interaction. The Fermi contact interaction is a scalar operator and can be expressed as

$$H_{FC} = \sum_i \alpha_i \mathbf{S} \cdot \mathbf{I}_i \tag{3.4}$$

The coupling constant α_i depends on the wavefunction amplitude of each of the individual electrons at the nucleus i, and, while it can in principle be predicted by theory [158], it is often more accurate to determine it empirically, which is what we do later in this chapter. The magnetic dipole-dipole interaction, which is much smaller, can be expressed as a rank-2 spherical tensor formed from the product of the electron and nuclear spins, which are rank-1 tensors,

$$H_{dd} = -\sum_i \frac{\sqrt{6}}{3} \sum_i d_i^q [\mathbf{S} \otimes \mathbf{I}_i]_q^{(2)} \tag{3.5}$$

where, once again, the d_i^q are general coupling constants that can be determined spectroscopically.

For states with $S = 0$, the hyperfine structure will be much smaller; typically only on the kHz scale. It is dominated by the interaction between the electric quadrupole moment of the nuclei and the electric field gradients of the molecule. This interaction can be expressed as [45]

$$H_{\mathrm{Q}} = \sum_i \sum_k \frac{eQ_i q_k^{\alpha}}{I_i(2I_i - 1)} \sqrt{(6)} T_k^2(\mathbf{I}_i, \mathbf{I}_i) \tag{3.6}$$

where $T_k^2(\mathbf{I}_i, \mathbf{I}_i)$ is the rank-2 spherical tensor formed by coupling $\mathbf{I}_i$ to itself (for explicit forms of the spherical tensor components see Section 5.5 of Ref. [45]). There are two additional terms that contribute generally on the 100 Hz level to the structure of bialkalis, consisting of scalar and tensor couplings between the two nuclear spins [4, 35],

$$H^{(0)}_{\mathrm{spin-spin}} = c_4 \mathbf{I}_i \cdot \mathbf{I}_\beta \tag{3.7}$$

$$H^{(2)}_{\mathrm{spin-spin}} = -c_3 \sqrt{6} T^2(\mathbf{C}) \cdot T^2(\mathbf{I}_i, \mathbf{I}_\beta) \tag{3.8}$$

where c_3 and c_4 are coupling constants and $T^2(\mathbf{C})$ is a rank-2 spherical tensor describing the angular dependence of the spin-spin interaction, the full form of which is given in Ref. [35]. Finally, there is a nuclear-spin-rotation coupling term originating from the interaction of the spins with the magnetic field produced by the rotating nuclear

charges, which can be written

$$H_{\text{spin}-\text{rot}} = \sum_i c_i \mathbf{N} \cdot \mathbf{I}_i \tag{3.9}$$

This term is generally very small and is often ignored even for $^1\Sigma$ states.

An applied magnetic field shifts the hyperfine states, and couples to electron spin, electron orbital angular momentum, rotation, and nuclear spin. This can be most easily expressed in the lab frame, assuming that the magnetic field $\mathcal{B}$ is uniform and oriented along the z-direction [4, 158]:

$$H_Z = \mu_B \mathcal{B}(g_S S_z + g_L L_z) + \mu_N \mathcal{B}(g_r R_z + \sum_i g_i(1-\sigma_i) I_{\alpha,z}) \tag{3.10}$$

where μ_B and μ_N are the Bohr and nuclear magnetons, respectively, the g are g-factors, and σ_i is a constant describing the shielding of the nuclear spins by the electrons. The dominant terms are the electronic couplings to S_z and L_z, with smaller contributions from the nuclear couplings which generally become important only for $^1\Sigma$ states. Note that, because the field interacts with the total lab frame angular momentum L_z, which is generally not a good quantum number in the molecular frame, the Zeeman effect can mix different electronic states.

3.1.5 The $c^3\Sigma_1^+$ and $X^1\Sigma^+$ states of NaCs

The $c^3\Sigma_1^+$ state of NaCs can be described in the Hund's case (a) basis, as we do here, or in the case (c) basis, in which it would be labelled $(3)\Omega = 1$ [151]. We choose to represent the state in the case (a) basis with quantum numbers $|\Lambda S\Sigma; J\Omega m_J\rangle\ |I_{\text{Na}} m_{I_{\text{Na}}}\rangle\ |I_{\text{Cs}} m_{I_{\text{Cs}}}\rangle$.

Uncoupled nuclear spins are appropriate given the high magnetic fields of 10-860 G used for the spectroscopy reported herein. The high degree of spin-orbit coupling in the *c*-*b*-*B* complex splits the $c^3\Sigma_1^+$ lines from equivalent $c^3\Sigma_0^-$ lines, which we have not observed experimentally, by as much as 1 THz [304]. We therefore do not consider any terms that mix $|\Omega| = 0, 1$ states. We model the hyperfine structure of the lowest few rotational levels of $c^3\Sigma_1^+$ using an effective Hamiltonian including rotational structure, electron spin-nuclear spin hyperfine interactions, Zeeman splitting, and an effective Ω-doubling interaction,

$$H_{c^3\Sigma_1^+} = B\mathbf{J}^2 + \alpha_{\mathrm{Na}}\mathbf{I}_{\mathrm{Na}} \cdot \mathbf{S} + \alpha_{\mathrm{Cs}}\mathbf{I}_{\mathrm{Cs}} \cdot \mathbf{S} + g_S\mu_B\mathcal{B}S_z + H_\Omega. \tag{3.11}$$

where B is the rotational constant of the molecule, $\mathcal{B}$ is the applied magnetic field and α_{Na} and α_{Cs} are effective hyperfine parameters for the two nuclei. We do not consider the nuclear quadrupole interaction (or any of the smaller terms) which, based on the hyperfine splittings of Na and Cs atoms, should be two-to-three orders of magnitude smaller than the dipolar term. The Ω-doubling Hamiltonian matrix elements, $\langle\Omega'|\, H_\Omega \,|\Omega\rangle = \frac{\omega_{ef}}{2}\delta_{\Omega',-\Omega}$, lift the Ω degeneracy, causing the eigenstates of $H_{c^3\Sigma_1^+}$ to be states of good parity $|P = \pm\rangle \sim |\Omega\rangle \pm |-\Omega\rangle$. Because we access only one of these parity states in the experiment, the value of ω_{ef} cannot be determined, so we fix it at an *ad hoc* value of 5 MHz and neglect the dependence of the doubling on J. To estimate its Franck-Condon couplings to the Feshbach and $X^1\Sigma^+$ states, we model the vibrational structure of the $c^3\Sigma_1^+$ state using the experimental potential of Ref. [105]. Given that we only consider states with $|\Omega| = 1$, we absorb terms that depend only on Ω into the overall vibronic energy, such that the line assignment is the same in both the Hund's case

(a) and (c) bases.

To model the $X^1\Sigma^+$ ground state we use the Hamiltonian and coupling constants from Ref. [4]. The rotational structure is given by

$$H_{\text{rot}} = B\mathbf{N}^2 \tag{3.12}$$

where, since $L = 0$, we have $\mathbf{N} = \mathbf{R}$ as a purely rotational quantum number.

The hyperfine Hamiltonian is given by the sum of equations 3.6 through 3.9 above:

$$H_{\text{hf}} = H_{\text{Q}} + H^{(0)}_{\text{spin}-\text{spin}} + H^{(2)}_{\text{spin}-\text{spin}} + H_{\text{spin}-\text{rot}} \tag{3.13}$$

and the Zeeman Hamiltonian is given by Equation 3.10, with $S_z = L_z = 0$.

3.2 Coupled channel models

When trying to determine the eigenstates of a molecule or scattering pair of atoms, it can be useful to represent states as a function of two parameters: the internuclear separation R and the internal state ξ, as $\Psi(\xi, R)$. Here, ξ can represent any combination of all the internal quantum numbers, but crucially it must be able to be represented as a linear combination of a finite set of basis states. By contrast, R is a continuous variable representing the vibrational wavefunction of the atom pair which, unless we approximate the interaction potential as fully harmonic, does not necessarily have a convenient decomposition into a set of basis functions. In general, the internal and vibrational states will be coupled by the molecular potential $V(\xi, R)$. To find the combined eigenstates of the internal state Hamiltonian and the molecular potential, we use a *coupled-channel*

model.

In the Ni lab, our approach to building a coupled-channel model was heavily influenced by the work of Jeremy Hutson, who describes the method in detail in Refs. [126–128], and has collaborated with us in the past to model the Feshbach resonance that we use to magnetoassociate NaCs molecules [44, 310]. The core idea of the coupled-channel model is that the total molecular state $\Psi(\xi, R)$ can be represented as a sum over channels corresponding to different molecular internal states, each of which has an associated vibrational wavefunction:

$$\Psi(\xi, R) = \frac{1}{R}\sum_i \Phi_i(\xi)\psi_i(R) \tag{3.14}$$

The $\Phi_i(\xi)$ here represent a complete orthonormal basis over relevant internal states of the molecule, which could, for example, encompass all of the different S and Λ molecular states which asymptote to the same unbound atomic state. The Schrödinger equation for the molecule can then be reformulated as a sum of coupled differential equations of the form

$$\frac{d^2\psi_i}{dR^2} = \sum_j (W_{ij}(R) - E\delta_{ij})\psi_j(R) \tag{3.15}$$

The $W_{ij}(R)$ are coupling matrix elements defined by

$$W_{ij}(R) = \int \Phi_i(\xi)^*(H_{int} + V(\xi, R))\Phi_i(\xi)d\xi \tag{3.16}$$

where H_{int} is the molecule internal state Hamiltonian, independent of vibration. The

coupled equations can be expressed in matrix form,

$$\frac{d^2\boldsymbol{\psi}}{dR^2} = (\mathbf{W}(R) - E\mathbf{I})\boldsymbol{\psi}(R) \tag{3.17}$$

where $\boldsymbol{\psi}$ is a column-vector of the original ψ_i.

Solutions to the coupled-channel problem can be found by discretizing R on a grid and numerically propagating trial solutions to converge at a wavefunction which solves Eq 3.17 and the boundary conditions at large and small R (which are generally that the wavefunction goes to zero). Such a solution will only exist at certain values of the energy E, which correspond to the vibrational eigenstates. In general, propagating a solution from within a classically allowed region, such as the inside of a potential well, to a classically forbidden region, such as the outside of a potential well, will be extremely numerically unstable. On the other hand, propagating in the opposite direction tends to be stable. As a result, a general stable approach to solution finding for a molecular binding problem is to propagate two sets of solutions, one starting from the classically forbidden region at small R and one starting from the classically forbidden region at large R. Eigenstates can then be found by matching the two solutions at a particular midpoint within the classically allowed region [126]. This process is illustrated in Fig. 3.4.

In practice, we actually propagate the log-derivative of the wavefunction, $Y(R) = \frac{d\ln\psi}{dR}$, which is more numerically stable. Once energy eigenvalues are found using the log-derivative, the full wavefunctions in each channel at those energies can be reconstructed. We use the coupled-channel model in two contexts in this chapter, first in section 3.4 to model the properties of the lowest energy unbound state of the atom

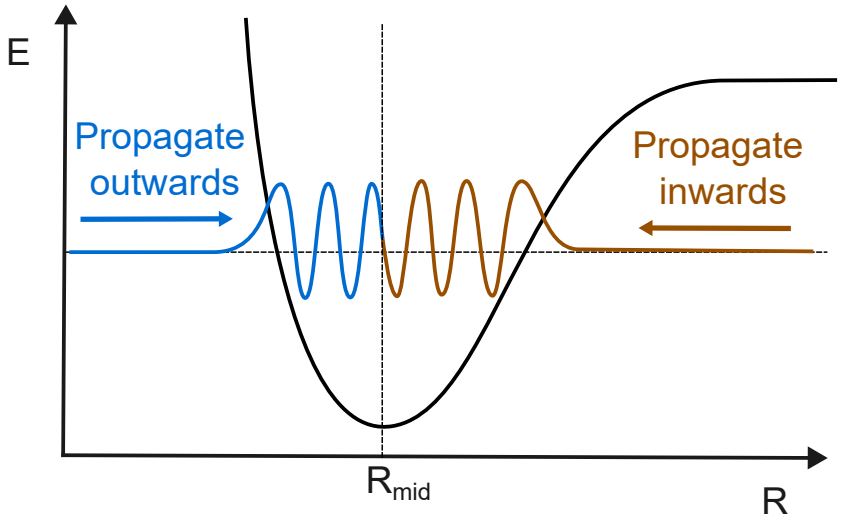

Figure 3.4: Illustration of matching condition for numerically finding a bound vibrational eigenstate $\psi(R)$ in a single channel by propagating solutions from both classically forbidden regions to a central point R_{mid} within the classically allowed region.

pair, and later in section 3.5 to perform a deperturbation analysis on the coupled $c^3\Sigma_1^+ - b^3\Pi_1 - B^1\Pi_1$ electronic states.

When modelling the lowest energy unbound state of the Na + Cs atom pair, the different channels correspond to the different atomic hyperfine states with the same total hyperfine projection m_F, which is the only quantum number strictly conserved by the interaction potential. In this case, the long-range confining potential is provided by the tweezer, while the short range repulsion is due to the molecular potential. The model Hamiltonian consists of Na and Cs hyperfine interactions, $H_{int} = H_{\text{Na,Cs}}$, singlet and triplet channel molecular potentials denoted by $V_{X^1\Sigma^+}(R)$ and $V_{a^3\Sigma_1^+}(R)$, a magnetic dipole-dipole interaction $V_d(R)$, and tweezer potential $V_{\text{trap}}(R)$:

$$H_{\text{F}}(R) = H_{\text{Na}} + H_{\text{Cs}} + \mathcal{P}_{S=0}\, V_{X^1\Sigma^+}(R) + \mathcal{P}_{S=1} V_{a^3\Sigma_1^+}(R) + V_d(R) + V_{\text{trap}}(R) \qquad (3.18)$$

where $\mathcal{P}_{S=0}$ and $\mathcal{P}_{S=1}$ are projectors onto singlet and triplet subspaces. We use functional forms of the singlet and triplet potentials and V_d term given in Ref. [44], with the former being a refinement of potentials originally defined in Ref. [80] designed to reproduce the Feshbach resonance in this channel at 864 G. We solve the coupled-channel problem in the spin-coupled basis $|N, m_N; S, m_S; I_{\mathrm{Na}}, m_{I_{\mathrm{Na}}}; I_{\mathrm{Cs}}, m_{I_{\mathrm{Cs}}}\rangle$, including only channels with no rotational angular momentum, $|N = 0, m_N = 0\rangle$. Depending on the choice of initial atomic state preparation, we restrict the incoming channels to only those with either $m_{\mathrm{tot}} = m_{I_{\mathrm{Na}}} + m_{I_{\mathrm{Cs}}} = 4$ or 6.

In the second case, we use the coupled channel model to describe the combined molecular potential formed by the coupling of the $c^3\Sigma_1^+$, $b^3\Pi_1$ and $B^1\Pi_1$ electronic states. The individual channels are the three so-called diabatic (non-interacting) potentials. We empirically tune the couplings between the potentials to reproduce the known positions of vibrational lines, in a process known as deperturbation. We can subsequently re-diagonalize the potentials to produce new adiabatic potentials, in which the vibrational states can be viewed as consisting of only a single channel.

3.3 The puzzle of anomalous broadening in NaCs

As described briefly in Section 2.3, preparation of rovibronic ground state NaCs molecules involves a two-photon transfer from the weakly bound Feshbach molecule state, via an electronically excited state. Although the two-photon transfer methods used (both STIRAP [216] and detuned Raman [309]) are designed specifically to avoid populating the intermediate state, the state's properties can nevertheless strongly influence the efficiency of the transfer process. Most critically, the effective two-photon

Rabi rate will be determined by the transition dipole moments from the intermediate state to both the initial and final states. Also significant, however, is the lifetime of the intermediate state. If this state's lifetime is too short compared to the time required for two-photon transfer, the approximation that it is unpopulated may break down, manifesting as decoherence or population loss during the transfer [235].

In searching for an intermediate state through which to transfer from the Feshbach to the ground state of NaCs, we have principally turned our attention to the $c^3\Sigma_1^+$ electronic potential. States within this potential have a high degree of singlet-triplet mixing, due to strong spin-orbit coupling with the nearby $B^1\Pi$ potential [151]. This allows these states to act as a bridge between the triplet-dominated Feshbach state and the singlet $X^1\Sigma^+$ ground state. In the limit of large internuclear separation, the $c^3\Sigma_1^+$ state asymptotically tends towards the Na(3s) + Cs($6p_{3/2}$) unbound atomic state, corresponding to a pair of Na and Cs atoms with the Cs electronically excited on the D_2 transition. It was thus initially anticipated that states within this potential, especially those relatively close to the dissociation threshold, would have lifetimes similar to that of the Cs $6p_{3/2}$ state, which has a natural linewidth of $\Gamma = 2\pi \times 5.2$ MHz, corresponding to a lifetime $1/\Gamma = 30$ ns [259]. This was, however, found to not be the case.

In the first high-resolution spectroscopic measurement of the $v' = 12, J = 2$ vibrational line of the $c^3\Sigma_1^+$ state performed using the optical association apparatus in the Ni group, the linewidth was found to be significantly broadened by two-photon stimulated absorption-emission processes induced by the optical tweezer light itself. This broadening mechanism is discussed in detail in [301]. The narrowest observed linewidth for this state in a shallow tweezer was $\Gamma = 2\pi \times 27(1)$ MHz. In subsequent

work using the apparatus with which this dissertation is concerned, we initially used the $v' = 26, J = 1, m_J = 1$ vibrational line as an intermediate for ground state transfer. This line, however, was observed to have a width of $\Gamma = 2\pi \times 120(30)$ MHz even without tweezer-induced broadening, more than an order of magnitude larger than the Cs D_2 linewidth [48]. The remainder of this chapter details our spectroscopic investigation of multiple vibrational lines within the $c^3\Sigma_1^+$ potential, through which we sought to identify trends in and possible mechanisms for this unexpected broadening. Our ultimate goal was to identify a narrow line which could be used for efficient two-photon transfer to the ground state.

3.4 Photoassociation spectroscopy

To probe the electronically excited $c^3\Sigma_1^+$ potential, we performed photoassociation (PA) spectroscopy on pairs of Na and Cs atoms co-trapped in a single optical tweezer [130]. Both atoms were Raman sideband cooled in separate optical tweezers, which were then adiabatically merged into a single trap [172, 302], as described in Section 2.2. The atom hyperfine states were initialized to either $|F = 2, m_F = 2\rangle_{\text{Na}} |F = 4, m_F = 4\rangle_{\text{Cs}}$, with total magnetic quantum number $m_{\text{tot}} = 6$, or $|F = 1, m_F = 1\rangle_{\text{Na}} |F = 3, m_F = 3\rangle_{\text{Cs}}$, with $m_{\text{tot}} = 4$. The $m_{\text{tot}} = 6$ scattering state was probed at a magnetic field of 8.8 G, while the $m_{\text{tot}} = 4$ state was probed at high magnetic field of 860 G, close to the Feshbach resonance in this channel [44, 310]. For this chapter we take the magnetic field as the quantization axis, which is parallel to the k-vector of the tweezer. The atoms were photoassociated using light resonant with the transition from the lowest energy unbound relative motional state of the atoms in the trap to bound molecular states of the $c^3\Sigma_1^+$

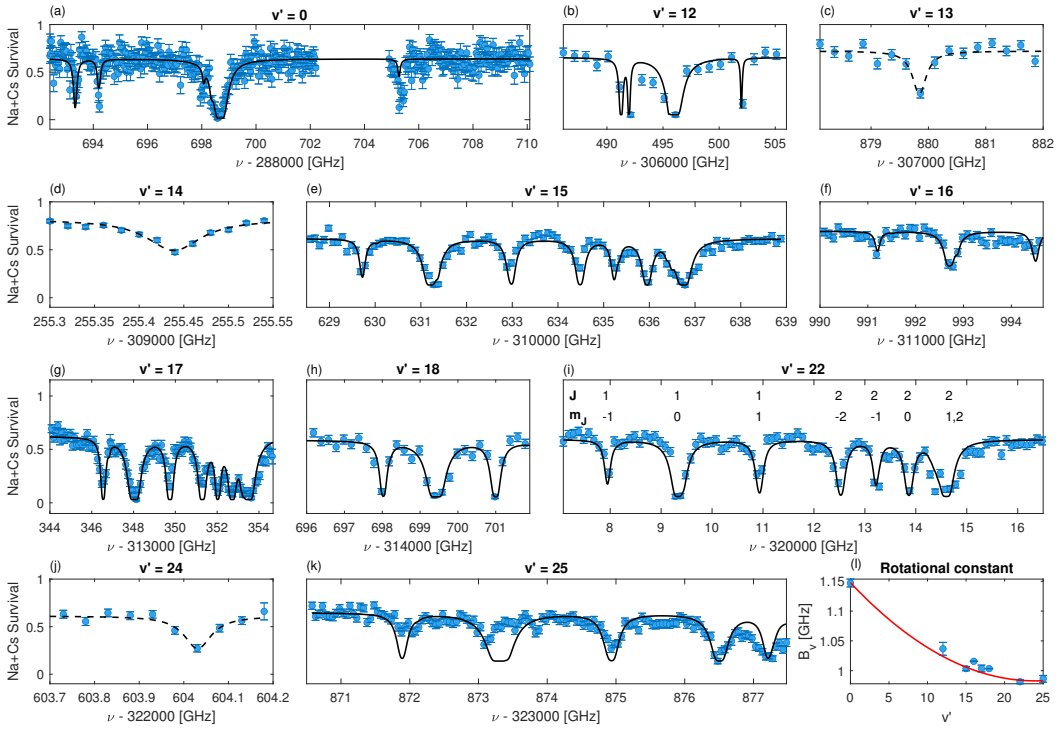

Figure 3.5: (a - k) Photoassociation spectra showing the $v' = 0$ (a), 12-18 (b - h), 22 (i), 24 (j), and 25 (k) vibrational manifolds of the $c^3\Sigma_1^+$ potential. The atoms were prepared in $|F = 2, m_F = 2\rangle_{\mathrm{Na}} |F = 4, m_F = 4\rangle_{\mathrm{Cs}}$ ($|F = 1, m_F = 1\rangle_{\mathrm{Na}} |F = 3, m_F = 3\rangle_{\mathrm{Cs}}$) for $v' = 0$ to 14 ($v' = 15$ to 25), and a constant magnetic field of $B = 8.8$ G ($B = 860$ G) was applied. The polarization of the photoassociation light was approximately σ^+ for $v' = 0$ to 14, and an equal mixture of σ^+ and σ^- for $v' = 15$ to 25. Solid lines are fits to the model of the $c^3\Sigma_1^+$ state described in Section 3.2 with the rotational constant B and the hyperfine constant α_{Na} along with a global frequency offset and scattering time as fit parameters. The fit values for each vibrational manifold are given in Table 3.3. The dashed lines indicate Lorentzian fits, which we use to fit the line position in cases where only a single state is observed without the rotational and magnetic sublevel resolution required to perform a fit to the complete $c^3\Sigma_1^+$ model. Frequencies of the highest energy line of the $J = 1$ manifold of each level are given in Table 3.4. We label the assignment of lines by their approximate J and m_J quantum numbers overlaid on the data for $v' = 22$. (l) Fit of the rotational constant dependence on vibrational level to second order using the model $B_v = B - \alpha(v' + \frac{1}{2}) + \gamma(v' + \frac{1}{2})^2$ [45], with parameter fit values $B = 1.154(9)$ GHz, $\alpha = 14(1)$ MHz, $\gamma = 0.29(4)$ MHz.

potential. The photoassociation light was provided either by the optical tweezer itself—the frequency of which can be widely tuned while still providing strong confinement of the atoms—or by an additional counter-propagating focused beam overlapping the

Table 3.3: Hamiltonian fit parameters of observed vibrational lines in the $c^3\Sigma_1^+$ potential. Levels $v' = 13$, 14, and 24 are not included, as only one line was observed in each of these vibrational manifolds, which does not provide sufficient data to reliably fit the full $c^3\Sigma_1^+$ Hamiltonian. In the case of the $v' = 12$ data, we did not measure the spectrum with magnetic sublevel resolution, so the hyperfine constants were fixed at the fit values for $v' = 15$ and only the rotational constant B was varied. Conversely, in the case of $v' = 16$ and 18, only the first rotational level was measured, precluding robust fitting of the rotational constant. For these levels, the rotational constant was fixed at the value predicted by the model fit in Fig. 3.5(l) for these vibrational levels.

v'	Initial state $\lvert F, m_F\rangle_{\mathrm{Na}}$ $\lvert F, m_F\rangle_{\mathrm{Cs}}$	Laser pol.	Magnetic field (G)	B (GHz)	α_{Na} (GHz)	Observed rotational lines
0	$\lvert 4,4\rangle \lvert 2,2\rangle$	σ^+	8.8	1.147(7)	0.69(3)	$J = 1, 2, 3$
12	$\lvert 4,4\rangle \lvert 2,2\rangle$	σ^+	8.8	1.04(1)	-	$J = 1, 2$
15	$\lvert 3,3\rangle \lvert 1,1\rangle$	$\sigma^+ + \sigma^-$	860	1.003(3)	0.63(1)	$J = 1, 2$
16	$\lvert 3,3\rangle \lvert 1,1\rangle$	$\sigma^+ + \sigma^-$	860	-	0.66(3)	$J = 1$
17	$\lvert 3,3\rangle \lvert 1,1\rangle$	$\sigma^+ + \sigma^-$	860	1.004(5)	0.47(5)	$J = 1, 2$
18	$\lvert 3,3\rangle \lvert 1,1\rangle$	$\sigma^+ + \sigma^-$	860	-	0.40(2)	$J = 1$
22	$\lvert 3,3\rangle \lvert 1,1\rangle$	$\sigma^+ + \sigma^-$	860	0.981(3)	0.41(2)	$J = 1, 2$
25	$\lvert 3,3\rangle \lvert 1,1\rangle$	$\sigma^+ + \sigma^-$	860	0.986(5)	0.46(2)	$J = 1$
26	$\lvert 3,3\rangle \lvert 1,1\rangle$	$\sigma^+ + \sigma^-$	860	0.953(3)	0.31(2)	$J = 1, 2, 3$

tweezer. In the former case, the tweezer/PA light was generated from a home-built tunable external cavity diode laser, while in the latter, the PA light was generated from a tunable Ti:Sapphire laser. When photoassociation occurs, the molecular state will generally rapidly decay, either to an excited atomic motional state that is likely to have sufficient energy to escape the trap, or to a lower energy molecular bound state that will be dark to the atom imaging step. We therefore detected photoassociation through correlated loss of Na and Cs atoms [173]. In the spectra presented here, we plot the joint Na and Cs survival conditioned on initial loading of both atoms in their respective traps.

We observed photoassociation to the $v' = 0, 12, 13, 14, 15, 16, 17, 18, 22, 24, 25$, and 26 vibrational manifolds of the $c^3\Sigma_1^+$ potential. Within some of these vibrational levels, we

were able to observe rotational structure up to the $J = 3$ rotational state, and resolve individual magnetic sublevels. The spectra of all observed lines in each vibrational level are shown in Fig. 3.5 along with corresponding fits to the effective Hamiltonian model. In Table 3.3 we report experimental parameters and fit values for all observed lines, and in Table 3.4 we report absolute frequency measurements and linewidths of the $|J = 1, m_J = 1\rangle$ sublevel for each vibrational level. We choose this line as a reference because it is a resolved state to which we can consistently strongly couple with pure σ^+ or $\sigma^+ + \sigma^-$ light, defined with respect to the magnetic quantization axis, at either high or low magnetic field, and because it is the intermediate state which we use for two-photon transfer to the rovibrational ground state, discussed in Sections 2.3 and 3.6.

For the initial atom pair state $|F = 2, m_F = 2\rangle_{\mathrm{Na}} |F = 4, m_F = 4\rangle_{\mathrm{Cs}}$, the angular momentum values are predominantly $N = 0,\ S = 1$, giving $J = 1$. By selection rules, this state couples most strongly to $J = 2$ states in the excited state manifold with predominantly σ^+ polarization, with a small coupling to $J = 3$ due to mixing of rotational states in $c^3\Sigma_1^+$. Experimentally, we observed stronger than expected coupling to $J = 3$, which we attribute to imperfect motional cooling of the atom pair, which would lead to having some initial population in a rotationally excited atom pair state that couples more strongly to $J = 3$.

On the other hand, the initial atom pair state $|F = 1, m_F = 1\rangle_{\mathrm{Na}} |F = 3, m_F = 3\rangle_{\mathrm{Cs}}$ is in a mixed singlet-triplet spin state, and can thus couple to both $J = 1$ and $J = 2$ via σ^+ polarized light. This scattering channel exhibits a Feshbach resonance at 864.11(5) G, which we use for adiabatic assembly of weakly bound Feshbach molecules [310]. Part

of the motivation for performing the spectroscopy in this chapter was to identify vibrational states in $c^3\Sigma_1^+$ suitable to use as an intermediate state for two-photon optical transfer from these Feshbach molecules to the rovibrational ground state. In Ref. [48], we showed spectra resolving the structure of the $v' = 26$ level with $\sigma^+ + \sigma^-$ light incident on Feshbach molecules, and used the $|J = 1, m_J = 1\rangle$ line of this vibrational state as an intermediate to prepare rovibrational ground state NaCs molecules via a detuned Raman process. Our choice of two-photon transfer method and transfer efficiency were constrained by the anomalously broad linewidth of $v' = 26$, discussed in Section 3.5.

For each vibrational level, we used the scattering and excited state models described previously in this chapter to fit the observed spectra. Our initial state was fixed to be either the $|F = 2, m_F = 2\rangle_{\mathrm{Na}} |F = 4, m_F = 4\rangle_{\mathrm{Cs}}$ state at low field or the $|F = 1, m_F = 1\rangle_{\mathrm{Na}} |F = 3, m_F = 3\rangle_{\mathrm{Cs}}$ state at high field, with the vibrational wavefunctions corresponding to each hyperfine component of these scattering channels determined by the coupled-channel model. Because we performed Raman sideband cooling on both atoms before PA, preparing each atom in its absolute motional ground state with high probability [173, 302, 308], we assumed that the initial scattering state was the lowest energy unbound eigenstate found when solving the coupled-channel problem. The forms of the spectra obtained for a given initial state are determined by a combination of the vibrational wavefunctions and the spin and angular momentum expansion factors for each of the available excitation channels. The transition dipole moment (TDM) to every excited state was found by first integrating the scattering wavefunction over internuclear separation R, multiplied by a function from *ab initio* theory describing the position dependence of the singlet-triplet character of the excited state [198, 303]

and then summing over the components of the scattering wavefunction weighted by their respective angular momentum coupling coefficients.

In fitting the spectra, we varied the rotational constant B and the hyperfine constant α_{Na} as free parameters. We found that if both α_{Cs} and α_{Na} were used as free parameters they exhibited a high degree of covariance, such that neither could be accurately uniquely determined by fitting the spectra. Given that the $c^3\Sigma_1^+$ potential asymptotes to the Na(3s) + Cs($6p_{3/2}$) pair, the Na ground state hyperfine splitting will be the dominant contribution to the molecule's hyperfine structure. As such, we approximated the α_{Cs} parameter by its $6p_{3/2}$ asymptotic value of 50.275 MHz [259]. We note that this may be an overestimate of the Cs contribution, and thus the Na hyperfine constants in Table 3.3 may represent a slight underestimate of the Na contribution to the hyperfine structure. Additionally, we used global frequency offset and scattering time variables to simultaneously fit all the line positions and the magnitude of the PA depletion signal, respectively. At each fit iteration, we diagonalized the excited state Hamiltonian to determine line positions and relative strengths, from which we derived the expected atom pair survival as a function of PA frequency. We performed a nonlinear least squares fit to minimize the difference between the simulated and observed spectra simultaneously for all four free parameters. Fit parameters for each vibrational level are given in Table 3.3. With the aid of the model, we can identify each of the lines, which are labeled, overlaid on the $v' = 22$ spectrum in Fig. 3.5(i), by J and m_J, which are approximately good quantum numbers for the state. The ordering of lines as a function of energy is the same for all of the vibrational levels. At the lower magnetic field used to probe v' = 0 to 14, the magnetic substructure of each rotational level is not fully resolved. In Fig.

v'	$\|J=1, m_J=1\rangle$ freq [GHz]	Linewidth [MHz]
0	288698.91(5)	39(13)
12	306496.6(1)	27(1) [301]
13*	307884.55(8)	-
14*	309260.150(4)	70(10)
15	310624.77(1)	12(3)
16	311986.30(2)	10(3)
17	313341.27(2)	12(8)
18	314692.77(1)	27(5)
22	320002.49(1)	17(3)
24*	322595.86(1)	-
25	323866.47(8)	42(9)
26	325121.31(7)	120(30) [48]

Table 3.4: Frequencies and narrowest observed linewidths of $|J=1, m_J=1\rangle$ states in each vibrational level. For levels v' = 13, 18, and 24, the lines were only observed in the presence of significant power broadening, so we do not report a narrow linewidth for these states. * denotes levels for which coupling to the state was weak enough that only one line could be observed experimentally, making rotational and hyperfine assignment impossible. For these levels, the reported frequency is the center of a Lorentzian fit to the observed line. For all other lines, the frequency of the $|J=1, m_J=1\rangle$ line is determined by fitting the whole spectrum to the $c^3\Sigma_1^+$ model as described in the text. The reported transition frequencies are given with respect to the hyperfine center of mass of the atom pair at the magnetic field used for spectroscopy. The hyperfine COM was calculated using the Breit Rabi formula. It is 4.711 GHz below the $|F=2, m_F=2\rangle_{\mathrm{Na}}|F=4, m_F=4\rangle_{\mathrm{Cs}}$ channel at 8.8 G and 8.175 GHz above the $|F=1, m_F=1\rangle_{\mathrm{Na}}|F=3, m_F=3\rangle_{\mathrm{Cs}}$ channel at 860 G. The frequency and linewidth of the $v'=26$ state, previously reported in [48], were determined using resonant depletion of Feshbach molecules, and are included here for completeness.

3.5(l), we fit the vibrational dependence of the rotational constant of the molecule to second order in v' using the functional form $B_v = B - \alpha(v'+\frac{1}{2}) + \gamma(v'+\frac{1}{2})^2$ [45] with parameter fit values $B = 1.154(9)$ GHz, $\alpha = 14(1)$ MHz, and $\gamma = 0.29(4)$MHz. We note also that there is a clear decrease in the effective Na hyperfine coupling constant a_{Na} as a function of v', indicating a reduction of electron density at the Na nucleus at higher vibrational levels [154].

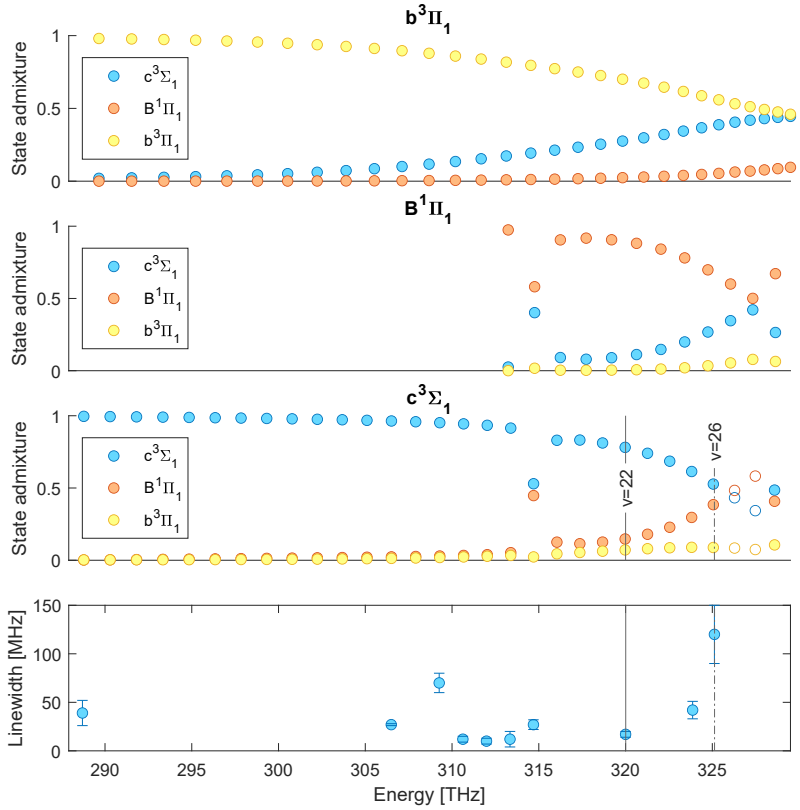

Figure 3.6: Predicted admixtures for each Hund's case (a) state as a function of energy from the Na(3s) + Cs(6s) threshold, shown from the bottom of the $c^3\Sigma_1^+$ potential to just below the Na(3s) + Cs($6p_{3/2}$) threshold. Particular eigenstates of the coupled potential are assigned to the uncoupled potential of which they have the largest admixture, with the exception of highly mixed states denoted by hollow circles, which are plotted for clarity with the $c^3\Sigma_1^+$ vibrational progression to which they belong, though they have a slightly larger admixtures of $B^1\Pi$. Also shown in the bottom panel are the experimentally observed linewidths, reported in Table 3.4, for all the $c^3\Sigma_1^+$ states identified in this work.

A distinctive feature of the vibrational spectra of the $c^3\Sigma_1^+$ potential is the presence of several vibrational lines with anomalously broad linewidths. Similar anomalous broadening of lines in the coupled $c^3\Sigma_1^+ - b^3\Pi_1 - B^1\Pi_1$ complex has been observed previously in other bialkalis, including Li_2[241], NaK [270] and NaRb [110], but the origin

of the broadening remains poorly understood. In Table 3.4, we report measurements of the narrowest observed linewidths of the $|J = 1, m_J = 1\rangle$ line for most of the vibrational states identified in this chapter. To measure the linewidth without power broadening, we systematically lowered the intensity of the photoassociation laser until only approximately 50% of the atom population was photoassociated. We then scanned the laser frequency across the line and performed a fit to a Lorentzian to determine the linewidth. Based on the model Hamiltonian, we expect each $m_J = 1$ line to be dominated by a single nuclear hyperfine component, with a small contribution from more weakly coupled nuclear states. As these different nuclear components of the lines are not resolved, we interpret the narrowest experimentally observed lines reported here as providing only an upper bound on the natural linewidths of the most strongly coupled hyperfine state. In Ref. [48], we investigated only the v' = 26 vibrational level with the goal of using it as an intermediate for ground state molecule production, and found it to have a linewidth of 120(30) MHz, more than an order of magnitude larger than the Cs D2 line to which the molecular potential asymptotes, which has a full width at half maximum of 5.2 MHz [259]. We note that independent work in Ref. [262] measured this same state to have a linewidth of 51(5) MHz, probed in a bulk sample of NaCs in a weak optical dipole trap. In our spectroscopic investigation, we identified several narrower vibrational lines, albeit with the narrowest having a linewidth of 10 MHz, still a factor of 2 larger than the Cs D_2 line. The narrowest lines we observed are v' = 15-17, with v' = 22 having a slightly larger linewidth of 17 MHz and v' = 25 and 26 both being significantly broader with linewidths of 42(9) and 120(30) MHz, respectively. We also measured a linewidth of 70(10) MHz for $v' = 14$, however, given that this line is unas-

signed, we note that it could potentially originate from the $J = 2$ rotational state and thus not be directly comparable to the other measured linewidths.

One of the possible mechanisms for the observed broadening is predissociation, meaning the coupling of a molecular state to another state at an energy above the latter's dissociation threshold, which can lead to rapid nonradiative dissociation of the molecule [45, 304]. This has previously been proposed as a potential mechanism for the anomalous broadening observed in Li_2 [241] and NaRb [110]. In NaCs, the $c^3\Sigma_1^+$ potential is mixed very strongly with the nearby $B^1\Pi_1$ and $b^3\Pi_1$ potentials via spin-orbit coupling. We note that while earlier widely used experimental potentials for NaCs [80] predict that the $a^3\Sigma_1^+$ curve does not cross any electronically excited potentials below the Cs(6p) threshold, a more recent refinement of the triplet scattering potential [44] shown in Fig. 3.1 exhibits a significantly sharper short-range repulsive wall, which crosses the $b^3\Pi_1$ curve well below threshold. This is the same potential that we use in the coupled-channel model, and which accurately reproduces the location of the Feshbach resonance in the lowest energy scattering channel. Though the precise short range behavior may be difficult to predict with confidence from scattering data, this new potential suggests that there may be lower energy crossings and more significant wavefunction overlap between bound and dissociative states than previously thought.

While predissociation remains difficult to observe directly, we seek to gain some understanding of the potential role of this mechanism in the broadening of some vibrational lines by modelling the nonradiative couplings of the $c^3\Sigma_1^+$ potential to $B^1\Pi_1$ and $b^3\Pi_1$. We do this using a process known as "deperturbation", which involves modifying theoretical molecular potential curves with small phenomenological perturbations,

which are numerically optimized to maximize the agreement between the deperturbation potential and experimental data [152, 305]. The name "deperturbation" refers to the fact that after adding these empirical perturbations, the final potentials should actually more closely resemble the real molecular potentials. We take as our starting point previous *ab initio* calculations of the spin-orbit couplings between the states in the $c - b - B$ complex as a function of internuclear separation R, performed by the group of Robert Moszyński [198, 255], which capture the overall coupling but do not accurately reproduce experimental spectra of the molecule. We then add R-dependent perturbations of the form $W(R) = c\,(R/R_0)^n \exp(-(R/R_0)^m)$ to the off-diagonal coupling matrix elements and the diagonal terms representing the *ab initio* potentials. We chose the deperturbation matrix element to have a relatively small number of free parameters and a simple functional form that goes to 0 at $R = 0, \infty$. We then optimize the parameters c, R_0, n and m for each term to minimize the residual between the resulting deperturbed potential and empirical adiabatic $c^3\Sigma_1^+$, $b^3\Pi_1$ and $B^1\Pi_1$ potentials [104, 105, 305].

Using the deperturbed potentials, we can estimate the energies and admixtures of each of the three states for all of the vibrational levels in the $c - b - B$ complex, as shown in Fig. 3.6. Note that, because the mixing depends significantly on the spacings between the closest vibrational levels from each series in the complex, the deperturbation step is critical for capturing trends in the mixing strength as a function of energy. However, the deperturbation elements themselves (Fig. 3.7) are phenomenological and do not necessarily reflect the actual form of the underlying couplings. With this caveat in mind, we note that the deperturbed potentials predict a very strong mixing of all

three levels, particularly $c^3\Sigma_1^+$ and $B^1\Pi_1$, in the region between v' = 23 and 32 of the $c^3\Sigma_1^+$ vibrational series. The most mixed states, v' = 27 and 28 of $c^3\Sigma_1^+$, are actually close to an even mixture of singlet and triplet, but for simplicity's sake we still label them as part of the $c^3\Sigma_1^+$ vibrational series. This region of predicted strong mixing coincides with our experimentally observed onset of anomalous line broadening, suggesting that the mixing may be responsible for inducing rapid predissociation or other nonradiative decay of the states. We also measured the $v' = 18$ line to have a width of 27(5) MHz, a factor of two larger than neighboring lines, which we attribute to its predicted high degree of mixing due to an accidental near-degeneracy with the $v' = 1$ state of $B^1\Pi$. While our experiment is not equipped to study the potential predissociation process directly, these results indicate that further study of nonradiative decay processes in NaCs and other bialkalis may prove fruitful.

3.5.1 Deperturbation matrix elements

We report in Table 3.5 the optimized parameters for the deperturbation functions that we add to each matrix element in the 3x3 coupled-channel Hamiltonian representing the $c - b - B$ complex. In Fig. 3.7, we show the *ab initio* and perturbed diagonal potentials and coupling matrix elements used to estimate the mixing between the channels in Section 3.5. To find the optimal deperturbation parameters, we performed an unconstrained search using MATLAB to minimize the residual between the deperturbed potential and the empirical potentials from Refs. [104, 105, 305] as a function of all the perturbing function parameters, in the range from $R = 3.6$ to 10.6 Å. The exponent parameters n and m are bounded to be greater than 0 to ensure the perturbations go to 0

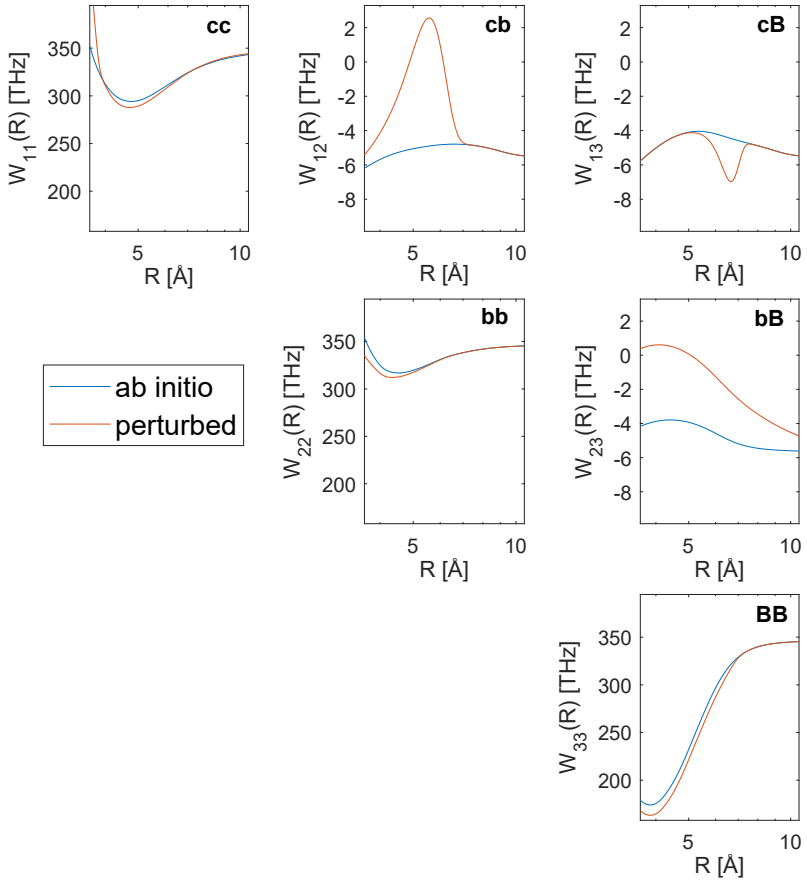

Figure 3.7: *Ab initio* and perturbed matrix elements, in THz, as a function of internuclear separation R for each channel in the coupled $c - b - B$ complex.

at $R = 0, \infty$, and all other terms are unbounded. We began by including six perturbing functions, one for each of the diagonal, cc, bb, and BB, and coupling, cb, cB and bB, matrix elements. Following initial optimization, we added additional perturbing functions until reasonable agreement with the empirical potentials was achieved. After optimization we found that the vibrational energies predicted using the perturbed potentials agreed with all the observed lines reported in Table 3.4 with a mean absolute deviation

of $<$ 40 GHz. We note that given the high dimensionality of the minimization problem, the parameters reported here likely do not represent a unique set of optimal deperturbing functions. However, we observe that the energy dependence of the mixing between the diabatic states shown in Fig. 3.6 is relatively insensitive to the precise form and relative weights of the deperturbing functions, but very sensitive to the spacings between particular vibrational levels. For this reason, we believe that any deperturbed model of the complex that is able to achieve close agreement with experimental data is sufficient to provide qualitative insight into the coupling and its potential link to the widths of the vibrational lines observed herein. We found that using a 2x2 coupled-channel model including only the $c^3\Sigma_1^+$ and $B^1\Pi_1$ states we could not achieve better than 1 THz agreement with experiment regardless of the number of deperturbing parameters used.

Channel	c [THz]	R_0 [Å]	n	m
cc	4032	2.912	2.057[-4]	7.29
cc	-26.56	3.809	2.272	2.3
cc	53.09	3.748	0.4164	42.09
cc	65.74	3.448	0.01794	5.972
cc	14.63	0.5263	1.484[-12]	0.3209
bb	-28.97	3.442	9.359[-3]	11.67
bb	-146.8	1.978	0.6053	1.69
BB	-10.91	6.687	5.156[-3]	19.89
bB	9.128	1.834	1.836	0.9779
cB	-6.4	6.49	19.66	14.18
cb	19.39	5.753	6.855	9.59

Table 3.5: Optimized parameters of deperturbation functions giving perturbed matrix elements shown in Fig. 3.7. Where used, the numbers in square brackets represent the power of 10 by which the preceding parameter is divided.

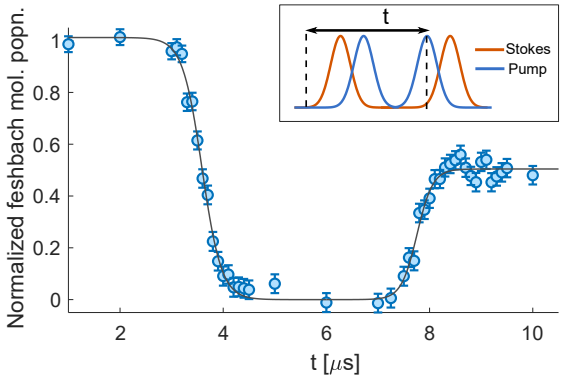

Figure 3.8: STIRAP transfer from Feshbach molecules to the rovibrational ground state of $X^1\Sigma^+$, via the $c^3\Sigma_1^+, v' = 22$ intermediate state, averaged over eight sites in a 1D optical tweezer array. The pump laser wavelength is 937 nm and the Stokes laser wavelength is 642 nm. The average one-way transfer efficiency is 73(3)%.

3.6 Two-photon transfer

In previous work [48, 309], we prepared up to five NaCs molecules in an optical tweezer array in the rovibrational ground state of the $X^1\Sigma^+$ potential through Feshbach association followed by detuned two-photon Raman transfer, using the $v' = 26$ level of $c^3\Sigma_1^+$ as an intermediate state. This level was initially chosen because of its expected high degree of singlet-triplet mixing, which leads to stronger coupling for the up-leg of the transfer. At that time, the correlation between singlet-triplet mixing and anomalous broadening was not well understood. Only once COVID-19 occupancy restrictions were lifted and we could perform extensive spectroscopy did we identify the nearby narrower vibrational lines (see Table 3.4).

For our first demonstration of ground state transfer, we chose to use detuned Raman transfer because the large linewidth of the $v' = 26$ state made the more standard STIRAP technique prohibitively lossy. Detuned Raman transfer can minimize scattering

from the intermediate, but remains more difficult to scale to a larger array of molecules since the two-photon resonance position is highly sensitive to local variations in the intensity of the Raman beams. Our first demonstration of parallel production of an array of ground state molecules was limited by a combination of scattering from the intermediate state and residual non-uniformity in our top hat shaped Raman beams [309].

Having identified several narrower vibrational lines in the $c^3\Sigma_1^+$ manifold, we selected the $v' = 22$ level as the new intermediate for ground state transfer. While it does not have the narrowest linewidth of all the lines observed, it was sufficiently close to $v' = 26$ to allow locking of our transfer lasers (pump laser at 937 nm, Stokes laser at 642 nm) to the same high finesse cavity that we used previously. It also had similar couplings strengths as $v' = 26$ to both our initial Feshbach molecule state and the rovibrational ground state. Using this new intermediate state, we were able to transfer molecules to the rovibrational ground state via STIRAP. We used Rabi frequencies of $2\pi \times 40$ MHz for the Stokes laser and $2\pi \times 14$ MHz for the pump laser, and performed resonant STIRAP ($\Delta \approx 0$) with an average one-way transfer efficiency of 73(3)%. The NaCs Feshbach molecule population during forward and reverse STIRAP pulses is shown in Fig. 3.8. We continue to use $v' = 22$ for ground state transfer throughout the remaining chapters, however as discussed in Chapter 5, we do return to using detuned Raman transfer in order to be able to tune the lasers out of resonance with transitions from the $N = 1$ states to allow for sequential detection of molecular states.

3.7 Open questions

While the deperturbation analysis conducted in this chapter provides a glimpse of the state mixings responsible for the anomalous broadening of $c^3\Sigma_1^+$ states in NaCs and ways to avoid them, it does not contain a detailed mechanism for that broadening. As discussed earlier, the most likely mechanism for the broadening is predissociation, although there are remaining open questions as to the exact predissociation pathway. In particular, predissociation requires coupling to unbound continuum states of another electronic potential, which in this case would most likely be the $a^3\Sigma_1^+$ potential, which is expected to intersect close to or below the Cs D_2 dissociation threshold with the excited electronic potentials. This mechanism is considered in detail in Ref. [241] in the case of the $b^3\Pi$ state of Li_2, which is coupled by rotation-orbit interactions to $a^3\Sigma_1^+$. This in turn leads to broadening of the nearby $A^1\Sigma^+$ state, which is coupled to $b^3\Pi$ by spin-orbit. This broadening in the *a*-*A*-*b* complex was again considered in the context of ultracold NaRb in Ref. [110], though not treated quantitatively at that time. A similar indirect coupling could lead to the broadening of $c^3\Sigma_1^+$ states considered in this chapter. This picture is slightly complicated by the fact that the dominant mixing that can be observed in Fig. 3.6 is actually to the $B^1\Pi$ state, the coupling of which to $a^3\Sigma_1^+$ has not been directly studied. The analysis conducted here does not, however, take into account the $\Omega = 0$ states (including $A^1\Sigma^+$), which could significantly complicate the picture with the introduction of the rotation-orbit and other interactions that do not conserve Ω.

An extremely valuable extension of this work would involve developing a comprehensive model of all the states that connect to the first three dissociation thresholds of NaCs. There are a total of eleven such states, assuming each different $|\Omega|$ state is

treated as a separate potential: $X^1\Sigma^+$, $a^3\Sigma^+_{0,1}$, $A^1\Sigma^+$, $b^3\Pi_{0,1,2}$, $B^1\Pi_{0,1}$ and $c^3\Sigma^+_{0,1}$. There also exists sufficient spectroscopic data on most of these states [80, 104, 105, 175, 286, 304, 305] that it may be feasible to perform a direct 11x11 deperturbation analysis to simultaneously fit all the known line positions. The predictions of such a model could also be benchmarked against the radiative lifetimes of states where known, as done in this chapter and in Ref. [305], which may provide a more complete picture of dominant predissociation pathways, or suggest other broadening mechanisms not yet considered. This would be of use not only to researchers working with NaCs, but also to the now rather large community of bialkali researchers, as the effects present in NaCs are likely to also be present to a greater or lesser extent in all heteronuclear bialkalis. A comprehensive understanding of the first few electronically excited states of the bialkalis may allow for further improvements to the fidelity of two-photon transfer from Feshbach molecules to the rovibrational ground state [25], or uncover states that could be used for narrow-line cooling and imaging [147] or coherent optical manipulation of ultracold molecules.

It's still magic even if you know how it's done.

Terry Pratchett

4

Magic ellipticity trapping and rotational coherence

Material in this chapter, including portions of the text and figures, originally appeared in print in [210].

4.1 Optical trapping of molecules

The ability to spatially confine molecules is an essential prerequisite for probing and controlling them precisely. Some of the earliest experimental demonstrations of molecule trapping used magnetic fields, as well as DC or AC electric fields to confine

bulk samples of molecules [28, 145, 276, 288]. These traps, which can have depths of hundreds of mK,* allowed confinement of molecules cooled using techniques such as Stark deceleration [29] and buffer gas cooling [288], which can achieve cold but not ultracold temperatures. One of the earliest observations of optical trapping of molecules, with a typical depth of 100s of μK, was achieved with Cs_2 molecules produced by photoassociation of atoms in a magneto-optical trap, with the molecules inheriting the initially cold temperature of their constituent atoms [266]. This same principle was subsequently used to coherently produce and trap ultracold molecules through Feshbach association in bulk optical dipole traps [124, 202] and optical lattices [60, 92, 209]. In the Ni group, we demonstrated that this method could be extended to the production of single NaCs molecules in optical tweezers, which are tightly focused and individually-controllable optical dipole traps [48, 173, 309, 310]. Other species have subsequently also been loaded into optical tweezers [230], including through direct laser cooling of molecules to ultracold temperatures [10, 280].

One problem with optical trapping is that the trap light can induce large differential light shifts between molecular states. This can be highly detrimental to applications that require coherence between superpositions of rotational states, such as quantum computing and simulation with molecules. Many approaches have been developed to reduce the differential light shift between rotational ground ($N = 0$) and excited ($N \geq 1$) states. These include selecting a specific angle between the confining light's linear polarization and static magnetic or electric fields [36, 153, 200, 247], using a particular trapping wavelength [26, 108, 150] or intensity [34], or a specific magnetic field [63].

*1 mK is equivalent to 20.2 GHz

In the first approach the static field determines the orientation of the excited rotational eigenstates and a specific polarization angle matches the polarizability of one excited state to the ground state. This method, however, is not applicable even at moderate trap depths when the differential light shifts are of similar magnitude to the shifts induced by the static fields, such as for polar molecules confined in optical tweezers. In this deep trap regime, the rotational eigenstates are determined by the polarization of the tweezer light, rather than an external field.

4.2 Anisotropic polarizability and magic ellipticity

In this chapter, I describe a method we employed to trap $X^1\Sigma^+$ NaCs molecules in optical tweezers with "magic" elliptical polarization, to reduce the differential light shift by more than three orders of magnitude. Here, "magic" refers to a specific degree of ellipticity near $\chi_m = \frac{1}{2}\cos^{-1}(1/3) \approx 35.26^\circ$ that nulls the differential light shift, proposed in Ref. [225]. Similar methods have been explored in atomic systems [70, 143, 265, 273]. We measured the reduction of the differential shift by microwave spectroscopy and used Ramsey interferometry to characterize the coherence. With the aid of dynamical decoupling pulses, we achieved a coherence time of up to 250(40) ms.

Some theoretical aspects of "magic" ellipticity trapping have been described in Ref. [225]. The ground state of rotation ($N = 0$) is illustrated in Fig. 4.1(a) as a spherically symmetric rotational wavefunction with isotropic polarizability $(2\alpha_\perp + \alpha_{||})/3$ for any optical polarization, where ($\alpha_{||}$) and ($\alpha_\perp$) are the molecule's parallel and perpendicular polarizability with respect to the internuclear axis. This approximation is valid when the trap depth is small compared to the energy of $N = 2$ excited states (the optical po-

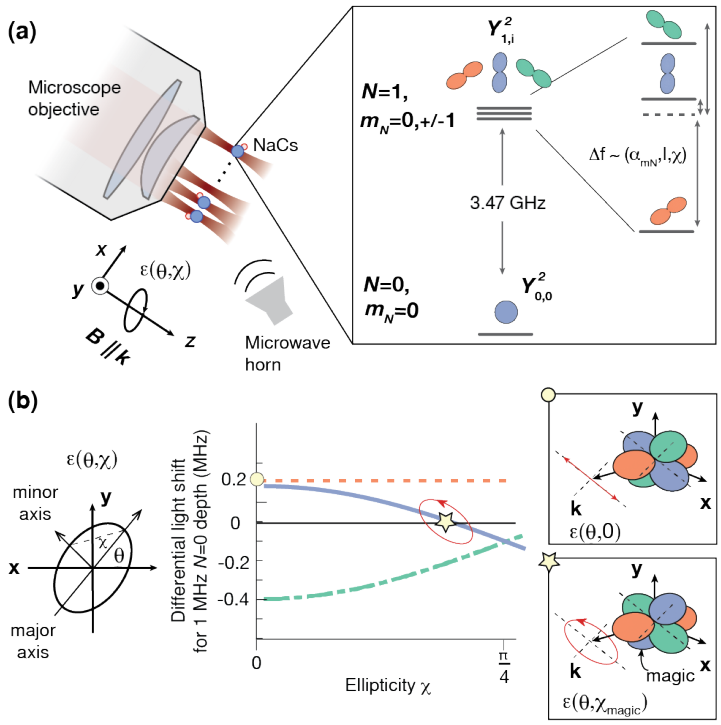

Figure 4.1: NaCs molecules in an optical tweezer array. (a) Schematic of the experimental setup, including the tweezer **k**-vector, magnetic field **B**, and trap polarization $\boldsymbol{\varepsilon}(\theta, \chi)$. Right is a simplified energy level diagram of ground ($N = 0$) and first excited ($N = 1$) rotational states, where the optical trap lifts the sublevel degeneracy. (b) The azimuthal angle θ and ellipticity χ of polarization determine the orientation and light shift, respectively, of the $N = 1$ sublevels. Unlike for linear polarization (circle), at the magic ellipticity χ_{m} (star), the differential light shift with respect to $N = 0$ is zero for one $N = 1$ sublevel.

tential couples states with both $\Delta N = 0$ and $\Delta N = 2$). Throughout the text, *trap depth* (U) refers to the optical potential experienced by the relatively unperturbed $N = 0$ state. We use frequency units that are implicitly related to energy by Planck's constant.

As shown in Fig. 4.1(b), for $N = 1$ the trap-induced light shift lifts the degeneracy of the three rotational sublevels ($m_N = -1, 0, 1$),[†] and strongly perturbs their wave-

[†]Note that throughout this chapter we choose the quantization axis to be along the minor axis of the polarization ellipse, which is the most convenient quantization axis for rotational sublevels. In Chapter 6, when we consider nuclear spin states, we instead define the quantization axis to be along the magnetic field.

functions, such that each sublevel has well-defined orientation relative to the optical polarization above a certain trap depth threshold. This threshold is relatively low for NaCs due to its hyperfine structure, small Zeeman interaction, and anisotropy of polarization. At the magnetic field of 864 G at which we produce and hold molecules, the rotational wavefunction of the lowest eigenstate aligns with the trap's polarization at a trap depth of around 100 kHz (>99.5 overlap with the eigenstate aligned along the trap's polarization). In a linearly polarized trap, the light shift is as large as 400.8 kHz/(MHz trap depth), corresponding to a ratio of shift to trap depth of 0.4. By tuning the ellipticity [41] near χ_m, we can eliminate this differential light shift to first order.

4.3 Dynamical polarization control of tweezer ellipticity

We implemented the magic ellipticity trapping scheme with an array of individual NaCs molecules in optical tweezers, prepared using the methods described in Chapter 2. For all data presented in this chapter, we prepared an array of eight molecules via stimulated Raman adiabatic passage—see Chapter 3—which predominately occupy the motional ground state of the traps [308]. After molecule creation, we applied a pulse resonant with the Cs D_2 transition to blast away any residual atoms. To detect molecules, we dissociated the molecules, separated the tweezers, lowered the magnetic field, and imaged both atomic species. In this chapter, we detected only the $|N = 0\rangle$ molecules. The Cs blast step provides a background free molecule signal.

Because atomic state preparation, cooling, and detection require linearly polarized tweezer light, it was necessary for us to change the polarization from linear to elliptical and back during the experiment sequence. For this purpose, we used a motorized stage

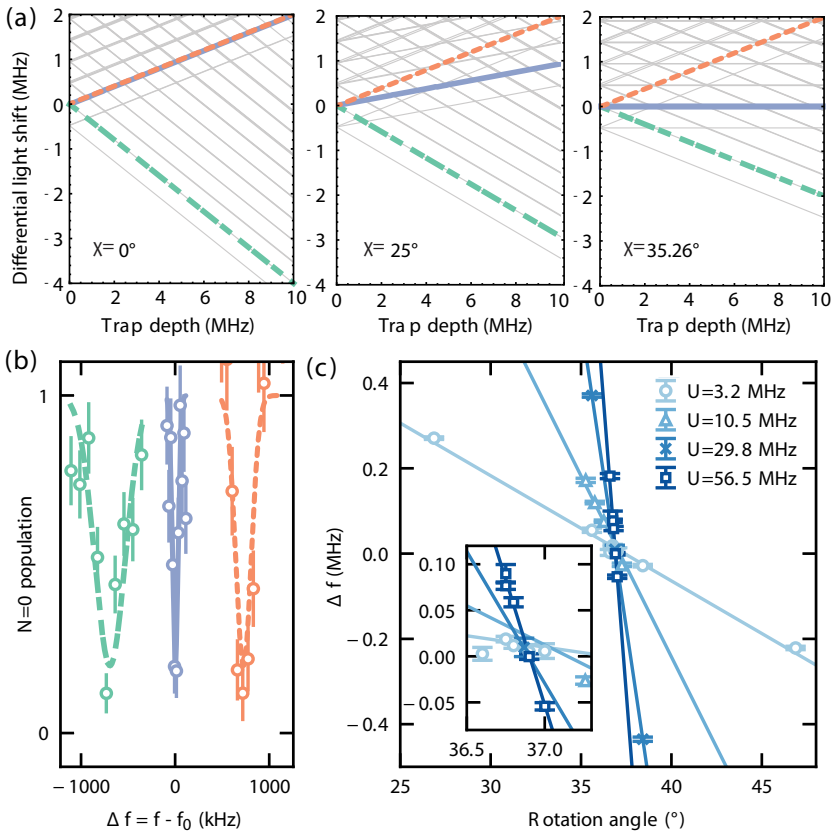

Figure 4.2: $N = 0$ to $N = 1$ rotational transition in the rovibrational ground state of NaCs. (a) Differential light shift as a function of $N = 0$ trap depth at three distinct trap ellipticities. The colored red, blue, and green lines correspond to the light shifts of $N = 1, m_N$ sublevels of the hyperfine state $|3/2, 3/2, 7/2, 5/2\rangle$, and the grey lines correspond to the same for other hyperfine states. (b) An example of a measured rotational spectrum in the magic elliptically polarized trap. (c) Extracted resonant frequencies of the middle state from the rotational spectroscopy at different trap depths (U) and QWP rotational angles. The solid lines are linear fits.

(Griffin Motion, RTS100) to rotate a quarter-wave plate (QWP) by χ_m in about 100 ms with a repeatability of $\pm 0.0007°$. To ensure polarization purity and minimize site-to-site polarization variation across the array, we used a Glan-Taylor polarizer to clean up the polarization and placed the QWP as the last element before the microscope objective. Before the QWP, the polarization extinction ratio was measured to be 300,000.

To characterize differential light shifts under various trap polarizations and intensities, we performed rotational microwave spectroscopy to selectively transfer the molecules from $N = 0$ to the relevant $N = 1$ sublevel with a transition frequency near 3.47 GHz. The microwave pulses were generated by a tunable source referenced to a stable Rubidium clock (see Fig. 2.13). As trap ellipticity increases (Fig. 4.2(a)), the degeneracy of the two upper sublevels is lifted. At an ellipticity near χ_m, the state with no differential light shift emerges. An example of the $N = 0$ to $N = 1$ microwave spectrum in an elliptical trap is shown in Fig. 4.2(b).

To find the precise QWP angle that achieves magic ellipticity, we scanned the microwave frequency over the transition with a 10 μs π-pulse at varying trap depths and recorded the resonance frequencies, as shown in Fig. 4.2(c). As expected, the slope of the resonance frequency as a function of QWP rotation is steeper at higher trap depths. The differential light shift is zero where the rotation angle dependence for all the trap depths intersect. We determined the angle of the intersection with a weighted fit to be $36.83(10)^\circ$, which deviates from the theoretically expected magic ellipticity angle by $\sim 1.6^\circ$. This discrepancy may be due to birefringence of the glass cell assembly and the microscope objective. Nulling the differential lights shift allows a determination of the $N = 0$ to $N = 1$ transition frequency $f_0 = 3.4713203(7)$ GHz, taken as the transition frequency at the optimal ellipticity at trap depth U =1.34 MHz. This value is consistent with the low-depth regime measurement of the transition in Ref. [32].

Residual light shift at the optimal QWP angle reveal site-to-site variations in frequency across the eight trap sites. To characterize these effects, we used a 60 μs microwave pulse to drive the rotational transition at a large trap depth of 41.2 MHz that

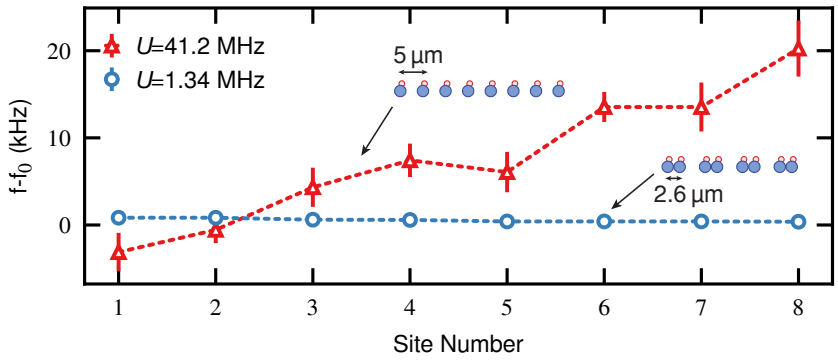

Figure 4.3: Variations in rotational transition frequency across the eight traps at two different trap depths U, and trap geometries and spacing. At a high trap depth of 41.2 MHz (red triangles), the transition frequency spans a range of 23 kHz across the array, and at a lower depth of 1.34 MHz (blue circles), it spans < 1 kHz.

magnifies light shifts. We found a site-to-site variation spanning 23 kHz (Fig. 4.3) with a 5(2) kHz average shift from the measured f_0, which constitutes a light shift to trap depth ratio of $1.2(5) \cdot 10^{-4}$. Despite the variation, this corresponds to a reduction in sensitivity by three orders of magnitude compared to the linearly polarized trap. The trap intensities across the array were made uniform to within 1%, such that they do not contribute significantly to the variation. We attribute the residual shifts to an ellipticity variation of 0.062° across the array.

4.4 Perturbations to magic condition

With the large linear differential light shift of the rotational transition eliminated by the magic ellipticity condition, other terms in the interaction between the molecule and the trapping potential can become important. These secondary interactions can perturb the magic condition and even limit the ultimate effectiveness of magic trapping. We discuss here the two effects that can appreciably perturb the magic condition at this

scale: trap-induced couplings between hyperfine states and motional-state-dependent shifts in the ellipticity condition due to trap aberrations. Calculations of the magnitudes of these perturbations were performed by Gabriel Patenotte.

4.4.1 Influence of hyperfine structure

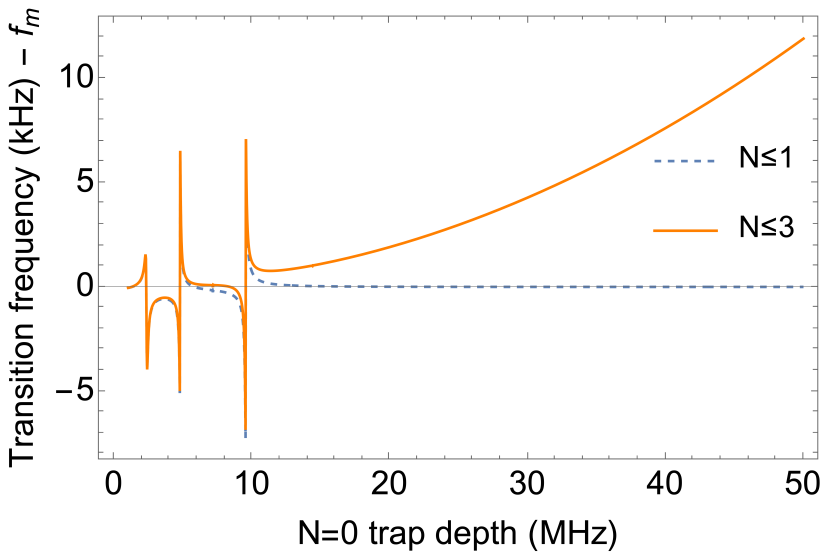

Figure 4.4: Calculation of the transition frequency to the magic $N = 1$ state (f_m). The effective Hamiltonian for the rotational/hyperfine manifold of NaCs was diagonalized with a basis extending up to either $N = 1$ or $N = 3$. The difference represents the second order light shift, or *hyperpolarizability*, which mixes $N = 0$ with $N = 2$ and $N = 1$ with $N = 3$. The three most prominent adiabatic crossings are produced by the coupling of high field seeking $N = 1$ hyperfine states $|M_{Na}, M_{Cs}\rangle = |\frac{1}{2}, \frac{7}{2}\rangle, |\frac{3}{2}, \frac{1}{2}\rangle, |\text{-}\frac{1}{2}, \frac{5}{2}\rangle$, and the low field seeking hyperfine state $|\frac{3}{2}, \frac{7}{2}\rangle$ with the magic $|\frac{3}{2}, \frac{5}{2}\rangle$ state.

We diagonalized the effective Hamiltonian for the rotational-hyperfine states of $X^1\Sigma^+$ NaCs given in [5] and found two effects in the "deep" trap regime that alter the ellipticity at which the transition frequency is first-order insensitive to light shifts. The first is adiabatic crossings of the magic N=1 state with other rotational hyperfine states. These crossings, visible in the region between 0 and 10 MHz depth in Fig. 4.4, occur when the

magic state becomes degenerate with light-shifted non-magic states with different nuclear hyperfine quantum numbers. The nuclear electric quadrupole interaction can couple these states, leading to an avoided crossing. The crossings introduce a first order light shift for the nominal magic ellipticity χ_m, which is made larger near depths at which the crossings occur. At a trap depth of 1.34 MHz, the first order sensitivity of the 'magic' transition is 270 Hz/MHz. The second effect is that the optical tweezer couples rotational states separated by $\Delta N = 2$. The mixing of anisotropic $N = 2$ and $N = 3$ states with $N = 0$ and $N = 1$ states, respectively, introduces a second order light shift, which is shown by the difference of the two curves in Fig. 4.4.

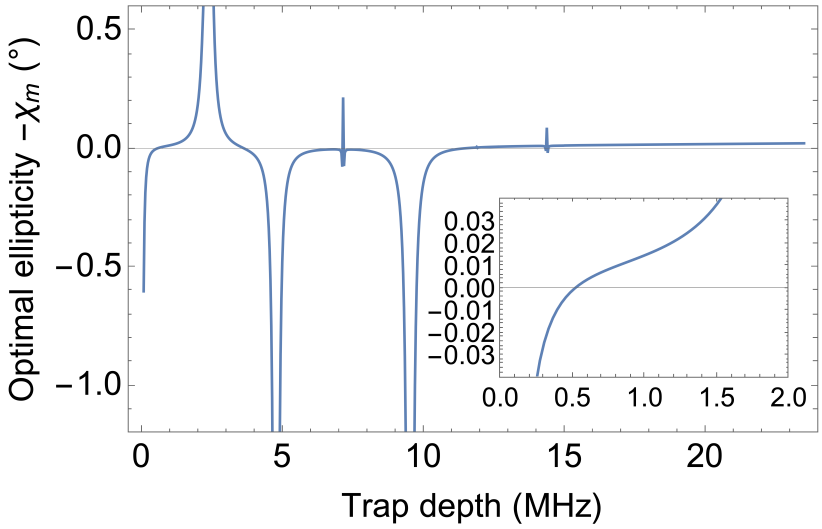

Figure 4.5: Ellipticity relative to χ_m for which the transition frequency is first order insensitive to intensity fluctuations. The inset highlights the optimal ellipticity for the range of trap depths used in coherence time measurements.

Both of these effects can, in principle, be corrected for by adjusting the ellipticity slightly away from the theoretical value of χ_m so as to make the sensitivity of the transition frequency to trap depth *locally* zero at some particular depth. The optimal elliptic-

ity to correct for these effects as a function of depth is shown in Fig. 4.5. We calculated the optimal ellipticity to be 0.025° larger than χ_m at a trap depth of 1.34 MHz. However, these non-linear shifts do slightly complicate the experimental calibration of the magic condition, as evidenced by the fact that the linear fits to the transition frequency dependence on waveplate angle in Fig. 4.2(c) for different depths do not perfectly intersect at the magic angle. The depth-corrected ellipticity can be more precisely determined using local measurements of the gradient of the transition frequency with depth, or using the coherence of the transition itself, as we do below in Fig. 4.7(b).

4.4.2 Aberrations and temperature

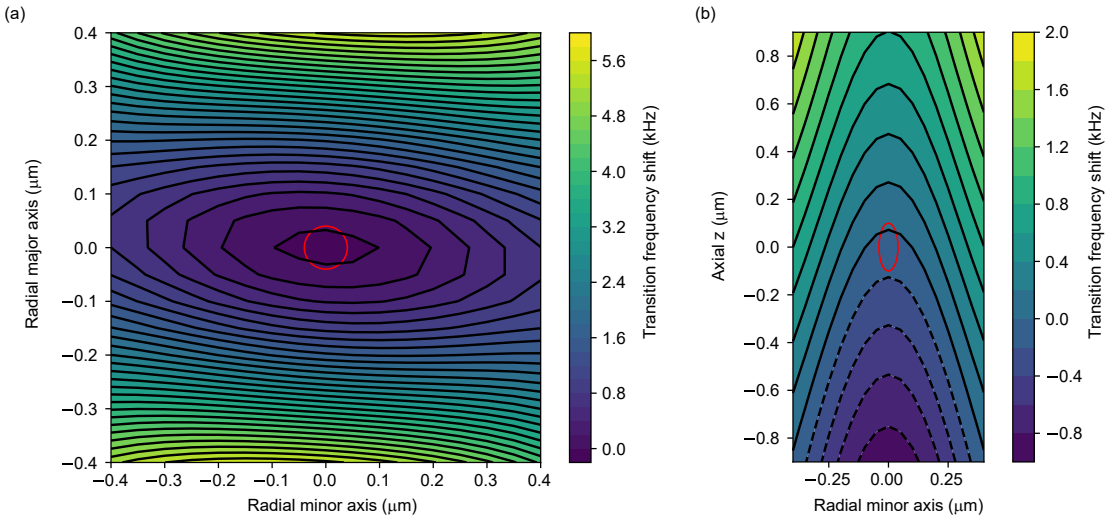

Figure 4.6: Shifts of rotational transition frequency as a function of molecule position in tweezer. (a) Shows a contour plot of the transition frequency relative to the trap center for a radial cross-section of the trapping potential, assuming a trap depth of $U = 1.34$ MHz. Contour lines are spaced by 200 Hz. The red circle represents the typical harmonic oscillator length $\sqrt{\frac{\hbar}{2m_{\mathrm{NaCs}}\omega}} = 80$ nm, where ω is the radial trapping frequency of the molecules. (b) Contour plot of transition frequency shift for an axial cross-section. Red ellipse again represents harmonic oscillator length, which is 200 nm along the axial direction.

In Chapter 6, we identify a critical role played by aberrations of the trapping poten-

tial and the temperature of the molecules in the coherence of the dipole interaction. At the time of publication of [210], we did model the effect of distortions of the ellipticity at the focus of a tweezer, which means that molecules with different amounts of motional excitation can sample different overall ellipticities. However, at that time, we did not consider the influence of aberrations of the tweezer. We thus revisit the effect here, using the astigmatism measured in section 6.6. We show in Fig. 4.6 the expected shift of the magic transition frequency as a function of displacement along both radial and axial cuts through the trap center, taking into account both astigmatism and the previously modelled distortion of the ellipticity at the tweezer focus. The energy shift is largest for displacement along the major axis of the polarization ellipse, though, as a result of aberrations, it is also significant for axial displacements. As a result of this position dependent shift, different motional states of molecules in the tweezer will experience different average transition frequencies. Unlike the perturbations to the magic condition due to higher order couplings to other states, this shift cannot be compensated for by changing the global ellipticity of the tweezer. In other words, it is not generally possible to achieve a perfect magic condition simultaneously for all motional states of a molecule in a tweezer. This is true even for an ideal tweezer due to the distortion of the ellipticity around the focus [271], but the effect is made more dramatic by the presence of aberrations.

For a trap depth of 1.34 MHz, the axial shift in trap centers between the $N = 0$ and $N = 1$ states shifts the transition frequency by 16 Hz away from the magic condition. Additional motional excitation along the axial direction makes relatively little difference, however, inducing further shifts of < 1 Hz per motional quantum. Motional exci-

tation along the radial directions aligned with the major and minor axes of the tweezer polarization ellipse are more significant, giving shifts of 43 and 161 Hz per motional quantum, respectively. In Section 6.6, we measure the axial ground state fraction of the molecules to be $34(4)\%$, which, assuming thermal equilibrium between the trap axes, would imply radial ground state populations of at least 93%. As such, the expected aberration and molecule temperature induced perturbations to the magic condition are currently significantly smaller than the limit imposed by residual ellipticity variations (Fig. 4.3). However, if the ellipticity variation were to be reduced by an additional order of magnitude in the future, molecule temperature would begin to set a more fundamental limit on the achievable cancellation of light shifts.

4.5 Rotational coherence

With the reduced light shift sensitivity, $N = 0$ and $N = 1$ rotational superpositions exhibit long coherence times, which we characterized via Ramsey spectroscopy. We use a spin-echo π-pulse to eliminate dephasing of the ensemble-averaged signal due to static light shift variation across the traps. The spin-echo pulse also decouples slow shot-to-shot variations in the detuning. For a linearly polarized trap ($U = 1.0$ MHz), the $1/e$ decay time is $\tau = 0.57(2)$ ms, in agreement with a simulated coherence decay that incorporates measured intensity noise and the strong light shift sensitivity (black line in Fig. 4.7(a)). With optimal magic ellipticity, the spin-echo coherence was extended by two orders of magnitude to 62(3) ms (blue circles in Fig. 4.7(a)). This coherence was further extended to 250(40) ms through the use of repeated XY-8 sequences (up to 72 total pulses) [167], which decouple noise on timescales slower than the spacing be-

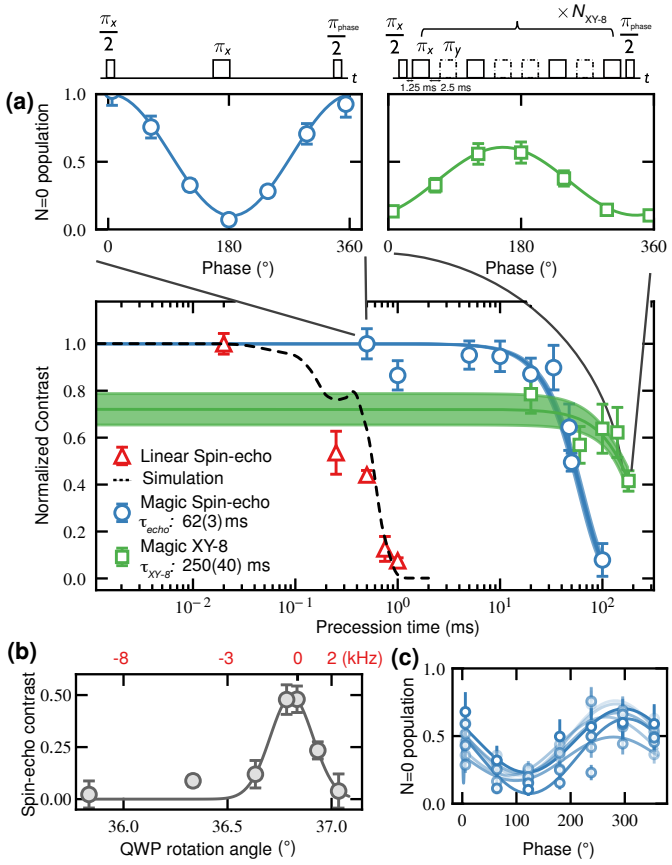

Figure 4.7: Rotational coherence times for 1.34 MHz trap depth. (a) The coherence time was characterized using a spin-echo phase Ramsey pulse sequence (shown in top left) in linear and magic elliptically polarized traps. In the linear trap, the phase Ramsey contrast as a function of the free precession time (red triangles) agrees well with the simulated coherence decay based on intensity noise (black dashed line). The spin-echo coherence time is extended by two orders of magnitude in the magic trap (blue circles), which can be further improved using the XY-8 pulse sequence (green squares) illustrated in the top right. The solid lines represent the fit to a Gaussian decay curve $C(t) = \exp[-(t/\tau)^2]$. For the XY-8 pulse sequence, the overall amplitude was left as an additional fit parameter to account for off-resonant population leakage during microwave pulses. For the spin echo data, all contrasts were normalized to the shortest time point. Example spin-echo and XY-8 phase Ramsey scans are shown in the top left and right insets, respectively. (b) Spin-echo phase Ramsey contrast at 50 ms as a function of the QWP rotation angle. A Gaussian fit yields an optimal rotation angle of 36.81(3) degrees. The top axis is the corresponding light shift expected from the ellipticity angle deviation relative to f_0. (c) Site-by-site Ramsey contrasts at 50 ms showing a global phase shift of 73(3)°. The contrast is normalized to the averaged N=0 population.

tween pulses. The maximum achievable contrast using the XY-8 sequence in Fig. 4.7 is slightly less than 0.8 even at short times, due to population leakage to the other non-magic rotational sublevels during the microwave pulses. In Chapter 6, we eliminated this issue by using slightly slower pulses and implementing truncated Gaussian pulse-shaping to reduce off-resonant coupling [40]. Fig. 4.7(b) shows that the observed spin-echo coherence depends sensitively on small changes of the QWP angle in the vicinity of the magic ellipticity. The spin-echo contrast for individual traps at a precession time of 50 ms (Fig. 4.7(c)) shows a small amount of dephasing between sites. An overall phase shift of $73(3)^\circ$ at long times (despite spin-echo) indicates a changing global frequency, the potential source of which is discussed further below.

4.6 Limitations on coherence

4.6.1 Tweezer intensity noise

We measured the 1064 nm tweezer light intensity on an out-of-loop photodiode to calculate an intensity-noise dominated coherence time. The signal was band-pass filtered and amplified through a low-noise SR560 pre-amplifier from Stanford Research Systems. We simulated the decay of coherence from the resulting noise spectrum using the Magnus and cumulant expansions. Details on the method can be found in [53] and references therein. Specifically, we consider only the second cumulant, which gives the highest order contribution to coherence decay. It is expressed as

$$c_2(t) = \frac{1}{2}\int_{-\infty}^{\infty} d\omega S(\omega)|F(\omega t)|^2 \tag{4.1}$$

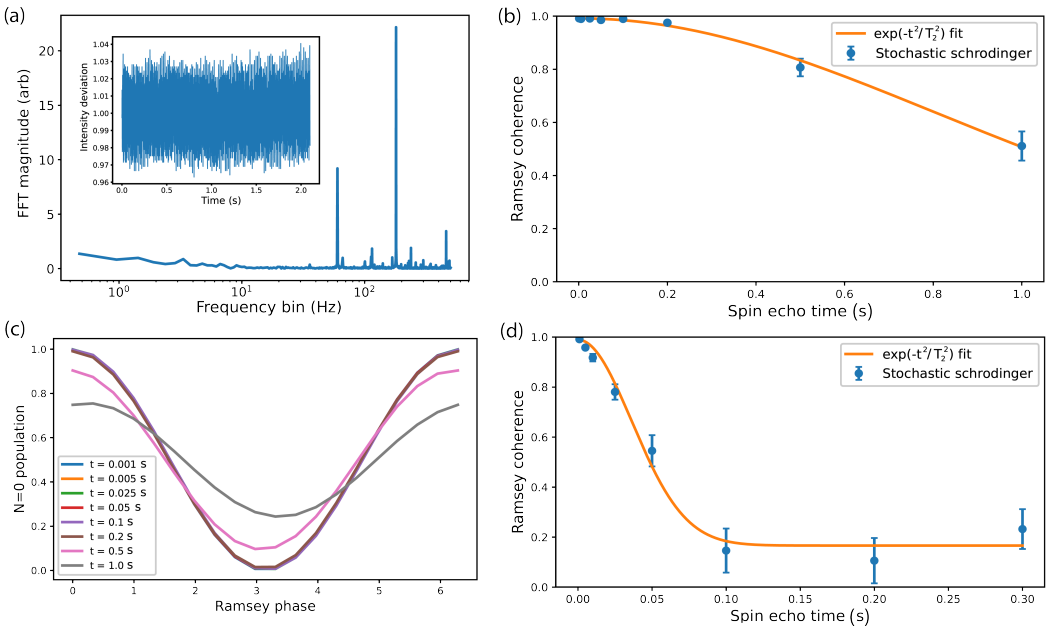

Figure 4.8: (a) Spectrum of measured intensity fluctuation of tweezer beam over 2 s. Inset shows the time-trace of the noise. (b) Normalized Ramsey coherence for average of eight sites predicted from Monte Carlo simulation using random sampling of intensity noise data and experimentally calibrated light shifts of each site. Fitting to a Gaussian decay gives a coherence time of $\tau_{\text{echo}} = 1.24$ s. (c) Corresponding simulated Ramsey phase scans for each time point in b, showing both decay of coherence and slight overall phase shift due to slow drifts. (d) Simulated Ramsey coherence assuming an additional random Gaussian noise source with a standard deviation of $2\pi \times 25$ Hz. Fitting to this data yields a decay time of $\tau_{\text{echo}} = 59$ ms.

where $S(\omega)$ is the power spectrum of the noise source, and $F(\omega t)$ is the transfer function of the pulse sequence. For spin-echo with an infinitely narrow π-pulse, the transfer function is

$$F(\omega, t) = \frac{4}{\omega} \sin\left(\frac{\omega T}{4}\right)^2 \tag{4.2}$$

Then the contrast follows

$$p = \exp(-c_2(t)) \tag{4.3}$$

We used this method to simulate decoherence due to intensity noise for molecules in a linearly polarized trap. The simulation curve is shown in Fig. 4.7(a) and is in good agreement with the observed coherence time.

With the three orders of magnitude reduction in sensitivity to intensity fluctuations achieved using magic ellipticity, we find that the decoherence predicted by this method no longer matches the experimentally-observed coherence time. To verify that intensity noise cannot in general explain the observed decoherence, we explicitly simulated the time-evolution and ensemble averaging of the quantum state of the molecules during the Ramsey experiment in the presence of experimentally sampled noise. This allowed us to model effects not captured by the second cumulant method, such as slow drifts on the Hz timescale that can give rise to overall phase shifts and shot-to-shot variation in the spin-echo Ramsey signal, reducing the contrast of the time-averaged signal. Because of the gradient of ellipticities across sites in the array, there is also a different phase shift accumulated for each site, which can further impact the averaged signal.

To model these effects, we first measured the slow drift of the tweezer intensity using an out-of-loop photodiode with no frequency filtering or amplification for a time of 2 s, which is the duration 1-2 experimental cycles. We then modelled the Schrödinger evolution of the rotational states of all eight array sites under a spin-echo pulse sequence with a time-varying detuning for each site sampled directly from the intensity fluctuation data, multiplied by the average light shift measured in Fig. 4.3. To capture the effect of shot-to-shot variations, we determined the coherence at each time using an ensemble average of 20 runs with randomly chosen $t = 0$ starting times within the intensity noise trace. Using this method, we found an expected coherence time that is well

described by a Gaussian $e^{-t^2/\tau_{\text{echo}}^2}$ decay with a characteristic timescale of $\tau_{\text{echo}} = 1.24\,\text{s}$, more than an order of magnitude longer than the spin echo decay time we observed experimentally. This expected coherence decay curve is shown in Fig. 4.8(b). This strongly suggests that the coherence is limited by a noise source other than intensity fluctuations.

To better understand how much noise would be needed to explain the decoherence, we modelled the expected coherence in the presence of a random Gaussian noise source sampled with a bandwidth of 1 kHz. Using this method, we estimated that detuning noise with a standard deviation on the order of $2\pi \times 25$ Hz would explain the observed spin echo coherence time, as shown in Fig. 4.8(d). This is also similar to the amount of white detuning noise required to model the observed single body decoherence using a Lindblad master equation simulation, as discussed in Section 6.4. In comparison, the standard deviation of the detuning noise produced by intensity fluctuation, averaged across all sites, is only 6 Hz.

To simulate slow drifts in detuning, which could give rise to the overall phase shift of the spin echo signal shown in Fig. 4.7, we assumed a detuning that varies linearly in time. We found that to explain our observed phase shift the rate of change of this detuning would need to be at least $\frac{d\Delta}{dt} = 2\pi \times 330\ \text{Hz / s}$, corresponding to a total change in detuning of $2\pi \times 16.5$ Hz over the course of the 50 ms spin echo wait time. This linear detuning drift is, again, not consistent with the measured fluctuation of the tweezer intensity, so it must have a different origin.

4.6.2 Polarization fluctuations

Another possible way in which the tweezer could be limiting the molecule coherence is if the polarization of the trapping light is fluctuating. Unlike intensity noise, at this stage we do not have a sensitive direct measurement of the time-variation of the polarization. However, we can place some bounds on it based on measurements of the static polarization purity before the objective.

4.6.2.1 Fast fluctuations and polarization extinction ratio

The polarization of light transmitted through a fiber is known to fluctuate over time due to interference between light propagating in different polarization modes. Such fluctuation can be mitigated using polarization maintaining (PM) fibers, which are designed to suppress cross-coupling and interference between modes. Even PM fibers still exhibit quite significant polarization fluctuation, however, as a result of thermal variation, vibrations, and other mechanical stress of the fiber [213]. These fluctuations generally manifest as a random walk in the output polarization at short times, possibly accompanied by overall linear drifts or periodic modulation at longer timescales, depending on the characteristics of the environment of the fiber [186]. These fluctuations are notoriously hard to predict or eliminate entirely and, in applications such as quantum communication schemes where polarization purity over time is critical, the polarization is often measured and stabilized in real-time [82, 186, 267]. Alternatively, one can attempt to simply clean up the output polarization after a fiber by attenuating unwanted polarization components, thus translating polarization fluctuation to intensity noise at the output. This is the approach we took, cleaning up the tweezer polar-

ization first with a polarizing beam splitter directly after the PM fiber, and again with a Glan-Taylor (GT) polarizer placed as close as possible to the objective. We measured the polarization extinction ratio (PER) after the GT using an additional polarizer on a rotation mount, which can be rotated to be either parallel or perpendicular to the polarization of the light transmitted through the GT. The PER, which we measured to be 3×10^5, is the ratio of the powers of the transmitted beam in these two configurations.

The PER alone does not, however, tell us everything about the polarization of the light after the GT. One interpretation of the PER could be that the transmitted light is slightly elliptically polarized, with a ratio of major to minor axes of $\sqrt{3 \times 10^5}$, which would correspond to an ellipticity of $\chi = 0.105°$. However, the measurement of the powers is time-averaged so the same observed PER could equally have resulted from a linear output polarization with an orientation θ that is rapidly fluctuating with a standard deviation of $0.105°$. These two pictures would lead to very different impacts on the magic ellipticity condition—a static residual ellipticity could be compensated for by changing the waveplate rotation angle, whereas a rapidly fluctuating polarization angle would necessarily lead to a fluctuating detuning.

It will be instructive at this point to introduce a more detailed description of what the polarizer is doing. To this end we can use the Stokes-Mueller formalism for the description of the polarization of light. In this formalism, the polarization state of a beam

is represented by the four-element Stokes vector [68]:

$$S = \begin{pmatrix} S_0 \\ S_1 \\ S_2 \\ S_3 \end{pmatrix} \tag{4.4}$$

The first element $S_0 = I$ corresponds to the intensity, and the remaining elements are related to the polarization angle θ and ellipticity χ by:

$$S_1 = S_0 \cos(2\theta) \cos(2\chi) \tag{4.5}$$

$$S_2 = S_0 \sin(2\theta) \cos(2\chi) \tag{4.6}$$

$$S_3 = S_0 \sin(2\chi) \tag{4.7}$$

The effect of polarizing optics are then described by 4×4 matrices M, known as the Mueller matrices, which multiply the Stokes vector. The Mueller matrix describing a partial polarizer is

$$M = \frac{1}{2} \begin{pmatrix} p_x^2 + p_y^2 & p_x^2 - p_y^2 & 0 & 0 \\ p_x^2 - p_y^2 & p_x^2 + p_y^2 & 0 & 0 \\ 0 & 0 & 2p_x p_y & 0 \\ 0 & 0 & 0 & 2p_x p_y \end{pmatrix} \tag{4.8}$$

where p_x and p_y describe the polarization along the horizontal and vertical directions [68], and $0 \leq p_x^2 + p_y^2 \leq 1$. For a horizontally aligned polarizer we have $p_x > p_y$

and the PER is defined as $R = p_x^2/p_y^2$ [155]. We can consider some limiting cases of the input polarization to understand how each one will be affected by the GT polarizer. For initially perfectly horizontally polarized light, we have

$$MS = \frac{1}{2}\begin{pmatrix} p_x^2+p_y^2 & p_x^2-p_y^2 & 0 & 0 \\ p_x^2-p_y^2 & p_x^2+p_y^2 & 0 & 0 \\ 0 & 0 & 2p_xp_y & 0 \\ 0 & 0 & 0 & 2p_xp_y \end{pmatrix}\begin{pmatrix} 1 \\ 1 \\ 0 \\ 0 \end{pmatrix} = \begin{pmatrix} p_x^2 \\ p_x^2 \\ 0 \\ 0 \end{pmatrix} \tag{4.9}$$

meaning that the polarization remains perfectly horizontal but the overall intensity is attenuated by a factor p_x^2. Conversely, if the light is initially polarized at 45° to horizontal, we have

$$MS = \frac{1}{2}\begin{pmatrix} p_x^2+p_y^2 & p_x^2-p_y^2 & 0 & 0 \\ p_x^2-p_y^2 & p_x^2+p_y^2 & 0 & 0 \\ 0 & 0 & 2p_xp_y & 0 \\ 0 & 0 & 0 & 2p_xp_y \end{pmatrix}\begin{pmatrix} 1 \\ 0 \\ 1 \\ 0 \end{pmatrix} = \frac{1}{2}\begin{pmatrix} p_x^2+p_y^2 \\ p_x^2-p_y^2 \\ 2p_xp_y \\ 0 \end{pmatrix} \tag{4.10}$$

This corresponds to light that is linearly polarized at an angle slightly offset from horizontal. The polarization angle is given by $\theta = \frac{1}{2}\tan^{-1}(\frac{2p_xp_y}{p_x^2-p_y^2}) \approx \frac{1}{2}\tan^{-1}(\frac{2}{\sqrt{R}})$ for $R \gg 1$. For the measured $R = 3 \times 10^5$ of the GT, this corresponds to $\theta = 0.105°$. Lastly, for right

circularly polarized light, we have

$$MS = \frac{1}{2}\begin{pmatrix} p_x^2+p_y^2 & p_x^2-p_y^2 & 0 & 0 \\ p_x^2-p_y^2 & p_x^2+p_y^2 & 0 & 0 \\ 0 & 0 & 2p_xp_y & 0 \\ 0 & 0 & 0 & 2p_xp_y \end{pmatrix}\begin{pmatrix} 1 \\ 0 \\ 0 \\ 1 \end{pmatrix} = \frac{1}{2}\begin{pmatrix} p_x^2+p_y^2 \\ p_x^2-p_y^2 \\ 0 \\ 2p_xp_y \end{pmatrix} \tag{4.11}$$

which corresponds to slightly elliptically polarized light with orientation $\theta = 0$ and ellipticity $\chi = \frac{1}{2}\sin^{-1}(\frac{2p_xp_y}{p_x^2+p_y^2}) \approx \frac{1}{2}\sin^{-1}(\frac{2}{\sqrt{R}})$. For $R \gg 1$, this also gives $\chi = 0.105°$. We thus see that the actual polarization after the GT will depend on the PER and the input polarization state, with fluctuations in the input polarization angle of up to 45° translating to output angle fluctuations of up to $\delta\theta = 0.105°$, and input ellipticity fluctuations from linear to circular translating to output ellipticity fluctuations $\delta\chi = 0.105°$.

What effect would these polarization changes have on the magic condition for the molecules? Variations of the input polarization angle are equivalent to variations of the waveplate rotation angle. As such, we can empirically determine the resulting expected shifts in transition frequency from the linear fits in Fig. 4.2(c). Extrapolating the measured rotation angle dependence at 3.2 MHz to the depth of 1.34 MHz used for the coherence measurements gives an expected detuning shift of 1.10 kHz for an angle change $\delta\theta = 0.105°$. We can theoretically predict the effect of ellipticity variations by diagonalizing the molecular rotation Hamiltonian, which gives an expected shift per degree of $\frac{9.87U\times10^{-3}}{°}$. For a trap depth of $U = 1.34$ MHz and ellipticity change $\delta\chi = 0.105°$, this gives a shift of 1.39 kHz. These shifts are significant—if fast polarization fluctuations of the tweezer light amount to even 2% of these maximum possible shifts, they would already

be sufficient to fully explain the observed decoherence.

4.6.2.2 Slow drift

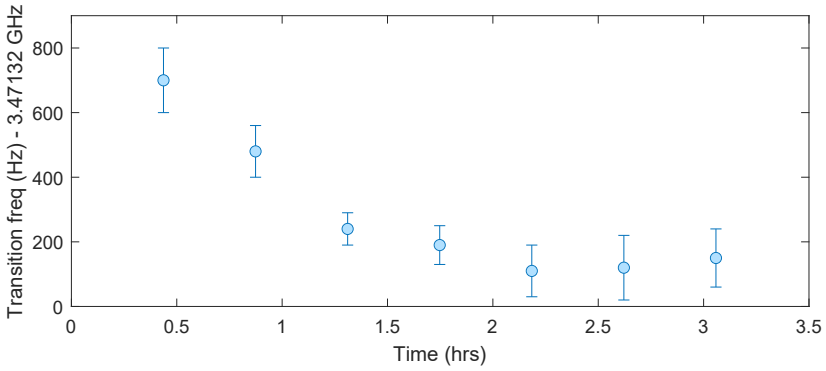

Figure 4.9: Slow drifts of the transition frequency over a period of three hours. Each point represents the transition frequency determined from fitting a scan of the resonance averaged over the preceding 23-minute period.

In addition to the decay of the coherence, we can directly observe detuning drifts at rates much slower than the experimental repetition rate (0.6 Hz) by scanning the resonance frequency and tracking how it evolves over long averaging periods. Fig. 4.9 shows such a scan taken over a three-hour period, during which time we observe a drift in the resonance of approximately 700 Hz. The rate of this drift is slow enough that its effect on coherence should be almost entirely eliminated by the spin-echo sequence. It does, however, point to the presence and possible origin of polarization fluctuations. In particular, the shape of the drift—initially changing rapidly and then appearing to stabilize by the second hour of the scan—suggests some association with the relatively slow thermal equilibration of the experiment. This may be due to temperature changes of the PM fiber delivering the light, though the resulting drifts in the polarization angle or ellipticity would have to be as large as 45° and 90°, respectively, to give this much of

a shift. This would also result in large intensity fluctuations after the first cleanup cube, which we have not observed experimentally.

Alternatively then, the polarization drifts could originate after the GT polarizer. One possible origin of such drifts could be changes in the tilt of the two dichroics after the GT (see Fig. 2.3). The final polarization purity was observed to be extremely sensitive to the vertical tilt of these dichroics, which needed to be carefully aligned to achieve the final measured PER of 3×10^5. In a separate systematic scan of the polarization purity of a beam passing through a dichroic, we estimated that the ellipticity changes by approximately 1.4° per degree of vertical misalignment of the dichroic. Given the sensitivity of the detuning to ellipticity, a 700 Hz shift could thus result from a change in the vertical tilt of either dichroic by 0.04°. Vibrations of the dichroics at acoustic frequencies may also contribute to the fast polarization noise that induces decoherence. Another source of slow drifts is the temperature-dependence of the waveplate itself. In measurements of the temperature dependence of a separate waveplate with a retardance of $0.304\,\lambda$ (used in Chapters 5 and 6), we found that the retardance changed with temperature by $0.0004\,\lambda/\mathrm{K}$. The effect of this retardance change on the tweezer ellipticity depends heavily on the choice of waveplate. For the QWP used in this chapter, the ellipticity is first-order insensitive to changes in retardance at the magic angle, meaning that this is unlikely to be a major contributor to the drift. However, for the $0.304\,\lambda$ waveplate used in later chapters to maximize the strength of dipolar interactions, the ellipticity varies approximately linearly with the retardance. This results in an expected detuning shift of $5.5\,U \times 10^{-4}\,/\mathrm{K}$ (or 740 Hz/K for a trap depth of 1.34 MHz).

4.6.3 External electric and magnetic fields

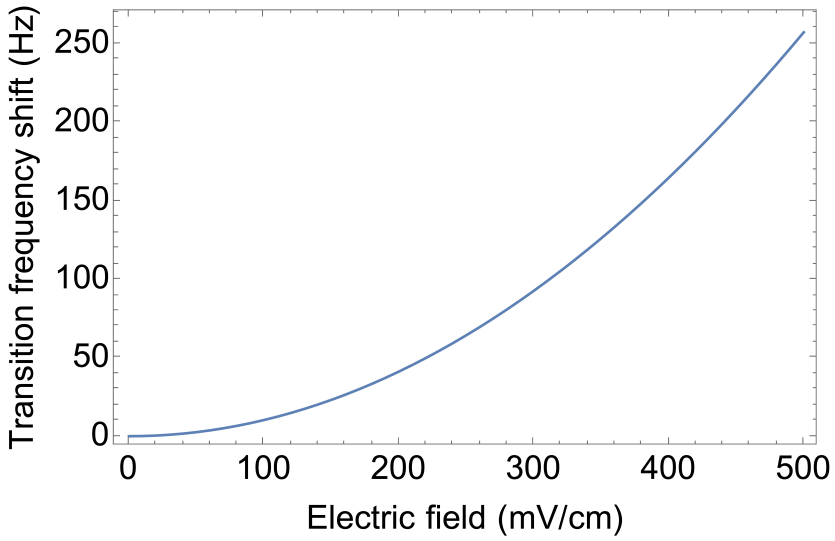

Figure 4.10: Shift of transition frequency from f_m at a trap depth of 1.34 MHz as a function of applied electric field oriented parallel to the major axis of the polarization ellipse.

Finally, we considered the effect of external electric and magnetic fields on the magic condition. We calculated the expected shift in the transition frequency as a function of applied electric field oriented parallel to the major axis of the polarization ellipse, which is the orientation that gives the maximum differential shift. The dependence on the field is quadratic, with a fitted dependence of $f = 0.1\,E^2$ Hz / (V m^{-1})^2, shown in Fig. 4.10. If we assume a background static electric field of 500 mV/cm, then a fluctuating component with a standard deviation of 25 mV/cm would be sufficient to generate the $2\pi \times 25$ Hz detuning noise required to explain our observed spin-echo coherence time. This is of a similar order to background fields measured using Rydberg atom electrometry in Ref. [208]. In that case, the electric field was induced by a build up of charged particles adsorbed on the surface of the glass vacuum cell, similar to the one used in our

experiment. The authors of Ref. [208] used a UV LED to induce desorption of charges on surfaces, thus reducing the stray electric fields. However, when we illuminated the glass cell with a 365 nm, 2 W UV LED, we saw no change in the rotational transition frequency. We did, however, observe changes in the loading rate of atoms in optical tweezers, indicating that the LED was inducing some desorption of atoms from the interior walls of the glass cell. Another possible source of background electric fields is the Feshbach coils. The overall voltage drop across the entire Feshbach coil circuit is 17 V, which is divided between the coils themselves and the IGBTs that are used to actively stabilize the current flowing through the circuit [308]. Based on the measured resistance of the coils, we expect the voltage drop across each coil to be approximately 4 V when the current is set to generate the 864 G magnetic fields at which we produce and probe molecules. Based on COMSOL simulations of the coil assembly, though not including additional conducting surfaces in the region of the glass cell, we expect that the electric field in the glass cell could be as high as 600 mV/cm. This field would, however, be dominantly along the same axis as the magnetic field, parallel to the tweezer k-vector. As a result, it would induce a shift of approximately half that produced by the field along the major axis of the tweezer simulated in Fig. 4.10. The magnetic field is stabilized to a precision of $\sim$ 1 in 10^5, meaning that the detuning fluctuations from this coil-induced electric field are expected to be $<$ 1 Hz. However, due to the quadratic Stark shift, the presence of the static background field will increase the sensitivity of the transition to any additional stray electric field fluctuations.

We also calculated the expected shift in the transition frequency due to magnetic field fluctuations about a static 864 G magnetic field parallel to the direction of prop-

agation of the optical tweezers. At this field we expect the ground and excited rotational states to be close to pure in the uncoupled basis, limited primarily by electric quadrupole interactions. We estimated the magnetic field sensitivty to be -0.3 Hz/G at a trap depth of 1.34 MHz. With a magnetic field instability of $\sim$10 mG, we can rule out magnetic fields as limiting our observed coherence time.

4.7 Outlook

In this chapter, we demonstrated a magic ellipticity scheme for cancelling light shifts of one $N = 0$ to $N = 1$ transition of NaCs. Using this scheme, we achieved rotational coherence times of 62(3) ms with a single spin-echo pulse and 250(40) ms using an XY-8 dynamical decoupling pulse sequence. The effectiveness of XY-8 dynamical decoupling indicates residual AC detuning noise, but measurements and simulations indicate that this remaining decoherence is not consistent with tweezer intensity noise. We considered other possible sources of detuning noise and determined that fluctuations of the tweezer polarization and stray electric fields are the most likely candidates. The extent of polarization fluctuations warrants further investigation, but it could potentially be reduced by improved thermal stabilization of the experiment, additional polarization cleanup before the fiber that delivers 1064 nm tweezer light, and mechanical isolation of the fiber itself. The influence of stray electric fields could be mitigated by surrounding the glass cell in a Faraday cage or, in a future iteration of the experiment, incorporating in-vacuum electrodes to actively null the DC electric field. With these improvements, we can reasonably expect to achieve intensity-noise-limited coherence times in excess of 1 s.

It's a rare gift, to know where you need to be, before you've been to all the places you don't need to be.

Ursula K. Le Guin

5

Rearrangement, state-preparation, and readout of an array of NaCs molecules

Material in this chapter, including portions of the text and figures, originally appeared in print in [216].

5.1 The problem of molecule detection

Quantum state detection using fluorescence from optical cycling transitions has become an indispensable technique in atomic physics. Real-time detection of individual atoms enables the rearrangement of occupied traps to produce densely-filled arrays

[21, 85, 250], as well as the selective readout of their internal states [178, 187]. Both capabilities are crucial for studying many-body interactions and executing large quantum circuits [37, 223, 244, 248]. For molecules, a subset [79, 269] do possess optical cycling transitions, which has enabled advances in their laser-cooling [252, 274], trapping [10, 280, 292], and rearrangement [117]. Other molecules can be produced by the coherent association of their constituent atoms [148, 202, 230, 303, 310] with the advantage that cold atom temperatures are preserved in the process of creating the molecules. However, optical cycling transitions for fluorescence or absorption imaging are generally not available for these molecules. Typically, absorption and spontaneous emission of a photon by a rovibrational ground state molecule will lead to scattering into a different rovibrational level, or even photodissociation of the molecule, which makes imaging of single molecules in this way impossible [282]. While far-detuned phase contrast imaging techniques can, in principle, be used to detect molecules without significantly populating excited states, these too generally fail in the limit of single molecule detection when the shot-noise limit on the maximum achievable signal-to-noise ratio is taken into account [109, 120].

As a result, the population of a specific state of associated molecules is generally detected through the adiabatic dissociation of the constituent atoms, which are then separated and imaged. To make use of the inherent multi-level structure of molecules, three capabilities for the molecule SPAM toolbox are highly desirable: rearrangement while maintaining low temperature, site-resolved state preparation, and resolved readout of multiple internal states. The first capability would allow for the production of deterministically filled arrays of molecules. The latter two would facilitate experiments

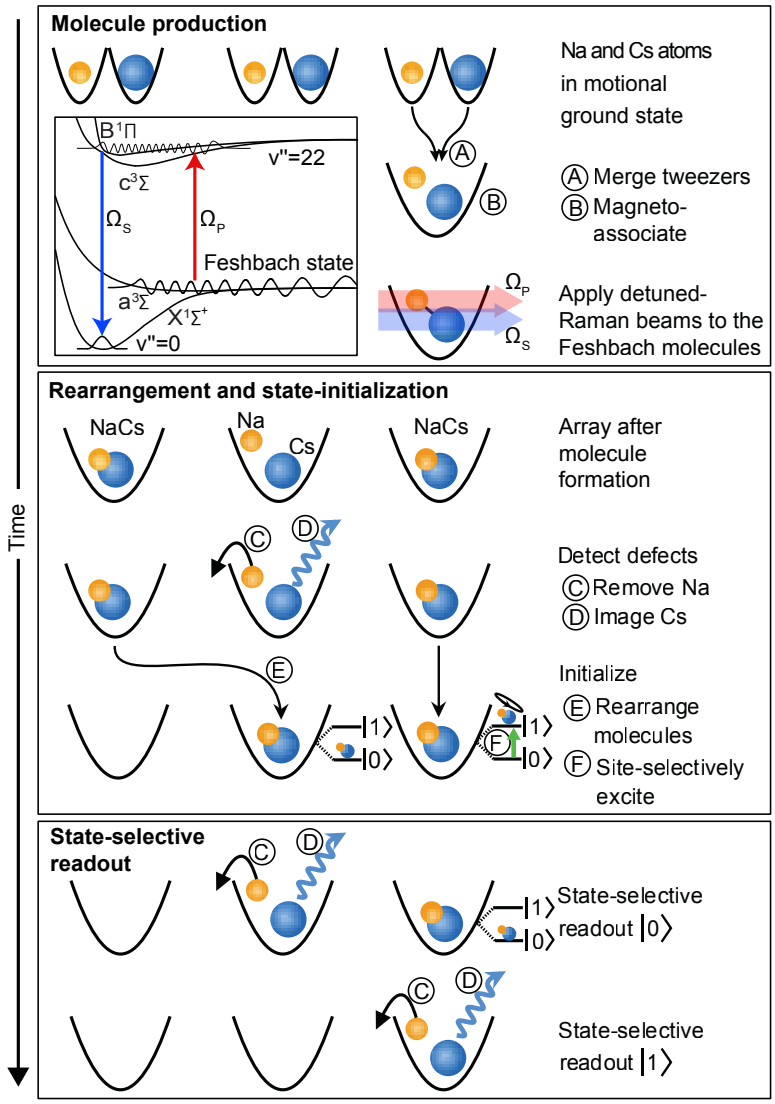

Figure 5.1: Overview of an experimental sequence with novel SPAM techniques showing the production, initialization, and readout of NaCs molecules. For details on the coherent association and transfer of atoms to the molecular ground state, see Chapter 2. The detection of unassociated Cs atoms (C-D) enables the rearrangement of molecules to a more densely-filled array (E). An auxiliary rotational state is used for site-selective initialization (F) in a noise-insensitive computational basis of two rotational states. In addition, the detection of atoms from state-selectively dissociated molecules is harnessed for multi-state readout of the computational basis.

using the many long-lived rotational states as a qudit system or a multi-level quantum simulator [119, 233]. Various proposals have been put forward for direct molecule readout via controlled coupling between a ground state molecule and an ancilla atom or optical cavity [50, 61, 109, 137, 161, 284, 291, 307]. However, these methods require the introduction of a new, coherently-controlled interaction between the molecule and the detection ancilla, which requires more experimental overhead to implement. In this chapter, I discuss an alternative scheme demonstrated in our lab for the removal of defects in a molecular array and sequential state-selective detection, which does not rely on non-destructive molecule detection. Our scheme uses fluorescence imaging of the constituent atoms of NaCs as shown in Fig. 5.1. Unassociated Cs atoms are detected immediately following molecule formation to infer which sites contain molecules. We rearrange those sites and increase the local filling probability at the edge of the array threefold. We also use the atom signal for the detection of the two molecular states in the ground $|0\rangle$ and the first excited $|1\rangle$ rotational levels that form our computational basis. In a single experimental cycle, molecules are sequentially dissociated from each state and the resulting Cs atoms are detected. Lastly, we demonstrated the ability to initialize an array of molecules in an arbitrary pattern of the computational basis states using global microwave pulses in combination with an auxiliary rotational state outside the computational basis for site-selective shelving of molecules.

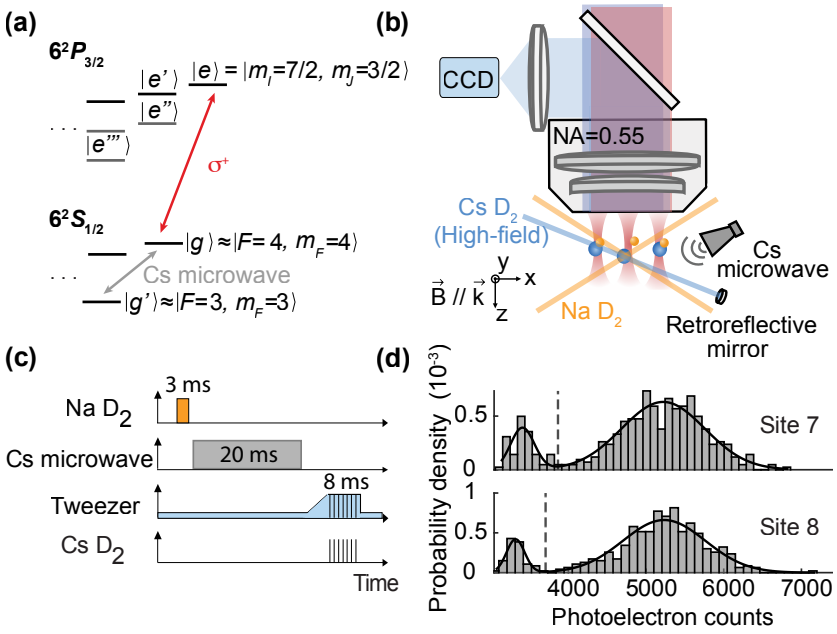

Figure 5.2: State-selective detection of Cs at 864 Gauss. (a) Simplified energy structure of Cs showing the hyperfine state $|g'\rangle$ that Cs atoms are initialized in as well as the optical cycling transition between $|g\rangle$ and $|e\rangle$ used for fluorescence imaging. (b) Schematic of the apparatus depicting the beams used for the ejection of Na atoms and for driving the Cs optical cycling transition. The Cs hyperfine transition is driven by a microwave horn antenna. Fluorescence is collected by a 0.55 numerical aperture (NA) objective and EMCCD camera. (c) Timing diagram for the imaging process, including Na ejection via near-resonant D_2 light, Cs microwave transfer from $|g'\rangle$ to $|g\rangle$, and optical cycling. The tweezer and imaging light are pulsed out of phase since $|e\rangle$ is anti-trapped. (d) Histograms of the collected fluorescence from Cs atoms.

Both the rearrangement of molecules and their sequential state-selective readout rely on the detection of atoms at or near the magnetic field at which molecules are assembled. Our preparation of NaCs in its rovibrational and electronic ground state is detailed in Chapter 2. In summary, we prepare parallel 1-by-8 arrays of hyperfine ground state Na and Cs atoms near the three dimensional motional ground state of their respective 616 nm and 1064 nm optical tweezers. Na atoms are then adiabatically trans-

ferred into the 1064 nm array, such that each 1064 nm tweezer contains, ideally, individual Na and Cs atoms in their motional and hyperfine ground states. Atom pairs are magnetoassociated into a weakly-bound molecule via a Feshbach resonance at 864 G and transferred to the rovibrational and electronic ground state via detuned Raman process. Crucially for the results in this chapter, we note that any atom pairs that are not in the relative motional ground state of the optical tweezer will fail to associate into Feshbach molecules, but will remain in the tweezer as a free atom pair.

To detect the unassociated atoms, we extended the low-field state-selective fluorescence imaging of Cs atoms in optical tweezers [62, 205] to a high magnetic field, similar to the high-field absorption detection of a cloud of potassium atoms [209]. In principle, one could also image Na atoms on the equivalent stretched D_2 transition. We opted to image Cs atoms due to the five times stronger polarizability of Cs in the 1064 nm tweezers, which reduces the tweezer intensity required to trap atoms that are heated during imaging. The magnetic field decouples the total angular momentum F of the excited fine structure levels, such that the quantum numbers $|m_I, m_J\rangle$ best describe the excited hyperfine states, where I is the nuclear spin ($I_{\mathrm{Cs}} = 7/2$), J is the total electronic spin, and m denotes their projections along the magnetic field axis. Detection was performed by exciting from the lowest to highest energy ground hyperfine state and optically cycling on the stretched D_2 transition $|g\rangle \equiv 6^2S_{1/2}\,|F = 4, m_F = 4\rangle$ to $|e\rangle \equiv 6^2P_{3/2}\,|m_I = 7/2, m_J = 3/2\rangle$. The optical cycling transition is depicted in Fig. 5.2(a) along with nearby states that can have non-zero coupling to non-σ^+ components of the imaging light. An advantage of the high-field regime is significant detuning protection against populating these off-resonant states.

Following molecule creation or dissociation, Cs atoms are initialized in $|g'\rangle_{\mathrm{Cs}} \approx |F = 3,\ m_F = 3\rangle$, and may share their optical tweezer with Na atoms in $|g'\rangle_{\mathrm{Na}} \approx |F = 1,\ m_F = 1\rangle$. We must eject Na atoms before exciting Cs to $|g\rangle_{\mathrm{Cs}}$ to avoid spin-changing inelastic collisions that occur when the atoms are not both in the ground hyperfine state or in spin-stretched hyperfine states [310]. As shown in Fig. 5.2(b), which depicts the geometry of the apparatus, we heated the Na atoms out of the trap using beams at the D_2 transition frequency that were originally used to produce the Na magneto-optical trap (MOT). The Cs atoms were then excited from $|g'\rangle$ to $|g\rangle$ using a microwave horn with negligible off-resonant coupling due to a $h \times 250$ MHz detuning with the next nearest transition. Lastly, we optically cycled on the $|g\rangle$ to $|e\rangle$ transition using a small retro-reflected imaging beam with a $1/e^2$ waist of $\sim$1 mm, collecting fluorescence photons through the 0.55 NA objective onto an EMCCD camera (see Fig. 2.3). The use of a small imaging beam helps suppress background noise due to light scattering from the surface of the glass cell into the objective. Vertical polarization was chosen to mitigate the π polarized $|g\rangle$ to $|e'\rangle \approx 6^2\mathrm{P}_{3/2}\,|m_I = 5/2, m_J = 3/2\rangle$ transition, which is the closest detuned by $h \times 67$ MHz. Crucially, none of the 589 nm Na D_2 light, the 852 nm Cs D_2 light, or the 11.34 GHz microwave measurably affected the NaCs molecules.

The timing diagram of high-field imaging is shown in Fig. 5.2(c). We observed complete ejection of Na from the trap within 3 ms. For the microwave transition, instability in the magnetic field on the 10 mG level limits the transfer efficiency given the available microwave Rabi frequency. To maximize efficiency in the presence of this noise, we used an adiabatic rapid passage pulse in which the frequency was linearly swept across a 400 kHz range about the resonance in 20 ms. As the imaging geometry pro-

vides little cooling during imaging except for red-detuned Doppler cooling along the imaging beam axis, we increased the peak trap intensity to 1.25 MW/cm^2 to collect sufficient fluoresced photons before atom loss to resolve the presence of an atom over background noise. The loss rate of molecules from $|0\rangle$ due to scattering of the trap light is 7 Hz/(MW/cm^2). To minimize the time that the molecules need to be held at high depth, the optical cycling transition was driven near-resonantly. Due to scattering, we observed a 5.6(8)% loss of molecules during high-field Cs imaging. We also strobed the imaging and tweezer light out of phase with a 10% and 70% duty cycle, respectively, at 500 kHz to prevent heating due to $|e\rangle$ being anti-trapped in the 1064 nm tweezers [130, 187].

To analyze the imaging fidelity, we prepared Cs atoms in $|g'\rangle$ co-trapped with Na atoms. The fidelity of Na ejection and subsequent Cs imaging were verified using the sequence shown in Fig. 5.2(c). By averaging the collected signal of the EMCCD camera for each site over many experimental cycles, we observed a distribution of electron counts consisting of two Gaussian peaks: a 'dark' peak corresponding to electronic read noise of the camera, and a 'bright' peak corresponding to atom fluorescence. This distribution is shown in Fig. 5.2(d). The 'dark' peak remains unchanged in the absence of imaging light, which indicates negligible scattering of the imaging beam off the glass cell into the CCD camera. We report a 0.38(9)% false positive rate and 0.089(2)% false negative rate for Cs atoms prepared in $|g\rangle$, corresponding to an overall imaging fidelity of 99.51(9)%. Due to imperfect microwave transfer and state-preparation fidelity, the false negative rate increased to 3.6(7)% for Cs atoms initialized in $|g'\rangle$, which is the case for molecule rearrangement and sequential imaging.

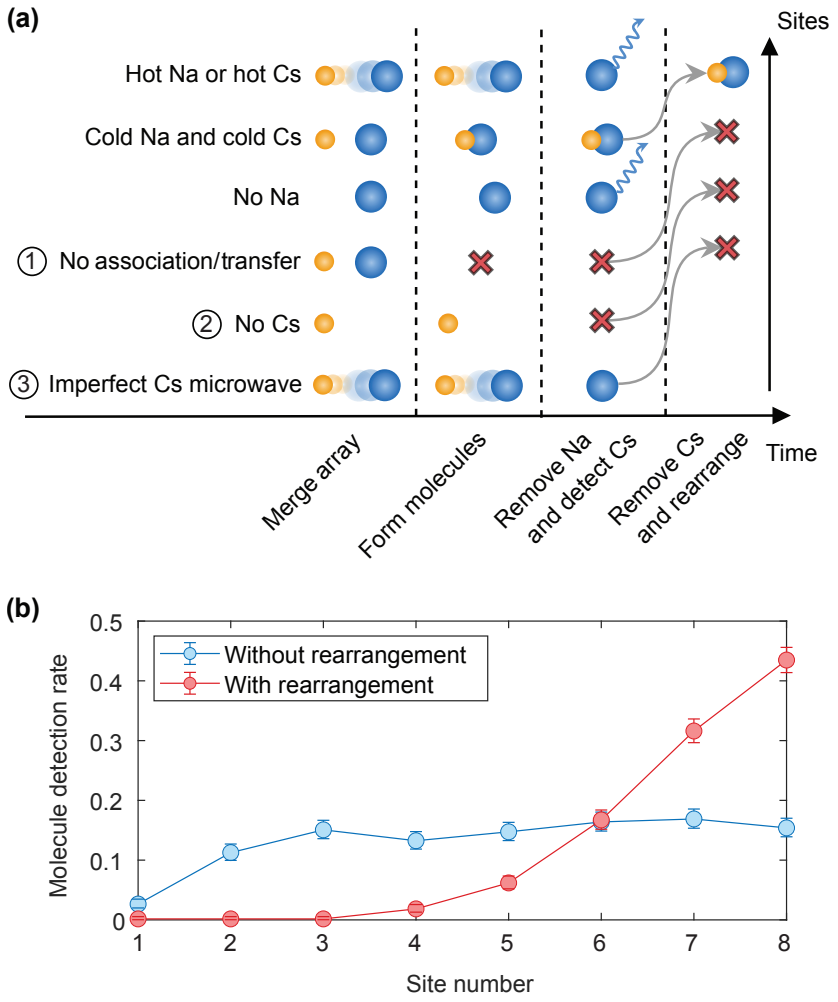

Figure 5.3: Rearrangement of molecules based on the detection of Cs atoms at 864 G. (a) Behavior of the rearrangement algorithm for possible occupations of the 1064 nm tweezers for sites where Na and Cs are both detected before Raman sideband cooling. Sites where Cs is not detected are rearranged. Such sites may not contain a ground state molecule if: 1. the molecule does not survive Raman transfer to the ground state; 2. the Cs atom is lost when the Na and Cs arrays are merged; or 3. the Cs transition from $|g'\rangle$ to $|g\rangle$ is not successful. (b) Ground state molecule population with and without molecular rearrangement that is detected by Cs imaging at high-field.

Using the high-field detection of Cs atoms, we can produce a dense array of

molecules without increasing their motional energy. To infer which traps contain molecules, we used a combination of three atom images. After the loading and rearrangement of atomic arrays, we detected the initial Na and Cs occupations with fluorescence imaging. The atoms were then Raman sideband cooled to near their motional ground state and the arrays were adiabatically combined. As stated in Section 5.2, Cs atoms were detected again at high-field following molecule production using previously determined thresholds. Molecules may only be found in sites where both atoms were detected at low-field in the first two images, because two atoms are needed to form a diatomic molecule, and where Cs was not detected at high-field in the third image, because the molecules are dark to high-field Cs detection. Such cases correspond to 27 % of the sites that will be preserved by the rearrangement algorithm.

Three relevant mechanisms can result in the preserved sites not containing ground-state molecules, as depicted in Fig. 5.3(a). First is when atom pairs that associate into Feshbach molecules are lost during detuned Raman transfer, which has one-way transfer efficiency of 76(3)%, limited by a combination of inhomogeneous intensities of the Raman beams across the array, time-variation of the intensities of the beams, and scattering from the intermediate state of the transfer [48, 309]. Second is that Cs atoms may be lost between low-field and high-field detection, which falsely appears as molecule production. Cs can be lost during the merging of the two arrays (0.7(9) %), or in spin-changing inelastic collisions with Na in several ms after merge (1(1) %) if either atom is prepared in the wrong hyperfine state. A third concern is that Cs atoms may not be detected due to imperfect microwave transfer and state preparation, as described in Section 5.2. Based on these mechanisms we estimate that 71(3)% of the preserved sites,

or 19(2)% of all sites, contain a ground-state molecule.

The rearrangement of molecules proceeds as follows. Optical tweezers for sites that are not preserved are turned off. Starting sequentially from the rightmost preserved site, tweezers are translated to the rightmost unoccupied site by means of a frequency ramp of the radiofrequency (RF) tones generating each tweezer. The translation is performed using a minimum-jerk trajectory for the start and end of the ramp, linked by a constant velocity region. At the same time, the RF amplitudes are ramped to compensate for changes in diffraction efficiency across the bandwidth of the acousto-optic deflector (AOD) generating the tweezers, which keeps the tweezer depth approximately constant during the move. The rearrangement of molecules was performed in the same way as atom rearrangement, which is described in Section 2.2.2.

The measured ground state molecule population is shown in Fig. 5.3(b). On average, we detected 13.2(4)% filling of ground state molecules without rearrangement. We note that we rearranged the atomic arrays to the rightmost sites prior to the creation of molecules, resulting in a lower detection rate of molecules on the left side of the array. Accounting for the loss from the detuned Raman process and the false negative rate of Cs high-field imaging, we estimate a 18.0(9)% filling of the array, which is consistent with the prior estimate. Molecular rearrangement significantly improved molecule density on the right side of the array. We detected a factor of 2.8(3) improvement in the filling of the rightmost site, and the detection rate of a pair of molecules in the two rightmost sites improved from 4.3(8)% to 16(2)%.

In order to quantify any molecule heating induced by the rearrangement process, we dissociated the molecules, unmerged the 616 nm and 1064 nm tweezers, lowered

the magnetic field, and measured the temperature of the resulting Cs atoms in the 1064 nm trap. This method can only provide an upper bound on the temperature of the molecules as the atoms undergo additional heating following dissociation. This can occur most notably during the unmerging of the 1064 nm and 616 nm tweezer arrays. However, atom thermometry can still provide a useful indication of any additional heating induced by the rearrangement process. The thermometry procedure, described in detail previously [172, 302, 309], involves using a pair of lasers detuned from the Cs D_2 transition to drive motional sidebands on the Raman transition between the $|F = 3, m_F = 3\rangle$ and $|F = 4, m_F = 4\rangle$ hyperfine states. Atoms in $|F = 4, m_F = 4\rangle$ are pushed out with resonant light at the end of the sequence, allowing the population in $|F = 3, m_F = 3\rangle$ to be inferred from the remaining atom survival.

In Fig. 5.4, we show Raman sideband spectra for the radial and axial axes of the tweezer trap. The weakly-confined axial direction corresponds to the tweezer k-vector, and the radial direction is in the plane of the array. To extract the temperature of the molecules we fit the heights of the peaks [302]. In order to constrain the fit, we fixed the frequency separation of the peaks based on the measured trap frequencies at the same tweezer depth that we use for Raman sideband cooling. In the radial direction, we measured motional ground state fractions of 92(7)% without rearrangement and 97(6)% with rearrangement, which is consistent to within one standard error with there being no radial heating during rearrangement. In the axial direction, we measured 39(20)% ground state population without rearrangement and 54(17)% with rearrangement, which is also consistent to within one standard error with no heating. Note that for the axial spectrum we introduced an additional optical pumping pulse to transfer atoms

to the $|F = 4, m_F = 4\rangle$ state before taking the spectrum. At the expense of inducing a small amount of heating, this pulse allowed us to more easily resolve the spectrum from the background.

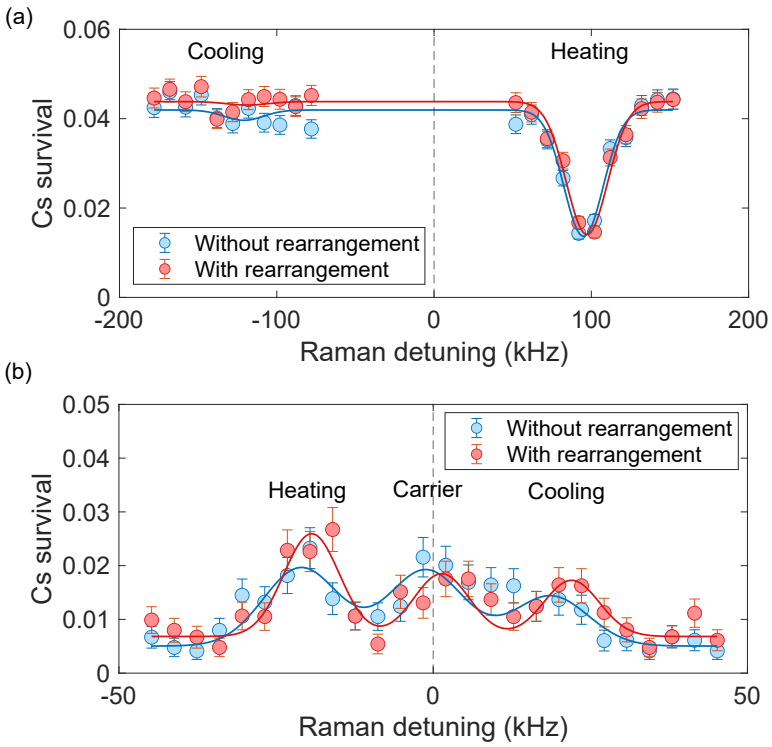

Figure 5.4: (a) Radial sideband thermometry on Cs atoms, starting in the $|F = 3, m_F = 3\rangle$ state and attempting to drive to heating and cooling sidebands of the transition to $|F = 4, m_F = 4\rangle$, both with and without the molecule rearrangement step active. (b) Axial sideband thermometry, starting in $|F = 4, m_F = 4\rangle$ and driving to $|F = 3, m_F = 3\rangle$.

5.4 Sequential readout of rotational states

The ability to perform sequential readout of multiple states of a particle is crucial for qudit-based computation or multi-level quantum simulation applications, due to the quadratic scaling of the number of measurements required for full quantum state to-

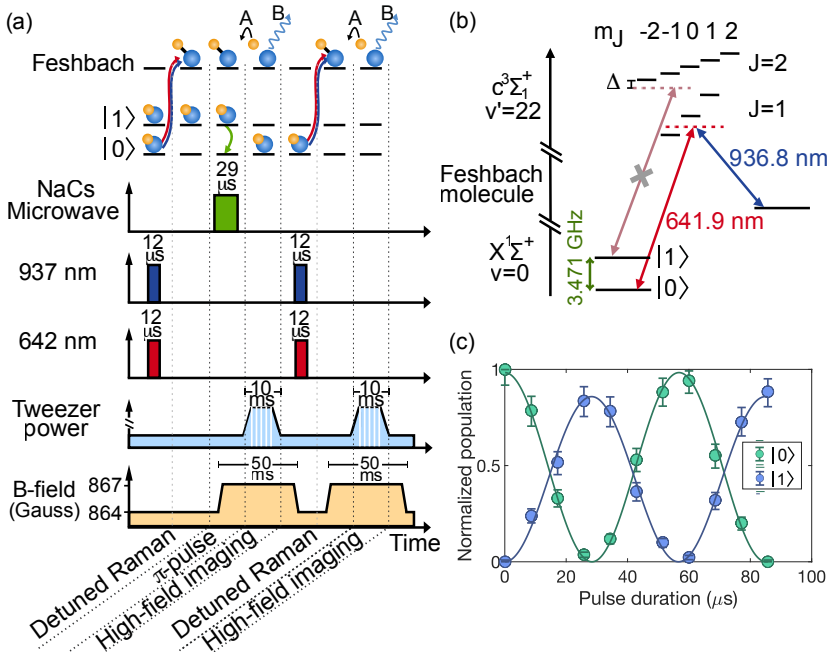

Figure 5.5: Sequential detection of multiple rotational states. (a) Timing diagram showing the sequential dissociation of $|0\rangle$ and $|1\rangle$, and imaging of the resulting Cs atoms. (b) Energy level diagram of NaCs showing the ground rotational levels, the excited intermediate states used for detuned Raman transfer [48, 309], and the weakly-bound Feshbach state. Population in $N = 1$ is protected during detuned Raman transfer by careful choice of the single photon detuning. (c) Multi-state detection of rotational population during driven Rabi oscillations between $|0\rangle$ and $|1\rangle$.

mography [182]. Multi-state readout via fluorescence imaging has been demonstrated in trapped ion qudits [178, 223], and would be highly applicable to molecules due to their abundance of long-lived rotational and hyperfine states [17].

In prior work and in Chapters 3 and 4 of this thesis we measured $|0\rangle \equiv |N = 0,\ m_N = 0\rangle$ population by reversing the adiabatic steps used for molecule formation: two-photon transfer to a weakly-bound Feshbach state, magnetodissociation, returning Na atoms into their original tweezer array, and detection of Na and Cs with fluorescence imaging at 5.5 G. Since neither the Na nor Cs D_2 imaging light in-

duces significant scattering of the molecules, we can instead perform multiple rounds of state-selective molecular dissociation and imaging to detect population in $|0\rangle$ and $|1\rangle \equiv \frac{1}{\sqrt{2}}\left(|N=1,\ m_N=-1\rangle - |N=1,\ m_N=1\rangle\right)$, where the rotational ($N$) quantization axis is defined by the magnetic field. Imaging atoms at high-field is advantageous for this application, as it avoids the 150 ms required to ramp the magnetic field down and up between 5.5 and 865 G.

The sequence of field ramps and pulses required for sequential readout of the rotational states $|0\rangle$ and $|1\rangle$ is shown in Fig. 5.5(a). The total time needed to detect each rotational state was 50 ms. Population in $|0\rangle$ was converted to a weakly-bound molecule via detuned Raman transfer. Prior to its detection, a microwave π-pulse transferred population in $|1\rangle$ to $|0\rangle$. The weakly-bound molecule was dissociated and the resulting Cs atoms, corresponding to the initial $|0\rangle$ population, were detected. Following imaging, a high intensity pulse resonant with the cycling transition was used to clean out any remaining Cs atoms before the next imaging step. Subsequently, the remaining population was dissociated and Cs atoms originally from $|1\rangle$ were also detected.

The frequency of the 642 nm Raman laser that connects the ground molecular state to the $c^3\Sigma$ potential was carefully selected to prevent population in the $|1\rangle$ state from scattering during the first transfer of $|0\rangle$ to the Feshbach state. The 642 nm laser can couple $|1\rangle$ to the $J = 1$ and $J = 2$ rotational levels of the excited $v' = 22$ manifold, where J denotes the sum of the orbital N and electronic spin S angular momenta of the molecule. To avoid this, we chose in this and subsequent chapters to form molecules using detuned Raman transfer, rather than STIRAP. We chose the frequency of the 642 nm laser to be 500 MHz blue detuned from $|J=1,\ m_J=-1\rangle$, such that direct excitation

from $|1\rangle$ would fall between the energy of the $J = 1$ and $J = 2$ levels, as shown in Fig. 5.5(b). The polarization of the two 642 nm and 937 nm Raman beams was therefore set to $\hat{\sigma}^-$ to maximize the Raman Rabi frequency contribution from the closest detuned $|J = 1,\ m_J = -1\rangle$ intermediate state.

To demonstrate sequential imaging, following molecule rearrangement, we applied a resonant microwave pulse and measured Rabi oscillations between $|0\rangle$ and $|1\rangle$, shown in Fig. 5.5(c). In the second image, we detected 95(3)% of the population in $|1\rangle$, consistent with expected losses of 5.6(8)% due to scattering of the tweezer-light during the first imaging step. The multi-state readout procedure provides full-state information on all the molecules in the array, allowing for direct single-shot readout of the diagonal elements of any multi-qubit density matrix.

5.5 Site-selective preparation of molecules

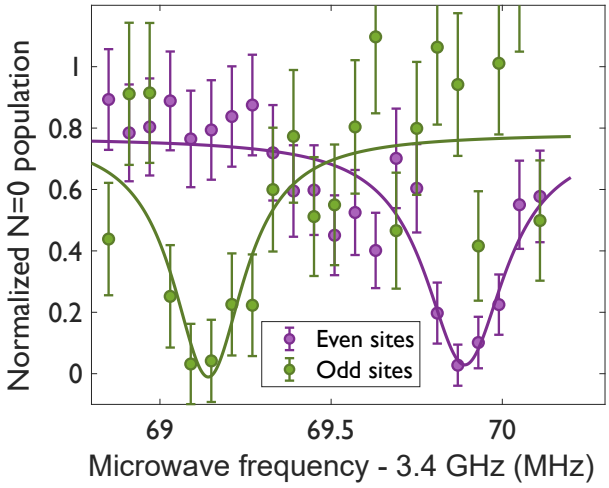

Figure 5.6: Microwave spectrum of molecule magic transition, with local 623 nm beams overlaid only on odd sites in a molecular array.

Site-resolved control of the quantum state of individual particles is necessary to implement local qubit operations in quantum gates, and to prepare arbitrary initial states in quantum simulators. Towards this goal, local control of fields on the scale of the separation between particles is required. In experiments with neutral atoms in optical tweezers, the conventional approach is to apply a global pulse to drive a transition that is made off-resonant for certain sites using some combination of tightly-focused AC-Stark-shifting beams [163, 294] and manipulation of position-defined sub-ensembles [38]. We demonstrated this method for molecules with NaCs [201], using the Na tweezers (which were at 623 nm at the time) to apply a local light shift to the molecules. An example of a molecular rotational spectrum with a light shift of close to 1 MHz applied to only the odd sites in an eight-site array, is shown in Fig. 5.6. This method has also been used for site-selective state preparation of CaF [17] molecules. Nevertheless, this method has significant drawbacks in the molecule case. Most notably, although the 623 nm light produces a relatively large molecule AC stark shift, it also leads to significant scattering and molecule losses. This problem was exacerbated when we began using 616 nm light for magic trapping of Na, which can drive rovibrational ground state molecules to above the Cs $6P_{1/2}$ dissociation threshold and couple to continuum states. We thus set out to develop a different solution.

A drawback of using a computational basis sensitive to differential AC Stark shifts is that intensity noise will result in decoherence. Intensity noise from the optical tweezer is the dominant source of noise for molecules due to their generally large tensor polarizability. For this reason, we seek to initialize molecules within a computational subspace that is insensitive to differential AC Stark shifts from the optical tweezer. The

ellipticity of the 1064 nm tweezer polarization is tuned to realize a "magic" state in each rotational level that is free from anisotropic polarizability (see Chapter 4). The lowest two "magic" states, $|0\rangle$ and $|1\rangle$, form our computational basis in this, whose transition offers a two orders-of-magnitude larger spin echo coherence time than the transition between $|0\rangle$ and a non-magic state $|1'\rangle \equiv \frac{1}{\sqrt{2}}(|N=1,\ m_N=-1\rangle + |N=1,\ m_N=1\rangle)$. Since the computational basis cannot be AC Stark-shifted with the 1064 nm tweezer, we made use of the large $h \times 5.55(1)$ MHz$/(\mathrm{MW/cm^2})$ differential AC Stark shift between $|0\rangle$ and $|1'\rangle$. The $|0\rangle$ population of certain sites was shelved in $|1'\rangle$, allowing the remaining sites to be excited to $|1\rangle$. Shelving avoids the use of an additional near-resonant AC-Stark-shifting beam, that could introduce unwanted scattering that would limit molecule lifetime and state preparation fidelity.

The scheme for site-selective state preparation is illustrated in Fig. 5.7(a). The array was divided into a set of target sites, which are to be transferred to the $|1\rangle$ state, and shelved sites, which are to remain in $|0\rangle$ at the end of the sequence. For the shelving process, the trap depths of the target sites were reduced to 25% of the depth of the shelved sites by ramping down the amplitude of the RF tones generating these tweezers. The site-selective initialization was then achieved with a sequence of three microwave pulses:

1. With both sites initially in $|0\rangle$, the shelved sites were selectively transferred to the non-magic $|1'\rangle$ state using a resonant microwave pulse. Due to the depth difference between the sites, the corresponding transition for the target sites is off-resonant.

2. With the shelved sites in $|1'\rangle$, the target sites were then transferred to the magic $|1\rangle$ state.

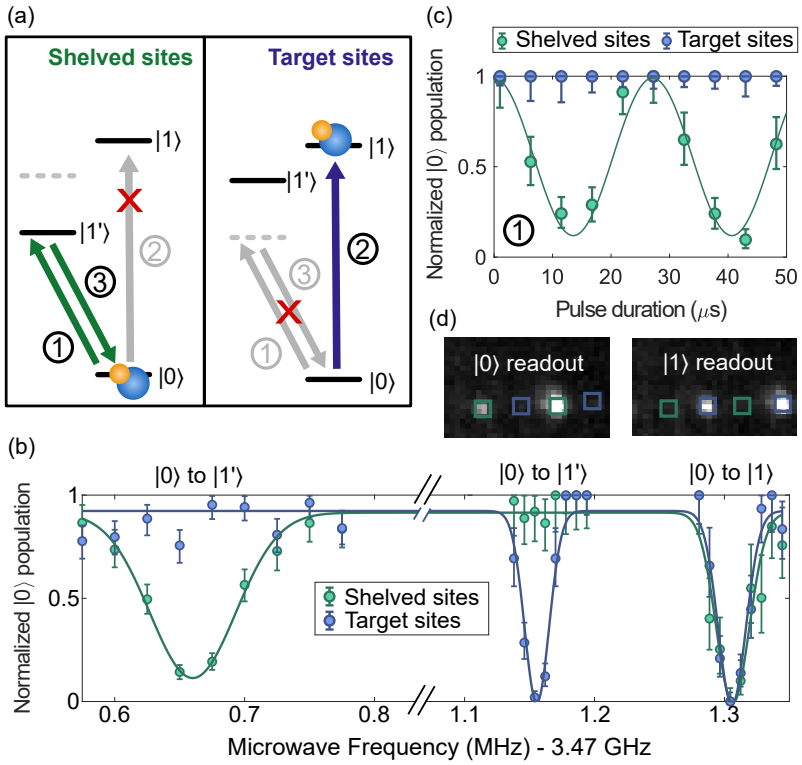

Figure 5.7: Site-selective state preparation in a rotational qubit subspace of $|0\rangle$ and $|1\rangle$. (a) Scheme for an array initialized in $|0\rangle$ showing the shelving of more intense traps to an auxiliary non-magic state $|1'\rangle$ in the $N = 1$ manifold. The remaining target sites are driven to $|1\rangle$ with a global microwave pulse. The shelved sites are then returned to $|0\rangle$ with a final resonant pulse. (b) Microwave spectra showing the resolved transition frequencies from $|0\rangle$ to $|1'\rangle$ for the shelved sites (left) and the target sites (center), as well as the magic $|0\rangle$ to $|1\rangle$ transition (right) that has the same frequency for all sites. We note that the three peaks are probed with different microwave powers and pulse times. (c) Step 1 of the site-selective initialization procedure, showing selective transfer of shelved sites to $|1'\rangle$, while target sites remain in $|0\rangle$. (d) Average sequential readout images corresponding to $|0\rangle$ and $|1\rangle$ population for a site-selective initialization of odd and even sites of the array in $|0\rangle$ and $|1\rangle$, respectively.

3. The shelved sites were then transferred back to $|0\rangle$.

At the end of the sequence, the depths of the target sites were ramped back up. Using this procedure, it is possible to initialize an array of molecules in an arbitrary configuration of states $|0\rangle$ and $|1\rangle$. In Fig. 5.7(b), we show the resolved microwave transitions to the $|1'\rangle$ state for the shelved and target sites at the depths used for initialization, along

with the $|0\rangle$ to $|1\rangle$ transition that has the same frequency for all sites. The site-selective shelving of some sites in $|1'\rangle$ is shown in Fig. 5.7(c). Using this sequence to initialize a four-molecule array into an alternating pattern of $|0\rangle$ and $|1\rangle$, we found we could prepare the target sites in $|1\rangle$ with an average error rate of 4.5(8)% and leave shelved sites in $|0\rangle$ with an error rate of 3.7(7)%. Error rates were determined by comparing the average population of each sub-ensemble measured in the target state and the incorrect computational basis state after the initialization sequence. An average fluorescence image showing the array state after site-selective preparation is shown Fig. 5.7(d). In the future, these error rates could be further reduced with the use of composite passband pulse sequences, that can reduce the sensitivity of a π-pulse to small detuning and pulse area errors while suppressing coupling to further off-resonant states [134].

5.6 Outlook

In this chapter, we demonstrated several SPAM capabilities for molecules associated from constituent atoms in optical tweezers: nondestructive detection of occupation, rearrangement, site-selective initialization, and sequential multi-state detection. Many of these techniques can be generalized to other systems. For example, multi-state detection is broadly applicable to bulk and lattice platforms, and site-selective initialization can be extended to other multi-level systems in optical tweezers.

Further technical improvements can increase the fidelity of these capabilities. The detuned Raman transfer efficiency—which limits molecule production, the confidence that a rearranged site contains a molecule, and the detection fidelity—can be increased with beam intensity and position stabilization, more laser power, and feedforward

cancellation of Raman laser phase noise [183]. The false negative rate of high-field Cs detection can be reduced by improving the transfer fidelity between $|g'\rangle$ and $|g\rangle$ with a stronger microwave Rabi frequency. The shelving of molecular population in $|1'\rangle$ for site-resolved initialization can be improved with shaped or dynamical decoupling pulses to overcome noise in the transition frequency and off-resonant coupling to other $N = 1$ states. Lastly, molecule loss due to the high tweezer intensity needed for Cs detection may be mitigated by separating and detecting Na atoms in a tweezer whose wavelength differs from 616 nm, which is destructive to ground state molecules due to nearby molecular transitions.

The SPAM capabilities presented in this chapter are vital for our implementation and characterization of a two-qubit gate based on the dipole-dipole exchange interaction, detailed in Chapters 6 and 7. Molecule rearrangement produced a fourfold increase of the rate at which pairs of molecules in neighboring sites could be produced, significantly reducing the data collection time needed for all dipolar studies. Sequential multi-state imaging also enables faster accumulation of statistics, such as a fourfold reduction in the time required for parity measurements to quantify Bell state entanglement fidelity. We use site-selective addressing of molecules in Section 7.2 to prepare the four input logic states of two qubits to measure the truth table of an iSWAP gate. In the long term, advances such as the ones described here will be necessary to use polar molecules as qudit or virtual qubit systems for quantum computation and simulation applications.

Nothing is connected to everything; everything is connected to something.

Donna Haraway

6

Entanglement of individual molecules via coherent dipole-dipole interactions

Material in this Chapter, including portions of the text and figures, have been distributed as a preprint [215], and are undergoing peer review as of the time of submission.

6.1 Ultracold polar molecules as qubits

Foundational work three decades ago used molecular systems with nuclear magnetic resonances for proof-of-concept quantum computation [94, 177], transforming theoret-

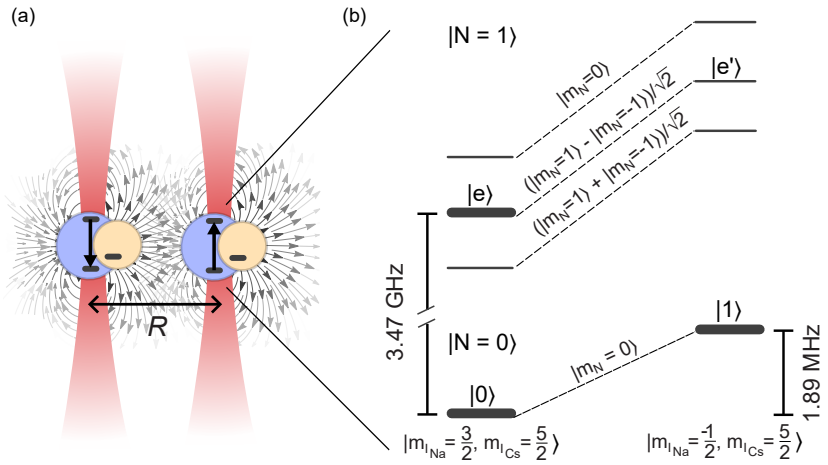

Figure 6.1: NaCs molecules in optical tweezers for dipolar interactions and quantum logic gates (a) Schematic of a pair of molecules trapped in neighbouring 1064 nm optical tweezers, with field lines representing the instantaneous electric field produce by the molecule-frame dipole moment of each molecule. (b) Relevant internal states are labeled by their dominant hyperfine states in the rotational ground and first excited manifolds of NaCs.

ical ideas into early experiments [141, 277]. These platforms enlisted the accessible complexity of molecules, using intrinsic nuclear spins as qubits and natural intramolecular spin-spin interactions to implement two-qubit gates. However, the platform was difficult to scale and lacked true entanglement [190] because the molecules were dissolved in a solvent at room temperature and subjected to ensemble averaging. Subsequent developments in quantum computing have shifted toward individually controllable systems with simpler structures, such as trapped ions [196], neutral atoms [37], and superconducting circuits [144].

As part of this trend towards individual control in quantum science, ultracold trapped polar molecules were proposed as a new kind of qubit in 2002, with long-range dipolar interactions between molecules used to create entanglement [77]. Subsequent works have expanded on this idea with proposals to use the rich structure of

molecules for dense and robust encoding of quantum information, which together may offer a new approach to scalability and fault-tolerance [3, 203, 233]. Ultracold molecules have also attracted a great deal of attention as a tool for quantum simulation, due to the anisotropy and exceptional tunability of the long-range dipolar interactions, which may provide a way to simulate exotic quantum phases of matter [98, 99, 119, 191, 239, 298].

Toward these goals, ultracold polar molecules have been prepared and isolated in optical traps [71, 164, 202]. In optical tweezer arrays, control and readout of single quantum states of molecules have been achieved [10, 48, 226, 230], and both hyperfine and rotational coherence have been extended well beyond the dipolar interaction timescale [47, 63, 101, 102, 169, 210, 212]. Most recently, entanglement between two isolated polar molecules has been realized [17, 117]. However, a universal two-qubit logic gate, which could apply to any arbitrary initial state, has not yet been demonstrated.

In this chapter, we demonstrate fast entanglement of qubits encoded in individual molecules using the electric dipole-dipole interaction between their rotational states. We characterized this interaction by creating a two-qubit Bell state within 664 μs with a measured fidelity of 94(3)%, after postselecting to remove trials with empty traps. The fidelity is limited by motion of molecules along the weakly confined axial dimension of the traps. We directly measured this motion via its coupling to molecular rotation, which allowed us to probe the motion of the molecules using applied microwave fields. Using this method, we determined an axial ground state fraction of 34(4)%, which is consistent with the measured Bell state fidelity. Subsequently, in Chapter 7, we demonstrate a universal two-qubit gate between molecules.

6.2 Molecule preparation and detection

Our experiment starts with a pair of individually-trapped NaCs molecules assembled from ground-state-cooled Na and Cs atoms following a procedure detailed in Chapter 2 and in Refs. [217, 308, 309]. After preparing the molecules in an 8-site array, we detect and remove any remaining unassociated Cs atoms and rearrange the molecules to a higher density region at one end of the array, using the method detailed in Chapter 5. All dipole-dipole interaction data reported in this chapter includes only the two sites with the highest molecule density at the end of the array. These molecules are held in magic ellipticity optical tweezers—as described in Chapter 4—where the polarization ellipticity is chosen to cancel first-order differential light shifts between the $N = 0$ and one sublevel ($|e\rangle$) of the $N = 1$ rotational states, yielding long rotational coherence times [210].

We define the quantization axis to be along the magnetic field of 863.9 G, which is kept constant during the experiment and is parallel to the k-vector of the optical tweezer.* The large magnetic field independently aligns the nuclear spins of the two atoms and decouples them from molecular rotation. The rotational sublevels are predominantly split by the AC electric field of the optical tweezer, which is elliptically polarized in the plane perpendicular to the quantization axis. We label three states relevant to this work: the state in which assembled molecules are initially prepared, $|0\rangle \equiv |N = 0, m_N = 0, m_{I_{\mathrm{Na}}} = 3/2, m_{I_{\mathrm{Cs}}} = 5/2\rangle$ [48]; the magic state in the first rotationally-excited manifold with the same nuclear hyperfine quantum numbers,

*This choice of quantization axis differs from Chapter 4, in which we used the minor axis of the polarization ellipse. The magnetic field direction is used here in order to allow us to express the nuclear spin states in the nearly-diagonal basis of m_I projections along the field axis.

$|e\rangle \equiv |N=1, m_{I_{\mathrm{Na}}}=3/2, m_{I_{\mathrm{Cs}}}=5/2\rangle \otimes \frac{1}{\sqrt{2}}(|m_N=1\rangle - |m_N=-1\rangle)$ [210]; and an additional nuclear hyperfine state in the rotational ground manifold that we use as one of our qubit states, $|1\rangle \equiv |N=0, m_N=0, m_{I_{\mathrm{Na}}}=-1/2, m_{I_{\mathrm{Cs}}}=5/2\rangle$.[†]

Molecules are initially assembled in $|0\rangle$ within the ground rotational manifold and can be transferred to $|e\rangle$ in the first rotationally-excited manifold via microwave excitation or dipolar exchange. Nuclear spin state $|1\rangle$ in the ground rotational manifold is selected to encode a hyperfine qubit in the molecule. For molecular detection, we sequentially detect $|0\rangle$ and $|e\rangle$ or $|0\rangle$ and $|1\rangle$ within a single experimental sequence by converting molecules back to atoms for fluorescence imaging as described in Chapter 5. To initially prepare a pair of molecules in different internal state combinations starting from the $|00\rangle$ state, we employ site-selective excitation of molecules using dynamic ramping of tweezer depths combined with microwave shelving pulses.

To study the interactions between molecules, we postselected on cases where two molecules were detected at the readout stage, which is enabled by the fact that we measured both $|0\rangle$ and $|e\rangle$ during each experimental run. The probability of detecting a molecular pair throughout all experimental runs is $\sim$3%, which is primarily limited by the inefficiency of molecule creation [216]. Postselection allows us to eliminate background in the interaction signal due to shots where one or both traps are empty, at the expense of discarding shots in which both molecules were present but one or both were not detected due to measurement error. The only remaining background on the postselected signal is due to the small 0.0038 false positive rate of the imaging step, giving a negligible contribution of 10^{-5} to the two-body signal, assuming uncorrelated false

[†]Note that we label the magic state $|e\rangle$ in this chapter, using a different labelling scheme to Chapter 4, in order to distinguish it from the state $|1\rangle$ that we use to encode a hyperfine qubit.

positives between sites [216]. The outcomes of each trial following post-selection are described by a binomial distribution,

$$p(S|X, N_{Trial}) = \begin{pmatrix} N_{Trial} \\ S \end{pmatrix} X^S (1-X)^{N_{Trial}-S},$$

where X is the underlying probability of measuring a particular two-qubit state, S is the number of trials in which that state is actually measured, and N_{Trial} is the total number of trials in which a pair of molecules is detected at all. Given a measurement of S, the maximum likelihood estimator of the population, $\hat{X}$, and associated 1σ confidence interval can be computed by inverting the distribution using the Clopper-Pearson method [66].

6.3 The dipole-dipole interaction

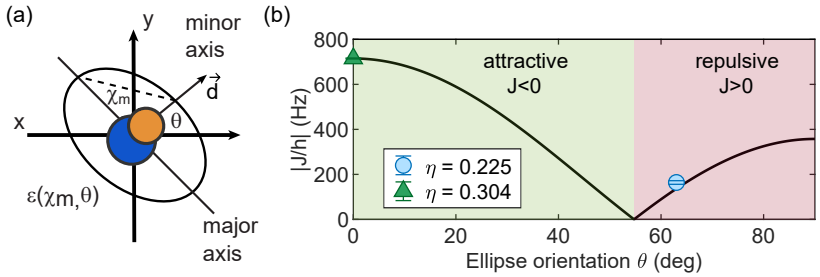

Figure 6.2: (a) Illustration of the polarization ellipse in the $x-y$ plane, perpendicular to the k-vector of the tweezer that sets the orientation of the rotational sublevels of the molecule. (b) Measured interaction strengths J between molecules separated by 1.9 µm at the magic ellipticity condition for two different choices of waveplate retardance η. The black curve shows the expected form of the interaction strength scaled to the maximum value of $|J/h|$ observed at $\eta = 0.304\,\lambda$.

A key reason for the choice of NaCs molecules is their large molecule-frame dipole moment of $d = 4.6$ Debye [15]. In the absence of an external electric field, the lab-

frame permanent dipole moment vanishes due to the fact that the rotational state of the molecule is an eigenstate of parity. However, when two dipolar molecules are brought close together they will nevertheless interact, as each rotating dipole experiences the field produced by the other. This can lead to coupling between the rotational states of the two molecules, which is the basis for the dipolar entanglement scheme demonstrated in this chapter.

The Hamiltonian describing the instantaneous energy of a pair of interacting electric point dipoles is

$$H_{\mathrm{DD}} = \frac{\vec{d}_i \cdot \vec{d}_j - 3(\vec{d}_i \cdot \hat{r}_{ij})(\vec{d}_j \cdot \hat{r}_{ij})}{4\pi\varepsilon_0 R^3}, \tag{6.1}$$

where $\hat{r}_{ij}$ is a unit vector along the line connecting the two dipoles and R is the distance between them. This expression holds both classically and quantum mechanically. The difference, though, is that in the quantum mechanical case we need to consider the fact that the dipoles are rotating, and determine how this dipole-dipole interaction term will perturb the existing rotational eigenstates. To do this, it is useful to rewrite the expression in terms of spherical tensors, as [39, 98]

$$H_{\mathrm{DD}} = \frac{\sqrt{6}}{4\pi\varepsilon_0 R^3} \sum_{q=-2}^{2} (-1)^q C^2_{-q}(\theta_{ij}, \varphi_{ij}) T^2_q(\vec{d}_i, \vec{d}_j). \tag{6.2}$$

In this expression, θ_{ij} and φ_{ij} are the polar and azimuthal angles, respectively, describing the orientation of the vector $\hat{r}_{ij}$ in the lab frame, and C^2_{-q} is a reduced spherical harmonic defined by $C^k_q(\theta, \varphi) = \sqrt{\frac{4\pi}{2k+1}} Y_{kq}(\theta, \varphi)$. The term $T^2_q(\vec{d}_i, \vec{d}_j)$ represents the rank-2 tensor formed from the product of the two rank-1 tensors (vectors) that are the individual dipoles. The components of this rank-2 tensor in both Cartesian and spherical

tensor form are, explicitly [45],

$$T^2_0(\vec{d}_i,\vec{d}_j) = \frac{1}{\sqrt{6}}(d_i^+ d_j^- + 2d_i^0 d_j^0 + d_i^- d_j^+) = \frac{1}{\sqrt{6}}(2d_i^z d_j^z - d_i^x d_j^x - d_i^y d_j^y) \tag{6.3}$$

$$T^2_{\pm1}(\vec{d}_i,\vec{d}_j) = \frac{1}{\sqrt{2}}(d_i^\pm d_j^0 + d_i^0 d_j^\pm) = \mp\frac{1}{2}(d_i^x d_j^z + d_i^z d_j^x \pm i(d_i^y d_j^z + d_i^z d_j^y)) \tag{6.4}$$

$$T^2_{\pm2}(\vec{d}_i,\vec{d}_j) = d_i^\pm d_j^\pm = \frac{1}{2}(d_i^x d_j^x - d_i^y d_j^y \pm i(d_i^x d_j^y + d_i^y d_j^x)) \tag{6.5}$$

The equivalence of expressions 6.1 and 6.2 can be verified by substituting in these components and the explicit forms of the $k = 2$ spherical harmonics, which are widely tabulated. The form of the interaction in 6.2 is very useful, because it separates out terms that depend on the relative orientations of the two dipoles, represented by $T^2_q(\vec{d}_i,\vec{d}_j)$, and those that depend on the relative positions of the molecules, represented by $C^2_q(\theta,\varphi)$.[‡] To determine what the effect of the dipole-dipole interaction on the rotational states will be, we can evaluate the matrix elements of $\hat{H}_{\mathrm{DD}}$. The matrix elements of the individual dipole operators of each molecule are [281]

$$\langle N', m'_N|\, d^p \,|N, m_N\rangle = d(-1)^{m_N}\sqrt{(2N'+1)(2N+1)}\begin{pmatrix} N' & 1 & N \\ -m'_N & p & m_N \end{pmatrix}\begin{pmatrix} N' & 1 & N \\ 0 & 0 & 0 \end{pmatrix}$$

Based on the selection rule of the Wigner 3-j symbols, the matrix elements are zero unless $m'_N + p - m_N = 0$, from which we can see that the spherical tensor components d^-, d^0, and d^+ correspond to changes of the lab-frame projection of rotation, m_N, by -1, 0, and 1, respectively. Correspondingly, the components of the two-molecule ten-

[‡]Note that, somewhat surprisingly, equation 6.2 contains only tensor components, with no scalar contribution. This is because the scalar term $\vec{d}_i \cdot \vec{d}_j$ in equation 6.1 is perfectly cancelled out by the scalar component of the $3(\vec{d}_i \cdot \hat{r}_{ij})(\vec{d}_j \cdot \hat{r}_{ij})$ term. Thanks to Gabriel Patenotte for pointing this out.

sor $T^2_{\pm 2}$, $T^2_{\pm 1}$, and T^2_0 represent processes that change the total rotational projection of the two molecules by ± 2, ± 1 and 0, respectively. If we make the assumption that the same two rotational states within each molecule are coupled by the rotational exchange, then by definition the total m_N does not change and we can neglect all terms except for $q = 0$. This assumption can be justified by the fact that, unless external fields are chosen specifically to make two rotational sublevels near-degenerate, any processes which change total m_N will be far off-resonant.

We can write the $q = 0$ component of equation 6.2 explicitly as

$$H_{\mathrm{DD};q=0} = \frac{1 - 3\cos^2(\theta)}{4\pi\varepsilon_0 R^3} \left(d_i^0 d_j^0 + \frac{d_i^+ d_j^- + d_i^- d_j^+}{2} \right) \tag{6.6}$$

This term leads to coherent exchange of rotational excitation between molecules i and j. Restricting ourselves to the subspace of two rotational levels $|0\rangle$ and $|e\rangle$, we can recast this Hamiltonian in the form of a spin-exchange interaction [73, 99, 203]

$$\hat{H}_{\mathrm{DD}} = \frac{J}{2}(\hat{s}_1^+ \hat{s}_2^- + \hat{s}_1^- \hat{s}_2^+) = \left(\frac{d}{\sqrt{3}}\right)^2 \frac{1 - 3\cos^2\theta}{4\pi\varepsilon_0 R^3} (|0e\rangle \langle e0| + |e0\rangle \langle 0e|) \tag{6.7}$$

where J is the effective rate of the spin exchange process within this manifold, which depends on the transition dipole moment $d/\sqrt{3}$ of the $|0\rangle \rightarrow |e\rangle$ transition associated with the raising, $\hat{s}_i^+ = |e\rangle \langle 0|_i$, and lowering, $\hat{s}_i^- = (\hat{s}_i^+)^\dagger$, operators [281].

The dipolar interaction can be tuned by changing R and θ. Uniquely to our system, the rotational eigenstates of molecules are dominantly quantized by the trapping light rather than static electric or magnetic fields. Therefore, the orientation of the tweezer polarization ellipse determines the angle θ, providing a way to switch between attrac-

tive ($J < 0$) and repulsive ($J > 0$) interactions. Experimentally, we realized two different θs by choosing waveplates with retardances of $\eta = 0.225\lambda$ and 0.304λ while maintaining the "magic" ellipticity polarization (χ_m) condition (Fig. 6.2). For the remainder of this chapter, we use the latter waveplate to achieve $\theta = 0$, maximizing the magnitude of interaction strength. In the future, the strength could be dynamically tuned using fast polarization control via optical interference of multiple tweezer beams [162, 174].

6.4 Coherent exchange of rotational excitations

We characterized the coherent exchange of rotational excitation between a pair of molecules using a spin-echo Ramsey sequence [258]. We began with a pair of molecules in the $|00\rangle$ state and applied a $\pi/2$-pulse to prepare the product state $\frac{1}{\sqrt{2}}(|0\rangle - i|e\rangle) \otimes \frac{1}{\sqrt{2}}(|0\rangle - i|e\rangle)$. The phase of this first pulse defines rotation about the x-axis of the Bloch sphere. We then allowed the system to evolve under H_{DD} for time τ before applying another $\pi/2$ pulse. To cancel out any phase accumulation due to finite detuning of the microwave pulse from resonance or slow drifts in the resonance frequency, we applied a spin-echo π-pulse in the middle of the interaction period, with a phase of $+90^\circ$ relative to the initial pulse, realizing an effective y-rotation. This sequence is illustrated in the inset of Fig. 6.3. The π-pulses have a total duration of 12.83 µs, and for all pulses addressing this transition we used a truncated Gaussian pulse shape with a width of 0.3 times the pulse duration to reduce off-resonant coupling to other rotational states [40]. The dipolar exchange interaction results in an output state with amplitudes determined by the interaction time:

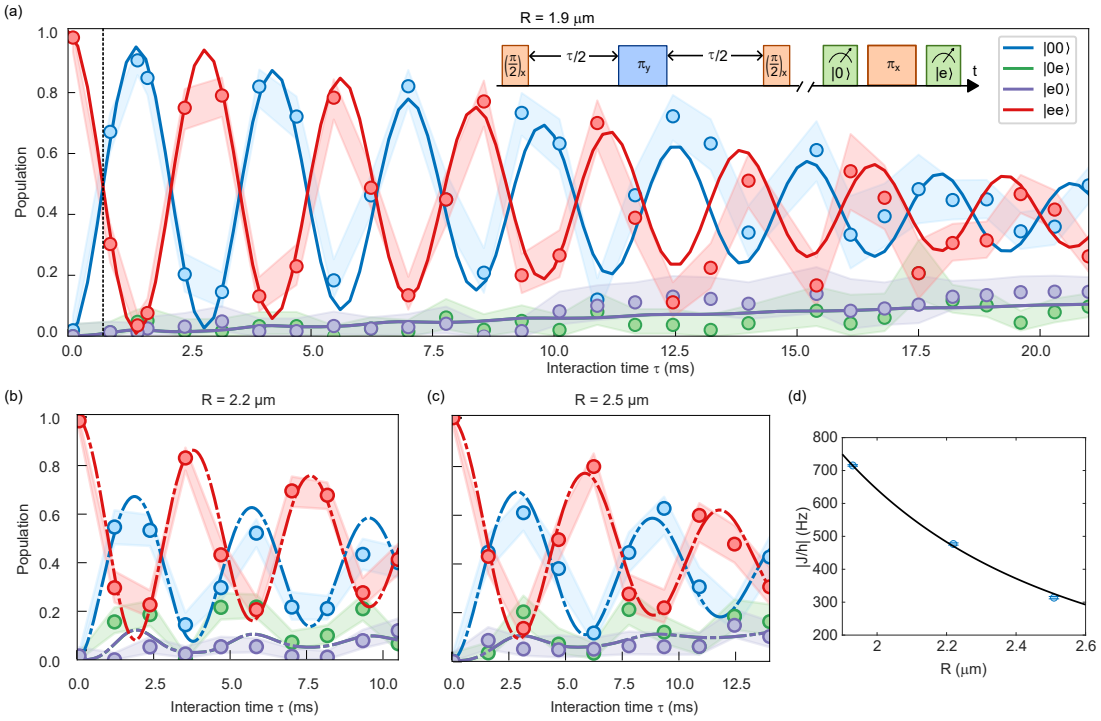

Figure 6.3: Characterization of dipole-dipole mediated rotational exchange interaction, using data postselected to include only cases where both molecules are detected. (a) Populations of four possible two-molecule states of a pair of molecules undergoing dipolar interaction at a separation of $R = 1.9\,\mu$m. The shaded bands indicate 1σ error bars, representing the standard deviation. The inset shows the spin-echo microwave pulse sequence used to probe the interaction, as well as the subsequent multi-state detection step. Here, we use the convention θ_i, where θ and i are the rotation angle and axis, respectively, to specify the microwave pulse. Solid lines are theory curves from a full quantum-mechanical simulation of the dipolar interaction and molecule motion, with temperature and motion parameters determined from separate single-molecule measurements (see Fig. 6.5), and tweezer separation and single molecule dephasing chosen to match the data. (b-c) The same interaction applied at separations of 2.2 μm and 2.5 μm. Dashed-dot lines represent fits to a master equation model with phenomenological decoherence rates. (d) Scaling of the interaction strength J as function of distance. The black line represents a single-parameter fit with the function a/R^3 with best fit value $a = 5.14(4)$ kHz μm^{-3}.

$$|\psi(\tau)\rangle = \tfrac{1}{2}(1 - e^{-i\frac{J\tau}{2\hbar}})\,|00\rangle + \tfrac{1}{2}(1 + e^{-i\frac{J\tau}{2\hbar}})\,|ee\rangle.$$

In Fig. 6.3(a), we show the evolution of the populations in each of the possible states, $|00\rangle$, $|0e\rangle$, $|e0\rangle$, and $|ee\rangle$, of a pair of molecules separated by 1.9 μm as a function of the total interaction time τ. We estimated the tweezer separation from the frequencies of

the RF tones applied to the acousto-optic deflector used to generate the tweezers and the expected propagation of beams through a 4f optical system [309]. This does not account for any systematic deviations of the tweezers from ideal Gaussian beams, such as could be caused by aberrations or by the overlap of the tweezers at small separations. The data are postselected to include only cases in which molecules were detected in both tweezers. The populations represent a maximum likelihood estimate of the probability of obtaining each state, and the shaded regions are 1σ confidence intervals.

We performed initial analysis of the strength and decoherence of the dipole-dipole interaction using a Lindblad master equation with three phenomenological decay channels corresponding to dephasing of the dipole-dipole interaction itself, relative detuning noise between the two molecules, and global detuning noise on both molecules. These processes are represented, respectively, by the jump operators:

$$L_J = \sqrt{\gamma_J}\left(|0e\rangle\langle e0| + |e0\rangle\langle 0e|\right) \tag{6.8}$$

$$L_\delta = \sqrt{\gamma_\delta}\left(|e0\rangle\langle e0| - |0e\rangle\langle 0e|\right) \tag{6.9}$$

$$L_\Delta = \sqrt{\gamma_\Delta}\left(|ee\rangle\langle ee| - |00\rangle\langle 00|\right) \tag{6.10}$$

We fit the master equation model to the data by minimizing the weighted least squares residual of the model and experimental data, using the Nelder-Mead algorithm to optimize the rates of the decoherence processes along with the interaction strength, J, and a static relative detuning, δ, between the molecules. We implemented the master equation model using the Julia Quantum Optics toolbox [156]. To estimate the uncertainties in the optimized parameters of the master equation model we applied the parametric

bootstrap method. This method relies on generating artificial datasets from the same distribution as the real data and using them to numerically estimate the expected distribution of the fit values given a particular set of experimental parameters [83]. For every dataset that we fit, we generated new bootstrap samples using the estimator $\hat{X}$ for each two-molecule state at each point, drawing from the distribution $p(S|\hat{X}, N_{Trial})$. We then repeated the fitting procedure for each bootstrapped sample, generating a distribution of optimal fit parameters. We generated 300 bootstrap samples for each experimental dataset. The uncertainties in the fit parameters represent the standard deviation of their distribution.

With the aid of the master equation, we extracted an interaction rate of $|J/h| = 715(2)$ Hz. We observed that the decoherence was dominated by noise on the interaction strength, which can also be seen in Fig. 6.3(a) by comparing the symmetric decay of the oscillations between $|00\rangle$ and $|ee\rangle$ with the slower rise of the $|0e\rangle$ and $|e0\rangle$ populations.

To understand the physical origin of this decoherence, we developed a full quantum mechanical simulation of the motion of the molecules, as described in section 6.6. The solid lines in Fig. 6.3 represent the decaying oscillations predicted by this model, with parameters extracted from independent single-molecule measurements shown in Fig. 6.5.

We performed the same experiment at separations of 2.2 and 2.5 µm and extracted J for each distance from the master equation simulation. In Fig. 6.3(d), we plot the interaction rate against the separation and perform a single parameter fit to the function a/R^3. We observe good agreement with the expected $1/R^3$ scaling of the dipole-

Separation (μm)	J/h (Hz)	δ/h (Hz)	γ_J (Hz)	γ_δ (Hz)	γ_Δ (Hz)
1.9	715(2)	17(17)	107(10)	25(3)	13(2)
2.2	477(3)	214(111)	125(29)	31(31)	16(16)
2.5	314(6)	159(159)	114(32)	53(53)	35(35)

Table 6.1: Fit values and bootstrapped uncertainty estimates for the phenomenological master equation model of interactions, for the three distances shown in Fig. 6.3. The bootstrapped distributions of fit values for the master equation dephasing rates and detuning $|\delta|$ are, in some cases, consistent with zero to within 1σ, and are truncated below zero due to the restriction that values must be positive. In these cases we report the value as 1σ above zero, but note that the distribution deviates from Normal due to the truncation.

dipole interaction, and extract a distance-independent interaction rate of $\frac{|J|}{hR^3} = 5.14(4)\ \text{kHz}\,\mu\text{m}^{-3}$. This rate is faster by 17% than expected from the dipole moment of NaCs [15], which could be explained by a systematic error of 4% in the distance calibration. The measured dipolar strength J is the fastest observed in work on ultracold molecules and magnetic atoms, even considering the closer spacings in optical lattice systems [59, 63, 296]. The master equation fit parameters for all three distances are given in Table 6.1.

6.5 Dipolar entanglement

The dipole-dipole interaction natively generates entanglement between the rotational states of the molecules [203]. Applying the spin-echo pulse sequence with an interaction time $|h/2J|$ maps the input $|00\rangle$ product state to the maximally entangled state $\frac{1}{\sqrt{2}}(|00\rangle - i\,|ee\rangle)$, which is equivalent up to a global rotation to the $|\Phi^{\pm}\rangle$ Bell states. This was first demonstrated experimentally with CaF molecules with a fidelity of up to 0.89, limited by thermal motion of the molecules due to their relatively hot initial temperature [17, 117]. In the case of CaF, the entanglement benefited from a sort of motional

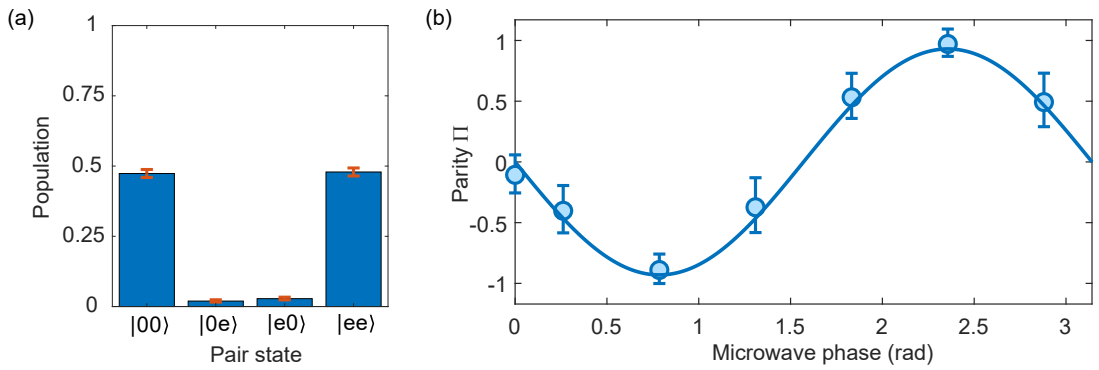

Figure 6.4: (a) Populations of the components of the Bell state created at an interaction time of 664 μs, indicated by a dashed line in Fig. 6.3. (b) Parity oscillation signal $\Pi = P_{00} + P_{ee} - P_{0e} - P_{e0}$ after applying an additional global microwave $\pi/2$-pulse with a variable phase to the Bell state.

narrowing effect, due to the fact that the interaction rate is much smaller than the axial trapping frequency. We expected our molecules with a large motional ground state fraction to do significantly better, although in our case the trap frequency and interaction strength are of the same order of magnitude, meaning that we did not expect to be aided by motional narrowing effects.

We prepared a maximally entangled Bell state at a molecule separation of 1.9 µm, using an interaction time of 664 µs. This interaction time, which is slightly less than $|h/2J|$, was chosen with the aid of the master equation fit to maximize the entanglement fidelity in the presence of decoherence. To verify the entanglement of the generated state, we measured the off-diagonal coherences of the density matrix by applying an additional global analysis microwave $\pi/2$ pulse with a variable phase to the pair of molecules. At each phase we measured the parity signal $\Pi = P_{00} + P_{ee} - P_{0e} - P_{e0}$, which is expected to oscillate with the applied phase φ as $\Pi = C\sin(2\varphi)$, where the amplitude, C, of the parity oscillation is the coherence [231]. The total entanglement fidelity is determined by the coherence and the diagonal populations, $F = \frac{1}{2}(C + P_{00} + P_{ee})$. In Fig.

6.4(b) we show this measured parity oscillation signal, along with the populations of all the two molecule states prior to the analysis pulse in (a). We extracted a coherence $C = 0.93(3)$ using a weighted least squares fit, and populations $P_{00} = 0.47(1)$ and $P_{ee} = 0.48(1)$. The total entanglement fidelity, conditioned on the detection of both molecules at the end of the sequence, is thus $F = 0.94(3)$. This is consistent to within 1σ with a maximum fidelity of 0.97 predicted given the currently observed decoherence of the dipole-dipole interaction.

6.6 Motion-rotation coupling

In section 6.4, we observed that the dominant dephasing mechanism of the two-body dipolar interaction was noise on the interaction strength. Such noise can be induced by relative motion of interacting molecules, which leads to fluctuation of R and θ in Equation 6.7. To investigate the effect of motion, we first focused on the rotational coherence between $|0\rangle$ and $|e\rangle$ of a single molecule in a tweezer. While a common way to remove noise and extend single-particle coherence is to apply dynamical decoupling [17, 63, 117, 210], we found empirically that the coherence was significantly reduced by an XY-8 pulse sequence when the π-pulse spacing τ_{xy8} was chosen to decouple noise close to the interaction timescale $|h/2J|$. In particular, we observed a dip in the coherence as a function of τ_{xy8}, the position of which shifted with the trap depth (Fig. 6.5(a)). We identified this dip as corresponding to the axial trapping frequency of the molecules, originating due to parametric heating of the molecules by pulses spaced by half the trap oscillation period. From a fine scan of this dip, we extracted an axial trap frequency of 4.95(1) kHz at the trap depth at which we performed dipolar interac-

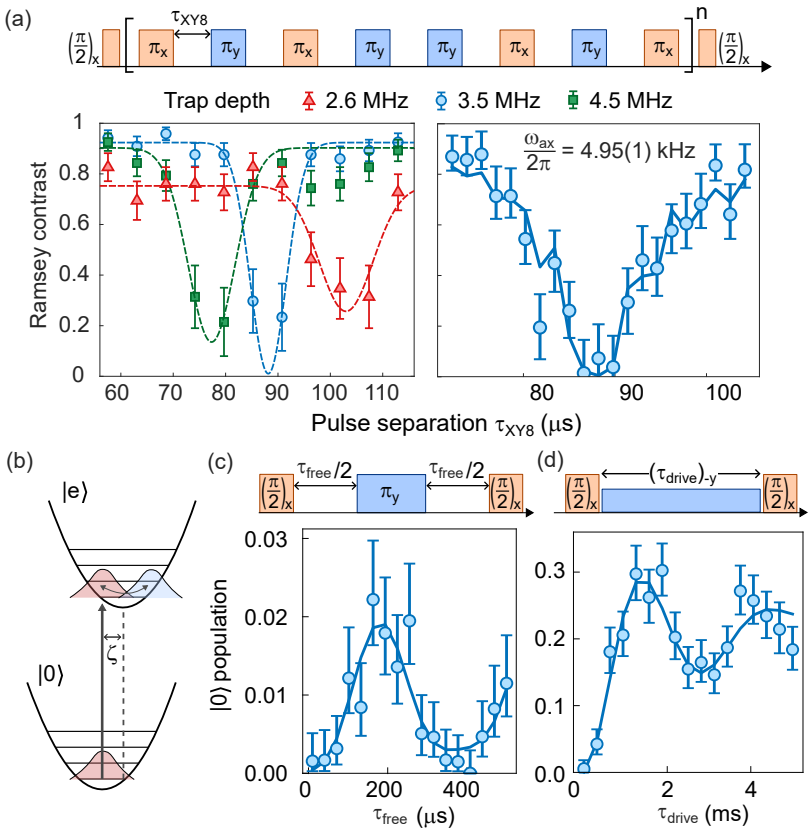

Figure 6.5: Coherent motion-rotation coupling to characterize molecule temperature and trap displacement ζ. (a) Measured Ramsey coherence as a function of pulse separation τ_{xy8} between XY-8 π-pulses. The left plot shows three different trap depths (inferred from theoretical polarizability of NaCs [210, 278]), at which we apply three XY-8 repetitions, totaling 24 π-pulses over an interrogation time of $24\tau_{xy8}$. By altering the tweezer depth during the measurement, we can modify the trapping frequency ω_{ax}, which shifts the τ_{xy8} that produces maximal decoherence. Dashed lines are a Gaussian fit serving as a guide to the eye. The right plot shows a detailed spectrum of the noise peak at the depth of 3.5 MHz; the depth used for dipolar interactions data in Fig. 6.3. From this spectrum, which was probed with six XY-8 repetitions, we extracted an axial trap frequency of 4.95(1) kHz. (b) Illustration of the motional wavefunction of a single molecule following excitation from $|0\rangle$ to $|e\rangle$ when the $|e\rangle$ trapping potential is displaced. (c) Observed oscillations in $|0\rangle$ at half the axial trapping frequency as a function of free evolution time τ_{free} during a spin-echo sequence. (d) Population in $|0\rangle$ under continuous microwave drive along the -Y direction, where the drive Rabi frequency of $\Omega/2\pi = 5.18(3)$ kHz was chosen to be close to the axial trapping frequency. The solid lines in a, c, and d were generated by the same theoretical model with temperature, trap displacement, and dephasing parameters chosen to match all of the data simultaneously.

tions.

To explain the parametric heating, there has to be a physical coupling between rotational and motional states, implying a deviation from ideal "magic" trapping. This could be caused either by a change in the trap depth or a displacement of the trap center between the $|0\rangle$ and $|e\rangle$ states. Because the tweezer polarization is empirically tuned to match the trap depths for the $|0\rangle$ and $|e\rangle$ states (see Fig. 4.2), we discarded the former, and turned towards characterizing the displacement. We constructed a minimal model with a state-dependent displacement of the trapping potential, as illustrated in Fig. 6.5(b), described by

$$\hat{H}_{\text{motion}-\text{rotation}} = \hbar\omega_{\text{ax}}\hat{a}^\dagger\hat{a} - \frac{\hbar\zeta\omega_{\text{ax}}}{2}\,|e\rangle\,\langle e|\,(\hat{a}+\hat{a}^\dagger) \tag{6.11}$$

Here, ζ is the displacement in units of harmonic oscillator length $\sqrt{\hbar/(2m\omega_{\text{ax}})} = 80$ nm, with $m = 156$ a.u. the mass of NaCs and ω_{ax} the axial trapping frequency. $\hat{a}$ is the lowering operator of the axial trap in the harmonic approximation. We attribute the origin of the coupling to optical aberrations, specifically astigmatism. Simulations of the dynamics of motion-rotation coupling using this model were performed by David Wellnitz from the research group of Ana Maria Rey, who also helped devise the experiments we performed to characterize the motion-rotation coupling. The details of the simulation are given in Appendix A and in Ref. [215].

To determine the best fit parameters to match the data, we first fixed the trap frequency using the XY-8 scan in Fig. 6.5(a) by generating simulated curves for a range of trap frequency values, computing the weighted squared residuals between the curve and the data for each point, and fitting a parabola to determine the best fit trap fre-

quency.

We now introduce a new method to measure the molecules' temperature by using the motion-rotation coupling to transfer motional excitation to internal rotational states, motivated by similar techniques for ions [95]. In a spin-echo Ramsey experiment (Fig. 6.5(c) inset), motion will lead to coherent dephasing and re-phasing with half the trap frequency, as the spatial wavepackets of the two internal states $|0\rangle$ and $|e\rangle$ separate and recombine. In harmonic approximation, the functional form of the population in $|0\rangle$ is given by $1 - \exp \frac{-2\zeta^2 \sin^4(\omega_{\mathrm{ax}} t/4)}{\tanh[\hbar\omega_{\mathrm{ax}}/(2k_B T)]}$ [149]. As a consequence, this measurement is sensitive to the joint parameter $\zeta^2/\tanh[\hbar\omega_{\mathrm{ax}}/(k_B T)]$, where T is the molecule temperature and k_B is the Boltzmann constant.

We can couple motion and rotation more directly by applying a continuous resonant drive with a Rabi frequency $\Omega = \omega_{\mathrm{ax}}$, which generates dressed rotational states $|\pm\rangle = (|0\rangle \pm i\,|e\rangle)/\sqrt{2}$ with an energy separation of $\hbar\Omega$. In the dressed state picture, the motion-rotation coupling in equation (6.11) enables resonant excitation transfer between motion and rotation driven by $\hat{H}_{\mathrm{eff}} = \zeta\omega_{\mathrm{ax}}/4\,(|+\rangle\langle -|\,\hat{a} + |-\rangle\langle +|\,\hat{a}^\dagger)$, where rotating terms at frequency ω_{ax} have been neglected. We prepared the initial state as the lower dressed state $|-\rangle$ by applying a $\pi/2$-pulse with a phase +90° with respect to the drive such that excitation can initially only be transferred from motion to rotation. A final $\pi/2$-pulse with the same phase maps the dressed states back to the $|0\rangle$, $|e\rangle$ basis for readout. Since this transfer only occurs if initial motional excitation is present, the oscillation amplitude is directly related to the motional ground state fraction. We performed this experiment using a Rabi frequency of $\Omega/2\pi = 5.18(3)$ kHz, slightly detuned from ω_{ax}, resulting in oscillation at the generalized motion-dependent Rabi frequency

$\sqrt{\hat{a}^\dagger \hat{a}\, \zeta^2 \omega_{\mathrm{ax}}^2/4 + (\Omega - \omega_{\mathrm{ax}})^2}$ with decreased amplitude.

The astigmatism is directly related to the displacement ζ. We computed theory curves for a grid with varying astigmatism, temperature, and motional dephasing, and extracted expectation values and error bars from parametric bootstrapping [83], following the same procedure as described above for the master equation model (except now with 500 bootstrap samples). We found $\hbar\omega_{\mathrm{ax}}/(k_B T) = 0.42(6)$ corresponding to an axial ground state fraction of 34(4)%, and $\zeta = 0.062(5)$ from an astigmatism of $0.13(1)\lambda$.

With these parameters, we can model the two-molecule contrast oscillations in Fig. 6.3(a). We used the discrete variable representation for single-molecule computations and projected dipole interactions into the motional subspace. We included single-molecule decoherence with a decoherence time of 80 ms to match the rise of $|e0\rangle$ and $|0e\rangle$ population and set the distance to 1.79 μm to match the observed oscillation frequency. We found good quantitative agreement between theory and data. We used our model to compute a Bell state infidelity of 3(1)%— consistent with the measurement— with a contribution of around 1% due to single-molecule dephasing, and the rest due to finite temperature and astigmatism.

The molecule ground state fraction measured here is consistent with the lower bound on the molecule temperature measured using thermometry of atoms after dissociation in Fig. 5.4, but is lower than expected given the measured Feshbach molecule production efficiency under the assumption of identical trapping frequencies for both atoms [310]. The cause of this lower-than-expected ground state fraction is not immediately clear. One possibility that we investigated is whether there could be excess heating during two-photon detuned Raman transfer to the rovibrational ground state.

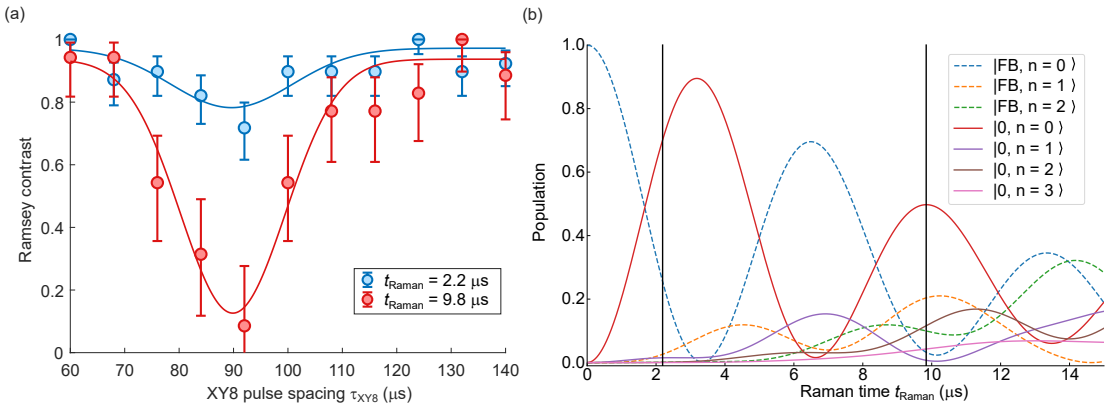

Figure 6.6: (a) Axial trap frequency heating resonance as a function of XY-8 pulse spacing for a single XY-8 repetition, for ground state molecules produced via detuned Raman transfer with a Raman pulse time of either approximately one or three π-times. (b) Simulated populations in different motional states as a function of Raman pulse time, for Feshbach molecules initially in the motional ground state of the tweezer. The Raman Rabi rate is chosen to match the rate observed in the experiment. Vertical black lines mark the two times used in (a).

In previous work [48], we estimated, based on a simple model of the momentum kick induced by absorption and emission of the Raman laser photons, that the probability of molecules leaving the motional ground state could be up to 14%. To make more detailed predictions, we explicitly simulated the populations in the first few motional states along the axial direction during detuned Raman transfer from the Feshbach to the ground state. This simulation, shown in Fig. 6.6(b), suggests that the Raman transfer can cause significant heating, but primarily for pulse durations longer than a single π-time. We confirmed this experimentally by measuring the XY-8 axial heating peak for molecules transferred to $|0\rangle$ using either a single detuned Raman π-pulse or a 3π-pulse. This measurement, shown in Fig. 6.6(a), reveals significantly more decoherence after a single set of XY-8 pulses for the molecules produced using the 3π-pulse. This is consistent with the much higher expected motionally excited state population of 10% for this pulse time, as opposed to 2% for a single π-pulse. Given the relatively small exci-

tation predicted for a π-pulse transfer, this mechanism does not immediately explain the measured 34(4)% ground state fraction. One possibility is that there is additional heating during the detuned Raman transfer that is not taken into account in this simulation. This could result, for example, from the vector or tensor shift of the Feshbach molecule—which have not yet been characterized—interacting with tweezer aberrations to produce a significant displacement of the trap center between the Feshbach and ground state molecules. Alternatively, there may be some heating during the rearrangement process preceding the interaction, which was not measurable in Fig. 5.4 due to being drowned out by later heating of the atoms during molecule dissociation and unmerging. Using the newly developed motion-rotation coupling measurements described in this section, we expect that it will be possible in the future to identify at what point in the sequence heating occurs and either mitigate or eliminate it to produce molecules at closer to the 80% total ground state fraction predicted from the Feshbach creation efficiency [310].

6.7 Expected fidelities

In this chapter, we demonstrated sub-millisecond entanglement of molecules mediated by the innate dipole-dipole interaction between molecules. We characterized the interaction by measuring a two-molecule Bell state entanglement fidelity of 94(3)%, with error primarily due to imperfect motional state preparation.

Looking ahead, without single-molecule dephasing and assuming a relatively modest improvement of the ground state fraction to 80%, our model predicts a Bell state infidelity of 0.4% limited by aberrations. Finally, by eliminating astigmatism, the in-

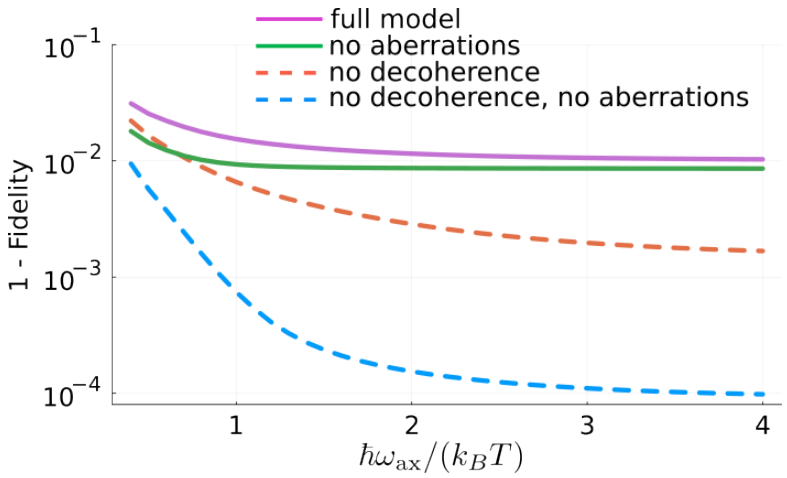

Figure 6.7: Bell state infidelity at the optimal time predicted as a function of inverse temperature. The solid purple curve illustrates the prediction of the full model including astigmatism of 0.13λ. The solid green curve illustrates the corresponding result without any astigmatism. The two dashed curves show simulations without single-molecule decoherence $\gamma_{\mathrm{deph}} = 0$, with (orange) and without (blue) astigmatism. Numbers quoted in the main text at 80% ground state fraction correspond to $\hbar\omega_{\mathrm{ax}}/(k_B T) = 1.6$. All curves are computed with motional level cutoffs $n = 25$ $[\hbar\omega_{\mathrm{ax}}/(k_B T) = 0.4]$; $n = 20$ $[0.5 \leq \hbar\omega_{\mathrm{ax}}/(k_B T) \leq 1.2]$; $n = 15$ $[1.3 \leq \hbar\omega_{\mathrm{ax}}/(k_B T) \leq 2]$; $n = 10$ $[2 \leq \hbar\omega_{\mathrm{ax}}/(k_B T)]$.

fidelity could be decreased to 2×10^{-4}, with approximately equal contributions from residual thermal motion and interaction back-action onto motion [57]. This back-action comes from the mechanical force that the dipoles exert on each other, which even at zero temperature can lead to off-resonant population transfer to motionally-excited states. This effect could ultimately be reduced by increasing tweezer separation or confinement, to either reduce the force $\sim 1/R^4$ or make population transfer more off-resonant. The contributions of these different effects to the infidelity as a function of temperature are shown in Fig. 6.7.

In the future, combining coherent entangling dipole-dipole interactions with excitation to multiple rotational levels will enable quantum simulation of complex many-body Hamiltonians [119, 263], as well as encoding of robust logical qubits [3] and qu-

dits [233]. In parallel, efforts to pursue efficient molecule production and detection remain important for the utility of the molecular platform, for example, in a hybrid molecule-Rydberg system with orders of magnitude faster gates and mid-circuit readout of molecular states [111, 161, 284, 307]. The coherent control of motion-rotation coupling offers a new sensitive probe of molecular temperature and confinement, adding a new degree of freedom to the molecule toolbox. This promises new opportunities for quantum simulation and metrology based on spin-motion entanglement [54, 95, 243].

In the following chapter, we show how the entangling dipole-dipole interaction characterized here can be used to engineer a universal two-qubit iSWAP gate for quantum computation with molecules.

[The Analytical Engine] might act upon other things besides number, were objects found whose mutual fundamental relations could be expressed by those of the abstract science of operations.

Ada Lovelace

7

Demonstrating an iSWAP gate between molecular qubits

Material in this Chapter, including portions of the text and figures, have been distributed as a preprint [215], and are undergoing peer review as of the time of submission.

A universal set of quantum gates is any group of single-qubit operations and at least one two-qubit gate with which any two-qubit unitary can be approximated with arbitrary accuracy. This, in turn, allows any quantum circuit on multiple qubits to be executed. The prototypical universal two-qubit gate is the CNOT gate [204]. This is far

from the only choice, however; in fact, any two-qubit entangling unitary is universal [42]. For polar molecules, a much more natural choice is the iSWAP gate, which is generated natively by the dipole-dipole interaction [203]. In Chapter 6 we verified that the dipole-dipole interaction between molecules in our system can produce a maximally entangled Bell state with a fidelity of 0.94(3). The CNOT gate can be constructed using two iSWAP gates and five single-qubit rotations [245], as shown in Fig. 7.1. In practice, however, directly decomposing a target circuit in terms of iSWAP gates is likely to be more efficient and less error-prone than simply replacing every CNOT in an existing circuit with its iSWAP decomposition [90].

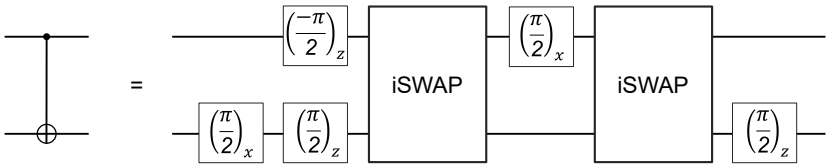

Figure 7.1: Decomposition of CNOT gate into iSWAP and single qubit rotations.

The Bell state creation protocol demonstrated thus far in section 6.4 and in [17, 117] limited the duration of the interaction using global pulses applied to a particular initial state. However, this method cannot be generalized to arbitrary initial states, making it unsuitable for performing useful quantum gates. To realize an iSWAP gate, we need to be able to switch the dipolar interactions on and off and show the desired logic outcomes for arbitrary input states within the computational basis. In this chapter, we achieve this by encoding a qubit in non-interacting hyperfine states of the rotational ground state, which we can transfer to or from the interacting $|e\rangle$ state to toggle the interaction on or off. In Section 7.2 we use this to demonstrate an iSWAP gate between molecular qubits and characterize its truth table.

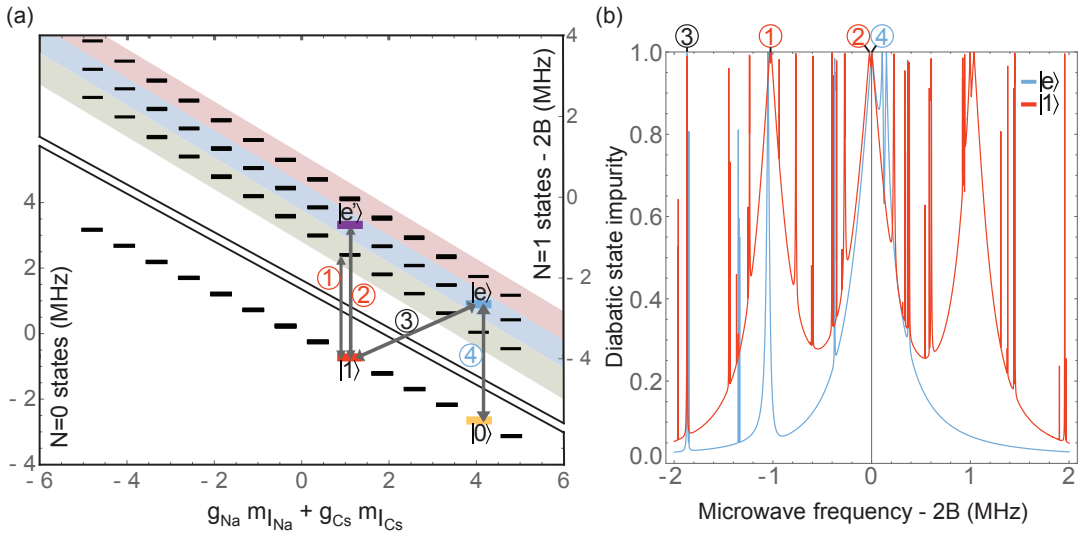

Figure 7.2: (a) Rotational-hyperfine structure of NaCs in the experimental regime. Color-shaded regions denote states of the same rotational sub-level. The x-axis represents the combined nuclear-spin contribution to the Zeeman shift, and is chosen to make the rotational structure apparent. (b) Estimated impurity of the states $|1\rangle$ and $|e\rangle$ when dressed by the microwave field used for the $|1\rangle \leftrightarrow |e\rangle$ transition, which depicts all available transitions from these states. The hyperfine-changing transition, labeled 3, is red-detuned from the $|0\rangle \leftrightarrow |e\rangle$ transition, labelled 4, by 1.9 MHz and comparably narrow. Off-resonant coupling is primarily due to the transitions 1, 2, and 4.

We introduce a third state, $|1\rangle$ (Fig. 7.2), within the ground rotational manifold, which we use to implement the iSWAP gate with a qubit that does not natively interact [203]. The qubit is encoded in a non-interacting hyperfine degree of freedom, which has been shown to be insensitive to external fields and capable of maintaining long coherence times [101, 169, 212]. The state $|1\rangle$ is weakly coupled to $|e\rangle$ by the nuclear quadrupole moment [4].

To identify a suitable hyperfine state to act as the $|1\rangle$ state of the hyperfine storage qubit, we spectroscopically investigated multiple nuclear-spin-changing transitions

from $|e\rangle$. Transitions that change nuclear spin are mediated by the electric quadrupole interaction [4], and are significantly weaker than those which do not. The state $|1\rangle$ was chosen because it is the state furthest detuned from $|0\rangle$ that still has significant coupling to $|e\rangle$, such that off-resonant coupling to $|e'\rangle$—an excited rotational state of the same hyperfine manifold as $|1\rangle$—is suppressed. The full hyperfine structure of NaCs is shown in Fig. 7.2, along with a simulated spectrum of the couplings of the $|1\rangle$ and $|e\rangle$ states under a strong microwave drive.

The interaction is toggled by transferring between $|1\rangle$ and the rotationally excited state $|e\rangle$. Time-evolution of the populations in both states during a microwave pulse on this transition is shown in Fig. 7.3. We note that $|1\rangle$ is also strongly coupled to the excited state $|e'\rangle$ with the same nuclear spin quantum numbers, which is an important consideration for the gate implementation, which is discussed in the following section.

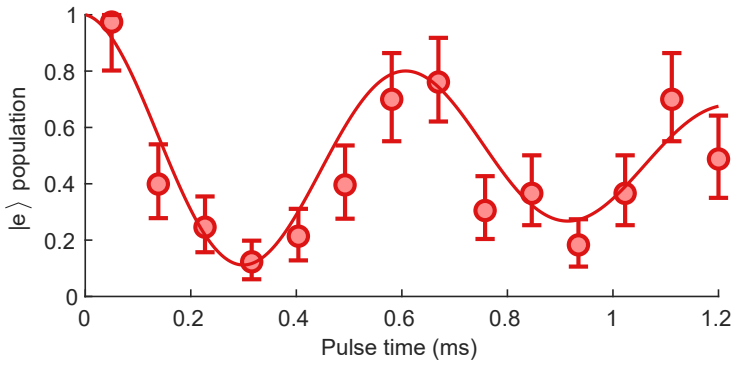

Figure 7.3: (a) Hyperfine-changing microwave pulse from $|e\rangle$ to $|1\rangle$. Fit is a $\cos^2$ function with symmetric exponential decay, giving a π-time of 0.307(9) ms and $1/e$ decay time of 1.2(4) ms.

7.2 iSWAP gate between molecules

We engineered the interaction between qubits using the pulse sequence shown in Fig. 7.4(a). We initialized a pair of molecules in the computational basis at a 5 μm trap separation with site-selective $|0\rangle$ to $|e\rangle$ transfer [216] and a 310 μs square π-pulse from $|e\rangle$ to $|1\rangle$. At 1.9 μm trap separation, we toggled the interaction with the same hyperfine state changing π-pulse ($|1\rangle \leftrightarrow |e\rangle$), and applied a spin-echo pulse on the $|0\rangle \leftrightarrow |e\rangle$ transition in the middle of the interaction period with a duration of 12.83 µs and a truncated Gaussian shape, as in Section 6.4.

For detection, we transferred $|1\rangle$ to $|e\rangle$ at a 5 μm trap separation and read out the $|0\rangle$ and $|e\rangle$ states. In Fig. 7.4(b), we show the dipolar interaction between two qubits initialized in the $|01\rangle$ state. Here, the data are postselected for trials where a pair of molecules are both detected within the qubit subspace. The exchange interaction leads to oscillation between the $|01\rangle$ and $|10\rangle$ states. The full exchange occurs 330 μs after the end of the toggling pulse, shorter than if the pulses were infinitely fast, because the interaction occurs already during the duration of the toggling pulse.

At the full exchange time, the sequence realizes the iSWAP gate up to a global rotation, originating from the spin-echo pulse. The total gate time, composed of the full exchange time and the duration of both toggling pulses, is 960 μs. The unitary corre-

sponding to the ideal implementation in the $(|0\rangle, |1\rangle)$ basis is given by

$$U = \begin{bmatrix} 0 & 0 & 0 & -1 \\ 0 & -i & 0 & 0 \\ 0 & 0 & -i & 0 \\ -1 & 0 & 0 & 0 \end{bmatrix} \tag{7.1}$$

Under the application of this gate, $|01\rangle$ and $|10\rangle$ obtain a non-trivial phase of $-i$ from the dipolar exchange, which is the same phase that we verified via the parity oscillation of the Bell state in Fig. 6.4(b). We characterized the logic outcomes of the iSWAP gate for each computational basis state and show the resulting population truth table in Fig. 7.4(c). For trials where two molecules were detected in the qubit subspace, an average of the probabilities for each input state to transform into the intended output state yields a truth table fidelity [116] of $0.92^{+0.05}_{-0.09}$.

The ease of choosing three states $|0\rangle$, $|1\rangle$, and $|e\rangle$, showcases the versatile structure of molecules, but the dense structure also risks causing leakage outside the computational basis [203]. To take leakage into account, we also normalized the detected outcomes to the population measured in the initial state $|00\rangle$ before performing site-selective state preparation and the iSWAP gate. The corresponding truth table is shown in Fig. 7.4(d) and the resulting truth table fidelity is $0.39^{+0.1}_{-0.09}$.

The current gate fidelity is primarily limited by leakage during four hyperfine-changing pulses, which are needed for state-preparation, the iSWAP gate, and read-out. Rotational transitions that change nuclear spin are two orders of magnitude weaker than those that conserve nuclear spin at a magnetic field of 864 G. The strong

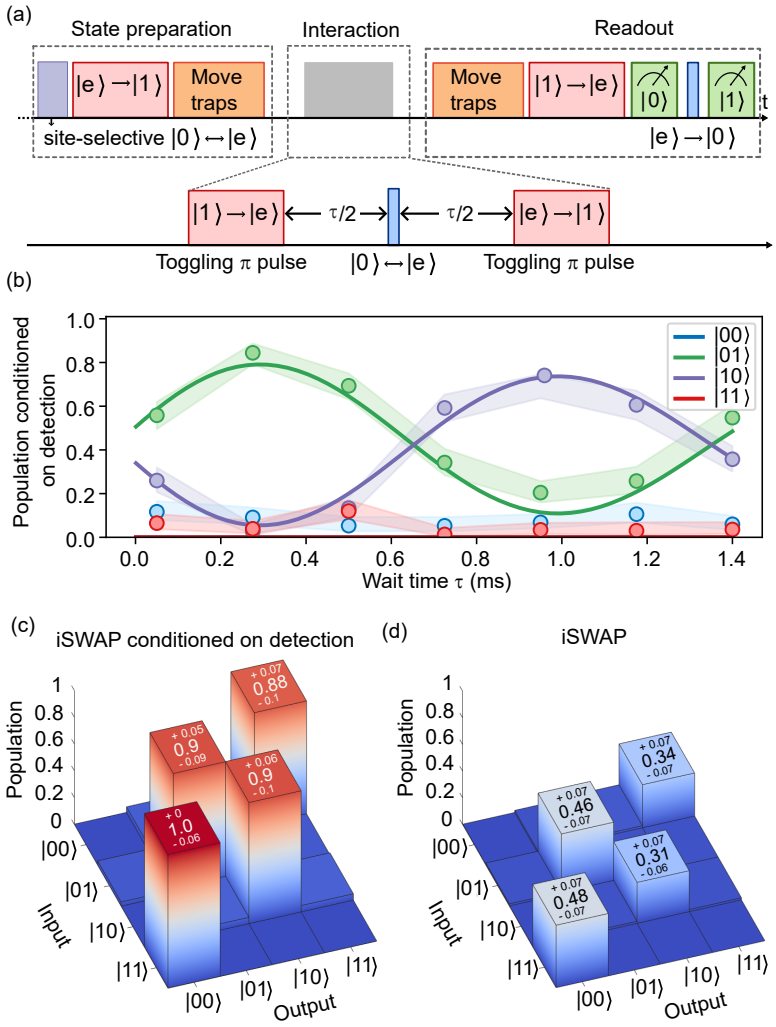

Figure 7.4: (a) Microwave pulse sequence for implementing an iSWAP gate between two hyperfine qubits. (b) Time-evolution of resonant dipolar exchange for a pair of molecules initially prepared in the two-qubit state $|01\rangle$. Solid lines are theory curves from a master equation model, using parameters extracted from the data in Fig. 6.3. (c) Measured truth tables for the full iSWAP gate sequence, showing the probabilities of measuring each two-qubit output state given each input state, conditioned on detection of two molecules in the $(|0\rangle, |1\rangle)$ manifold. This represents the truth table for the entangling interaction with leakage errors caused by the single-qubit gate removed. (d) iSWAP truth table showing the probabilities relative to the probability of detecting the $|00\rangle$ state with no pulses applied. Losses here are dominated by leakage to the $|e\rangle$ state due to imperfect hyperfine-state-changing pulses both during state-preparation and measurement and in the toggling pulses that start and end the gate. Populations detected in all 16 input-output combinations are shown in Fig. 7.5.

microwave pulse required to drive the hyperfine-changing transition introduces off-resonant Stark shifts from nearby transitions making the transfer pulse sensitive to microwave amplitude noise. The Stark shifts specifically from non-magic rotational states fluctuate with trap intensity noise and further decohere the transition. Due to these decoherence sources, the one-way transfer efficiency reported here was limited to 89% (see Fig. 7.3).

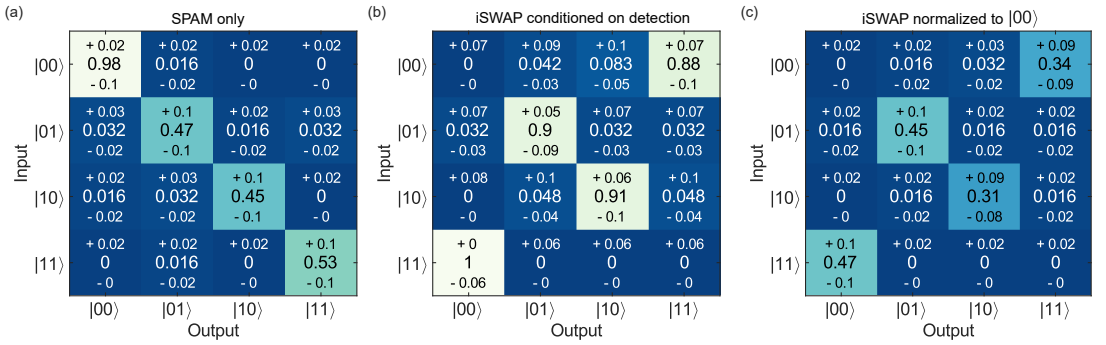

Figure 7.5: Full outcomes of truth table measurements for hyperfine gate. (a) Populations measured in each two-qubit state following state-preparation in that state, relative to population in $|00\rangle$, representing the relative SPAM fidelity of each state. (b) Populations measured in each two-qubit state as a fraction of the total detected molecule population in the $(|0\rangle, |1\rangle)$ manifold for each of the input states to the iSWAP gate. This corrects for leakage to the $|e\rangle$ state during state-preparation and measurement as well as during the hyperfine gate itself. (c) Populations measured in each two-qubit state following application of the iSWAP gate sequence, relative to the initial population in $|00\rangle$ in (a), illustrating the amount lost to leakage.

The hyperfine-changing transfer could be made more coherent with active microwave amplitude stabilization and polarization control. The latter also mitigates depopulation of the $|0\rangle$ state, allowing faster driving of the transition. Another source of leakage is due to interactions during the toggling pulses. We anticipate that 9% of population leaves the computational basis with perfect hyperfine-changing transfer at the current toggling duration. Nevertheless, this leakage may be reduced given the approximately quadratic decrease with pulse duration. Other methods could reduce such

leakage errors, including faster optical or microwave Raman transfers, a lower magnetic field to enhance hyperfine-changing coupling for a faster transfer, and moving traps to toggle the interaction. Both leakage sources described here lead to populations remaining in $|e\rangle$ and $|e'\rangle$, the latter occurring due to the spin-echo pulse. In the future, these populations could be detected without disturbing the computational basis by state-selective transfer to the $N = 2$ rotational states for readout. Such detectable errors may be correctable using erasure conversion schemes [181, 244].

Real truth about it is

No one gets it right

Real truth about it is

We're all supposed to try

Jason Molina, Farewell Transmission

8

Conclusion

8.1 The molecular toolbox

With this thesis, I have sought to bring together our recent work demonstrating a complete set of tools for quantum computation and simulation with ultracold molecules in optical tweezers. In Chapter 3, I described our efforts to find an efficient pathway to the rovibrational ground state of NaCs. This allowed us to achieve a 73(3)% one-way transfer efficiency averaged across an eight molecule array, and opened up the possibility of using either resonant STIRAP or near-detuned Raman transfer, which we used throughout the remaining chapters. In Chapter 4, I detailed our experimental demon-

stration of magic ellipticity trapping of molecules in optical tweezers, which we used to achieve rotational coherence times of up to 250(40) ms with the aid of dynamical decoupling. In Chapter 5, I described our development of new state-preparation and measurement techniques for molecules. Crucially these enabled single-shot readout of multiple molecule rotational states and rearrangement of molecules in an array, leading to a fourfold increase in the rate at which pairs of molecules can be produced in neighboring tweezers. All of these techniques were then put to use in Chapters 6 and 7, in which we demonstrated record high speed and fidelity entanglement of molecules, and a universal two-qubit iSWAP gate between qubits encoded in molecular hyperfine states. With this, we now have a minimally complete toolbox for coherent quantum simulation and computation with individual ultracold molecules, and can turn our attention towards future applications of this system which leverage the distinctive features of molecular qubits.

8.2 Future directions

8.2.1 Quantum simulation and synthetic dimensions

Quantum simulation was among the first quantum science applications envisioned for individually-controlled polar molecules [281]. Pioneering theoretical works 20 years ago proposed to use the anisotropy of the dipolar interaction combined with strong microwave dressing of multiple states to engineer a range of exotic lattice spin models [20, 191]. Subsequent theoretical works have further developed these ideas, proposing concrete ways of using molecules in lattices to engineer states of matter displaying properties such as spin-orbit coupling, topologically protected edge states, and non-

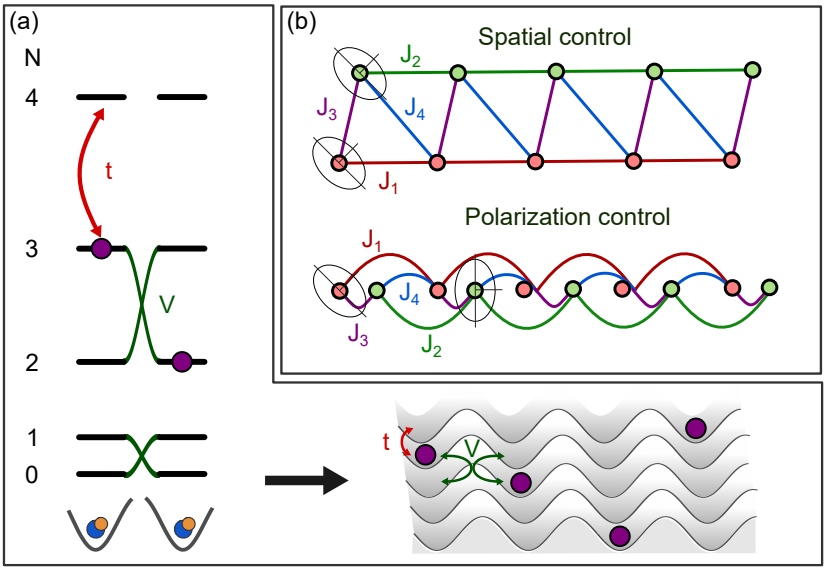

Figure 8.1: Illustration of possible quantum simulation schemes using ultracold molecules in tweezers. (a) Use of multiple rotational levels of molecules in a 1D optical tweezer array as a synthetic dimension to simulate tunneling of bosonic excitations in a 2D lattice, as described in [264]. Red arrows represent single-molecule microwave couplings t corresponding to tunneling along the synthetic dimension, and green lines represent dipole coupling between molecules, corresponding to correlated tunneling of two excitations along the real and synthetic dimensions. (b) Two possible ways of realizing an SSH model using molecules in optical tweezers. Top shows two sub-lattices defined by spatially separating two 1D arrays of tweezers, with the inter- and intra-layer couplings tuned using the relative x and y positions of the arrays, assuming a fixed polarization ellipticity for all sites. Bottom shows a way of defining sub-lattices using two different polarization orientations for even and odd tweezers, allowing the dipole intra- and inter-lattice couplings to be tuned using the polarization angles and the linear separation of the tweezers.

Abelian anyonic excitations [98, 246, 297, 298]. The fully coherent multilevel control of large molecular arrays required to realize the most exotic spin models has not yet been realized, but remarkable experimental progress in this direction has been made in recent years. Dipolar interactions between molecules in an optical lattice were first observed with KRb in [296], and the same experiment has since been used to engineer a tunable XXZ model [167] and t-J model [54]. Interacting NaRb molecules were observed with single-site resolution in an optical lattice in [63], which also demonstrated the

use of Floquet engineering to realize an XXZ model without applying an external field. Other works have begun to explore the strong microwave dressing regime necessary for many of the proposed exotic spin models [20, 98, 191]. Notably, collisional shielding using microwave dressing has been used to produce a Bose-Einstein condensate of NaCs [33] and a degenerate Fermi gas of NaK molecules [236]. Strong microwave dressing has also been used in NaCs to engineer a magic trapping condition for molecules [311].

The site-resolved control of dipolar interactions for molecules in optical tweezers demonstrated in this thesis, as well as in Refs [17, 117], brings us yet closer to realizing the advanced quantum simulations that have been theoretically proposed. The high degree of reconfigurability and single-site control afforded by optical tweezers have already been used to great effect for quantum simulation with Rydberg atoms [242, 244, 248]. Using ultracold molecules, it may be possible even in the near term to engineer models with non-trivial topological characteristics such as the Su–Schrieffer–Heeger (SSH) model [140]. The widely-studied SSH model consists of a lattice composed of two coupled 1D sub-lattices, with different tunneling rates within and between each sub-lattice. In certain ranges of tunneling rates, the system can exhibit topologically-protected edge states [14]. As illustrated in Fig. 8.1(b), ultracold molecules in tweezers could be used to implement an SSH model with rotational excitations acting as hard-core bosons that tunnel via the dipole-dipole interaction [140]. Using the flexibility of the magic ellipticity tweezer platform, coupling strengths in an ultracold molecule SSH model could be controlled in two ways: 1. spatially, by defining two sub-lattices of identical tweezers in a 2D plane and using the separation and angle between them to tune dipolar exchange rates, as demonstrated with Rydberg atoms in

[74]; and 2. via polarization control, defining sub-lattices with different tweezer polarization orientations, allowing the dipolar coupling to be tuned continuously between attractive and repulsive interactions (see Fig. 6.2).

Another promising direction for quantum simulation with ultracold molecules is to use the ladder of rotational states as a "synthetic dimension", treating microwave and dipolar couplings between rotational states as tunneling of a bosonic excitation in a lattice [263]. This allows a real 1D array of molecules to emulate a 2D lattice, or a 2D array to emulate a 3D lattice. Such models are expected to exhibit quantum phase transitions from freely propagating excitations to bound strings or membranes in synthetic space [87, 264]. A 2D synthetic lattice composed of a 1D array of molecules is illustrated in Fig. 8.1. Multiple levels of a molecule can also be used to represent higher-dimensional spins, or even a combination of spin and hole states, as explored in a recent proposal to simulate bosonic $t - J$ models using Floquet engineering of dipole-coupled molecules in optical tweezers [119]. Finally, the coupling of motion and rotation of a molecule via the dipole-dipole interaction, as observed in Section 6.6, could itself be used to study the propagation of phononic excitations through a lattice, potentially leading to topologically interesting states [78]. Entanglement between motional and internal degrees of freedom has recently been studied in bulk samples of KRb molecules [54] and in Rydberg atoms [31, 243], but, overall, it remains a relatively unexplored tool in atomic and molecular physics.

8.2.2 Quantum computing: Qudits and robust encoding

The vast majority of quantum computing research focuses on binary logic, such that the qubit is viewed as the fundamental building block of a quantum computer. Since the early days of the field, however, there has been an undercurrent of interest in harnessing higher dimensional quantum systems [100]. Experimentally, this makes sense: the world itself is not binary, and most physical realizations of qubits are embedded in some kind of multilevel quantum system. There have been attempts to exploit this multilevel structure in various physical platforms, that have been described using different theoretical frameworks depending on the intended purpose of the higher levels. One important framework is the extension of binary quantum logic to d-valued quantum logic [43]. Here, the qubit is replaced by a *qudit*, a d-dimensional quantum system consisting of the states $|0\rangle$, $|1\rangle$, ..., $|d-1\rangle$ that encode a base-d integer. Such an encoding does not *a priori* lead to greater computational power than the binary encoding, but it may, in some cases, allow more efficient implementations of quantum algorithms or error correction protocols [178, 285]. Qudit encodings and key ingredients of qudit-based quantum computation have been demonstrated in a number of experimental systems, including superconducting qubits [199], photons [165], and nuclear spins embedded in crystals and quantum dots [58, 197]. A universal qudit-based quantum processor with up to eight qudits has been demonstrated using trapped ions [223].

One can also envision encoding multiple *virtual* qubits in a single multilevel system [251]. In general, n qubits can be represented by a multilevel system with $d = 2^n$ states [51]. This differs slightly from the qudit concept, since the fundamental design of quantum gates and algorithms remains binary. The physical implementation of the gates

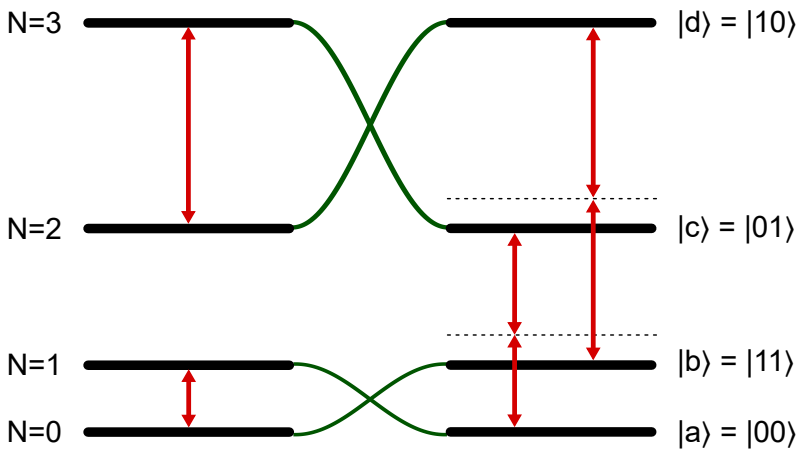

Figure 8.2: Illustration of one possible encoding of quantum information in the first four rotational levels of NaCs in a magic ellipticity optical tweezer. Red arrows illustrate possible one- and two-photon microwave couplings, and green lines represent dipolar coupling the states of different molecules. There is no microwave or dipolar coupling between $N = 1$ and $N = 2$ states in a magic ellipticity tweezer, but couplings to non-magic rotational sublevels allow this gap to be bridged using detuned two-photon microwave pulses. States are labelled by two possible encoding schemes, a qudit encoding with states $|a\rangle$, $|b\rangle$, $|c\rangle$, $|d\rangle$, and a virtual qubit encoding where each level represents a combined state of two qubits labelled.

may change, however, because some two-qubit entangling gates can be realized using transitions between levels within the same physical system. This can be advantageous, potentially allowing lower fidelity gates between physical systems to be replaced by higher fidelity intra-system pulses, and can also potentially lower the total number of gates required for some operations [251]. Such virtual qubit encodings have been demonstrated or shown to be feasible in superconducting, trapped ion, and neutral atom systems [51, 52, 139, 142, 243, 251]. This idea is also closely related to the so-called optical-metastable-ground-state (*omg*) architecture for trapped ion and neutral atom qubits, where transfer of quantum information between different qubit subspaces within a single atom is used for efficient selective addressing and mid-circuit readout of qubits [7, 170].

The rotational-hyperfine structure of bialkali molecules may prove ideal for implementing qudit or virtual qubit encodings [233]. Using either the magic ellipticity or magic wavelength techniques for cancelling light shifts in ultracold molecules allows a magic condition to be achieved simultaneously for many rotational states [102, 225]. Using microwaves to couple higher rotational states would thus allow for arbitrary single-qudit gates. Resonant pairs of rotational states are also generally coupled by the dipole-dipole interaction, meaning that the connectivity for inter-molecule gates remains high. This provides a great deal of flexibility for efficient compilation of quantum circuits into intra- and inter-molecules gates. At the same time, each rotational state also possesses nuclear spin structure, which can be accessed using microwave pulses as demonstrated in Section 7.1. The rotational and hyperfine substructure are relatively uncoupled, meaning that it may be possible to simultaneously transfer information encoded in multiple hyperfine states between rotational levels or even from one molecule to another. One could thus also envision taking the *omg* qubit approach with molecules, using the multilevel structure for local shelving and midcircuit operations [170].

Fig. 8.2 illustrates one possible multilevel encoding of quantum information in the first four rotational levels of NaCs in a magic ellipticity tweezer. Two potential interpretations of this encoding are given: a $d = 4$ qudit interpretation where each rotational level is a single qudit state, and a virtual qubit interpretation where each level encodes a two-qubit state. In a magic ellipticity tweezer, there is no transition dipole moment or dipolar coupling between the $N = 1$ and $N = 2$ magic states. Nevertheless, two-photon detuned microwave pulses that couple to non-magic states can be used to bridge this gap. Both the $N = 0, 1$ and $N = 2, 3$ rotational state pairs are coupled by the inter-

molecular dipole-dipole interaction. Considering the virtual qubit encoding, we can interpret the action of the dipole-dipole interaction sequence demonstrated in Section 6.4 as transforming from the four-qubit product state $|aa\rangle \equiv |0000\rangle$ to the GHZ state

$$\frac{1}{\sqrt{2}}(|aa\rangle + |bb\rangle) \equiv \frac{1}{\sqrt{2}}(|0000\rangle + |1111\rangle).$$

The same interaction sequence applied on the $N = 2$ to $N = 3$ transition starting with the product state $|cc\rangle \equiv |0101\rangle$ would produce another four-qubit cat state:

$$\frac{1}{\sqrt{2}}(|cc\rangle + |dd\rangle) \equiv \frac{1}{\sqrt{2}}(|0101\rangle + |1010\rangle).$$

Both of these four-qubit entangled states can be generated efficiently using only two intra-molecular $\pi/2$-pulses and one inter-molecular $\sqrt{iSWAP}$ dipolar gate.

A related quantum information application of the multilevel structure of molecules is the design of inherently error-robust qubit encodings within single molecules. This approach was pioneered in [3], which proposed a way of encoding GKP-like error correcting codes in the ladder of rotational states of a molecular rotor. Subsequent work in this direction led to the proposal of absorption-emission codes, which are defined as robust encodings of information in a finite, experimentally accessible set of molecular rotational states for error-correction of a family of common spontaneous emission, absorption and dephasing errors [135]. This approach of encoding robust logical qubits in single molecules could, in the long term, prove to be one of their most attractive computational features if it helps solve the scaling issue imposed by the large number of physical qubits required to implement most logical error-correction codes in existing

quantum computers [37].

8.3 Remaining challenges

There is, of course, still significant room both to further expand the existing molecular toolbox and to sharpen our tools. Although the first few demonstrations of entangling gates with molecules ([17, 117] and this thesis) have begun with higher fidelities than comparable early demonstrations in superconducting, trapped ion and neutral atom qubits [132, 218, 240], molecules must also advance more quickly than those platforms did to catch up with the state-of-the-art for quantum science. There are also significant remaining technical challenges to the molecule platform that need to be overcome to allow the sort of rapid scaling demonstrated recently for neutral atom qubits [37, 185, 206]. In this section, I will discuss some key challenges and possible ways to address them.

8.3.1 Array filling

One of the key practical limitations to large-scale quantum computing or simulation with individually trapped molecules is the difficulty of producing densely-filled molecular arrays. In neutral atoms, though arrays are initially stochastically loaded with incomplete filling, it is possible to reliably generate almost defect-free arrays using site-resolved imaging and rearrangement [21, 85]. This method has also been applied to laser-cooled CaF molecules, which can be directly imaged [117]. In Chapter 5, we demonstrated that a similar approach could be applied to coherently-assembled molecules, using imaging of unassociated atoms to locate and remove defects in the

molecular array, allowing us to achieve peak filling fractions of just over 40%. A similar work published in parallel using RbCs was able to produce arrays with approximately 65% peak filling [229]. These filling fractions are dominated by molecule losses during both the forward and backwards ground-state transfer (as well as the molecule trapping lifetime in the RbCs case), which are not detectable since they do not lead to individual atoms remaining trapped in the tweezers. One path towards increasing array filling is thus simply to increase the ground state transfer efficiency. This may require the use of a lower energy and more long-lived intermediate state in the $b^3\Pi$ manifold for two-photon transfer, which was the approach taken by experiments using NaRb and RbCs that achieved over 90% one-way transfer efficiency [195, 299]. Another promising method is to apply one of several recently developed techniques for feedforward cancellation of phase noise in the ground state transfer lasers [55, 168], which have been used to achieve ground state transfer efficiencies as high as 98.7% in RbCs [183]. Alternatively, if a method could be devised for reliable direct detection of molecules with single-site resolution—a challenge discussed more below—then the standard atom rearrangement method could be applied directly to produce arrays with close to unity filling.

Another approach is to attempt to directly produce arrays of molecules with high filling by starting with a large number of molecules at every site and deterministically removing all but one. This bears some similarity to the idea of enhanced loading of atoms using light that couples to the repulsive molecular potential, leading to elastic atomic collisions which can preferentially eject one atom of a pair from a trap (see Section 2.2.1.2). With polar molecules, even nonreactive ones, the challenge of this method

is avoiding rapid loss due to short-range inelastic collision [24]. Repulsive elastic collisions can, in fact, be achieved using the dipole-dipole interaction itself, with the aid of electric field or microwave shielding schemes to guarantee that colliding molecules are coupled to the repulsive arm of the dipolar interaction potential [9, 33, 188, 236]. Tuning of such an engineered repulsive pair interaction could potentially be used in combination with evaporation from an optical trap to produce arrays with a high probability of containing one molecule per site.

8.3.2 Molecule detection

The ability to directly detect molecules in tweezers with both single-site and rotational state resolution would be a powerful experimental tool for quantum science experiments. Indeed, it has already been used to great effect with laser-cooled CaF molecules [10] for rearrangement and erasure conversion in a tweezer array [117, 118]. Coherently assembled molecules cannot in general be non-destructively imaged due to a lack of closed optical cycling transitions. Thus, alternative detection techniques need to be developed. The coherent dissociation and imaging of the molecule's constituent atoms does allow for detection of multiple rotational states, as shown in Chapter 5, but the detection fidelity is limited by the lossy transfer from the rovibrational ground state to the Feshbach state. Even if that transfer is improved significantly, as described above, the technique would still be destructive, making it suitable only for readout of the final state of a quantum circuit or simulation, and not for rearrangement or mid-circuit operations.

A leading candidate method for performing non-destructive molecule detection is

to couple the molecules to a Rydberg atom via either Van der Waals or resonant dipole-dipole interactions [159–161, 306]. Such a coupling could be used to coherently transfer information on the molecular state to the atom for subsequent readout via fluorescence imaging [284, 307]. Such a scheme obviously carries with it some significant experimental overhead in the form of introducing Rydberg atoms into the system. In the case of coherently assembled molecules, however, this can be alleviated by using one of the constituent atoms of the molecule as the Rydberg species. With control over Rydberg-molecule interactions, it would be possible to achieve not only detection of the molecular state but also molecule-Rydberg or Rydberg-mediated molecule-molecule gates [284, 307]. Such a capability could provide useful flexibility to a molecular quantum computing platform, offering the choice during compilation of a quantum circuit between fast Rydberg-mediated gates and slower but potentially very high fidelity molecule-molecule gates [203]. Significant experimental progress has recently been made towards coherent molecule-Rydberg interactions with the observation of the Rydberg blockade effect induced by a single molecule in an optical tweezer [111].

Another possible detection method relies on dispersive imaging of molecules enhanced by coupling to an optical cavity, which could allow minimally destructive readout, although the expected signal-to-noise ratios remain extremely low for the limit of single-molecule detection [109, 234]. Finally, molecules could potentially be detected through quantum Zeno suppression of atom tunneling into a molecule-containing tweezer due to rapid atom-molecule losses through photoassociation [84, 137].

8.3.3 Temperature and coherence

The primary limitation to the fidelity of all currently demonstrated instances of molecule-molecule entanglement has been the finite temperature of the molecules in tweezers. This is an area where coherently-assembled molecules generally possess an advantage over laser-cooled molecules, due to the extremely cold molecule temperatures that can be inherited from Raman-sideband cooled atoms. Nevertheless, in Chapter 6, we found that our molecule-molecule entanglement fidelity was still limited by the axial 34(4)% ground-state fraction of the molecules. Axial motion also limited the fidelity in the first demonstrations of entanglement with CaF molecules, though in that case axial ground state fractions were closer to the $\sim$1% order [17, 117]. CaF molecules in tweezers have subsequently been Raman-sideband cooled to significantly lower temperatures, at the expense of some additional molecule loss to dark states due to imperfect optical pumping [18, 180]. Some small number of Raman-sideband cooling steps could feasibly be applied to bialkali molecules in optical tweezers using, for example, optical pumping via the narrow transition from the rovibrational ground state to the lowest vibrational level of the $b^3\Pi$ state [146, 147]. This would necessarily lead to some molecule loss but could be enough to purify the already cold motional state of the molecules sufficiently to achieve entanglement fidelities of greater than 0.99 (see Section 6.7). As noted in Chapter 6, the measured axial ground state fraction is also lower than expected from the measured atom temperatures and molecule creation efficiency [48], indicating that there may be some additional axial heating process during or after molecule creation that can be identified and eliminated.

After molecule temperature, the next limitation on the molecule-molecule entangle-

ment fidelity in our system is the single-body coherence time of the magic rotational states. In Section 4.6 we discussed several possibilities for the current limitation on the coherence time, including most plausibly tweezer polarization fluctuations and stray electric field noise. Both these effects could be experimentally mitigated in the future, using improved passive or active polarization stabilization and Faraday isolation of the experiment, respectively. Additionally, elimination of tweezer astigmatism would suppress the motion-rotation coupling that prevents us from applying a large number of dynamical decoupling pulses during the molecule entanglement sequence. This would allow us to apply an XY-8 sequence and to extend the single-body coherence time to as long as 250(40) ms.

8.4 Final thoughts

Working with molecules is rarely straightforward—their inherent complexity requires an equally complex set of tools to fully control their quantum state. Even fifteen years ago, this complexity may have seemed an insurmountable barrier. Despite this the work continued, and a host of technical challenges were overcome, enabling the significant leaps forward in molecular control that we have seen in the last few years. In the same way that a cold atom MOT went from a Nobel-prize-winning innovation to a product that can be bought off-the -shelf, we can hope that many of the challenges that have taken years for early single-molecule experiments to overcome will in the future be viewed as manageable complexities with standard solutions. As a result, it may soon to be possible for experimentalists to dive in earnest into the varied and complex physical applications of ultracold molecules. So far, we have barely scratched the surface.

A

Motion-rotation coupling simulation

This appendix describes the methods used to simulate the dynamics of molecules in tweezers in the presence of motion-rotation coupling in Chapter 6. The method described here was devised by Ana Maria Rey and David Wellnitz. The simulations were written by David Wellnitz in the Julia programming language [30] using the KrylovKit package [112]. The details of the simulation are included here for completeness, and can also be found in Ref. [215].

To simulate the dynamics with motion-rotation coupling, we used a combination of discrete variable representation (DVR) and exact diagonalization. We computed the local electromagnetic field of a single tweezer in the presence of astigmatism following

Ref. [254]. Of the primary aberrations, astigmatism and coma produce displacement of the $|0\rangle$ and $|e\rangle$ states in the axial and radial directions, respectively, by altering the ellipticity of the tweezer polarization at the focus. The local energy of the two states was determined from their polarizabilities α_0 and $\alpha_0 + \alpha_2 \frac{1-3\cos(2\chi)}{10}$, where α_0 and α_2 are the theoretical scalar and tensor polarizabilities of NaCs in a 1064 nm tweezer [278]. We identified the position of minimal energy, corresponding to the point of maximum intensity for $|0\rangle$, by gradient descent.

This gave us a DVR of the potential energy, from which we got the DVR Hamiltonian $\hat{H}_{\text{motion},0/e}$ for each rotational state following Ref. [67]. We numerically computed the n lowest motional eigenenergies and corresponding eigenstates of each rotational state. We chose the tweezer depth to match the numerically extracted level spacing to the experimentally measured value of $h \times 4.95$ kHz.

To compute the two-body Hamiltonian of dimension $4n^2$, we replaced the fixed molecule positions $\hat{r}_{ij}$ of equation 6.7 with an integral over the positions of both molecules in states $|0\rangle$ and $|e\rangle$,

$$\hat{H}_{\text{DD}} = \frac{1}{2}\int d^3\vec{r}_i d^3\vec{r}_j \frac{1-3\cos^2(\theta)}{4\pi\varepsilon_0|\vec{r}_i-\vec{r}_j|^3}(\hat{\psi}_e^\dagger(\vec{r}_i)\hat{\psi}_0^\dagger(\vec{r}_j)\hat{\psi}_e(\vec{r}_j)\hat{\psi}_0(\vec{r}_i) + h.c.) \tag{A.1}$$

We then projected this Hamiltonian into the low-energy eigenstates, where we replaced integrals with sums over discrete grid values. Analogously, we also projected the pulse/drive Hamiltonian

$$\hat{H}_{\text{pulse}} = \frac{\Omega}{2}|0\rangle\langle e| + \frac{\Omega^*}{2}|e\rangle\langle 0| + \Delta|e\rangle\langle e| \tag{A.2}$$

into the DVR basis, which couples different motional levels according to their state overlap. We chose Δ such that the microwave pulse is exactly in resonance $\Delta = -\langle\psi_0|\hat{H}_{\text{motion},e}|\psi_0\rangle + \langle\psi_0|\hat{H}_{\text{motion},0}|\psi_0\rangle$, where $|\psi_0\rangle$ is the ground state of $\hat{H}_{\text{motion},0}$. We numerically verified that residual detuning $\lesssim h \times 1\,\text{kHz}$ is removed by spin-echo.

Finally, we included a phenomenological single-molecule dephasing term with a rate γ_{deph} described by the Lindblad operators

$$\hat{L}_j = \sqrt{\frac{\gamma_{\text{deph}}}{2}}(|e\rangle\langle e|_j - |0\rangle\langle 0|_j)\,. \tag{A.3}$$

For the single-molecule simulations, we further included motional dephasing modeled by the diagonal matrix

$$\hat{L}_{\text{motion},j} = \sqrt{2\gamma_{\text{motion}}}\begin{pmatrix} 1 & 0 & \cdots & 0 \\ 0 & 2 & \cdots & 0 \\ \vdots & \vdots & \ddots & \vdots \\ 0 & 0 & \cdots & n \end{pmatrix}. \tag{A.4}$$

We then propagated the resulting master equation in real time to reproduce the experimental data. We ignored any dephasing that occurs during the pulses for simplicity, which is expected to be insignificant for pulse durations $\sim 10\mu$s, but kept dipolar interactions on during the pulses.

To make the two-particle simulations more efficient, we ignored off-diagonal elements between motional states whose energies differed by more than $h \times 200$ Hz when computing the lines for Fig. 6.3. Since the coupling between these manifolds due to

dipolar interactions is $\lesssim h \times 10$ Hz close to the ground state, this only affects dynamics during pulses. It removes small oscillations with an amplitude of a few percent, smaller than experimental error bars, from the theory curves.

In all simulations, we set $\Omega = h \times 38$ kHz, $\gamma_{\text{deph}} = 1/(80\text{ ms})$, and $R = 1.79\ \mu$m, with the separation set slightly smaller than the experimentally measured value to match the observed interaction rate for a molecule frame dipole moment $d = 4.6$ D. We chose a temperature-dependent cutoff for the number of motional eigenstates included in the simulations. For the single-molecule simulations, we chose the cutoffs $n = 30$ $[0.6 \leq \hbar\omega_{\text{ax}}/(k_B T)]$; $n = 40$ $[0.4 \leq \hbar\omega_{\text{ax}}/(k_B T) < 0.6]$; $n = 50$ $[\hbar\omega_{\text{ax}}/(k_B T) < 0.4]$. For the two-molecule simulations in Fig. 6.3, we set $n = 30$.

References

[1] Abraham, E. R. I., Ritchie, N. W. M., McAlexander, W. I., & Hulet, R. G. (1995). Photoassociative spectroscopy of long-range states of ultracold $^6Li_2$ and $^7Li_2$. *J. Chem. Phys.*, 103(18), 7773.

[2] Aikawa, K., Frisch, A., Mark, M., Baier, S., Rietzler, A., Grimm, R., & Ferlaino, F. (2012). Bose-Einstein condensation of erbium. *Phys. Rev. Lett.*, 108(21), 210401.

[3] Albert, V. V., Covey, J. P., & Preskill, J. (2020). Robust Encoding of a Qubit in a Molecule. *Phys. Rev. X*, 10(3), 031050.

[4] Aldegunde, J. & Hutson, J. M. (2017). Hyperfine structure of alkali-metal diatomic molecules. *Phys. Rev. A*, 96, 042506.

[5] Aldegunde, J., Ran, H., & Hutson, J. (2009). Manipulating ultracold polar molecules with microwave radiation: The influence of hyperfine structure. *Phys. Rev. A*, 80(4), 043410.

[6] Aliyu, M. M., Zhao, L., Quek, X. Q., Yellapragada, K. C., & Loh, H. (2021). D 1 magic wavelength tweezers for scaling atom arrays. *Phys. Rev. Res.*, 3(4), 043059.

[7] Allcock, D. T. C., Campbell, W. C., Chiaverini, J., Chuang, I. L., Hudson, E. R., Moore, I. D., Ransford, A., Roman, C., Sage, J. M., & Wineland, D. J. (2021). omg blueprint for trapped ion quantum computing with metastable states. *Applied Physics Letters*, 119(21), 214002.

[8] Anderegg, L., Augenbraun, B. L., Chae, E., Hemmerling, B., Hutzler, N. R., Ravi, A., Collopy, A., Ye, J., Ketterle, W., & Doyle, J. M. (2017). Radio frequency magneto-optical trapping of CaF with high density. *Phys. Rev. Lett.*, 119, 103201.

[9] Anderegg, L., Burchesky, S., Bao, Y., Yu, S. S., Karman, T., Chae, E., Ni, K.-K., Ketterle, W., & Doyle, J. M. (2021). Observation of microwave shielding of ultracold molecules. *Science*, 373(6556), 779–782.

[10] Anderegg, L., Cheuk, L. W., Bao, Y., Burchesky, S., Ketterle, W., Ni, K.-K., & Doyle, J. M. (2019). An optical tweezer array of ultracold molecules. *Science*, 365(6458), 1156–1158.

[11] Anderson, M. H., Ensher, J. R., Matthews, M. R., Wieman, C. E., & Cornell, E. A. (1995). Observation of bose-einstein condensation in a dilute atomic vapor. *Science*, 269(5221), 198–201.

[12] Andreev, V., Ang, D. G., DeMille, D., Doyle, J. M., Gabrielse, G., Haefner, J., Hutzler, N. R., Lasner, Z., Meisenhelder, C., O'Leary, B. R., Panda, C. D., West, A. D., West, E. P., & Wu, X. (2018). Improved limit on the electric dipole moment of the electron. *Nature*, 562(7727), 355–360.

[13] Arora, B., Safronova, M. S., & Clark, C. W. (2007). Determination of electric-dipole matrix elements in K and Rb from stark shift measurements. *Phys. Rev. A*, 76(5), 052516.

[14] Asbóth, J. K., Oroszlány, L., & Pályi, A. (2016). The Su-Schrieffer-Heeger (SSH) Model. In J. K. Asbóth, L. Oroszlány, & A. Pályi (Eds.), *A Short Course on Topological Insulators: Band Structure and Edge States in One and Two Dimensions* (pp. 1–22). Cham: Springer International Publishing.

[15] Aymar, M. & Dulieu, O. (2005). Calculation of accurate permanent dipole moments of the lowest $^{1,3}\Sigma^+$ states of heteronuclear alkali dimers using extended basis sets. *J. Chem. Phys.*, 122(20), 204302.

[16] Balakrishnan, N. (2016). Perspective: Ultracold molecules and the dawn of cold controlled chemistry. *J. Chem. Phys.*, 145(15), 150901.

[17] Bao, Y., Yu, S. S., Anderegg, L., Chae, E., Ketterle, W., Ni, K.-K., & Doyle, J. M. (2023). Dipolar spin-exchange and entanglement between molecules in an optical tweezer array. *Science*, 382(6675), 1138–1143.

[18] Bao, Y., Yu, S. S., You, J., Anderegg, L., Chae, E., Ketterle, W., Ni, K.-K., & Doyle, J. M. (2024). Raman Sideband Cooling of Molecules in an Optical Tweezer Array to the 3D Motional Ground State. *Phys. Rev. X*, 14(3), 031002.

[19] Barakhshan, P., Marrs, A., Bhosale, A., Arora, B., Eigenmann, R., & Safronova, M. S. (2022). Portal for high-precision atomic data and computation (version 2.0). University of Delaware, Newark, DE, USA. URL: https://www.udel.edu/atom [February 2022.].

[20] Barnett, R., Petrov, D., Lukin, M., & Demler, E. (2006). Quantum Magnetism with Multicomponent Dipolar Molecules in an Optical Lattice. *Phys. Rev. Lett.*, 96(19), 190401.

[21] Barredo, D., de Léséleuc, S., Lienhard, V., Lahaye, T., & Browaeys, A. (2016). An atom-by-atom assembler of defect-free arbitrary two-dimensional atomic arrays. *Science*, 354(6315), 1021–1023.

[22] Barry, J. F., McCarron, D. J., Norrgard, E. B., Steinecker, M. H., & DeMille, D. (2014). Magneto-optical trapping of a diatomic molecule. *Nature*, 512(7514), 286–289.

[23] Barry, J. F., Shuman, E. S., Norrgard, E. B., & DeMille, D. (2012). Laser Radiation Pressure Slowing of a Molecular Beam. *Phys. Rev. Lett.*, 108(10), 103002.

[24] Bause, R., Christianen, A., Schindewolf, A., Bloch, I., & Luo, X.-Y. (2023). Ultracold Sticky Collisions: Theoretical and Experimental Status. *The Journal of Physical Chemistry A*, 127(3), 729–741.

[25] Bause, R., Kamijo, A., Chen, X.-Y., Duda, M., Schindewolf, A., Bloch, I., & Luo, X.-Y. (2021). Efficient conversion of closed-channel-dominated Feshbach molecules of ^{23}Na^{40}K to their absolute ground state. *Phys. Rev. A*, 104(4), 043321.

[26] Bause, R., Li, M., Schindewolf, A., Chen, X.-Y., Duda, M., Kotochigova, S., Bloch, I., & Luo, X.-Y. (2020). Tune-out and magic wavelengths for ground-state ^{23}Na^{40}K molecules. *Phys. Rev. Lett.*, 125, 023201.

[27] Bell, M. T. & Softley, T. P. (2009). Ultracold molecules and ultracold chemistry. *Molecular Physics*, 107(2), 99–132.

[28] Bethlem, H. L., Berden, G., Crompvoets, F. M. H., Jongma, R. T., van Roij, A. J. A., & Meijer, G. (2000). Electrostatic trapping of ammonia molecules. *Nature*, 406(6795), 491–494.

[29] Bethlem, H. L., Berden, G., & Meijer, G. (1999). Decelerating neutral dipolar molecules. *Phys. Rev. Lett.*, 83(8), 1558.

[30] Bezanson, J., Edelman, A., Karpinski, S., & Shah, V. B. (2017). Julia: A fresh approach to numerical computing. *SIAM Review*, 59(1), 65–98.

[31] Bharti, V., Sugawa, S., Kunimi, M., Chauhan, V. S., Mahesh, T. P., Mizoguchi, M., Matsubara, T., Tomita, T., de Léséleuc, S., & Ohmori, K. (2024). Strong Spin-Motion Coupling in the Ultrafast Dynamics of Rydberg Atoms.

[32] Bigagli, N., Warner, C., Yuan, W., Zhang, S., Stevenson, I., Karman, T., & Will, S. (2023). Collisionally stable gas of bosonic dipolar ground-state molecules. *Nature Physics*, 19(11), 1579–1584.

[33] Bigagli, N., Yuan, W., Zhang, S., Bulatovic, B., Karman, T., Stevenson, I., & Will, S. (2024). Observation of Bose–Einstein condensation of dipolar molecules. *Nature*, 631, 289–293.

[34] Blackmore, J. A., Gregory, P. D., Bromley, S. L., & Cornish, S. L. (2020a). Coherent manipulation of the internal state of ultracold $^{87}Rb^{133}Cs$ molecules with multiple microwave fields. *Physical Chemistry Chemical Physics*, 22, 27529–27538.

[35] Blackmore, J. A., Gregory, P. D., Hutson, J. M., & Cornish, S. L. (2023). Diatomic-py: A Python module for calculating the rotational and hyperfine structure of $^1\Sigma$ molecules. *Computer Physics Communications*, 282, 108512.

[36] Blackmore, J. A., Sawant, R., Gregory, P. D., Bromley, S. L., Aldegunde, J., Hutson, J. M., & Cornish, S. L. (2020b). Controlling the ac Stark effect of RbCs with dc electric and magnetic fields. *Phys. Rev. A*, 102(5), 053316.

[37] Bluvstein, D., Evered, S. J., Geim, A. A., Li, S. H., Zhou, H., Manovitz, T., Ebadi, S., Cain, M., Kalinowski, M., Hangleiter, D., Ataides, J. P. B., Maskara, N., Cong, I., Gao, X., Rodriguez, P. S., Karolyshyn, T., Semeghini, G., Gullans, M. J., Greiner, M., Vuletić, V., & Lukin, M. D. (2023). Logical quantum processor based on reconfigurable atom arrays. *Nature*, 624, 1–3.

[38] Bluvstein, D., Levine, H., Semeghini, G., Wang, T. T., Ebadi, S., Kalinowski, M., Keesling, A., Maskara, N., Pichler, H., Greiner, M., Vuletić, V., & Lukin, M. D. (2022). A quantum processor based on coherent transport of entangled atom arrays. *Nature*, 604(7906), 451–456.

[39] Bohn, J. L. (2009). Electric Dipoles at Ultralow Temperatures. In *Cold Molecules*. CRC Press.

[40] Boradjiev, I. I. & Vitanov, N. V. (2013). Control of qubits by shaped pulses of finite duration. *Phys. Rev. A*, 88(1), 013402.

[41] Born, M. & Wolf, E. (1980). *Principles of Optics, 6th ed.* Cambridge University Press.

[42] Bremner, M. J., Dawson, C. M., Dodd, J. L., Gilchrist, A., Harrow, A. W., Mortimer, D., Nielsen, M. A., & Osborne, T. J. (2002). Practical Scheme for Quantum Computation with Any Two-Qubit Entangling Gate. *Phys. Rev. Lett.*, 89(24), 247902.

[43] Brennen, G., O'Leary, D., & Bullock, S. (2005). Criteria for exact qudit universality. *Phys. Rev. A*, 71(5), 052318.

[44] Brookes, S. G. H. & Hutson, J. M. (2022). Interaction Potential for NaCs for Ultracold Scattering and Spectroscopy. *The Journal of Physical Chemistry A*, 126(25), 3987–4001.

[45] Brown, J. M. & Carrington, A. (2003). *Rotational Spectroscopy of Diatomic Molecules*. Cambridge Molecular Science. Cambridge: Cambridge University Press.

[46] Brown, M., Thiele, T., Kiehl, C., Hsu, T.-W., & Regal, C. (2019). Gray-Molasses Optical-Tweezer Loading: Controlling Collisions for Scaling Atom-Array Assembly. *Phys. Rev. X*, 9(1), 011057.

[47] Burchesky, S., Anderegg, L., Bao, Y., Yu, S. S., Chae, E., Ketterle, W., Ni, K.-K., & Doyle, J. M. (2021). Rotational Coherence Times of Polar Molecules in Optical Tweezers. *Phys. Rev. Lett.*, 127(12), 123202.

[48] Cairncross, W. B., Zhang, J. T., Picard, L. R. B., Yu, Y., Wang, K., & Ni, K.-K. (2021). Assembly of a rovibrational ground state molecule in an optical tweezer. *Phys. Rev. Lett.*, 126, 123402.

[49] Campbell, W. C. & Doyle, J. M. (2009). Cooling, Trap Loading, and Beam Production Using a Cryogenic Helium Buffer Gas. In *Cold Molecules*. CRC Press.

[50] Campbell, W. C. & Hudson, E. R. (2020). Dipole-phonon quantum logic with trapped polar molecular ions. *Phys. Rev. Lett.*, 125, 120501.

[51] Campbell, W. C. & Hudson, E. R. (2022). Polyqubit quantum processing. arXiv:2210.15484.

[52] Cao, S., Bakr, M., Campanaro, G., Fasciati, S. D., Wills, J., Lall, D., Shteynas, B., Chidambaram, V., Rungger, I., & Leek, P. (2024). Emulating two qubits with a four-level transmon qudit for variational quantum algorithms. *Quantum Science and Technology*, 9(3), 035003.

[53] Cappellaro, P. (2012). Cambridge MA. MIT OpenCourseWare.

[54] Carroll, A. N., Hirzler, H., Miller, C., Wellnitz, D., Muleady, S. R., Lin, J., Zamarski, K. P., Wang, R. R. W., Bohn, J. L., Rey, A. M., & Ye, J. (2024). Observation of generalized t-j spin dynamics with tunable dipolar interactions.

[55] Chao, Y.-X., Hua, Z.-X., Liang, X.-H., Yue, Z.-P., You, L., & Tey, M. K. (2024). Pound–Drever–Hall feedforward: laser phase noise suppression beyond feedback. *Optica*, 11(7), 945–950.

[56] Chen, X.-Y., Biswas, S., Eppelt, S., Schindewolf, A., Deng, F., Shi, T., Yi, S., Hilker, T. A., Bloch, I., & Luo, X.-Y. (2024). Ultracold field-linked tetratomic molecules. *Nature*, 626(7998), 283–287.

[57] Chew, Y., Tomita, T., Mahesh, T. P., Sugawa, S., de Léséleuc, S., & Ohmori, K. (2022). Ultrafast energy exchange between two single Rydberg atoms on a nanosecond timescale. *Nature Photonics*, 16(10), 724–729.

[58] Chicco, S., Allodi, G., Chiesa, A., Garlatti, E., Buch, C. D., Santini, P., De Renzi, R., Piligkos, S., & Carretta, S. (2024). Proof-of-Concept Quantum Simulator Based on Molecular Spin Qudits. *Journal of the American Chemical Society*, 146(1), 1053–1061.

[59] Chomaz, L., Ferrier-Barbut, I., Ferlaino, F., Laburthe-Tolra, B., Lev, B. L., & Pfau, T. (2023). Dipolar physics: a review of experiments with magnetic quantum gases. *Reports on Progress in Physics*, 86(2), 026401.

[60] Chotia, A., Neyenhuis, B., Moses, S. A., Yan, B., Covey, J. P., Foss-Feig, M., Rey, A. M., Jin, D. S., & Ye, J. (2012). Long-Lived Dipolar Molecules and Feshbach Molecules in a 3D Optical Lattice. *Phys. Rev. Lett.*, 108(8), 080405.

[61] Chou, C.-W., Kurz, C., Hume, D. B., Plessow, P. N., Leibrandt, D. R., & Leibfried, D. (2017). Preparation and coherent manipulation of pure quantum states of a single molecular ion. *Nature*, 545(7653), 203–207.

[62] Chow, M. N. H., Little, B. J., & Jau, Y.-Y. (2023). High-fidelity low-loss state detection of alkali-metal atoms in optical tweezer traps. *Phys. Rev. A*, 108, 032407.

[63] Christakis, L., Rosenberg, J. S., Raj, R., Chi, S., Morningstar, A., Huse, D. A., Yan, Z. Z., & Bakr, W. S. (2023). Probing site-resolved correlations in a spin system of ultracold molecules. *Nature*, 614(7946), 64–69.

[64] Cirac, J. I. & Zoller, P. (1995). Quantum Computations with Cold Trapped Ions. *Phys. Rev. Lett.*, 74(20), 4091–4094.

[65] Cleeton, C. E. & Williams, N. H. (1934). Electromagnetic Waves of 1.1 cm Wave-Length and the Absorption Spectrum of Ammonia. *Physical Review*, 45(4), 234–237.

[66] Clopper, C. J. & Pearson, E. S. (1934). The use of confidence or fiducial limits illustrated in the case of the binomial. *Biometrika*, 26(4), 404–413.

[67] Colbert, D. T. & Miller, W. H. (1992). A novel discrete variable representation for quantum mechanical reactive scattering via the S-matrix Kohn method. *J. Chem. Phys.*, 96(3), 1982–1991.

[68] Collett, E. (2005). *Field Guide to Polarization*. SPIE Press.

[69] Colzi, G., Durastante, G., Fava, E., Serafini, S., Lamporesi, G., & Ferrari, G. (2016). Sub-doppler cooling of sodium atoms in gray molasses. *Phys. Rev. A*, 93, 023421.

[70] Cooper, A., Covey, J. P., Madjarov, I. S., Porsev, S. G., Safronova, M. S., & Endres, M. (2018). Alkaline-Earth Atoms in Optical Tweezers. *Phys. Rev. X*, 8(4), 041055.

[71] Danzl, J. G., Haller, E., Gustavsson, M., Mark, M. J., Hart, R., Bouloufa, N., Dulieu, O., Ritsch, H., & Nägerl, H.-C. (2008). Quantum gas of deeply bound ground state molecules. *Science*, 321(5892), 1062–1066.

[72] Davis, K. B., Mewes, M. O., Andrews, M. R., van Druten, N. J., Durfee, D. S., Kurn, D. M., & Ketterle, W. (1995). Bose-Einstein Condensation in a Gas of Sodium Atoms. *Phys. Rev. Lett.*, 75(22), 3969–3973.

[73] de Léséleuc, S., Barredo, D., Lienhard, V., Browaeys, A., & Lahaye, T. (2017). Optical Control of the Resonant Dipole-Dipole Interaction between Rydberg Atoms. *Phys. Rev. Lett.*, 119(5), 053202.

[74] de Léséleuc, S., Lienhard, V., Scholl, P., Barredo, D., Weber, S., Lang, N., Büchler, H. P., Lahaye, T., & Browaeys, A. (2019). Observation of a symmetry-protected topological phase of interacting bosons with Rydberg atoms. *Science*, 365(6455), 775–780.

[75] De Marco, L., Valtolina, G., Matsuda, K., Tobias, W. G., Covey, J. P., & Ye, J. (2019). A degenerate fermi gas of polar molecules. *Science*, 363(6429), 853–856.

[76] Deiß, M., Willitsch, S., & Hecker Denschlag, J. (2024). Cold trapped molecular ions and hybrid platforms for ions and neutral particles. *Nature Physics*, 20(5), 713–721.

[77] DeMille, D. (2002). Quantum computation with trapped polar molecules. *Phys. Rev. Lett.*, 88(6), 067901.

[78] Di Liberto, M., Kruckenhauser, A., Zoller, P., & Baranov, M. A. (2022). Topological phonons in arrays of ultracold dipolar particles. *Quantum*, 6, 731.

[79] Di Rosa, M. D. (2004). Laser-cooling molecules - concept, candidates, and supporting hyperfine-resolved measurements of rotational lines in the A-X(0,0) band of CaH. *Eur. Phys. J. D*, 31, 395.

[80] Docenko, O., Tamanis, M., Zaharova, J., Ferber, R., Pashov, A., Knöckel, H., & Tiemann, E. (2006). The coupling of the $X^1\Sigma^+$ and $a^3\Sigma^+$ states of the atom pair Na + Cs and modelling cold collisions. *Journal of Physics B: Atomic, Molecular and Optical Physics*, 39(19), S929–S943.

[81] Durr, S., Volz, T., Marte, A., & Rempe, G. (2004). Observation of molecules produced from a bose-einstein condensate. *Phys. Rev. Lett.*, 92(2), 020406.

[82] Ecker, S., Sohr, P., Bulla, L., Ursin, R., & Bohmann, M. (2022). Remotely Establishing Polarization Entanglement Over Noisy Polarization Channels. *Phys. Rev. Applied*, 17(3), 034009.

[83] Efron, B. & Tibshirani, R. J. (1994). *An Introduction to the Bootstrap*. New York.

[84] Elkamshishy, A. A. & Greene, C. H. (2023). Triatomic Photoassociation in an Ultracold Atom–Molecule Collision. *The Journal of Physical Chemistry A*, 127(1), 18–28.

[85] Endres, M., Bernien, H., Keesling, A., Levine, H., Anschuetz, E. R., Krajenbrink, A., Senko, C., Vuletic, V., Greiner, M., & Lukin, M. D. (2016). Atom-by-atom assembly of defect-free one-dimensional cold atom arrays. *Science*, 354(6315), 1024–1027.

[86] Estermann, I. (1946). Molecular Beam Technique. *Reviews of Modern Physics*, 18(3), 300–323.

[87] Feng, C., Manetsch, H., Rousseau, V. G., Hazzard, K. R. A., & Scalettar, R. (2022). Quantum membrane phases in synthetic lattices of cold molecules or Rydberg atoms. *Phys. Rev. A*, 105(6), 063320.

[88] Finkelstein, R., Tsai, R. B.-S., Sun, X., Scholl, P., Direkci, S., Gefen, T., Choi, J., Shaw, A. L., & Endres, M. (2024). Universal quantum operations and ancilla-based readout for tweezer clocks. arXiv:2402.16220.

[89] Fioretti, A., Comparat, D., Crubellier, A., Dulieu, O., & Pillet, F. M.-S. P. (1998). Formation of cold Cs_2 molecules through photoassociation. *Phys. Rev. Lett.*, 80(20), 4402.

[90] Foxen, B., Neill, C., Dunsworth, A., Roushan, P., Chiaro, B., Megrant, A., Kelly, J., Chen, Z., Satzinger, K., Barends, R., Arute, F., Arya, K., Babbush, R., Bacon, D., Bardin, J., Boixo, S., Buell, D., Burkett, B., Chen, Y., Collins, R., Farhi, E., Fowler, A., Gidney, C., Giustina, M., Graff, R., Harrigan, M., Huang, T., Isakov, S., Jeffrey, E., Jiang, Z., Kafri, D., Kechedzhi, K., Klimov, P., Korotkov, A., Kostritsa, F., Landhuis, D., Lucero, E., McClean, J., McEwen, M., Mi, X., Mohseni, M., Mutus, J., Naaman, O., Neeley, M., Niu, M., Petukhov, A., Quintana, C., Rubin, N., Sank, D., Smelyanskiy, V., Vainsencher, A., White, T., Yao, Z., Yeh, P., Zalcman, A., Neven, H., Martinis, J., & Google AI Quantum (2020). Demonstrating a Continuous Set of Two-qubit Gates for Near-term Quantum Algorithms. *Phys. Rev. Lett.*, 125(12), 120504.

[91] Franzen, A. (2006). ComponentLibrary: a free vector graphics library for optics. www.gwoptics.org/ComponentLibrary/.

[92] Freericks, J. K., Maśka, M. M., Hu, A., Hanna, T. M., Williams, C. J., Julienne, P. S., & Lemański, R. (2010). Improving the efficiency of ultracold dipolar molecule formation by first loading onto an optical lattice. *Phys. Rev. A*, 81(1), 011605.

[93] Friesicke, C. & Rohrdantz, B. (2015). inkscape schematic symbols.

[94] Gershenfeld, N. A. & Chuang, I. L. (1997). Bulk Spin-Resonance Quantum Computation. *Science*, 275(5298), 350–356.

[95] Gilmore, K. A., Affolter, M., Lewis-Swan, R. J., Barberena, D., Jordan, E., Rey, A. M., & Bollinger, J. J. (2021). Quantum-enhanced sensing of displacements and electric fields with two-dimensional trapped-ion crystals. *Science*, 373(6555), 673–678.

[96] Gordon, J. P., Zeiger, H. J., & Townes, C. H. (1955). The Maser—New Type of Microwave Amplifier, Frequency Standard, and Spectrometer. *Physical Review*, 99(4), 1264–1274.

[97] Gordy, W. (1948). Microwave Spectroscopy. *Reviews of Modern Physics*, 20(4), 668–717.

[98] Gorshkov, A. V., Hazzard, K. R., & Rey, A. M. (2013). Kitaev honeycomb and other exotic spin models with polar molecules. *Molecular Physics*, 111(12-13), 1908–1916.

[99] Gorshkov, A. V., Manmana, S. R., Chen, G., Ye, J., Demler, E., Lukin, M. D., & Rey, A. M. (2011). Tunable superfluidity and quantum magnetism with ultracold polar molecules. *Phys. Rev. Lett.*, 107, 115301.

[100] Gottesman, D. (1999). Fault-Tolerant Quantum Computation with Higher-Dimensional Systems. In C. P. Williams (Ed.), *Quantum Computing and Quantum Communications* (pp. 302–313). Berlin, Heidelberg: Springer.

[101] Gregory, P. D., Blackmore, J. A., Bromley, S. L., Hutson, J. M., & Cornish, S. L. (2021). Robust storage qubits in ultracold polar molecules. *Nature Physics*, 17(10), 1149–1153.

[102] Gregory, P. D., Fernley, L. M., Tao, A. L., Bromley, S. L., Stepp, J., Zhang, Z., Kotochigova, S., Hazzard, K. R. A., & Cornish, S. L. (2024). Second-scale rotational coherence and dipolar interactions in a gas of ultracold polar molecules. *Nature Physics*.

[103] Griesmaier, A., Werner, J., Hensler, S., Stuhler, J., & Pfau, T. (2005). Bose-Einstein Condensation of Chromium. *Phys. Rev. Lett.*, 94(16), 160401.

[104] Grochola, A., Kowalczyk, P., & Jastrzebski, W. (2010). Investigation of the $B^1\Pi$ state in NaCs by polarisation labelling spectroscopy. *Chemical Physics Letters*, 497(1-3), 22–25.

[105] Grochola, A., Kowalczyk, P., Szczepkowski, J., Jastrzebski, W., Wakim, A., Zabawa, P., & Bigelow, N. P. (2011). Spin-forbidden $c^3\Sigma^+ \leftarrow X^1\Sigma^+$ transition in NaCs: Investigation of the $\Omega = 1$ state in hot and cold environments. *Phys. Rev. A*, 84, 012507.

[106] Grynberg, G. & Courtois, J.-Y. (1994). Proposal for a Magneto-Optical Lattice for Trapping Atoms in Nearly-Dark States. *Europhysics Letters (EPL)*, 27(1), 41–46.

[107] Grünzweig, T., Hilliard, A., McGovern, M., & Andersen, M. F. (2010). Near-deterministic preparation of a single atom in an optical microtrap. *Nature Physics*, 6(12), 951–954.

[108] Guan, Q., Cornish, S. L., & Kotochigova, S. (2021). Magic conditions for multiple rotational states of bialkali molecules in optical lattices. *Phys. Rev. A*, 103, 043311.

[109] Guan, Q., Highman, M., Meier, E. J., Williams, G. R., Scarola, V., DeMarco, B., Kotochigova, S., & Gadway, B. (2020). Nondestructive dispersive imaging of rotationally excited ultracold molecules. *Physical Chemistry Chemical Physics*, 22(36), 20531–20544.

[110] Guo, M., Vexiau, R., Zhu, B., Lu, B., Bouloufa-Maafa, N., Dulieu, O., & Wang, D. (2017). High-resolution molecular spectroscopy for producing ultracold absolute-ground-state $^{23}Na^{87}Rb$ molecules. *Phys. Rev. A*, 96, 052505.

[111] Guttridge, A., Ruttley, D. K., Baldock, A. C., González-Férez, R., Sadeghpour, H. R., Adams, C. S., & Cornish, S. L. (2023). Observation of rydberg blockade due to the charge-dipole interaction between an atom and a polar molecule. *Phys. Rev. Lett.*, 131, 013401.

[112] Haegeman, J. (2024). Krylovkit.

[113] He, X., Wang, K., Zhuang, J., Xu, P., Gao, X., Guo, R., Sheng, C., Liu, M., Wang, J., Li, J., Shlyapnikov, G. V., & Zhan, M. (2020). Coherently forming a single molecule in an optical trap. *Science*, 370, 331–335.

[114] Hemmerling, B., Chae, E., Ravi, A., Anderegg, L., Drayna, G. K., Hutzler, N. R., Collopy, A. L., Ye, J., Ketterle, W., & Doyle, J. M. (2016). Laser slowing of CaF molecules to near the capture velocity of a molecular MOT. *Journal of Physics B: Atomic, Molecular and Optical Physics*, 49(17), 174001.

[115] Herbig, J., Kraemer, T., Mark, M., Weber, T., Chin, C., Nägerl, H.-C., & Grimm, R. (2003). Preparation of a Pure Molecular Quantum Gas. *Science*, 301(5639), 1510–1513.

[116] Hofmann, H. F. (2005). Complementary classical fidelities as an efficient criterion for the evaluation of experimentally realized quantum operations. *Phys. Rev. Lett.*, 94, 160504.

[117] Holland, C. M., Lu, Y., & Cheuk, L. W. (2023). On-demand entanglement of molecules in a reconfigurable optical tweezer array. *Science*, 382(6675), 1143–1147.

[118] Holland, C. M., Lu, Y., Li, S. J., Welsh, C. L., & Cheuk, L. W. (2024). Demonstration of Erasure Conversion in a Molecular Tweezer Array. arXiv:2406.02391.

[119] Homeier, L., Harris, T. J., Blatz, T., Geier, S., Hollerith, S., Schollwöck, U., Grusdt, F., & Bohrdt, A. (2024). Antiferromagnetic bosonic t-j models and their quantum simulation in tweezer arrays. *Phys. Rev. Lett.*, 132, 230401.

[120] Hope, J. J. & Close, J. D. (2005). General limit to nondestructive optical detection of atoms. *Phys. Rev. A*, 71(4), 043822.

[121] Hsiao, Y.-F., Lin, Y.-J., & Chen, Y.-C. (2018). Λ-enhanced gray-molasses cooling of cesium atoms on the D_2 line. *Phys. Rev. A*, 98(3), 033419.

[122] Hu, M.-G., Liu, Y., Grimes, D. D., Lin, Y.-W., Gheorghe, A. H., Vexiau, R., Bouloufa-Maafa, N., Dulieu, O., Rosenband, T., & Ni, K.-K. (2019). Direct observation of bimolecular reactions of ultracold KRb molecules. *Science*, 366(6469), 1111–1115.

[123] Hu, M.-G., Liu, Y., Nichols, M. A., Zhu, L., Quéméner, G., Dulieu, O., & Ni, K.-K. (2021). Nuclear spin conservation enables state-to-state control of ultracold molecular reactions. *Nature Chemistry*, 13, 435–440.

[124] Hudson, E. R., Gilfoy, N. B., Kotochigova, S., Sage, J. M., & DeMille, D. (2008). Inelastic Collisions of Ultracold Heteronuclear Molecules in an Optical Trap. *Phys. Rev. Lett.*, 100(20), 203201.

[125] Hummon, M. T., Yeo, M., Stuhl, B. K., Collopy, A. L., Xia, Y., & Ye, J. (2013). 2D Magneto-Optical Trapping of Diatomic Molecules. *Phys. Rev. Lett.*, 110(14), 143001.

[126] Hutson, J. M. (1994). Coupled channel methods for solving the bound-state Schrödinger equation. *Computer Physics Communications*, 84(1), 1–18.

[127] Hutson, J. M. & Le Sueur, C. R. (2019). molscat: A program for non-reactive quantum scattering calculations on atomic and molecular collisions. *Computer Physics Communications*, 241, 9–18.

[128] Hutson, J. M., Tiesinga, E., & Julienne, P. S. (2008). Avoided crossings between bound states of ultracold cesium dimers. *Phys. Rev. A*, 78(5), 052703.

[129] Hutzler, N. R. (2020). Polyatomic molecules as quantum sensors for fundamental physics. *Quantum Science and Technology*, 5(4), 044011.

[130] Hutzler, N. R., Liu, L. R., Yu, Y., & Ni, K.-K. (2017). Eliminating light shifts for single atom trapping. *New J. Phys.*, 19(2), 023007.

[131] Hutzler, N. R., Lu, H.-I., & Doyle, J. M. (2012). The Buffer Gas Beam: An Intense, Cold, and Slow Source for Atoms and Molecules. *Chemical Reviews*, 112(9), 4803–4827.

[132] Isenhower, L., Urban, E., Zhang, X. L., Gill, A. T., Henage, T., Johnson, T. A., Walker, T. G., & Saffman, M. (2010). Demonstration of a Neutral Atom Controlled-NOT Quantum Gate. *Phys. Rev. Lett.*, 104(1), 010503.

[133] Itano, W. M., Bergquist, J. C., & Wineland, D. J. (1987). Laser Spectroscopy of Trapped Atomic Ions. *Science*, 237(4815), 612–617.

[134] Ivanov, S. S. & Vitanov, N. V. (2015). Composite two-qubit gates. *Phys. Rev. A*, 92(2), 022333.

[135] Jain, S. P., Hudson, E. R., Campbell, W. C., & Albert, V. V. (2023). \AE\ codes.

[136] Jaksch, D., Cirac, J. I., Zoller, P., Rolston, S. L., Côté, R., & Lukin, M. D. (2000). Fast Quantum Gates for Neutral Atoms. *Phys. Rev. Lett.*, 85(10), 2208–2211.

[137] Jamadagni, A., Ospelkaus, S., Santos, L., & Weimer, H. (2021). Quantum zeno-based detection and state engineering of ultracold polar molecules. *Phys. Rev. Res.*, 3, 033208.

[138] Jankunas, J. & Osterwalder, A. (2015). Cold and Controlled Molecular Beams: Production and Applications. *Annual Review of Physical Chemistry*, 66(1), 241–262.

[139] Jia, Z., Huie, W., Li, L., Sun, W. K. C., Hu, X., Aakash, Kogan, H., Karve, A., Lee, J. Y., & Covey, J. P. (2024). An architecture for two-qubit encoding in neutral ytterbium-171 atoms. arXiv:2402.13134.

[140] Jiang, J., Zhang, J.-H., Mei, F., Ji, Z., Hu, Y., Ma, J., Xiao, L., & Jia, S. (2022). Topological phases of ultracold molecules in an optical tweezer ladder. *Phys. Rev. A*, 106(2), 023318.

[141] Jones, J. A. & Mosca, M. (1998). Implementation of a quantum algorithm on a nuclear magnetic resonance quantum computer. *The Journal of Chemical Physics*, 109(5), 1648–1653.

[142] Kiktenko, E. O., Fedorov, A. K., Man'ko, O. V., & Man'ko, V. I. (2015). Multilevel superconducting circuits as two-qubit systems: Operations, state preparation, and entropic inequalities. *Phys. Rev. A*, 91(4), 042312.

[143] Kim, H., Han, H. S., & Cho, D. (2013). Magic polarization for optical trapping of atoms without stark-induced dephasing. *Phys. Rev. Lett.*, 111, 243004.

[144] Kjaergaard, M., Schwartz, M. E., Braumüller, J., Krantz, P., Wang, J. I.-J., Gustavsson, S., & Oliver, W. D. (2020). Superconducting Qubits: Current State of Play. *Annual Review of Condensed Matter Physics*, 11, 369–395.

[145] Kleinert, J., Haimberger, C., Zabawa, P. J., & Bigelow, N. P. (2007). Trapping of Ultracold Polar Molecules with a Thin-Wire Electrostatic Trap. *Phys. Rev. Lett.*, 99(14), 143002.

[146] Kobayashi, J., Aikawa, K., Oasa, K., & Inouye, S. (2014). Prospects for narrow-line cooling of KRb molecules in the rovibrational ground state. *Phys. Rev. A*, 89(2), 021401.

[147] Kobayashi, J., Ogino, A., & Inouye, S. (2015). Ultracold molecular spectroscopy: toward the narrow-line cooling of molecules. *New Journal of Physics*, 17(3), 035013.

[148] Kohler, T., Goral, K., & Julienne, P. S. (2006). Production of cold molecules via magnetically tunable Feshbach resonances. *Rev. Mod. Phys.*, 78(4), 1311.

[149] Koller, A. P., Mundinger, J., Wall, M. L., & Rey, A. M. (2015). Demagnetization dynamics of noninteracting trapped fermions. *Phys. Rev. A*, 92(3), 033608.

[150] Kondov, S. S., Lee, C.-H., Leung, K. H., Liedl, C., Majewska, I., Moszynski, R., & Zelevinsky, T. (2019). Molecular lattice clock with long vibrational coherence. *Nature Physics*, 15(11), 1118–1122.

[151] Korek, M., Bleik, S., & Allouche, A. R. (2007). Theoretical calculation of the low laying electronic states of the molecule NaCs with spin-orbit effect. *J. Chem. Phys.*, 126(12), 124313.

[152] Kotlar, A. J., Field, R. W., Steinfeld, J. I., & Coxon, J. A. (1980). Analysis of perturbations in the $A^2\Pi^+X^2\Sigma^+$ "Red" system of CN. *Journal of Molecular Spectroscopy*, 80(1), 86–108.

[153] Kotochigova, S. & DeMille, D. (2010). Electric-field-dependent dynamic polarizability and state-insensitive conditions for optical trapping of diatomic polar molecules. *Phys. Rev. A*, 82, 063421.

[154] Kowalczyk, P. (1989). High resolution laser spectroscopy of the $c^3\Sigma^+ \leftarrow X^1\Sigma^+$ and $b^3\Pi \leftarrow X^1\Sigma^+$ forbidden transitions in NaK. *The Journal of Chemical Physics*, 91(5), 2779–2789.

[155] Kraemer, M. & Baur, T. G. (2018). Extinction ratio measurements on high purity linear polarizers. In D. B. Chenault & D. H. Goldstein (Eds.), *Polarization: Measurement, Analysis, and Remote Sensing XIII* (pp.4). Orlando, United States: SPIE.

[156] Krämer, S., Plankensteiner, D., Ostermann, L., & Ritsch, H. (2018). QuantumOptics.jl: A Julia framework for simulating open quantum systems. *Computer Physics Communications*, 227, 109–116.

[157] Krems, R. V. (2008). Cold controlled chemistry. *Physical Chemistry Chemical Physics*, 10(28), 4079.

[158] Krems, R. V. (2018). *Molecules in Electromagnetic Fields: From Ultracold Physics to Controlled Chemistry*. Wiley, 1 edition.

[159] Kuznetsova, E., Rittenhouse, S. T., Beterov, I. I., Scully, M. O., Yelin, S. F., & Sadeghpour, H. R. (2018). Effective spin-spin interactions in bilayers of Rydberg atoms and polar molecules. *Phys. Rev. A*, 98(4), 043609.

[160] Kuznetsova, E., Rittenhouse, S. T., Sadeghpour, H. R., & Yelin, S. F. (2011). Rydberg atom mediated polar molecule interactions: a tool for molecular-state conditional quantum gates and individual addressability. *Physical Chemistry Chemical Physics*, 13(38), 17115.

[161] Kuznetsova, E., Rittenhouse, S. T., Sadeghpour, H. R., & Yelin, S. F. (2016). Rydberg-atom-mediated nondestructive readout of collective rotational states in polar-molecule arrays. *Phys. Rev. A*, 94(3), 032325.

[162] La Porta, A. & Wang, M. D. (2004). Optical Torque Wrench: Angular Trapping, Rotation, and Torque Detection of Quartz Microparticles. *Phys. Rev. Lett.*, 92(19), 190801.

[163] Labuhn, H., Ravets, S., Barredo, D., Béguin, L., Nogrette, F., Lahaye, T., & Browaeys, A. (2014). Single-atom addressing in microtraps for quantum-state engineering using Rydberg atoms. *Phys. Rev. A*, 90(2), 023415.

[164] Lang, F., Winkler, K., Strauss, C., Grimm, R., & Hecker Denschlag, J. (2008). Ultracold triplet molecules in the rovibrational ground state. *Phys. Rev. Lett.*, 101, 133005.

[165] Lanyon, B. P., Barbieri, M., Almeida, M. P., Jennewein, T., Ralph, T. C., Resch, K. J., Pryde, G. J., O'Brien, J. L., Gilchrist, A., & White, A. G. (2009). Simplifying quantum logic using higher-dimensional Hilbert spaces. *Nature Physics*, 5(2), 134–140.

[166] Lett, P. D., Helmerson, K., Phillips, W. D., Ratliff, L. P., Rolston, S., & Wagshul, M. E. (1993). Spectroscopy of Na_2 by photoassociation of laser-cooled Na. *Phys. Rev. Lett.*, 71(14), 2200.

[167] Li, J.-R., Matsuda, K., Miller, C., Carroll, A. N., Tobias, W. G., Higgins, J. S., & Ye, J. (2023). Tunable itinerant spin dynamics with polar molecules. *Nature*, 614(7946), 70–74.

[168] Li, L., Huie, W., Chen, N., DeMarco, B., & Covey, J. P. (2022). Active Cancellation of Servo-Induced Noise on Stabilized Lasers via Feedforward. *Phys. Rev. Applied*, 18(6), 064005.

[169] Lin, J., He, J., Jin, M., Chen, G., & Wang, D. (2022). Seconds-scale coherence on nuclear spin transitions of ultracold polar molecules in 3d optical lattices. *Phys. Rev. Lett.*, 128, 223201.

[170] Lis, J. W., Senoo, A., McGrew, W. F., Rönchen, F., Jenkins, A., & Kaufman, A. M. (2023). Midcircuit Operations Using the omg Architecture in Neutral Atom Arrays. *Phys. Rev. X*, 13(4), 041035.

[171] Liu, L. (2019). *Building Single Molecules – Reactions, Collisions, and Spectroscopy of Two Atoms*. PhD thesis, Harvard University.

[172] Liu, L., Hood, J., Yu, Y., Zhang, J., Wang, K., Lin, Y.-W., Rosenband, T., & Ni, K.-K. (2019). Molecular Assembly of Ground-State Cooled Single Atoms. *Phys. Rev. X*, 9(2), 021039.

[173] Liu, L. R., Hood, J. D., Yu, Y., Zhang, J. T., Hutzler, N. R., Rosenband, T., & Ni, K.-K. (2018). Building one molecule from a reservoir of two atoms. *Science*, 360(6391), 900–903.

[174] Liu, W., Dong, D., Yang, H., Gong, Q., & Shi, K. (2020a). Robust and high-speed rotation control in optical tweezers by using polarization synthesis based on heterodyne interference. *Opto-Electronic Advances*, 3(8), 200022.

[175] Liu, W., Wu, J., Ma, J., Li, P., Sovkov, V. B., Xiao, L., & Jia, S. (2016). Observation and analysis of the hyperfine structure of near-dissociation levels of the NaCs c $^3\Sigma^+$ state below the dissociation limit 3 $S_{1/2}$ + 6 $P_{3/2}$. *Phys. Rev. A*, 94(3), 032518.

[176] Liu, Y., Hu, M.-G., Nichols, M. A., Grimes, D. D., Karman, T., Guo, H., & Ni, K.-K. (2020b). Photo-excitation of long-lived transient intermediates in ultracold reactions. *Nat. Phys.*, 16, 1132–1136.

[177] Lloyd, S. (1993). A Potentially Realizable Quantum Computer. *Science*, 261(5128), 1569–1571.

[178] Low, P. J., White, B., & Senko, C. (2023). Control and readout of a 13-level trapped ion qudit. arXiv:2306.03340.

[179] Lu, M., Burdick, N. Q., Youn, S. H., & Lev, B. L. (2011). Strongly Dipolar Bose-Einstein Condensate of Dysprosium. *Phys. Rev. Lett.*, 107(19), 190401.

[180] Lu, Y., Li, S. J., Holland, C. M., & Cheuk, L. W. (2024). Raman sideband cooling of molecules in an optical tweezer array. *Nature Physics*, 20(3), 389–394.

[181] Ma, S., Liu, G., Peng, P., Zhang, B., Jandura, S., Claes, J., Burgers, A. P., Pupillo, G., Puri, S., & Thompson, J. D. (2023). High-fidelity gates and mid-circuit erasure conversion in an atomic qubit. *Nature*, 622(7982), 279–284.

[182] Ma, X., Jackson, T., Zhou, H., Chen, J., Lu, D., Mazurek, M. D., Fisher, K. A. G., Peng, X., Kribs, D., Resch, K. J., Ji, Z., Zeng, B., & Laflamme, R. (2016). Pure-state tomography with the expectation value of Pauli operators. *Phys. Rev. A*, 93(3), 032140.

[183] Maddox, B. P., Mortlock, J. M., Hepworth, T. R., Raghuram, A. P., Gregory, P. D., Guttridge, A., & Cornish, S. L. (2024). Enhanced quantum state transfer via feed-forward cancellation of optical phase noise. arXiv:2407.09119.

[184] Madjarov, I. S., Covey, J. P., Shaw, A. L., Choi, J., Kale, A., Cooper, A., Pichler, H., Schkolnik, V., Williams, J. R., & Endres, M. (2020). High-fidelity entanglement and detection of alkaline-earth Rydberg atoms. *Nature Physics*, 16(8), 857–861.

[185] Manetsch, H. J., Nomura, G., Bataille, E., Leung, K. H., Lv, X., & Endres, M. (2024). A tweezer array with 6100 highly coherent atomic qubits. arXiv:2403.12021.

[186] Martinelli, M., Martelli, P., & Pietralunga, S. M. (2006). Polarization Stabilization in Optical Communications Systems. *Journal of Lightwave Technology*, 24(11), 4172–4183.

[187] Martinez-Dorantes, M., Alt, W., Gallego, J., Ghosh, S., Ratschbacher, L., & Meschede, D. (2018). State-dependent fluorescence of neutral atoms in optical potentials. *Phys. Rev. A*, 97, 023410.

[188] Matsuda, K., De Marco, L., Li, J.-R., Tobias, W. G., Valtolina, G., Quéméner, G., & Ye, J. (2020). Resonant collisional shielding of reactive molecules using electric fields. *Science*, 370(6522), 1324–1327.

[189] Maxwell, S. E., Brahms, N., deCarvalho, R., Glenn, D. R., Helton, J. S., Nguyen, S. V., Patterson, D., Petricka, J., DeMille, D., & Doyle, J. M. (2005). High-Flux Beam Source for Cold, Slow Atoms or Molecules. *Phys. Rev. Lett.*, 95(17), 173201.

[190] Menicucci, N. C. & Caves, C. M. (2002). Local realistic model for the dynamics of bulk-ensemble NMR information processing. *Phys. Rev. Lett.*, 88, 167901.

[191] Micheli, A., Brennen, G., & Zoller, P. (2006). A toolbox for lattice-spin models with polar molecules. *Nat. Phys.*, 2(5), 341.

[192] Mies, F. H., Tiesinga, E., & Julienne, P. S. (2000). Manipulation of Feshbach resonances in ultracold atomic collisions using time-dependent magnetic fields. *Phys. Rev. A*, 61, 022721.

[193] Miller, J. D., Cline, R. A., & Heinzen, D. J. (1993). Photoassociation spectrum of ultracold Rb atoms. *Phys. Rev. Lett.*, 71(14), 2204.

[194] Mitra, D., Leung, K. H., & Zelevinsky, T. (2022). Quantum control of molecules for fundamental physics. *Phys. Rev. A*, 105(4), 040101.

[195] Molony, P. K., Gregory, P. D., Kumar, A., Le Sueur, C. R., Hutson, J. M., & Cornish, S. L. (2016). Production of Ultracold ^{87}Rb^{133}Cs in the Absolute Ground State: Complete Characterisation of the Stimulated Raman Adiabatic Passage Transfer. *ChemPhysChem*, 17(22), 3811–3817.

[196] Monroe, C. & Kim, J. (2013). Scaling the Ion Trap Quantum Processor. *Science*, 339(6124), 1164–1169.

[197] Moro, F., Fielding, A. J., Turyanska, L., & Patanè, A. (2019). Realization of Universal Quantum Gates with Spin-Qudits in Colloidal Quantum Dots. *Advanced Quantum Technologies*, 2(10), 1900017.

[198] Moszynski, R. & González-Férez, R. (2020). Private communication.

[199] Neeley, M., Ansmann, M., Bialczak, R. C., Hofheinz, M., Lucero, E., O'Connell, A. D., Sank, D., Wang, H., Wenner, J., Cleland, A. N., Geller, M. R., & Martinis, J. M. (2009). Emulation of a Quantum Spin with a Superconducting Phase Qudit. *Science*, 325(5941), 722–725.

[200] Neyenhuis, B., Yan, B., Moses, S. A., Covey, J. P., Chotia, A., Petrov, A., Kotochigova, S., Ye, J., & Jin, D. S. (2012). Anisotropic polarizability of ultracold polar ^{40}K^{87}Rb molecules. *Phys. Rev. Lett.*, 109, 230403.

[201] Ni, K.-K. (2022). Fully controlled individual diatomic polar molecules for quantum science. In *Bulletin of the American Physical Society*, volume 67(7) Orlando, Florida.

[202] Ni, K.-K., Ospelkaus, S., de Miranda, M. H. G., Pe'er, A., Neyenhuis, B., Zirbel, J. J., Kotochigova, S., Julienne, P. S., Jin, D. S., & Ye, J. (2008). A High Phase-Space-Density Gas of Polar Molecules. *Science*, 322(5899), 231–235.

[203] Ni, K.-K., Rosenband, T., & Grimes, D. D. (2018). Dipolar exchange quantum logic gate with polar molecules. *Chem. Sci.*, 9, 6830–6838.

[204] Nielsen, M. & Chuang, I. (2000). *Quantum Computation and Quantum Information*.

[205] Nikolov, B., Diamond-Hitchcock, E., Bass, J., Spong, N. L. R., & Pritchard, J. D. (2023). Randomized Benchmarking Using Nondestructive Readout in a Two-Dimensional Atom Array. *Phys. Rev. Lett.*, 131(3), 030602.

[206] Norcia, M. A., Kim, H., Cairncross, W. B., Stone, M., Ryou, A., Jaffe, M., Brown, M. O., Barnes, K., Battaglino, P., Bohdanowicz, T. C., Brown, A., Cassella, K., Chen, C.-A., Coxe, R., Crow, D., Epstein, J., Griger, C., Halperin, E., Hummel, F., Jones, A. M. W., Kindem, J. M., King, J., Kotru, K., Lauigan, J., Li, M., Lu, M., Megidish, E., Marjanovic, J., McDonald, M., Mittiga, T., Muniz, J. A., Narayanaswami, S., Nishiguchi, C., Paule, T., Pawlak, K. A., Peng, L. S., Pudenz, K. L., Rodríguez Pérez, D., Smull, A., Stack, D., Urbanek, M., Van De Veerdonk, R. J. M., Vendeiro, Z., Wadleigh, L., Wilkason, T., Wu, T.-Y., Xie, X., Zalys-Geller, E., Zhang, X., & Bloom, B. J. (2024). Iterative Assembly of 171 Yb Atom Arrays with Cavity-Enhanced Optical Lattices. *PRX Quantum*, 5(3), 030316.

[207] Norcia, M. A., Young, A. W., & Kaufman, A. M. (2018). Microscopic control and detection of ultracold strontium in optical-tweezer arrays. *Phys. Rev. X*, 8, 041054.

[208] Ocola, P. L., Dimitrova, I., Grinkemeyer, B., Guardado-Sanchez, E., Đorđević, T., Samutpraphoot, P., Vuletić, V., & Lukin, M. D. (2024). Control and Entanglement of Individual Rydberg Atoms near a Nanoscale Device. *Phys. Rev. Lett.*, 132(11), 113601.

[209] Ospelkaus, C., Ospelkaus, S., Humbert, L., Ernst, P., Sengstock, K., & Bongs, K. (2006). Ultracold Heteronuclear Molecules in a 3D Optical Lattice. *Phys. Rev. Lett.*, 97(12), 120402.

[210] Park, A. J., Picard, L. R., Patenotte, G. E., Zhang, J. T., Rosenband, T., & Ni, K.-K. (2023a). Extended Rotational Coherence of Polar Molecules in an Elliptically Polarized Trap. *Phys. Rev. Lett.*, 131(18), 183401.

[211] Park, J. J., Lu, Y.-K., Jamison, A. O., Tscherbul, T. V., & Ketterle, W. (2023b). A Feshbach resonance in collisions between triplet ground-state molecules. *Nature*, 614(7946), 54–58.

[212] Park, J. W., Yan, Z. Z., Loh, H., Will, S. A., & Zwierlein, M. W. (2017). Second-scale nuclear spin coherence time of ultracold $^{23}Na^{40}K$ molecules. *Science*, 357(6349), 372–375.

[213] Penninckx, D., Beck, N., Gleyze, J.-F., & Videau, L. (2006). Signal Propagation Over Polarization-Maintaining Fibers: Problem and Solutions. *Journal of Lightwave Technology*, 24(11), 4197–4207.

[214] Phillips, W. D. (1998). Nobel Lecture: Laser cooling and trapping of neutral atoms. *Reviews of Modern Physics*, 70(3), 721.

[215] Picard, L. R. B., Park, A. J., Patenotte, G. E., Gebretsadkan, S., Wellnitz, D., Rey, A. M., & Ni, K.-K. (2024a). Sub-millisecond Entanglement and iSWAP Gate between Molecular Qubits. arXiv:2406.15345.

[216] Picard, L. R. B., Patenotte, G. E., Park, A. J., Gebretsadkan, S. F., & Ni, K.-K. (2024b). Site-Selective Preparation and Multistate Readout of Molecules in Optical Tweezers. *PRX Quantum*, 5(2), 020344.

[217] Picard, L. R. B., Zhang, J. T., Cairncross, W. B., Wang, K., Patenotte, G. E., Park, A. J., Yu, Y., Liu, L. R., Hood, J. D., González-Férez, R., & Ni, K.-K. (2023). High resolution photoassociation spectroscopy of the excited $c^3\Sigma_1^+$ potential of $^{23}Na^{133}Cs$. *Phys. Rev. Research*, 5(2), 023149.

[218] Plantenberg, J. H., De Groot, P. C., Harmans, C. J. P. M., & Mooij, J. E. (2007). Demonstration of controlled-NOT quantum gates on a pair of superconducting quantum bits. *Nature*, 447(7146), 836–839.

[219] Rabl, P., DeMille, D., Doyle, J. M., Lukin, M. D., Schoelkopf, R. J., & Zoller, P. (2006). Hybrid Quantum Processors: molecular ensembles as quantum memory for solid state circuits. *Phys. Rev. Lett.*, 97(3).

[220] Ramsey, N. F. (1956). *Molecular Beams*.

[221] Regal, C. A., Ticknor, C., Bohn, J. L., & Jin, D. S. (2003). Creation of ultracold molecules from a Fermi gas of atoms. *Nature*, 424, 47.

[222] Reinaudi, G., Osborn, C. B., McDonald, M., Kotochigova, S., & Zelevinsky, T. (2012). Optical production of stable ultracold $^{88}Sr_2$ molecules. *Phys. Rev. Lett.*, 109, 115303.

[223] Ringbauer, M., Meth, M., Postler, L., Stricker, R., Blatt, R., Schindler, P., & Monz, T. (2022). A universal qudit quantum processor with trapped ions. *Nature Physics*, 18(9), 1053–1057.

[224] Rio Fernandes, D., Sievers, F., Kretzschmar, N., Wu, S., Salomon, C., & Chevy, F. (2012). Sub-Doppler laser cooling of fermionic ^{40} K atoms in three-dimensional gray optical molasses. *EPL (Europhysics Letters)*, 100(6), 63001.

[225] Rosenband, T., Grimes, D. D., & Ni, K.-K. (2018). Elliptical polarization for molecular stark shift compensation in deep optical traps. *Opt. Express*, 26(16), 19821–19825.

[226] Rosenberg, J. S., Christakis, L., Guardado-Sanchez, E., Yan, Z. Z., & Bakr, W. S. (2022). Observation of the Hanbury Brown–Twiss effect with ultracold molecules. *Nature Physics*, 18(9), 1062–1066.

[227] Rosi, S., Burchianti, A., Conclave, S., Naik, D. S., Roati, G., Fort, C., & Minardi, F. (2018). Λ-enhanced grey molasses on the D2 transition of Rubidium-87 atoms. *Scientific Reports*, 8(1), 1301.

[228] Roussy, T. S., Caldwell, L., Wright, T., Cairncross, W. B., Shagam, Y., Ng, K. B., Schlossberger, N., Park, S. Y., Wang, A., Ye, J., & Cornell, E. A. (2023). An improved bound on the electron's electric dipole moment. *Science*, 381(6653), 46–50.

[229] Ruttley, D. K., Guttridge, A., Hepworth, T. R., & Cornish, S. L. (2024). Enhanced Quantum Control of Individual Ultracold Molecules Using Optical Tweezer Arrays. *PRX Quantum*, 5(2), 020333.

[230] Ruttley, D. K., Guttridge, A., Spence, S., Bird, R. C., Le Sueur, C. R., Hutson, J. M., & Cornish, S. L. (2023). Formation of ultracold molecules by merging optical tweezers. *Phys. Rev. Lett.*, 130, 223401.

[231] Sackett, C. A., Kielpinski, D., King, B. E., Langer, C., Meyer, V., Myatt, C. J., Rowe, M., Turchette, Q. A., Itano, W. M., Wineland, D. J., & Monroe, C. (2000). Experimental entanglement of four particles. *Nature*, 404(6775), 256–259.

[232] Saskin, S., Wilson, J. T., Grinkemeyer, B., & Thompson, J. D. (2019). Narrow-line cooling and imaging of ytterbium atoms in an optical tweezer array. *Phys. Rev. Lett.*, 122, 143002.

[233] Sawant, R., Blackmore, J. A., Gregory, P. D., Mur-Petit, J., Jaksch, D., Aldegunde, J., Hutson, J. M., Tarbutt, M. R., & Cornish, S. L. (2020). Ultracold polar molecules as qudits. *New Journal of Physics*, 22(1), 013027.

[234] Sawant, R., Dulieu, O., & Rangwala, S. A. (2018). Detection of ultracold molecules using an optical cavity. *Phys. Rev. A*, 97(6), 063405.

[235] Scala, M., Militello, B., Messina, A., & Vitanov, N. V. (2010). Stimulated Raman adiabatic passage in an open quantum system: Master equation approach. *Phys. Rev. A*, 81(5), 053847.

[236] Schindewolf, A., Bause, R., Chen, X.-Y., Duda, M., Karman, T., Bloch, I., & Luo, X.-Y. (2022). Evaporation of microwave-shielded polar molecules to quantum degeneracy. *Nature*, 607(7920), 677–681.

[237] Schine, N., Young, A. W., Eckner, W. J., Martin, M. J., & Kaufman, A. M. (2022). Long-lived Bell states in an array of optical clock qubits. *Nature Physics*, 18(9), 1067–1073.

[238] Schlosser, N., Reymond, G., Protsenko, I., & Grangier, P. (2001). Sub-poissonian loading of single atoms in a microscopic dipole trap. *Nature*, 411(6841), 1024–7.

[239] Schmidt, M., Lassablière, L., Quéméner, G., & Langen, T. (2022). Self-bound dipolar droplets and supersolids in molecular bose-einstein condensates. *Phys. Rev. Res.*, 4, 013235.

[240] Schmidt-Kaler, F., Häffner, H., Riebe, M., Gulde, S., Lancaster, G. P. T., Deuschle, T., Becher, C., Roos, C. F., Eschner, J., & Blatt, R. (2003). Realization of the Cirac–Zoller controlled-NOT quantum gate. *Nature*, 422(6930), 408–411.

[241] Schmidt-Mink, I. & Meyer, W. (1985). Predissociation lifetimes of the $b^3\Pi u$ state of Li_2 and the accidental predissociation of its $A^1\Sigma_u^+$ state. *Chemical Physics Letters*, 121(1), 49–56.

[242] Scholl, P., Schuler, M., Williams, H. J., Eberharter, A. A., Barredo, D., Schymik, K.-N., Lienhard, V., Henry, L.-P., Lang, T. C., Lahaye, T., Läuchli, A. M., & Browaeys, A. (2021). Quantum simulation of 2D antiferromagnets with hundreds of Rydberg atoms. *Nature*, 595(7866), 233–238.

[243] Scholl, P., Shaw, A. L., Finkelstein, R., Tsai, R. B.-S., Choi, J., & Endres, M. (2023a). Erasure-cooling, control, and hyper-entanglement of motion in optical tweezers. arXiv:2311.15580.

[244] Scholl, P., Shaw, A. L., Tsai, R. B.-S., Finkelstein, R., Choi, J., & Endres, M. (2023b). Erasure conversion in a high-fidelity Rydberg quantum simulator. *Nature*, 622(7982), 273–278.

[245] Schuch, N. & Siewert, J. (2003). Natural two-qubit gate for quantum computation using the XY interaction. *Phys. Rev. A*, 67(3), 032301.

[246] Schuster, T., Flicker, F., Li, M., Kotochigova, S., Moore, J. E., Ye, J., & Yao, N. Y. (2021). Floquet engineering ultracold polar molecules to simulate topological insulators. *Phys. Rev. A*, 103(6), 063322.

[247] Seeßelberg, F., Luo, X.-Y., Li, M., Bause, R., Kotochigova, S., Bloch, I., & Gohle, C. (2018). Extending rotational coherence of interacting polar molecules in a spin-decoupled magic trap. *Phys. Rev. Lett.*, 121, 253401.

[248] Semeghini, G., Levine, H., Keesling, A., Ebadi, S., Wang, T. T., Bluvstein, D., Verresen, R., Pichler, H., Kalinowski, M., Samajdar, R., Omran, A., Sachdev, S., Vishwanath, A., Greiner, M., Vuletić, V., & Lukin, M. D. (2021). Probing topological spin liquids on a programmable quantum simulator. *Science*, 374(6572), 1242–1247.

[249] Shaffer, J. P., Chalupczak, W., & Bigelow, N. P. (1999). Photoassociative Ionization of Heteronuclear Molecules in a Novel Two-Species Magneto-optical Trap. *Phys. Rev. Lett.*, 82(6), 1124–1127.

[250] Shaw, A. L., Scholl, P., Finklestein, R., Madjarov, I. S., Grinkemeyer, B., & Endres, M. (2023). Dark-State Enhanced Loading of an Optical Tweezer Array. *Phys. Rev. Lett.*, 130(19), 193402.

[251] Shivam, S., Pokorny, F., Vazquez-Brennan, A., Sotirova, A. S., Leppard, J. D., Decoppet, S. M., Ballance, C. J., & Sondhi, S. L. (2024). Utility of virtual qubits in trapped-ion quantum computers. arXiv:2406.19332.

[252] Shuman, E. S., Barry, J. F., & DeMille, D. (2010). Laser cooling of a diatomic molecule. *Nature*, 467(7317), 820–823.

[253] Sievers, F., Kretzschmar, N., Fernandes, D. R., Suchet, D., Rabinovic, M., Wu, S., Parker, C. V., Khaykovich, L., Salomon, C., & Chevy, F. (2015). Simultaneous sub-Doppler laser cooling of fermionic ^{6}Li and ^{40}K on the D_1 line: Theory and experiment. *Phys. Rev. A*, 91(2), 023426.

[254] Singh, R. K., Senthilkumaran, P., & Singh, K. (2009). Tight focusing of vortex beams in presence of primary astigmatism. *J. Opt. Soc. Am. A, JOSAA*, 26(3), 576–588.

[255] Skomorowski, W., Pawłowski, F., Koch, C. P., & Moszynski, R. (2012). Rovibrational dynamics of the strontium molecule in the $A^1\Sigma_u^+$, $c^3\Pi_u$, and $a^3\Sigma_u^+$ manifold from state-of-the-art ab initio calculations. *The Journal of Chemical Physics*, 136(19), 194306.

[256] Smalley, R. E., Wharton, L., & Levy, D. H. (1976). Molecular optical spectroscopy with supersonic beams and jets. *Accounts of Chemical Research*.

[257] Sompet, P., Carpentier, A. V., Fung, Y. H., McGovern, M., & Andersen, M. F. (2013). Dynamics of two atoms undergoing light-assisted collisions in an optical microtrap. *Phys. Rev. A*, 88, 051401.

[258] Souza, A. M., Álvarez, G. A., & Suter, D. (2012). Robust dynamical decoupling. *Philosophical Transactions of the Royal Society A: Mathematical, Physical and Engineering Sciences*, 370(1976), 4748–4769.

[259] Steck, D. A. (2019). Cesium D line data.

[260] Stellmer, S., Pasquiou, B., Grimm, R., & Schreck, F. (2012). Creation of ultracold Sr_2 molecules in the electronic ground state. *Phys. Rev. Lett.*, 109, 115302.

[261] Stenger, J., Inouye, S., Andrews, M. R., Miesner, H.-J., Stamper-Kurn, D. M., & Ketterle, W. (1999). Strongly enhanced inelastic collisions in a Bose-Einstein condensatenear Feshbach resonances. *Phys. Rev. Lett.*, 82(12), 2422.

[262] Stevenson, I., Lam, A. Z., Bigagli, N., Warner, C., Yuan, W., Zhang, S., & Will, S. (2023). Ultracold Gas of Dipolar NaCs Ground State Molecules. *Physical Review Letters*, 130(11), 113002.

[263] Sundar, B., Gadway, B., & Hazzard, K. R. A. (2018). Synthetic dimensions in ultracold polar molecules. *Scientific Reports*, 8(1), 3422.

[264] Sundar, B., Thibodeau, M., Wang, Z., Gadway, B., & Hazzard, K. R. A. (2019). Strings of ultracold molecules in a synthetic dimension. *Phys. Rev. A*, 99(1), 013624.

[265] Taichenachev, A. V., Yudin, V. I., Ovsiannikov, V. D., & Pal'chikov, V. G. (2006). Optical lattice polarization effects on hyperpolarizability of atomic clock transitions. *Phys. Rev. Lett.*, 97, 173601.

[266] Takekoshi, T., Patterson, B. M., & Knize, R. J. (1998). Observation of Optically Trapped Cold Cesium Molecules. *Phys. Rev. Lett.*, 81(23), 5105–5108.

[267] Tan, Y., Wang, J., Wu, J., & He, Z. (2024). Real-time polarization compensation method in quantum communication based on channel Muller parameters detection. *Communications Engineering*, 3(1), 1–10.

[268] Tarbutt, M., Hudson, J., Sauer, B., & Hinds, E. (2009). Prospects for measuring the electric dipole moment of the electron using electrically trapped polar molecules. *Faraday Discussions*, 142(0), 37–56.

[269] Tarbutt, M. R. (2018). Laser cooling of molecules. *Contemp. Phys.*, 59(4), 356–376.

[270] Temelkov, I., Knöckel, H., Pashov, A., & Tiemann, E. (2015). Molecular beam study of the $a^3\Sigma^+$ state of NaK up to the dissociation limit. *Phys. Rev. A*, 91(3), 032512.

[271] Thompson, J. D., Tiecke, T. G., Zibrov, A. S., Vuletić, V., & Lukin, M. D. (2013). Coherence and Raman Sideband Cooling of a Single Atom in an Optical Tweezer. *Phys. Rev. Lett.*, 110(13), 133001.

[272] Thorsheim, H. R., Weiner, J., & Julienne, P. S. (1987). Laser-induced photoassociation of ultracold sodium atoms. *Phys. Rev. Lett.*, 58(23), 2420.

[273] Trautmann, J., Yankelev, D., Klüsener, V., Park, A. J., Bloch, I., & Blatt, S. (2023). $^1S_0 - ^3P_2$ magnetic quadrupole transition in neutral strontium. *Phys. Rev. Res.*, 5, 013219.

[274] Truppe, S., Williams, H. J., Hambach, M., Caldwell, L., Fitch, N. J., Hinds, E. A., Sauer, B. E., & Tarbutt, M. R. (2017). Molecules cooled below the doppler limit. *Nat. Phys.*, 13, 1173.

[275] Tully, J. C. (2000). Perspective on "Zur Quantentheorie der Molekeln". *Theoretical Chemistry Accounts*, 103(3), 173–176.

[276] Van Veldhoven, J., Bethlem, H. L., & Meijer, G. (2005). ac Electric Trap for Ground-State Molecules. *Phys. Rev. Lett.*, 94(8), 083001.

[277] Vandersypen, L. M. K., Steffen, M., Breyta, G., Yannoni, C. S., Sherwood, M. H., & Chuang, I. L. (2001). Experimental realization of Shor's quantum factoring algorithm using nuclear magnetic resonance. *Nature*, 414(6866), 883–887.

[278] Vexiau, R., Borsalino, D., Lepers, M., Orban, A., Aymar, M., Dulieu, O., & Bouloufa-Maafa, N. (2017). Dynamic dipole polarizabilities of heteronuclear alkali dimers: optical response, trapping and control of ultracold molecules. *Int. Rev. Phys. Chem.*, 36(4), 709–750.

[279] Vilas, N. B., Hallas, C., Anderegg, L., Robichaud, P., Winnicki, A., Mitra, D., & Doyle, J. M. (2022). Magneto-optical trapping and sub-Doppler cooling of a polyatomic molecule. *Nature*, 606(7912), 70–74.

[280] Vilas, N. B., Robichaud, P., Hallas, C., Li, G. K., Anderegg, L., & Doyle, J. M. (2024). An optical tweezer array of ultracold polyatomic molecules. *Nature*, 628(8007), 282–286.

[281] Wall, M. L., Hazzard, K. R. A., & Rey, A. M. (2015). *From atomic to mesoscale: The Role of Quantum Coherence in Systems of Various Complexities*, chapter Quantum magnetism with ultracold molecules.

[282] Wang, D., Neyenhuis, B., de Miranda, M. H. G., Ni, K.-K., Ospelkaus, S., Jin, D. S., & Ye, J. (2010). Direct absorption imaging of ultracold polar molecules. *Phys. Rev. A*, 81(6), 061404.

[283] Wang, H., Gould, P. L., & Stwalley, W. C. (1996). Photoassociative spectroscopy of ultracold ^{39}K atoms in a high-density vapor-cell magneto-optical trap. *Phys. Rev. A*, 53(3), R1216.

[284] Wang, K., Williams, C. P., Picard, L. R., Yao, N. Y., & Ni, K.-K. (2022). Enriching the Quantum Toolbox of Ultracold Molecules with Rydberg Atoms. *PRX Quantum*, 3(3), 030339.

[285] Wang, Y., Hu, Z., Sanders, B. C., & Kais, S. (2020). Qudits and High-Dimensional Quantum Computing. *Frontiers in Physics*, 8.

[286] Warner, C., Bigagli, N., Lam, A. Z., Yuan, W., Zhang, S., Stevenson, I., & Will, S. (2023). Efficient pathway to NaCs ground state molecules. *New Journal of Physics*, 25(5), 053036.

[287] Weidemüller, M., Esslinger, T., Ol'shanii, M. A., Hemmerich, A., & Hänsch, T. W. (1994). A Novel Scheme for Efficient Cooling below the Photon Recoil Limit. *Europhysics Letters*, 27(2), 109.

[288] Weinstein, J. D., deCarvalho, R., Guillet, T., Friedrich, B., & Doyle, J. M. (1998). Magnetic trapping of calcium monohydride molecules at millikelvin temperatures. *Nature*, 395(6698), 148–150.

[289] Wiederkehr, A., Schmutz, H., Motsch, M., & Merkt, F. (2012). Velocity-tunable slow beams of cold O_2 in a single spin-rovibronic state with full angular-momentum orientation by multistage Zeeman deceleration. *Molecular Physics*, 110(15-16), 1807–1814.

[290] Wineland, D. J. (2013). Nobel Lecture: Superposition, entanglement, and raising Schrödinger's cat. *Reviews of Modern Physics*, 85(3), 1103–1114.

[291] Wolf, F., Wan, Y., Heip, J. C., Gebert, F., Shi, C., & Schmidt, P. O. (2016). Non-destructive state detection for quantum logic spectroscopy of molecular ions. *Nature*, 530(7591), 457–460.

[292] Wu, Y., Burau, J. J., Mehling, K., Ye, J., & Ding, S. (2021). High Phase-Space Density of Laser-Cooled Molecules in an Optical Lattice. *Phys. Rev. Lett.*, 127(26), 263201.

[293] Wynar, R., Freeland, R. S., Han, D. J., Ryu, C., & Heinzen, D. J. (2000). Molecules in a Bose-Einstein condensate. *Science*, 287, 1016.

[294] Xia, T., Lichtman, M., Maller, K., Carr, A. W., Piotrowicz, M. J., Isenhower, L., & Saffman, M. (2015). Randomized Benchmarking of Single-Qubit Gates in a 2D Array of Neutral-Atom Qubits. *Phys. Rev. Lett.*, 114(10), 100503.

[295] Xu, K., Mukaiyama, T., Abo-Shaeer, J. R., Chin, J. K., Miller, D. E., & Ketterle, W. (2003). Formation of quantum-degenerate sodium molecules. *Phys. Rev. Lett.*, 91, 210402.

[296] Yan, B., Moses, S. A., Gadway, B., Covey, J. P., Hazzard, K. R. A., Rey, A. M., Jin, D. S., & Ye, J. (2013). Observation of dipolar spin-exchange interactions with lattice-confined polar molecules. *Nature*, 501(7468), 521–525.

[297] Yao, N. Y., Gorshkov, A. V., Laumann, C. R., Läuchli, A. M., Ye, J., & Lukin, M. D. (2013). Realizing fractional chern insulators in dipolar spin systems. *Phys. Rev. Lett.*, 110, 185302.

[298] Yao, N. Y., Zaletel, M. P., Stamper-Kurn, D. M., & Vishwanath, A. (2018). A quantum dipolar spin liquid. *Nat. Phys.*, 14(4), 405–410.

[299] Ye, X., Guo, M., González-Martínez, M. L., Quéméner, G., & Wang, D. (2018). Collisions of ultracold $^{23}Na^{87}Rb$ molecules with controlled chemical reactivities. *Science Advances*, 4(1).

[300] Yelin, S. F., Kirby, K., & Côté, R. (2006). Schemes for robust quantum computation with polar molecules. *Phys. Rev. A*, 74(5), 050301.

[301] Yu, Y. (2020). *Coherent Creation of Single Molecules from Single Atoms*. Doctoral, Harvard University.

[302] Yu, Y., Hutzler, N. R., Zhang, J. T., Liu, L. R., Hood, J. D., Rosenband, T., & Ni, K.-K. (2018). Motional-ground-state cooling outside the lamb-dicke regime. *Phys. Rev. A*, 97, 063423.

[303] Yu, Y., Wang, K., Hood, J. D., Picard, L. R. B., Zhang, J. T., Cairncross, W. B., Hutson, J. M., Gonzalez-Ferez, R., Rosenband, T., & Ni, K.-K. (2021). Coherent optical creation of a single molecule. *Phys. Rev. X*, 11(3), 031061.

[304] Zabawa, P. (2012). *Production of ultracold, absolute vibrational ground state NaCs molecules*. PhD thesis, University of Rochester.

[305] Zaharova, J., Tamanis, M., Ferber, R., Drozdova, A. N., Pazyuk, E. A., & Stolyarov, A. V. (2009). Solution of the fully-mixed-state problem: Direct deperturbation analysis of the $a\,^1\Sigma^+ \sim b\,^3\Pi$ complex in a nacs dimer. *Phys. Rev. A*, 79(1), 012508.

[306] Zeppenfeld, M. (2017). Nondestructive detection of polar molecules via Rydberg atoms. *EPL (Europhysics Letters)*, 118(1), 13002.

[307] Zhang, C. & Tarbutt, M. (2022). Quantum computation in a hybrid array of molecules and rydberg atoms. *PRX Quantum*, 3, 030340.

[308] Zhang, J. T. (2021). *Assembling an array of polar molecules with full quantum-state control*. Doctoral, Harvard University.

[309] Zhang, J. T., Picard, L. R. B., Cairncross, W. B., Wang, K., Yu, Y., Fang, F., & Ni, K.-K. (2022). An optical tweezer array of ground-state polar molecules. *Quantum Science and Technology*, 7(3), 035006.

[310] Zhang, J. T., Yu, Y., Cairncross, W. B., Wang, K., Picard, L. R. B., Hood, J. D., Lin, Y.-W., Hutson, J. M., & Ni, K.-K. (2020). Forming a single molecule by magnetoassociation in an optical tweezer. *Phys. Rev. Lett.*, 124, 253401.

[311] Zhang, S., Yuan, W., Bigagli, N., Warner, C., Stevenson, I., & Will, S. (2024). Dressed-State Spectroscopy and Magic Trapping of Microwave-Shielded NaCs Molecules. arXiv:2406.19308.

[312] Zhelyazkova, V., Cournol, A., Wall, T. E., Matsushima, A., Hudson, J. J., Hinds, E. A., Tarbutt, M. R., & Sauer, B. E. (2014). Laser cooling and slowing of CaF molecules. *Phys. Rev. A*, 89(5), 053416.

This thesis was typeset using LaTeX, originally developed by Leslie Lamport and based on Donald Knuth's TeX. A template that can be used to format a PhD thesis with this look and feel has been released under the permissive mit (x11) license, and can be found online at github.com/suchow/Dissertate.